Registration and Analysis of Thermal Images in Medicine

by

Lila Iznita Izhar

A Thesis submitted in fulfilment of requirements for
the degree of Doctor of Philosophy and Diploma of
Imperial College London

2014

Communications and Signal Processing Group
Department of Electrical and Electronic Engineering
Imperial College London

In the name of Allah, the Most Gracious, the Most Merciful

To my husband, Khairurrizal.

Thank you for your perseverance.

To the memory of my PhD supervisor, Professor Maria Petrou.

Abstract

Analyzing and interpreting of thermograms has been increasingly employed in the diagnosis and monitoring of diseases thanks to its non-invasive, non-harmful nature and low cost. This thesis explores methods for thermal image analysis systems based on image registration for two medical applications; skin disease diagnosis and cooling study. In the first application, a novel system is proposed to improve the diagnosis and monitoring of morphoea based on a face sketch and the published lines of Blaschko. In the latter, a novel semi-automated system is proposed to investigate a cooling mask for maxillofacial surgery patients based on thermogram data of normal subjects. In both applications, image registration based on global and local registration methods are found inevitable. A modified normalized gradient cross-correlation (NGC) method to reduce large geometrical differences between two multimodal images of different subjects that are represented by smooth gray edge maps is proposed for the global registration approach. To correct for small displacements between the global outcomes, a simple stochastic based non-rigid affine registration (NRAR) method is proposed. The NRAR method is driven by a cost function that takes into consideration the similarity between two images by a correlation coefficient. A geometric based intensity distortion to ensure only small distortions are accepted, and an overlapping pixel rate are also incorporated. Smooth deformation controlled by an exponential Euclidean based smoothing operator is employed to only edge pixels navigated by a distance function as both the images are represented by edge maps and thus reduces computation time. The NRAR method has shown good performance in correcting for small, varying displacements between images with fairly reliable flexibility and elasticity for both convex and concave objects with the help of the NGC to minimize the initial displacements. A semi-automated approach that includes the NGC and/or the NRAR method followed by determination of cooling area based on the Otsu's thresholding and a seed-based region growing method is found to achieve reliable and reproducible cooling patterns with good correlation with the clinical assessment, for potential cooling study of maxillofacial surgery patients.

Acknowledgement

All praise and glory is due to Allah s.w.t (God) who blesses me with His guidance and mercy in the search of knowledge and wisdom. With His will and mercy, I have been guided to all those great people who have helped and supported me in completing this thesis.

I would especially like to acknowledge my husband, Khairurrizal Zahudin for his love, support, encouragement, and prayers, my children, Muhd Afif Falah, Mimi Aidilia Izdihar, Mimi Nurzahirah Izdihar, Muhd Akif Faris (Late), Muhd Akif Fayyadh and Muhd Khairuzzaim Furqan for their love, to my mother, Maizul Aini Hj. Meor Yahya, my father, Hj. Izhar Hj. Saidin, my mother in law, Saripah Abdullah, and my grandfather, Hj. Saidin Tak, for their encouragement and prayers, and my siblings, Lila Amilia, Al Izaini, Lila Maslina, Al Izham, Lila Azima and Al Fitri for their prayers.

I am indebted to Professor Maria Petrou (Late) for accepting me in the doctorate program, for her exceptional supervision, support and guidance even during illness. Her kindness and wisdom will live forever in the memories of her. I express my deepest gratitude to Dr. Tania Stathaki for her outstanding assistance, support and guidance throughout the past 2 years towards the completion of this thesis. I owe much of my knowledge, discipline and passion for research to her and my late supervisor.

I am also grateful to Dr. Kevin Howell from the Royal Free Hospital who supplied me with data for the cooling study and for his expert advice, constant support, kindness and assistance. I would also like to extend my humblest gratitude to Dr. Imad Jaimoukha for his kindness, constant support and guidance towards the completion of this thesis. Special thanks are also due to Sithan Khanna for his many helpful comments and advice on the manuscript.

I am also thankful to the many friends I have made within the CSP Group; Dr. Khurom, Dr. Emi, Amanjit, Stratos, Zhou, Ali, Hamdi, Dr. David, Dr. Bokhari, Dr. Dahir, Sepideh, Dr.

Maria, Zati, Hana, Dr. Zaid, those contributed to the thermogram data, Miss Lauren and Ms. Hough. I also thank the community of Du Cane Housing, my colleagues at University Teknologi PETRONAS (UTP) and those who have been supportive and well-wishers to me in this phase of my life.

I am very fortunate to have been supported by UTP throughout my studies.

Contents

Abstract **3**

Acknowledgement **4**

Contents **6**

List of Figures **10**

List of Tables **22**

Abbreviations **24**

Statement of Originality **26**

Copyright Declaration **27**

1 Introduction **28**

1.1 Background and Motivation 30

1.1.1 The Physics behind Thermal Imaging - in application to medicine 30

1.1.2 Thermal Imaging in Morphoea in Children 33

1.1.3 Thermal-Enabled Therapy - hilotherapy cooling system 37

1.2 Thesis Aims and Objectives 40

1.3 Thesis Outline 41

1.4 Thesis Contributions 43

2 Thermal Imaging in Medicine **46**

2.1 Medical Thermal Imaging 47

2.2 IR Thermal Imaging in the Detection and Diagnosis of Various Medical Problems 52

2.2.1 Raynaud's Phenomenon 52

2.2.2 Assessment of Pain . . . 53
2.2.2.1 Diseases of the Skeletal and Neuromuscular Systems . . . 53
2.2.2.2 Headache and Migraine . . . 56
2.2.2.3 Vascular Related Disorders . . . 60
2.3 Data Processing Methods used in the Analysis of Medical Thermograms . . . 61
2.3.1 Extracting Indicators from Thermogram Images . . . 62
2.3.1.1 Image Segmentation for ROI Detection . . . 62
2.3.1.2 Asymmetry based Features . . . 72
2.3.1.3 Other Features . . . 79
2.3.2 Classification Methods . . . 82
2.3.3 Discussion on the Merits and Demerits of the Indicators Extraction Approach in Thermal Image Processing and Analysis . . . 85
2.3.4 Image Registration . . . 86
2.4 Conclusions . . . 87

3 Normalized Gradient cross-correlation (NGC) Method in Multimodal Image Registration 89

3.1 Method Overview . . . 92
3.2 Image Pre-Processing . . . 94
3.3 Phase Correlation (PC) . . . 100
3.3.1 Phase Correlation (PC) for Translation . . . 100
3.3.2 Phase Correlation (PC) for Scaling and Rotation . . . 101
3.4 Normalized Gradient Cross-Correlation (NGC) . . . 105
3.5 Results and Analysis . . . 107
3.5.1 Performance Analysis based on Artificial Image Pair . . . 109
3.5.2 Comparison Analysis between the NGC and the PC Methods . . . 113
3.5.2.1 Quantitative Analysis I . . . 115
3.5.2.2 Quantitative Analysis II . . . 122
3.6 A Hybrid NGC . . . 126
3.7 Discussion and Conclusions . . . 129

4 A Stochastic based Non-Rigid Affine Registration (NRAR) Method 133

4.1 Introduction . . . 134
4.1.1 Deformation Models . . . 135
4.1.2 Registration Metrics . . . 137

4.1.2.1 Similarity Measure Using Raw Image Intensities 137
4.1.2.2 Information based Similarity Measure 138
4.1.3 Resampling and Transformation 140
4.1.3.1 Neigbour Interpolation Methods 140
4.1.3.2 Triangulation of a Scattered/Irregular Point Set 143
4.1.4 Stochastic Approach for Optimization 144
4.2 Stochastic Non-rigid Affine Registration 145
4.2.1 The Methodology 145
4.2.2 Dissimilar Criterion (DC) 152
4.2.2.1 Explatory Runs for Parameters α and β in the Dissimilar Criterion (DC) 155
4.2.3 The Delaunay based Image Construction 157
4.2.4 Termination Criterion 159
4.3 Performance Analysis with Ground Truth Models 160
4.4 Potential Application in Morphoea 170
4.5 Discussion and Conclusions 173

5 Thermal Analysis for Cooling Study of Cryotherapy Techniques 175
5.1 Thermogram Data Acquisition for Cooling Study 177
5.2 Image Processing Approach 178
5.3 Determination of Cooling Areas (ROIs) 179
5.3.1 Manual Mask Approach 180
5.3.2 Semi-Automated Mask Approach 184
5.3.2.1 Seed-Based Region Growing (SRG) 187
5.3.2.2 Image Differencing 188
5.4 Results and Analysis 188
5.4.1 Anterior View based Cooling Study 189
5.4.1.1 The Hilotherapy System 189
5.4.1.2 Cooling with the Ice Pack 197
5.4.2 Left Lateral View based Cooling Study 205
5.4.3 Right Lateral View based Cooling Study 208
5.4.4 Left Lateral View vs. Right Lateral View vs. Anterior View 212
5.4.5 Comparison Analysis based on the Clinical Assessment 215
5.5 Discussion and Conclusions 221

6 Conclusions and Future Work **224**

6.1 Potential Diagnosis and Monitoring of Morphoea based on the Blaschko's Lines . 224

6.2 Cooling Pattern Identification and Analysis for Cooling Study based on Thermal Imaging 226

List of Figures

1.1 Simplified block diagram of an IR camera system. (Redrawn from [80].) 30

1.2 (a) A 10-year-old girl with scleroderma en coup de sabre along her left scalp, forehead, nose and chin. (b) Horizontal broad bands of localized scleroderma affecting the back of an 8-year-old girl. (c) Bow-shaped bands on the chest showing clear mid-line demarcation in a 10-year-old girl with extensive linear morphoea. Reproduced from [238]. 36

1.3 Example of thermograms of morphoea patients. 37

1.4 (a) Skin lesions of 38 patients with linear morphoea of the face obtained by manually plot the lesions based on clinical photographs.The distribution of these lines reveals a good visual correlation with the lines of Blaschko on the head and neck (b), as described by Happle and Assim [85]. Reproduced from [238]. 38

1.5 Some of the cooling masks (cuffs) available for different parts of body for the hilotherapy system 40

2.1 Factors affecting skin surface temperature. (Redrawn from Fujimasa [66].) 48

2.2 Thermograms showing inflammations (from yellow to red to white) in conjunction with various medical problems. (a) Headache with an allergy/sinus condition causing vascular dilation tracing the forehead leading to the right eye with inflammation and drainage from both eyes, more pronounced on the left side. (b) Lymph activation as a result of gum/dental inflammation. (c) Breast abnormalities. (d) Carotid artery inflammation, earliest stage indication of artery disease, years before occlusion. (Reproduced from [105], with permission.) 48

2.3 An application of IR imaging for breast screening: (a) healthy and (b) pathological breast. (Reproduced from Nicholas et al. [162], with permission). 51

2.4 A thermogram showing heat (hot spots are represented as red while cold spots are represented as blue) in the head and neck caused by migraine. (Reproduced from [105], with permission.) 58
2.5 Young woman with endometriosis (dotted circle) and colon dysfunction (solid circle). (Reproduced from [138], with permission.) 59
2.6 Segmentation of face region in a thermogram. (a) original thermogram; (b) extracted face region. (Reproduced from Akhloufi and Bendada [6], with permission.) 64
2.7 Segmentation of the hand in a thermogram. (Reproduced from Papez et al.[169], with permission.) 65
2.8 Segmentation of a hand in thermograms. Examples of (a) a successful segmentation and (b) an unsuccessful segmentation due to low contrast between the fingers and their background. (Reproduced from Herry et al. [91], with permission.) . . 66
2.9 Image segmentation results by Zhang et al. [249]. (a) Input image with low level of noise; (b) segmented low-noise image; (c) blurred and very noisy input image; (d) segmented blurred and very noisy image. (Reproduced from Zhang et al. [249], with permission.) 66
2.10 Segmentation results of breast thermograms. (Reproduced from Motta et al. [152], with permission.) 68
2.12 Example of asymmetry analysis: (a) difference image between left and right knee; (b) clusters found by thresholding the difference image. (Reproduced from Herry et al. [92], with permission.) 70
2.11 Morphological image segmentation process. (a) Original image; (b) coarse segmentation result; (c) marked image through the top-hat transformation by reconstruction at the breast scale; (d) refined result obtained by applying the "AND" operator to (b) and (c); (e) extracted marker through extended extrema transformation; (f) filtered heat patterns; (g) final segmentation result. See text for details. (Reproduced from Tang and Ding [223], with permission.) 71
2.13 Nonsymmetrical temperature distribution for pneumonia with corresponding X ray image. (Reproduced from Wiecek et al. [240], with permission.) 72
2.14 Region of interest of a thermal image and its histogram. (Reproduced from [240], with permission.) 73
2.15 Symmetrically located trapezoidal pairs of the affected and contralateral healthy side of a body. (Reproduced from Mabuchi et al. [141], with permission.) 74

2.16 (a) Abnormal thermogram with strong veining on the left breast; (b) normal thermogram with both breasts symmetrical without any hot spots or veins. (Reproduced from Zavisek [247], with permission.) 75
2.17 A Neural network example with inputs, two hidden layers, and an output layer ([169]). 83
2.18 Results of k-means clustering. (a) Original Image A; (b) original image B; (c) classified image A in labeled format; (d) classified image B in labeled format; (e) profiles of the mean value of pixels in each cluster for the left and right breast segments of classified image A; (f) profile of the mean value of pixels in each cluster for the left and right breast segments of classified image B. (Reproduced from Qi et al. [190], with permission.) 83

3.1 (a) Face thermogram as a reference image, (b) a drawing of the face or a face sketch as a target image (Reproduced from [238].) and (c) a face sketch with the Blaschko's lines that represent lesion patterns of linear morphoea (Reproduced from [238].) 90
3.2 Pre-processing of the face thermogram; (a) edge map obtained using Sobel edge detector, (b) edge map after thickening and (c) after the Gaussian smoothing. . . 96
3.3 Pre-processing of the drawing of the face; (a) inverse of the drawing, (b) after thickening and (c) after the Gaussian smoothing. 96
3.4 Resultant images after windowing using a Tukey window with $r = 0.6$ for (a) edge map of face thermogram and (b) the pre-processed drawing of the face. 98
3.5 1-dimensionalTukey windows in time domain and frequency domain for different r values. 99
3.6 Image overlay (a) before image registration is performed, (b) after removing of the scaling of the target image and (c) after translation is corrected (fully registered image) using the NGC method, between the face sketch and a face thermogram of Subject S4. 106
3.7 Image overlay (a) before image registration is performed, (b) after removing of the scaling from the target image, (c) after removing of the scaling and rotation from the target image and (d) after translation is corrected (fully registered image) using the NGC method, between the face sketch and a face thermogram of Subject S2. 107

3.8 The face sketch with the Blaschko's lines (a) prior to registration and (b) after registered to a reference thermal image. 108
3.9 Artificially created images (of equal size) to be compared by taking two cropped images from a bigger image with a difference in translation of (20, 20); (a) Reference image and (b) Target image. 109
3.10 The gray edge maps for the (a) reference image and the (b) target image. 110
3.11 After multiplication of the edge maps with a Tukey window for the (a) reference image and the (b) target image. 110
3.12 The inverse cross power spectrum with a significant peak at the translation between the two images. 110
3.13 Image overlay between the reformed target image (by translation) and the reference image. 111
3.14 (a) Original image as a reference image, (b) A replica of the original image after scaling, rotation and translation. 111
3.15 The inverse cross power spectrum of the two images and its maximum peak for finding the scale and angle of rotation based on the NGC method. 112
3.16 The inverse cross power spectrum of the two images and its maximum peak for finding the shift. 112
3.17 Result of accuracy analysis; image overlay for the target and reference images (a) before image registration is performed, (b) after down scaling of the target image and (c) after removing the translational difference from the target image (complete registration). 113
3.18 Result of accuracy analysis; image overlay for the target and reference images (a) after down scaling of the target image, (b) after undoing the rotation of the target image and (c) after removing the translation difference from the target image (complete registration). 114
3.19 Some examples of real data used for the multimodal registration; (a) training data of Subject S1 (no rotation needed); (b) training data of Subject S2 (rotation needed); (c) test data of Subject S9 (no rotation needed); (d) test data of Subject S8 (rotation needed). 114
3.20 Registration result for a training data (Subject S1) using the NGC method; (a) the reference thermogram, (b) its input gray edge map, (c) before registration, and (d) after registration. 115

3.21 Registration result for a training data (Subject S2) using the NGC method; (a) the reference thermogram, (b) its input gray edge map, (c) before registration, and (d) after registration. 116
3.22 Registration result for a training data (Subject S9) using the NGC method; (a) the reference thermogram, (b) its input gray edge map, (c) before registration, and (d) after registration. 117
3.23 Registration result for test data S8 using the NGC method (a) the original thermogram, (b) its input gray level edge map, (c) before registration, and (d) after registration. 118
3.24 Registration results using the PC method for (a) Subject S1 (at 9 am), (b) Subject S2 (at 9 am), (c) Subject S9 (at 10 am) and (d) Subject S8 (at 10 am). 119
3.25 (a) Manually traced outlines from a thermogram (Subject S9) and (b) its extracted traced lines; (c) another example of manually traced outlines from a thermogram (Subject S8) and, (d) its extracted traced lines. 120
3.26 An example of the procedure of selecting points of correspondences for both the (a) face sketch (target image) and (b) a face thermogram (reference image) . . . 124
3.27 An example of a bad registration result; (a) the original thermogram (Subject S6), (b) its input gray edge map, (c) after windowing and (d) overlay result between the registered sketch and the thermogram. 127
3.28 An example of a bad registration result; (a) the original thermogram (Subject S11), (b) its input gray level edge map, (c) after windowing and (d) overlay result between the registered sketch and the thermogram. 128
3.29 Improved registration results obtained by the NGC performed in the spatial domain for recovering the translational difference based on the NCC algorithm. (a),(d) Initial registration results. After translation recovery performed in the spatial domain; improved registration results in (b),(e) edge maps and (c),(f) in intensity image. 130

4.1 Neighbour based interpolation methods; (a) nearest neighbour interpolation, (b) bilinear neighbour interpolation and (c) bicubic neighbour interpolation. In these illustrations, black circles represent original pixel positions while white circles represent moved pixels at new non-integer locations. 140

4.2 Natural neighbour interpolation. (a) Voronoi diagram and Delaunay triangulation (dashed lines) in 2D (Reproduced from [132]. (b) The colored circles which represent the interpolating weights, w_i , are generated using the ratio of the shaded area to that of the cell area of the surrounding points. The shaded area is due to the insertion of the point to be interpolated into the Voronoi tessellation. (Reproduced/Excerpted from [156]) 142

4.3 Empty Circle (Sphere) Property: No other vertex is contained within the circumcircle (circumsphere) of any triangle (tetrahedron) (Reproduced/Excerpted from [46]) 144

4.4 A flowchart of the NRAR method with input edge maps, A and B. 146

4.5 Overlays between registered face thermogram (reference image) and the face sketch (target image) using only the NGC method shown (a) in gray edge maps and (b) in intensity image; (c) in intensity image with the Blaschko's lines. . . . 147

4.6 Overlays between a registered target image and its reference image after the proposed NRAR method is performed; (a) in gray edge maps and (b) in intensity images. 148

4.9 The processes involved prior to transformation/deformation of pixels in the randomly selected transform window in the NRAR method. 150

4.7 A distance transform image of the target image (i.e., the face sketch). Black pixels represent edge pixels while gray to white pixels represent non-edge pixels. 151

4.8 (a) The deformation field obtained after the registration with the NRAR method. (b) The same deformations are performed for the face sketch with the Blaschko's lines and overlayed with the face thermogram. 151

4.10 Registration results between a C shaped object (reference image) and a ring shaped object (target image); (a) Registered target image in edge map and (b) in its intensity image 156

4.11 An example showing a neighbourhood of 'o' pixels which are the old integer positions that are subjected to local transformations, '+' pixels that are only considered during interpolation and 'x' pixels with new pixel positions. New gray values are needed to be assigned to the old integer positions 'o' of the 8 moved pixels (central pixel is excluded). Delaunay triangulation is performed between the '+' and 'x' pixels followed by natural based interpolation to give new gray values to 'o' pixels [113]. 159

4.12 (a) Target image, (b) reference image and (c) deformed target image after the NRAR method is performed between the target image and the reference image based on their gray edge maps. 160
4.13 Image pair of Case 1; gray edge maps of the (a) reference image of a circle and (b) target image (translated version of the reference image). (c) Overlay between the reference image and the target image, (d) an absolute difference image between them. 161
4.14 Image pair of Case 1; intensity images of the (a) reference image of a circle and (b) target image (translated version of the reference image). (c) Overlay between the reference image and the target image, (d) an absolute difference image between them. 161
4.15 After the NRAR method is performed between the image pair of Case 1. Based on the gray edge map for (a) the registered target image, (b) overlay between the reference image and the registered target image, (c) its corresponding difference image. Based on the intensity image for (d) the registered target image, (e) overlay between the reference image and the registered target image and (f) its corresponding difference image. 162
4.16 Image pair of Case 2; gray edge maps of the (a) reference image of a square and (b) target image of a circle, (c) overlay between the reference image and the target image, (d) an absolute difference image between them. 163
4.17 Image pair of Case 2; intensity images of the (a) reference image of a square and (b) target image of a circle, (c) overlay between the reference image and the target image, (d) an absolute difference image between them. 163
4.18 After the NRAR method is performed between the image pair of Case 2; Based on the gray edge map for (a) the registered target image, (b) overlay between the reference image and the registered target image, (c) its corresponding difference image. Based on the intensity image for (d) the registered target image, (e) overlay between the reference image and the registered target image and (f) its corresponding difference image. 164
4.19 Image pair of Case 3; gray edge maps of the (a) reference image of a circle and (b) target image of a circle with some distortions at the top part of the circle, (c) overlay between the reference image and the target image, (d) a difference image between them. 165

4.20 Image pair of Case 3; intensity images of the (a) reference image of a circle and (b) target image of a circle with some distortions at the top part of the circle, (c) overlay between the reference image and the target image, (d) an absolute difference image between them. 165
4.21 After the NRAR method is performed between the image pair of Case 3; Based on the gray edge map for (a) the registered target image, (b) overlay between the reference image and the registered target image, (c) its corresponding difference image. Based on the intensity image for (d) the registered target image, (e) overlay between the reference image and the registered target image and (f) its corresponding difference image. 165
4.22 Image pair of Case 4; gray edge maps of the (a) reference image of a square and (b) target image of a circle, (c) overlay between the reference image and the target image, (d) an absolute difference image between them. 166
4.23 Image pair of Case 4; Intensity images of the (a) reference image of a C shaped object and (b) target image of a ring/ellipse, (c) overlay between the reference image and the target image, (d) an absolute difference image between them. . . . 166
4.24 After the NRAR method is performed between the image pair of Case 4; Based on the gray edge map for (a) the registered target image, (b) overlay between the reference image and the registered target image, (c) its corresponding difference image. Based on the intensity image for (d) the registered target image, (e) overlay between the reference image and the registered target image and (f) its corresponding difference image. 167
4.25 Resultant images for Case 4 using the FFD method. 169
4.26 Comparison of results obtained by the developed method (left) and the FFD method (right) for image pairs of cases 1 to 3. 170
4.27 (a),(b),(c),(d) Integrations between the face sketch with Blaschko's lines and face thermograms, (Left) before NRAR and (Right) after NRAR is performed. 172

5.1 Four regions of interest for extracting temperature data from the thermograms. (Reproduced from [100].) 176
5.2 Thermograms of the face of Subject 4 taken at 10 minutes during the hilotherapy cooling procedure in 3 views, (a) anterior, (b) left lateral, (c) right lateral. . . . 177
5.3 Thermograms of the face of Subject 4 taken at 10 minutes during the cooling procedure by ice compress in 3 views, (a) anterior, (b) left lateral, (c) right lateral. 178

5.4 (a) Baseline image of Subject 1, (b) During a hilotherapy cooling mask treatment procedure, and (c) Manually segmented mask on the baseline image of Subject 1 to form an atlas image 180
5.5 An example of intrasubject (same subject) analysis in the manual mask approach 182
5.6 A flowchart of the processes involved in the construction of a new atlas image for other subject (intersubject). 182
5.7 Manual mask approach (for same subject (Subject 1)); (a) overlay result between globally registered atlas image and a follow-up image, (b) globally registered mask overlaid on the follow-up image. 182
5.8 An example of obtaining a new atlas image for a different subject based on the atlas image of Subject 1 using the manual mask approach (between different subjects);(a) Overlay result between reference image (image to be analyzed) and target image (baseline image) after the NGC is performed and (b) overlay result between the reference image and the globally registered mask; In gray edge maps, (c) overlay result after the NGC method is performed, (d) overlay result after the NRAR method is performed to the globally registered target image; (e) Overlay result between the target image and a globally and locally registered mask to form a new atlas image for the new subject. 183
5.9 A flowchart of the processes involved in the semi-automated mask approach. . . . 184
5.10 Example of results obtained after image differencing and SRG are performed in the semi-automated mask approach;(a) Registration result between the baseline image of the subject and its follow-up image after 30 minutes of cooling treatment. (b) The resulting difference image between the two globally registered images. (c) Semi-automatically determined cooling areas before SRG is performed. Some unwanted regions can be seen as well. (d) Result after SRG is performed to give true ROI for cooling study. 186
5.11 Applying the SRG in selection of true cooling areas/ROIs in the semi-automated mask approach; (a) an absolute difference image, (b) the extracted ROIs obtained by thresholding of image (a). The arrows show the seed pixel placements for the SRG to select true ROIs from the extracted ROIs, and (c) the selected true ROIs overlayed onto the image to be analyzed (a follow-up image). 186
5.12 Cooling areas/ROIs determined based on (a) the manual mask approach and (b) the semi-automated mask approach for cooling with Hilotherm and (c) for cooling with the ice pack. 187

5.13 Resultant image overlays for follow-up images (at minutes 5, 10, 20, 30 and 35) of Subject 1 for hilotherapy mask. (a) Overlays between each follow-up image and its determined cooling area obtained using the manual mask approach; (b) Overlays between each follow-up image and its determined cooling area obtained using the semi-automated mask approach 190
5.14 Cooling patterns achieved by the manual mask approach for the first 4 subjects who underwent cooling with hilotherm, based on the change of (a) actual intensity and (b) actual temperature during the cooling procedure. 191
5.15 Cooling patterns achieved by the semi-automated mask approach for the first 4 subjects who underwent cooling with hilotherm, based on the change of actual (a) actual intensity and (b) temperature values. 192
5.16 Absolute change analysis; cooling patterns achieved by the semi-automated mask for the first 4 subjects who underwent cooling with hilotherm, based on the absolute (a) intensity and (b) temperature changes. 193
5.17 Comparisons between the cooling patterns obtained for cooling with the hilotherapy by the manual mask approach and the semi-automated mask approach for 4 subjects based on both the change of actual (a) intensity and (b) temperature values. 196
5.18 Cooling patterns achieved by the semi-automated mask approach for 8 subjects for cooling with the hilotherapy based on the change of actual (a) intensity and (b) temperature values. 198
5.19 Absolute change analysis; cooling patterns achieved by the semi-automated mask for 8 subjects who underwent cooling with the hilotherapy, based on the absolute (a) intensity and (b) temperature changes. 199
5.20 Cooling patterns achieved by the semi-automated mask approach for 12 subjects for cooling with the hilotherapy, based on the change of actual (a) intensity and (b) temperature values. 200
5.21 Absolute change analysis; cooling patterns achieved by the semi-automated mask approach for 12 subjects who underwent cooling with the hilotherapy, based on the absolute (a) intensity and (b) temperature changes. 201
5.22 Resultant image overlays for follow-up images (at minutes 5, 10, 20, 30 and 35) of the anterior view data of Subject 3 for the ice pack cooling study; (Left to right) The determined cooling areas obtained using the semi-automated mask approach for each of the follow-up image. 202

5.23 Cooling patterns achieved for the cooling with ice pack for 2 subjects based on the change of actual (a) intensity and (b) temperature, and based on the absolute (c) intensity and (d) temperature changes. 203
5.24 Cooling patterns achieved for the cooling with ice pack for 10 subjects based on the change of actual (a) intensity and (b) temperature, and based on the absolute (c) intensity and (d) temperature changes. 204
5.25 Resultant image overlays for follow-up images (at minutes 5, 10, 20, 30 and 35) of the left lateral view data of Subject 7; (a) overlay between registered baseline image and its follow-up images for each time-point, (b) the determined cooling area based on the semi-automated mask approach for each follow-up images. . . 205
5.26 Cooling patterns of the left lateral view data for 12 subjects based on the change of actual (a) intensity and (b) temperature values. 206
5.27 Absolute change analysis; cooling patterns obtained from analysis of the left lateral view data based on the absolute (a) intensity and (b) temperature changes. . 207
5.28 Resultant image overlays for follow-up images (at minutes 5, 10, 20, 30 and 35) using the right lateral view data of Subject 1; (a) Overlay between registered baseline image and its follow-up images for each time-point; (b) The determined cooling area based on the semi-automated mask approach for each follow-up images. 209
5.29 Cooling patterns obtained from analysis of the right lateral view data based on the change of actual (a) intensity and (b) temperature value. 210
5.30 Absolute change analysis; cooling patterns achieved for the cooling study with the hilotherapy mask for 12 subjects using the right lateral view data based on the absolute (a) intensity and (b) temperature changes 211
5.31 Comparison analysis between the two lateral view data of 12 subjects; (a) Intensity based analysis (the cooling patterns at the upper part represents absolute change analysis while the ones at the bottom represents actual intensity analysis), and (b) temperature based analysis (the cooling patterns at the upper part represents actual temperature analysis while the ones at the bottom represents absolute change analysis). 213
5.32 Comparison analysis between the lateral views and the anterior view data of 12 subjects based on intensity (the cooling patterns at the upper part represents absolute change analysis while the ones at the bottom represents actual intensity analysis). 215

5.33 Comparison analysis between the lateral views and the anterior view data of 12 subjects based on temperature (the cooling patterns at the upper part represents absolute change analysis while the ones at the bottom represents actual intensity analysis). 216
5.34 Comparison analysis for cooling with hilotherm (9 subjects) between the left lateral view and right lateral view data using the clinical assessment approach based on the change of actual temperature. 219
5.35 Comparison analysis for cooling with hilotherm (9 subjects) between the left lateral view and right lateral view data using the clinical assessment approach based on the temperature change. 219
5.36 Comparison analysis for cooling with hilotherm between the proposed semi-automated method (12 subjects, all the three views) and the clinical assessment approach (9 out of the 12 subjects, lateral left and right views) based on the change of actual temperature. 220
5.37 Comparison analysis for cooling with hilotherm between the proposed semi-automated method (12 subjects, all the three views) and the clinical assessment approach (9 out of the 12 subjects, lateral left and right views) based on the temperature change. 220

List of Tables

2.1 Medical Applications and IR Imaging Methods 50

2.2 Five diagnostic steps of clinical thermography. 74

3.1 Performance comparison between the NGC method and the PC method for Case A and Case B based on the under-detection error, e_u, and over-detection error, e_o obtained based on 7 images for each subjects. The best results for each case are shown in bold. 123

3.2 Performance comparison between the NGC method and the PC method for Case A and Case B based on the under-detection error, e_u, and over-detection error, e_o obtained based on 77 images from 11 subjects. 124

3.3 The average error between the scaling factor obtained by the semi-automated registration method and by the methods being compared; the NGC and the PC methods from 11 subjects (7 images for each subjects). The lowest and the highest average scale error for each method are shown in bold. 125

4.1 Results of the first explatory runs for the selection of parameters α and β for the DC used. The best result for each similarity metric is shown in bold. 157

4.2 Results of the second explatory runs (narrower range forβ) for the selection of parameters α and β for the DC. The best parameter β is shown in bold. 157

4.3 Average results for 5 runs for 3 pairs of parameters ($\alpha = 0.0005$ and $\beta = 0.001$, $\alpha = 0.1$ and $\beta = 0.001$, and $\alpha = 0.1$ and $\beta = 0.004$). The best parameters are shown in bold. 158

4.4 Registration result in average for all the 4 cases of registration problems, based on varying sizes of M for the NRAR method and varying sizes of control point grid for the FFD method. 168

5.1 The average maximum, minimum and median values based on the change of actual intensity and temperature values at 6 time-points obtained for the cooling study of the 12 subjects based on the left lateral view data. 208
5.2 The average maximum, minimum and median values based on the absolute intensity and temperature changes at 6 time-points obtained for the cooling study of the 12 subjects based on the left lateral view data. 208
5.3 The average maximum, minimum and median values based on the change of actual intensity and temperature values at 6 time-points obtained for the cooling study of the 12 subjects based on the right lateral view data. 209
5.4 The average maximum, minimum and median values based on the absolute intensity and temperature changes at 6 time-points obtained for the cooling study of the 12 subjects based on the right lateral view data. 209
5.5 Comparison analysis between two different views. 215
5.6 Clinically obtained results for cooling with hilotherapy mask based on the change of actual temperature values for the left lateral data. 217
5.7 Clinically obtained results for cooling with hilotherapy mask based on the change of actual temperature values for the right lateral data. 218
5.8 Clinically obtained results for cooling with hilotherapy mask based on the temperature change for the left lateral view data. 218
5.9 Clinically obtained results for cooling with hilotherapy mask based on the temperature change for the right lateral view data. 219

Abbreviations

CC Correlation Coefficient

DC Dissimilar Criterion

FFD Free-Form Deformation

FFT Fast Fourier Transfrom

FPA Focal Plane Array

GC Gradient Correlation

MI Mutual Information

NGC Normalized Gradient Cross-Correlation

NMI Normalized Mutual Information

NRAR Non-Rigid Affine Registration

PC Phase Correlation

PDF Probability Distribution Function

ROIs Region of Interests

SAD Sum of Absolute Differences

SRG Seed-Based Region Growing

SSD Sum of Squared Differences

Statement of Originality

I declare that this thesis is my own work. Where other sources of information have been used, they have been acknowledged. This thesis was not and will not be submitted to any other institution to fulfil the requirements of a degree.

Copyright Declaration

The copyright of this thesis rests with the author and is made available under a Creative Commons Attribution Non-Commercial No Derivatives licence. Researchers are free to copy, distribute or transmit the thesis on the condition that they attribute it, that they do not use it for commercial purposes and that they do not alter, transform or build upon it. For any reuse or redistribution, researchers must make clear to others the licence terms of this work.

Chapter 1

Introduction

Thanks to the advances in infrared (IR) thermal imaging technology, image processing techniques, and the pathophysiological understanding of thermograms, IR imaging is very suitable for use as a first-line supplement to both health monitoring and clinical diagnosis [106]. A thermal IR camera captures temperature/heat pattern radiated by the skin surface that can serve as important indicators in medical IR diagnostic [11, 12, 161, 163]. Nevertheless, a thermal image can be quite ambiguous due to its low spatial resolution. One of the ways to reduce this ambiguity is by incorporating information or data from different imaging sensors into a thermal image that also enables the information from a thermal image to be accessed more easily and more accurately [204].

To incorporate information into a thermal image based on image of different sensors, it is of vital importance to register/align these images into one coordinate system beforehand. Alignment between two or more images that can be of different imaging modalities, or taken at different times or angles into one coordinate system is commonly known as image registration [36, 72, 79, 253, 254]. Image registration can be performed using an entire image or based on locally adaptive, patch-based manner (e.g. neighborhood of pixels, control point grid). The first approach is commonly known as a global or a rigid registration method [28, 204, 13, 36] while the latter is known as a local or a non-rigid registration method [113, 126, 200, 201, 202, 213, 214, 217].

In this thesis, attempts are made to improve thermal imaging capabilities in two specific medical applications based on image processing and analysis techniques. The first application is with regards to diagnosis and monitoring of treatment efficacy of a skin disorder known as morphoea

[237, 238, 146]. Face thermograms of normal subjects acquired by a thermal camera are considered for this first application. For the purpose of increasing the low spatial resolution of the face thermograms and also to improve the access of information from the thermograms, this study proposes an integration between the thermograms and a face sketch realized by a global and a local registration methods. The integration with the face sketch also enables a set of lines known as the lines of Blaschko [16] that are reported to be highly correlated with patterns of linear morphea [238] to be incorporated into the thermograms for potential diagnosis and monitoring of treatment efficacy of morphoea as the same registration parameters obtained for the face sketch can also be used to register the set of lines to the thermograms. Both the global and the local registration methods proposed have shown to be successfully employed in the integration between these multimodal data.

On the other hand, the second application involves study of cooling treatment by a hilotherapy cooling mask [94] intend for determination of the optimal cooling configuration (cooling temperature and speed across cooling area) for maxillofacial post-surgery treatment based on thermal imaging. Since patient data is not accessible for this study, the experiments are carried out based on thermograms gathered from healthy control subjects. This second application also involves face thermograms but acquired in the clinical setting, in three different views (i.e., anterior view, left lateral view, and right lateral view) at 6 time-points from each subject for a cooling period of 30 minutes using the hilotherapy cooling mask and ice pack (for comparison purpose). A proposed semi-automated approach based on image registration methods and image processing and analysis techniques has successfully been employed in the cooling study. By the use of the computerised based approach, the subjectivity and tedious processes involved in the current clinical based cooling study [100], can be removed and the analysis time can be reduced.

In this chapter, the background and motivation leading to the research studies are described in three sections, namely the physics behind thermal imaging - in application to medicine, thermal imaging in morphoea in children and thermal enabled therapy - hilotherapy cooling system. Then, the objectives of the research studies followed by the structure and outline of the thesis are presented. Finally, the contributions of the thesis are summarized.

1.1 Background and Motivation

1.1.1 The Physics behind Thermal Imaging - in application to medicine

Thermography enables the noncontact measurement of an object's temperature to be displayed and recorded. Thermal imaging was initially designed for military purposes in the 1950s, mainly for night vision [80]. It was later used not only for night vision but also to increase situational awareness by enhancing the vision of military vehicle drivers through smoke, dust, light fog, and rain, as well as for target acquisition, surveillance, homing, and tracking. Its application, however, has been extended to engineering applications across a wide range of industries, such as in building inspection, electrical and mechanical automation, petrochemical industries, medicine and veterinary medicine, for more than 50 years now, as a result of the continual technological developments and improvements of the thermal imaging systems. Generally, thermal imaging applications can be categorized into four main areas: predictive maintenance, condition monitoring, problem diagnosis, and research and development.

In IR thermal imaging, a thermal camera system converts IR radiation (approximately $0.9\mu m$ to $14\mu m$ in wavelength), which is not detectable by the human eye, into a visual image that depicts thermal variation or heat pattern across an object or a scene [80]. All objects at temperatures above absolute zero emit IR radiation and the amount of the emitted radiation increases with temperature.

An IR camera system is similar to a digital video camera system (Figure 1.1). It consists of a lens that focuses IR onto a focal plane array (FPA) camera detector, composed of materials sensitive to IR wavelengths as well as electronics and software for processing and displaying the signals and images. The resolution range of the FPA is from about 160×120 pixels up to 1024×1024 pixels.

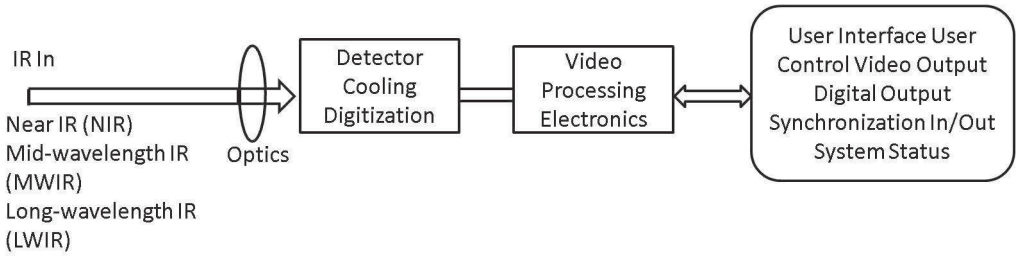


Figure 1.1: Simplified block diagram of an IR camera system. (Redrawn from [80].)

All objects above the temperature of absolute zero ($-273.15°C$) radiate energy to their surrounding environment in the form of electromagnetic waves; the waves move in all directions and at the speed of light [180]. This natural process is known as *thermal radiation* which does not require an intervening medium to carry it. The strength of the energy radiated/emitted by an object varies with its temperature, the distribution of the radiation wavelengths, the surface area, and the type of surface [80, 102]. An ideal object, which is called a *perfect black body*, does not reflect or transmit radiation from its surface or its body. It absorbs 100% of the incident radiation, which makes it a perfect absorber, and inversely it is also a perfect radiator/emitter of radiant energy.

The radiative properties of an object/material are expressed by its global emittance, or emissivity, ε. The global emissivity of a body is the ratio of the energy emitted by an isothermal radiating body over the energy emitted by a black body at the same temperature. It is a measure of the body's ability to radiate absorbed energy. Since a perfect black body is a perfect emitter, the value of its emissivity is 1 [56]. The emissivity at frequency ν, ε_ν, is defined in a similar manner just by considering radiation with frequencies in the interval $[\nu,\ \nu + d\nu]$. In thermal equilibrium, the emitted energy must be balanced by the energy absorbed by the surroundings of the body [111]. Kirchoff's Law states that for any uniform medium in thermal equilibrium, the emissivity and the absorption coefficient for any spectral range equals the ratio of the body's surface emissive power over the emissive power of a black body. This relationship serves to define the emissivity, ε_ν, of a body [111] as

$$\varepsilon_\nu \equiv \frac{E_\nu}{E_{b\nu}} \tag{1.1}$$

where E_ν is the body's surface emissive power at frequency ν, $E_{b\nu}$ is the emissive power of a black body at frequency ν, and ε_ν measures the fraction of the incident radiation absorbed per unit time by a thin layer of unit thickness at the same frequency. Hence, the emissivity, ε_ν, is a number between 0 and 1. The higher the emissivity of the object is, the better its radiative properties.

Planck's black body law describes the characteristics of the radiation emitted by an object in terms of its spectral radiant emittance. The spectral radiant emittance is also known as the *emissive power*. As a function of wavelength, Planck's law is written as [43, 76, 186]

$$E_\lambda = \varepsilon_\lambda \frac{2\pi hc^2}{\lambda^5}[\exp(\frac{hc}{\lambda kT}) - 1]^{-1} \quad Wcm^{-2}\mu m^{-1} \tag{1.2}$$

or in terms of the number of photons emitted as

$$P_\lambda = \varepsilon_\lambda \frac{2\pi c}{\lambda^4}[\exp(\frac{hc}{\lambda kT}) - 1]^{-1} \quad photons \quad s^{-1}cm^{-2}\mu m^{-1} \tag{1.3}$$

where:

h (Planck's constant) = 6.6261×10^{-34} J s.

c (speed of light in vacuum) = 2.9979×10^{8} ms^{-1}.

k (Boltzmann's constant) = 1.3807×10^{-23} WsK^{-1}.

λ = wavelength in μm.

T = temperature in degrees Kelvin (K).

ε_λ = the emissivity of the surface at a given wavelength.

E_λ = spectral radiant emittance/emissive power per unit wavelength and unit area $[Wcm^{-2}\mu m^{-1}]$.

Planck's equation describes the spectral characteristics of the source as a function of wavelength. The wavelength at which E_λ is maximum shifts to shorter wavelengths as the temperature of the object of interest increases. This peak wavelength is described by Wien's displacement law [76]

$$\lambda_{max} T = 0.002898 \tag{1.4}$$

where λ_{max} is the wavelength (in metres) of the maximum emissive power at temperature T (in degrees Kelvin). In accordance with Wien's displacement law, the emissive power of a black body decreases exponentially with temperature and the wavelength of the maximum emissive power moves to longer wavelengths as the temperature falls [111]. Because the black body is a perfect absorber and emitter, this implies that a black body absorbs and emits the maximum theoretically possible energy at a given temperature. The amount of radiation (total emissive power) emitted by a black body, E_b, is proportional to the 4th power of its thermodynamic temperature, T (also called absolute temperature, measured in degree Kelvin), as described by the Stefan-Boltzmann law [111, 180]

$$E_b = \sigma T^4 \tag{1.5}$$

where σ (the Stefan-Boltzmann constant) is 5.669×10^{-8} Wm^{-2} K^{-4}. The total emissive power from a black body, E_b (in Wm^{-2}) can also be obtained by integrating Planck's function over all wavelengths (from 0 to ∞) [185]. A *grey body* is an object that has a constant value for its

emissivity for all wavelengths [80]. For a grey body, the total emissive power, E_g, defined by the Stefan-Boltzmann law, takes the form

$$E_g = \varepsilon \sigma T^4 \tag{1.6}$$

which indicates that the total emissive power of a grey body, E_g, is the same as that of a black body, E_b, of the same temperature, reduced in proportion to the value of ε of the object [80]. However, most bodies are neither black bodies nor gray bodies but rather selective radiators. A *selective radiator* is an object with emissivity that varies strongly with wavelength. Nevertheless, it is often possible to treat objects as grey bodies as thermography operates only inside limited spectral ranges.

IR radiation emitted by the human skin is mainly in the range of $2 - 20$ μm wavelength and with an average peak at $9 - 10$ μm. It was found, with the application of Planck's equation and Wien's Law, that approximately 90% of the emitted radiation by humans is in the longer wavelengths ($6 - 14$ μm) [161]. Further, there is no difference in emissivity in black, white and burnt skin, whether measured *in vivo* or *in vitro*. Therefore, the temperature distribution or the measurements of the heat pattern recorded in an IR thermogram are from the outer surface layer of the skin and is independent of race [219].

Hence, it is useful to use thermal imaging to study underlying physiological changes that are associated with many type of diseases including inflammatory diseases, complex regional pain syndrome and Raynaud's phenomenon (further review in Chapter 2). Thermal imaging is shown to provide objective measurement of temperature changes that are clinically significant in certain medical application. With critical use of the technology and proper understanding of thermal physiology, thermal imaging can be a credible and accepted diagnosis tool in medicine [198].

1.1.2 Thermal Imaging in Morphoea in Children

Localized scleroderma (LS) or morphoea is a rare fibrosing disorder of the skin and underlying tissues as shown in Figure 1.2. Even though the disease is usually confined to the skin and subcutaneous tissues and of benign, it may involve underlying muscle and bone that could lead to irreversible structural deformities, joint contractures and severe functional, cosmetic and physiological disabilities [237, 238, 146]. This has caused morphoea to be severely debilitating as the lesions can affect limb growth when it crosses joint lines and extracutaneous features of

articular and neurologic can occur in significant proportion of children [237, 238, 146]. In a recent study of children in the UK and Ireland, the incidence of morphoea was 2.5/1 million children per year over a study period of 2 years (from 2005 to 2007) [88]. In an earlier study, the incidence of morphoea in adults and children was 2.7/100 000 population per year over a study period of 33 years (from 1960 to 1993) [176]. Even though the disease is quite uncommon, it is 20 times more common than systemic sclerosis/scleroderma (multisystem autoimmune disease) [236]. However, the epidemiological information of morphoea remains limited [238] but it is of value to know the prevalence of a disease so that planned services can be carried out appropriately, better diagnostic can be given by clinicians and clues to the etiology could be provided.

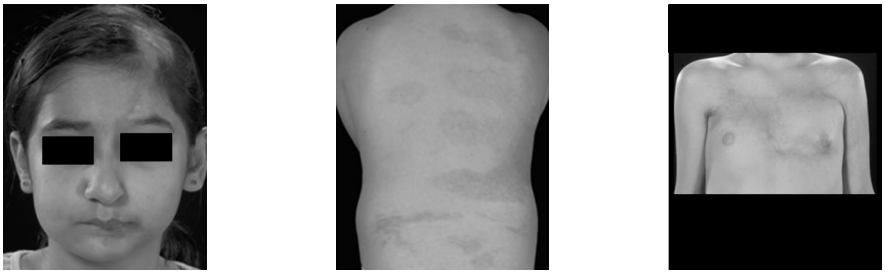
Morphoea in children can result in irreversible structural deformities, particularly when the lesions affect the face or the limbs resulting in joint contractures and limb length discrepancy. Hence, it is of paramount important to detect the disease in its early stage, especially in children so that treatment can be carried out to arrest the disease early in its course in order to avoid from the development of cosmetic and functional complications. This requires reliable and reproducible methods to detect disease activity (for evaluation of the need of treatment) and to evaluate treatment efficacy. To date, there are several skin scoring systems proposed and validated for systemic scleroderma (that also affects internal organ) based on skin thickening extension and its changes over time, but this system is found not applicable to isolated lesions [146]. This is because, the exact border of the lesion in morphoea is difficult to be defined that resulted in the serial measurement of the lesions conducted by this system becomes unreliable. This system also involves some subjective finding such as the sensation of warmth to touch that is used to suggest lesion activity.

Since the initial phase of morphoea can be characterized by inflammation (Figure 1.3) that is followed by progressive fibrosis, thermography imaging has been researched for its potential role in morphoea lesion detection [4, 15, 146]. The first study ever reported on the use of thermography in morphoea was conducted in 1987 by Allen [4] who suggested that thermography is likely to have application in monitoring the response to treatment. Their study showed that thermography was able to confirm on the clinical improvement after a cooling therapy of morphoea lesions is performed. In [146], thermographic assessments were compared with clinical descriptions of lesion activity recorded at the time of imaging. Based on the comparison results achieved, Martini et al. [146] reported that they find thermography to be 92% sensitive and 68% specific (higher in lesion examined within 2 years of onset) in detection of lesion activity with a high positive predictive value (0.87). Their results have demonstrated thermography as

a promising diagnostic modality in discriminating disease activity in clinical settings. However, they have suggested that the thermography diagnostic modality to not be applied to lesions with a severe degree of skin and subcutaneous fat atrophy that is usually found in old skin lesions [146, 237]. Since it is of great importance to detect morphoea in children at its early stage by the use of thermal imaging as the inital phase of morphoea lesion activity is related to inflammation, the limitation of thermography in being applied for severe degree of skin and subcutaneous fat atrophy will not be an issue.

Doctors in the Royal Free Hospital and the Great Ormond Street Hospital use thermal imaging to diagnose and monitor morphea activities in conjunction with clinical symptoms such as condition of morphea skin lesions [98, 99, 146]. They perform diagnosis and monitoring of morphoea based on temperature readings from affected regions that are represented as 'hot spots' in a thermal image of a morphoea patient. The temperature readings from the same regions are repeated over time for the purpose of monitoring the disease and its treatment efficacy. They also need to decide whether the affected regions identified previously look better (i.e., cooler) or worse (i.e., hotter) than before and whether these affected regions are extending. If there is no extension in this affected area for at least 2 to 3 years, the treatment is stopped. However, it is reported that there is a good evidence that to stop the treatment too early can cause the morphoea lesions to flare again [98, 99]. This current way in diagnosis and monitoring of the disease is based entirely on human judgment that leads to subjectivity in the analysis and diagnosis made. This method also suffers from false positives when old skin lesions are present as the skin has become thinner due to the reduction of fat in the affected regions [237, 238, 146]. By incorporating information from different image sensors such as from optical [98, 99, 204] (e.g. photograph of skin lesions) or magnetic resonance imaging (e.g. to capture subcutaneous fat reduction), false positives from old skin lesions can be avoided, subjectivity in diagnosis can be removed and thus the diagnosis of morphoea based on thermal imaging can be improved.

On the other hand, morphoea involves thickening of the dermis which results in a linear pattern of patches usually formed on the head, arms, trunk and legs [237, 238]. The linear patterns are seen to trace the Blaschko's lines [16], which are considered to correlate with genetic mosaicism [237, 238]. These lines are skin lines that are invisible under normal conditions and become apparent when some diseases of the skin or mucosa manifest themselves according to these patterns [wikipedia]. This correlation between the linear morphoea patterns and the Blaschko's lines was investigated by Weibel and Harper based on visual correlation alone [238]. In the assessment of disease activity in morphoea, Weibel and Harper [238] reported that inflammations

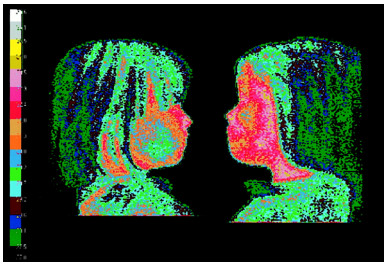


(a) (b) (c)

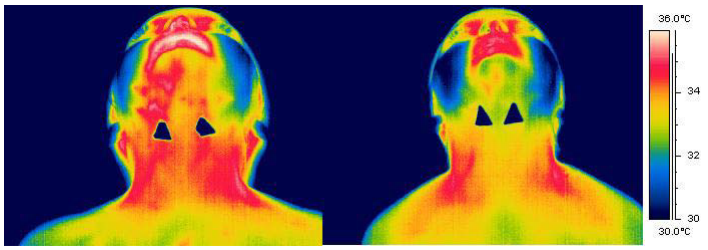
Figure 1.2: (a) A 10-year-old girl with scleroderma en coup de sabre along her left scalp, forehead, nose and chin. (b) Horizontal broad bands of localized scleroderma affecting the back of an 8-year-old girl. (c) Bow-shaped bands on the chest showing clear mid-line demarcation in a 10-year-old girl with extensive linear morphoea. Reproduced from [238].

that are associated with hardening of skin patches are able to be observed using thermal imaging system [237]. However, Howell et al. [98] has claimed that it is found difficult to specify a suitable region of interest (ROI) for temperature readings in morphoea since the lesion border is poorly defined in thermograms due to its low spatial resolution. Furthermore, Howell at al. also reported about an issue associated with follow-up readings of temperature for the same patients on whether the size of the previously specified ROI should be revised or not [98]. It is therefore found useful to cross-reference the resulting thermograms with visual images of patients or a body atlas, to increase the understanding of the anatomy affected by the disease and to investigate the efficacy of a treatment given to a patient [204]. Using thermal imaging with image processing and analysis and by utilizing the lines of Blaschko, there is a potential of diagnosing this disease automatically which can be less tedious, more reliable and accurate, repeatable and less subjectivity compared to the scoring systems or based on interpreting thermograms alone.

In this study, the lines of Blaschko (Figure 1.4) are utilized for potential diagnosis and monitoring of morphoea based on thermal image processing and analysis. This is aspired by the outcome of the study conducted by Weibel and Harper [238] as introduced earlier. The approach in this study is based on manually drawn morphoea lines on a standardized body chart according to clinical photographs of patients with morphoea skin lesions by a graphic artist. These plotted lines are then compared with the lines of Blaschko. Weibel et al. claimed that there is an excellent match between the distribution of morphoea lines and the lines of Blaschko based on the high visual correlation between the distribution of the recorded skin lesions and the original drawings of Blaschko achieved in 65 morphoea patients among children [238]. Weibel et al. also confirms that linear morphoea follows the Blaschko's lines based on the observation in the 65 patients [238]. The processes involved in the study can be simplified and automated by the use of thermal imaging, and image processing and analysis tools; clinical thermograms can be used instead of



(a) Area of hyperthermia over the left side of the face (image on the right) in a patient with active en coup de sabre scleroderma. Temperature range 27–36°C. Reproduce from [146].



(b) Example of a "thermography positive" lesion at the neck (left), which is "thermography negative" after five months of treatment (right). Reproduced from [98].

Figure 1.3: Example of thermograms of morphoea patients.

photographs to make use of the information from the underlying inflammation of the skin lesions at its early stage. Based on abnormal temperatures that correlates with morphoea, segmentation can also be performed to obtain underlying morphoea patterns from the thermograms. Then, these patterns can be compared with the lines of Blaschko to investigate their correlations. High correlation between the segmented heat patterns and the Blaschko's lines can be an important indicator for early stage diagnosis of morphoea. This proposed automated system is the first of its kind in diagnosis and monitoring of morphoea based on the findings in [238].

It is also worth mentioning that if a better morphoea analysis can be achieved by an automated system, other skin conditions can benefit from the system too. Dr. K. Howell of the Royal Free Hospital has identified a similar imaging problem seen in morphoea among patients involved in a new research drug trial who has experience skin inflammation.

1.1.3 Thermal-Enabled Therapy - hilotherapy cooling system

The registration between two images is also employed in another medical application; a study of cooling treatment based on healthy subjects intended for optimal cooling of maxillofacial surgery

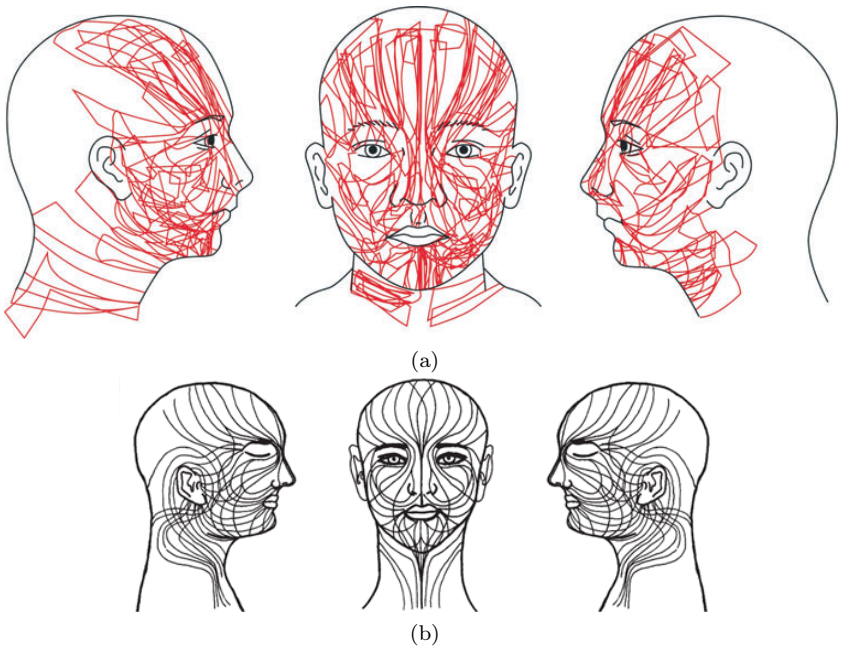


Figure 1.4: (a) Skin lesions of 38 patients with linear morphoea of the face obtained by manually plot the lesions based on clinical photographs.The distribution of these lines reveals a good visual correlation with the lines of Blaschko on the head and neck (b), as described by Happle and Assim [85]. Reproduced from [238].

patients. This section gives the overview of cooling therapy in medical application.

Water has been a source of cure since the ancient time; for either pain relief (i.e., to stimulate blood circulation) or treatment (to treat symptoms of certain diseases such as nerve pain, drug addicts) from its physical properties such as temperature and pressure. The use of water as a part of medicine is commonly known as hydrotherapy [23]. When a treatment involves cold water, a term called cryotherapy is used [151]. Cryotherapy is a form of hydrotherapy that originates from treating health problems by cold water immersion or ice bath commonly used by physical therapist, sports medicine facilities and rehabilitation clinics. The cold water is claimed to have components that could improve the return of blood flow and by-products of cellular breakdown to the lymphatic system and more efficient recycling [14, 151, 193]. For patients who have injuries or underwent surgeries, the underlying inflammation could also be reduced by cryotherapy by the use of ice packs to speed up the healing process [23].

When oedemas (swelling) and haemorrhages (bleeding) present, the oxygen and nutrient supply to the affected tissues are obstructed considerably [77, 94]. This causes circulation disorders to the sufferers. This leads to increase of metabolic speed as the tissue is overwarmed through inflammation of the affected area that resulted in a considerable increase in oxygen demand. As the damaged area is no longer supplied with the necessary amount of oxygen needed for

maintenance and regeneration, the affected area will suffer from lack of oxygen (due to ischemia) that could cause:

- Dying of further cells;
- Freeing of liquid-binding proteins which lead to additional oedema formation;
- Starting of a vicious circle that leads to hypoxic damage (effect from a condition of the body in which oxygen intake or use is inadequate);

To prevent ischemia, the need for oxygen of the damaged area should be reduced by reducing the temperature in the affected area by around $10°C$ in order to reduce the speed of the tissue metabolism by 50%. Hence, the amount of oxygen that is supplied to the affected areas is sufficient for regeneration. Apart from the oxygen supply, the return of by-products of cellular breakdown through lymphatic drainage is also as important. By a reduction in temperature of not below $15°C$, this function could be guaranteed. The level of reduction in temperature is difficult to be controlled just by the use of ice packs. The negatives of a cooling treatment found in the use of ice packs are such as disturbance of lymphatic drainage for temperature below $15°C$, disruption of the microcirculation for temperature below $10°C$ and disruption of nerve function that could cause ischemic damage to tissues for temperature that reach below $5°C$.

However, the use of cold water for the healing process of post-surgery, injured and/or traumatized tissue could be improved by replacing ice packs with a cooling system based on hilotherapy cooling masks (Figure 1.5) [14, 100, 151, 193]. The hilotherapy cooling system is designed with the aim to achieve reduction in swelling and bleeding, that resulted in reduction of pain without any negative effects [94]. The hilotherapy achieves this by means of water, which circulates in a closed-loop circulation system through anatomically formed cuffs with the water temperature being set to the exact value needed for any period of time (without temperature deviations). The cuffs are available for a variety of head, face and body areas as single-use or multiple-use as shown in Figure 1.5. Many studies have reported on the efficiency and the benefits of hilotherapy as the ideal solution for traumatic, pre- and post-operative healing in many medical sectors such as traumatology orthopedics, oral and maxillofacial surgery, ENT (ear, nose and throat) therapy, plastic/aesthetic surgery, rheumatology, urology to name but a few [14, 100, 101, 151, 193]. However, in most of the studies conducted, the efficiency of hilotherapy is investigated by the



Figure 1.5: Some of the cooling masks (cuffs) available for different parts of body for the hilotherapy system

reduction in swelling and pain intensity and duration recorded using a 3D optical scanning device (FaceScan3D), by neurologic complaint using pinprick test, by duration of hospital admission and by filling of questionnaires by patients, doctors and medical attendants [150]. It is claimed by Howard et al. that not only there is no quantitative study based on the cooling speed achieved by the hilotherapy application but the actual temperature achieved across the cooling area are also not known [100]. As hilotherapy is considered as a thermal-enabled therapy, thermal imaging can be used for both qualitative and quantitative studies of the cooling effect of hilotherapy as performed by Howell et al. [100]. In [100], using the FLIR (forward looking infrared) thermal camera and software, the effectiveness of hilotherapy is investigated based on the cooling patterns achieved during the cooling procedures performed in comparison to the ice compress [100]. The study also found that hilotherapy was markedly more effective than the ice compress in cooling all the four facial skin regions specified. It is also reported that the result is reproducible for maxillofacial post-surgery treatment. However, data from only one subject for each cooling method was compared in the study.

In this thesis, based on face thermogram data acquired from healthy control subjects, a pioneer work in developing a semi-automated system based on image registrations and image processing and analysis techniques for the study of cooling treatment is proposed. The proposed system could reduce subjectivity in the current clinical based cooling study [100] to a great extent. Furthermore, it could also assist clinicians in identifying the optimal cooling configuration for maxillofacial post-surgery treatment based on the hilotherapy system with better accuracy, shorter time and in a simpler way.

1.2 Thesis Aims and Objectives

In this section, a brief summary of the thesis's objectives and aims are given as follows:

- To improve the low spatial resolution of a thermal image by incorporating information from different imaging modalities by means of image registration methods both global (i.e., rigid) and local (i.e., non-rigid), and image processing approach towards an automated system for potential detection and monitoring of morphoea based on the Blaschko's lines.

- To improve the capability of thermal imaging as a useful tool for facial cooling study with cryotherapy techniques by pioneering a semi-automated method that is able to not only produce reliable analysis in less time and in a much simpler and easier way but also able to reduce the subjectivity in the current clinical based approach. The proposed method should also be able to show that the hilotherapy cooling system is better than ice pack in cooling treatment and that the result should be able to be reproduced for maxillofacial post-surgery patients.

1.3 Thesis Outline

Chapter 2 provides a thorough literature survey in the area of thermal imaging in medicine as a mean of motivation towards the studies presented in this thesis. This chapter reviews the physics behind thermal imaging and its applications in medicine so far. Two major approaches in the extraction of information or interpreting of thermal images are identified: physics based approach, where models of heat transport are adopted and used to infer physiological parameters, and image processing based approach where features are extracted from the image and used as cues to the identification of various conditions of the human body. However, only the latter is discussed in this chapter as the first approach is beyond the scope of study of this thesis. This chapter aims to show how thermal imaging has become another important and useful tool in medicine, especially by incorporating image processing and analysis in developing an automatic system for diagnosis or monitoring of medical problems. Reviews for a numerous type of diseases and medical conditions have been given in terms of the useful thermal properties identified for each problem as well as the approach and limitations in detecting and analyzing these properties based on image processing and analysis techniques that can be found to date. However, some of the reviews are not included in this chapter but can be found in Lila and Petrou [106].

Chapter 3 presents a global based registration method in aligning between two images of different modalities i.e., between face thermogram and a face sketch with and without the Blaschko's lines, to not only improve the current clinical based diagnosis and monitoring of morphoea and its treatment efficacy but also for potential early detection of the disease. First, a background introduction to this chapter is given, followed by some surveys on image registration methods. Then, the methodology of the global registration method employed is explained. The global registration method is a modification of a normalized gradient cross correlation (NGC) method developed in [231]. Some changes are made to fit the method into our application that involves registration between two images that are not only acquired by different imaging modalities but also of different subjects. The challenge that exists in the global registration between these images is mainly due to the local differences in the images that are not of the same subject. However, since there is also large geometrical differences between them, a global or rigid registration method is found necessary to remove these differences prior to the removal of small, and varying differences between them by a local or non-rigid based registration method (presented in Chapter 4). The face thermogram data used in this chapter is taken from healthy subjects while the face sketch used is a drawn image of a face taken from Weibel et al. [238]. The pre-processing of the images to be registered in order to bring them into the same image representation is also explained in this chapter. Then, the modified NGC method employed is described and its performance in the registration of this type of image pair is compared against a phase correlation method. This chapter also proposed a hybrid NGC method to improve on the recovering of translational differences by the modified NGC method especially for registrations that involve very low contrast thermograms (especially between jawline and neck area) where the method has failed by using a normalized cross-correlation (NCC) technique in the spatial domain. The hybrid NGC approach that includes computation in both the Fourier and the spatial domain is also discussed in a later part of this chapter.

Chapter 4 describes a local registration method based on a simple stochastic affine based non-rigid registration (NRAR) method performed to fine-tune the alignment achieved by the global NGC method especially by reducing small, and varying differences that are still present between the globally registered images. First, each of the components in the NRAR method such as its deformation model, the interpolation method employed (based on Delaunay triangulation), the registration metric and the selection of its parameters, is briefly reviewed in general. Then, the methodology of the NRAR method is explained and discussed in depth. This method is a modification and integration of non-rigid registration approaches employed in Kovalev and

Petrou [126], Bejo [213], and Karamitrou [113]. Finally, the performance of the NRAR method is analyzed based on four artificially created image pairs with different levels of registration problems which are considered as ground truths. Some registration results for the morphoea application are also presented in a later part of the chapter.

Chapter 5 describes a proposed semi-automated approach that consists of the developed image registration methods and some image processing and analysis techniques for study of cooling treatment using cryotherapy techniques based on thermal imaging. In the beginning of the chapter, cooling treatments based on the hilotherapy cooling system and the conventional ice pack are briefly discussed and compared. First, the chapter describes the methodologies of two cooling analysis approaches proposed and investigated for the cooling study; based on (1) manually drawn mask and (2) semi-automatically extracted mask (the selected method for the cooling study). In both the approaches, the use of the NGC and/or the NRAR registration methods is/are involved. In the cooling study, registration is performed between two face thermograms of the same subject (intrastudy) as well as of different subjects (interstudy), taken at six intervals of time. The aim of the registration between the two thermograms in this application is mainly to determine the area involved during the cooling procedure (cooling areas/ROIs) based on their intensity information. Then, statistical parameters from these cooling areas are extracted from both the intensity and the temperature data in order to obtain the patterns of changes in both temperature and intensity. The patterns of increase and decrease in the statistical values obtained during a cooling procedure are also known as *cooling pattern* in this chapter. Using the cooling patterns obtained, comparison analysis surrounding the cooling study are presented.

Finally, the thesis is concluded in Chapter 6. In this chapter, the contributions of the thesis are laid out based on the two applications presented in the thesis; (1) morphoea application and (2) cooling study application. Some suggestions for future work for each application are also discussed.

1.4 Thesis Contributions

In this section, the contributions of the thesis are summarized as follows:

- A stochastic, affine based non-rigid registration method to match elastically between two

globally registered multimodal images is proposed. This is in contrast to a non-rigid registration method based on solving for the unknown transformation parameters that uses control points and spline based interpolation methods. The proposed method is motivated by the fact that it is developed to cater for small and varying local deformations. Without having to use any analytical methods, the affine parameters are randomly selected from a range of value that is kept small to ensure only small deformations are applied. The use of control points or point grid can also be avoided in the proposed method as transformation only takes place when the central pixel of an image patch (transform window) selected randomly is an edge pixel. This has resulted in less data being considered for local deformations without compromising on the registration output. This is also to avoid large changes in the information carried by pixels that lie on object's surface (i.e., the skin surface). In terms of the interpolation method used, since the transformed/moved pixels in an image patch are scattered, it is more suitable and efficient to use the Delaunay triangulation based intensity interpolation method to give the vacant pixels new values. All these employed approaches have enable the method to elastically solve for small and varying differences in shapes and contours as long as the overlapping area between the images exist, with less computation complexity and time. The methodologies of the method are described in Chapter 4.

- A new integration between face thermogram and a face sketch is proposed to improve the low spatial resolution of a face thermogram.

- A new integration between face thermogram and a set of lines known as the Blaschko's lines is proposed for a potential development of an automated system for diagnosis and monitoring of morphoea in order to remove subjectivity and to improve the current diagnosis system.

- A new approach to improve the performance of the modified NGC method is proposed especially in recovering translational differences based on a hybrid NGC method. By replacing the phase correlation performed for solving translational differences in the spatial Fourier domain in the modified NGC method with the normalized cross-correlation (NCC) technique performed in the spatial domain, better accuracy in registration between a low contrast thermogram and a face sketch can be achieved.

- A semi-automated system is proposed to improve the current clinical approach in cooling study with cryotherapy techniques especially for the hilotherapy cooling mask system

based on thermal imaging. The analysis obtained by this system is also reproducible for investigation of the optimal cooling configuration for the hilotherapy cooling system for maxillofacial post-surgery treatment. The proposed system is based on the developed global NGC and/or the NRAR methods and image processing and analysis techniques. By using this system, subjectivity, time and tedious processes involved in the current clinical approach can be reduced to a great extent.

- A new representation of thermogram as a smooth gray edge map that enables good registration between a thermogram and an image of different imaging modality is proposed. Not only the amount of data to be processed during a registration procedure can be reduced that resulted in less computation time, performance of image registration can also be improved even for monomodal registration (Chapter 5) as the edge pixels carry salient information of an image (as described in Chapter 3) .

- A modified NGC method that is performed based on gray edge maps is proposed. Sobel operator is chosen to extract the gradient images of both input images as the operators are known to give good performance in detecting edges in low noise images like the thermal image involves in this study. For the first FFT in the modified NGC, image gradients are combined by taking the magnitudes of the gradients for both the images while for the second FFT, image gradients are combined in a complex representation.

- An extensive review of thermal imaging in medicine is laid out as appeared in L. Izhar and M. Petrou, "Thermal Imaging in Medicine", *Advances in Imaging and Electron Physics*, 171(2):41–114, 2012.

Chapter 2

Thermal Imaging in Medicine

Thermal imaging technology has made significant advances in the recent years. Its use in military has been already widespread, but less so in medicine. This chapter reviews thermal imaging applications in medicine so far in order to provide more detailed background of thermal imaging and analysis in medical application and to highlight the number of ways this imaging technique can be employed to realize automated or non-automated system to assist in disease diagnosis and monitoring that is also the center of motivation of this research study. Two major approaches used to extract information from thermal images are identified: physics-based approaches, where models of heat transport are adopted and used to infer physiological parameters, and image processing-based approaches, where features are extracted from the image and used as cues to the identification of various conditions of the human body. The first type of method requires the knowledge of the values of some physiological parameters, in order to work out the values of others, as well as the use of carefully designed models. A review of this method can be found in [106]. The second type of approach is phenomenological, ignoring the underlying physics that contribute to the appearance of the image, and working only with the collected data. This makes such approaches easier to use, but the derived measurements are related only indirectly to the actual physiological measurements of the imaged tissue.

This chapter is structured as follows. In Section 2.1, a brief review of the physiological principles behind thermal imaging in medicine is presented. In Section 2.2, the way thermal imaging is used to diagnose various medical conditions is discussed. In Section 2.3, the methodologies used to analyze medical thermograms based on image processing approaches are reviewed. This chapter

is concluded in Section 2.4.

2.1 Medical Thermal Imaging

Physiology is the study of the functions in a living creature. Medical IR imaging enables the investigation of the physiology of human tissue and body. This is possible because the mechanical, physical, and biochemical functions of humans involve heat. Heat regulation or thermoregulation is presented as a physiological way of handling metabolic heat, instead of temperature regulation [241]. The skin is the largest organ in the human body that performs thermoregulation to maintain the core temperature of the body by modifying heat transfer from the body to the environment and vice versa. Body thermoregulation employs all three mechanisms of heat transfer, namely conduction (through the tissue layers), convection (through the vascular system) and radiation (mainly to and from the environment) (see Figure 2.1). The complicated physiological processes in heat transfer include blood circulation, sweating, metabolic heat generation and, sometimes, heat dissipation via the hair or fur above the skin surface [161]. In Figure 2.1, it is shown that an IR image can be obtained from the heat radiated by the skin surface. The skin in this figure is divided into three layers, namely the skin surface or epidermis (the skin outermost layer), the cutaneous tissue or dermis and the deep body tissue or the subcutaneous tissue [38]. It is shown that heat dissipates to the environment through convection, radiation and evaporation (from sweating that occurs on the skin surface). In the box underneath the skin surface, the separation between the cutaneous tissue layer and the deep body tissue layer is shown by a dashed line. Here, it is also shown that the heat transfers between the two layers is carried out by conduction and in particular by tissue conduction and blood flow conduction. The box with a dashed outline below the deep body tissue layer represents the control mechanisms in each segment of the body, namely the vasomotor adjustment i.e. vasoconstriction (narrowing of the blood vessels that can result in retaining heat) and the evaporative cooling mechanism by sweat production. Via the central nervous system or regional reflex arch and the signals to the segmental vasomotor center, two sets of thermoreceptors, namely the peripheral receptors in the dermis or epidermis and the central receptors in the hypothalamus, provide temperature information to the thermoregulatory center. Sensory receptors such as nociceptor, vasopressor, chemoreceptor and mechanoreceptor enable the skin to sense pain, pressure, touch, vibration, chemical substance, and so on [38].

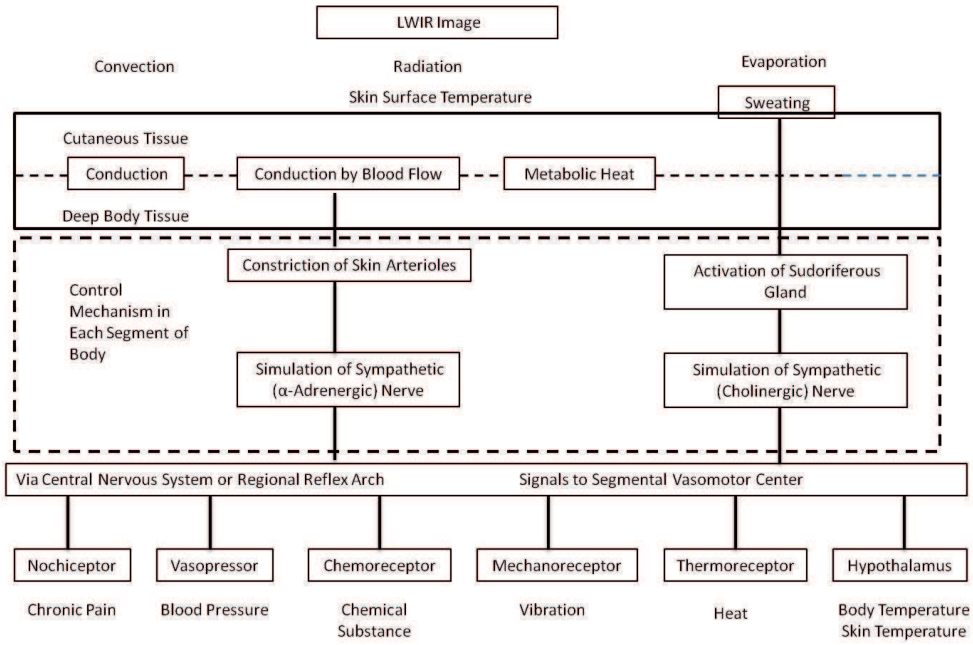
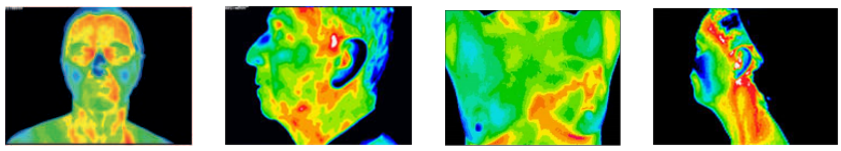


Figure 2.1: Factors affecting skin surface temperature. (Redrawn from Fujimasa [66].)

Abnormalities in human physiology or any changes of normal mechanical, physical, and biochemical functions either by a disease or resulting from an abnormal syndrome are under the study of pathophysiology. A definition of *pathophysiology* is "the study of the biological and physical manifestations of disease as they correlate with the underlying abnormalities and physiological disturbances" [37]. The pathophysiology of thermal behaviour of the human skin can be manifested in two principal modalities [8]: (1) pathological changes in the spatial distribution of temperature over the skin surface and (2) pathological changes in the dynamic behaviour (i.e. warming, cooling or periodic modulation of temperature of a given sub-area of the skin). The temperature gradient in the human skin is in the range of 0.2°C to 0.5°C/mm and much higher close to a malignant tumor. The temperature of a disease-affected region is reported to be $0.7° - 1°$C above that of the normal regions due to slow blood circulation [11].



(a) (b) (c) (d)

Figure 2.2: Thermograms showing inflammations (from yellow to red to white) in conjunction with various medical problems. (a) Headache with an allergy/sinus condition causing vascular dilation tracing the forehead leading to the right eye with inflammation and drainage from both eyes, more pronounced on the left side. (b) Lymph activation as a result of gum/dental inflammation. (c) Breast abnormalities. (d) Carotid artery inflammation, earliest stage indication of artery disease, years before occlusion. (Reproduced from [105], with permission.)

Apart from local changes in heat production as a symptom of pathological processes, changes in the blood flow pattern of the affected organs or tissues are also important indicators used in medical IR diagnostics [12]. Hot spots or inflammation (increased metabolism) and cold spots (decreased metabolism) in thermograms can be manifested as abnormalities (Figure 2.2); that is, showing places of cancer development or deficit blood flow [163]. A hot spot is usually the precursor to many cancers and other degenerative diseases, such as arthritis, infections, sympathetic nerve malfunction, heart disease, stroke, diabetes, and high blood pressure [163]. Hot spots are usually related to tumors, as blood flow to a tumor usually increases at the early stages due to the growth of new blood vessels from the pre-existing vessels (angiogenesis) [12, 111, 250].

The blood flow rate, structure of subcutaneous tissue and activities of the sympathetic nervous system, which regulate heat dissipation from the body surface, determine the skin temperature. This enables the noninvasive detection of many physiological functions from thermograms by IR thermal imaging [66]. In digital thermography, changes of radiant heat in a human body as small as 1/100th of a degree can be measured. This allows the detection of alterations in the human microcirculation caused by pain, which are nearly impossible or very difficult to be detected with other imaging modalities, such as X rays, computed tomography (CT) or magnetic resonance imaging (MRI) [89]. Wilson and Spence (1988) proposed the use of the cold stress test as a way of to obtain more reliable estimates of physiological parameters. This test involves touching the skin with a cold metal object. They observed that after a cold stress test, the skin of a normal limb reheats faster than the skin of an ischemic limb. This also shows that the rate of increase of skin temperature following the transient cold challenge is independent of thermoregulatory or environmental factors and thus gives a more reliable estimate of physiological parameters. These measurements can also serve as indicators that can reveal signs of tumors, toxins and diseases months or even years earlier than traditional imaging procedures [2].

Long-wavelength IR or body IR rays that are usually measured for diagnostic purposes occupy a narrow band at wavelengths of 8μm -12μm. Thermal IR (TIR), which is another terminology that is widely used in medical thermal imaging, covers wavelengths beyond $\sim 1.4\mu$m, which is primarily heat or thermal radiation, and hence the term *thermography* [191]. TIR imaging is a leading and growing technology due to its advantages such as being nonintrusive, noninvasive, nondestructive, radiation-free, fast, and cost effective compared with other anatomical imaging modalities such as X rays, CTs, MRIs and so on. [12, 66, 111, 124, 206].

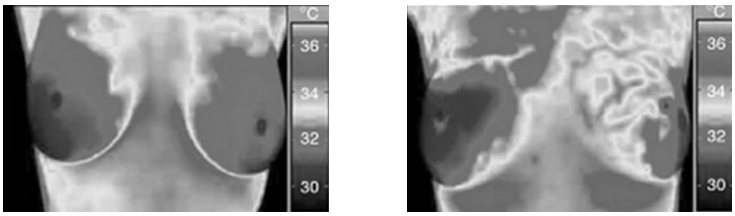
The instrumentation of medical thermal imaging using IR has recently been improved with increased thermal resolution, implementation of digital signal processing, and the introduction of new matrices of FPA detectors [163]. These have made the medical thermal imaging systems more sensitive, fast, and economic with standardized image format for processing purposes, and highly portable, supporting real time imaging. This has led to the increased use of thermal imaging as a tool for diagnostic imaging procedures, particularly for early detection of various diseases, including breast cancer, fibrocystic breast disease, benign tumors, cancer in other parts of body, mastitis, and diabetes, as well as physical injuries, often before they can be detected by standard medical tests (see Figure 2.2) [3, 65, 82, 87, 149, 158, 161, 188, 189, 208].

The onset of several other conditions - such as migraines, headaches, back pain, leg pain, sinusitis, lower extremities vessel disease, nerve problems, respiratory dysfunctions, cardiovascular and circulatory disorders and many others - may also be detected [10, 11, 12, 24, 37, 31, 33, 35, 40, 74, 206, 208]. The major medical areas in which IR thermography is being used successfully are neurology, vascular disorders, rheumatic diseases, tissue viability, oncology (especially breast cancer), dermatological disorders, neonatal, ophthalmology, and surgery [111]. IR thermography has also been successfully applied during the most recent epidemic of atypical pneumonia (SARS) at airports and is useful for monitoring asthma, allergies, bronchitis, influenza, and so on. It is usually considered as a physiological test that measures physiological changes and functioning of the body (i.e. normal and abnormal physiological functions of the nervous, vascular, and muscular systems and local inflammatory processes) compared with CT imaging, X rays or mammography, which are considered as anatomical tests that assess the structure of the body [161]. IR thermography can thus serve as a complement to standard anatomical investigations based on X rays and three-dimensional (3D) scanning techniques such as CT and MRI [112]. Table A list of current medical applications and IR imaging methods is given in Table 2.1 [162].

Table 2.1: Medical Applications and IR Imaging Methods

Applications	**IR Imaging methods**
Oncology (breast, skin, etc.)	Static (classical)
Pain (management/control)	Dynamic (DAT, subtraction)
Vascular Disorders (diabetes, DVT)	Dynamic (active)
Arthritis/rheumatism	Multispectral/hyperspectral
Neurology	Multimodality
Surgery (open heart, transplant, etc.)	Sensor Fusion
Ophthalmic (cataract removal)	
Tissue viability (burns, etc.)	
Dermatological disorders	
Monitoring efficacy of drugs and therapies	

There is a contralateral symmetry or uniform and symmetric temperature variations in the skin temperature distribution in a healthy subject, as shown in Figure 2.3a, while an asymmetry above a certain level, such as abrupt variations in temperature, is a strong indicator of an abnormality, as shown in Figure 2.3(b) [89, 111, 161, 209]. It has been found that the average temperature difference in corresponding areas of interest on both sides of the body is only 0.24°C for healthy subjects [111]. The peripheral parts of the body, where small temperature changes are more readily detected, have been mostly successfully examined by IR thermography because they are away from the central or core region of the body [11, 86, 111]. As the temperature of extremities is largely dependent on peripheral blood flow vessels, IR thermal imaging is also very useful in relation to vascular diseases [11, 12, 111].



(a) Healthy (b) Pathological

Figure 2.3: An application of IR imaging for breast screening: (a) healthy and (b) pathological breast. (Reproduced from Nicholas et al. [162], with permission).

In general, thermologists interpret thermograms in terms of identification and quantification of abnormalities to evaluate the severity of the diseases. Thermography is very useful in investigating abnormalities in impaired persons or children who could not report pain or discomfort in any part of their bodies in words or point out the level of pain on a specific scale. Physicians usually make a diagnosis based on symptoms that are reported by the patients. Hence, patients with difficulties in explaining their symptoms and infants tend to be misdiagnosed or under diagnosed. With the aid of a thermogram, the early detection of any abnormalities or inflammation in such patients could help save lives. However, it is not easy to interpret accurately the underlying physiological condition from a particular given temperature, because a thermogram is usually affected by changes in the body's thermoregulatory state or other factors, such as damage, pressure, and age, that can influence these physiological processes and the thermal properties of the skin [161, 241]. In addition, thermogram interpretation is very difficult due to variations in temperature distribution that may be very subtle. Interpretation primarily depends on the expertise of the individual thermologist. Therefore, thermogram interpretation tends to be subjective and labor intensive.

In conclusion, the study of the abnormalities in thermograms and the study of the heat exchange processes of the human body can provide information on the pathology of the underlying diseases [66, 161]. To overcome the subjectivity involved in human interpretation, it is desirable to develop automated image-processing systems to aid in the interpretation of thermograms, particularly for early detection of abnormalities.

2.2 IR Thermal Imaging in the Detection and Diagnosis of Various Medical Problems

This section presents the wide application of IR thermal imaging in the detection and diagnosis of various medical problems that are related to symptoms that can be presented by the underlying vascular system such as cancers, Raynaud's syndrome, neuropathic pain, skeletal and neuromuscular diseases, vascular disorder, migraine to name but a few. In this section, the reviews for some of these diseases are given. More reviews on other diseases can be found in [106].

2.2.1 Raynaud's Phenomenon

Raynaud's phenomenon (RP) is a disease that involves a painful vasoconstriction of small arteries and arterioles of extremities (i.e., fingers and toes) that may follow a cold or some emotional stress. It is estimated that 4 to 15% of the population has evidence of RP. The feeling of extreme cold and pain in the extremities following exposure to low temperatures, which lasts for 10 to 15 minutes, is usually associated with changes in skin color [234]. This disease can be primary (PRP) or secondary to scleroderma (SSc) and can be associated with a connective tissue disease [148]. It may also precede the development of systemic autoimmune disorders, particularly scleroderma, by many years and evolve into secondary RP. Hence, it is crucial to distinguish between PRP and SSc and to establish proper therapies for patients. As the temperature of the skin is indirectly affected by the changes in RP, IR thermography is one tool that can be used for its investigation [197, 234].

Merla and Romani [148] developed a quantitative diagnostic application that is now routinely used in clinical settings, particularly in discriminating SSc from idiophatic finger thermoregula-

tory incompetence. The algorithms developed are further discussed in [106]. It is reported that, based on the results obtained, IR thermography provides highly effective diagnostic parameters. Furthermore, the method is not only highly sensitive, but also highly specific in discriminating different conditions of the same disease.

2.2.2 Assessment of Pain

Nociceptive pain (caused by stimulus) can be categorized under neuropathic and *somaesthetic* (somatic) pain [97]. Neuropathic pain is usually associated with thermal (vasomotor) changes, involving the neurovascular structure, leading to different types of pain, such as causalgia, deafferentation, and sensitization, as well as abnormally evoked pain, such as hyperphatic regional pain and allodynic pain evoked even by minimal tactile simulation. However, this is not the case for somatic pain, as it is usually not accompanied by circulatory dysfunction but by involvement of afferent somatic nerves. The main diagnostic tools applied to the management of somatic pain have been the anatomical tests such as MRI and CT scans and physiological tests such as electromyography (EMG) and nerve conduction velocity (NCV) tests [97]. Most neuropathic and some nociceptive pain pathologies are associated with an alteration of the thermal distribution in the form of hyperthermic (hot) or hypothermic (cold) regions. Hence, the neurovascular involvement in neuropathic pain requires tests such as IR thermal imaging and quantitative sudomotor axon reflex test (QSART) that address autonomic (i.e., thermal) changes for a more accurate diagnosis and treatment [97].

2.2.2.1 Diseases of the Skeletal and Neuromuscular Systems

Inflammation - that is, pain, swelling, heat redness, and loss of function - is a complex phenomenon that may be triggered by various forms of tissue injury [198]. In rheumatology the assessment remains complex due to the absence of any single parameter for routine investigation, even though the increase in heat can be detected by touch when a joint is acutely inflamed [196]. Objective assessment by imaging modalities, such as CT scan, positron emission tomography (PET) and MRI, may yield special quantitative indicators but these modalities are limited because of their invasive nature. IR imaging, on the other hand, with the advancement of modern technology has proven to be reliable and useful in rheumatology [198]. Studies by Collins and Cosh [32] and Rings and Collins [196] showed that the surface temperature of an arthritic joint was related to the intra-articular joint and other biochemical markers of inflammation obtained from the exudates. In a thermal stress test for inflamed knees, Ring and Ammer [198] showed

that the mean temperature of the anterior surface of the knee joint could be measured either by IR radiometry or quantitative thermal imaging. In a series of experiments with different analogs of prednisolone (all corticosteroid drugs), the duration and degree of reduction in inflammation could be determined by the temperature measured by thermal imaging in groups of patients.

Ring and Collins [196] and Collins et al. [33] devised a system to facilitate the use and understanding of joint temperature changes based on the distribution of isotherms from a standard region of interest. They compiled a thermal index to represent the mean temperature difference from a reference temperature. Many of the clinical trials involved the monitoring of hands, elbows, knees, and ankle joints from a large study of 600 normal control subjects. The normal index figure obtained from control subjects ranged from 1 to 2.5 on this scale. In inflammatory arthritis, this figure was increased to $4-5$, while in osteoarthritic joints, the increase in temperature was usually less, $3-4$, and in gout and infection higher values were obtained, namely, $6-7$. However, it is very difficult to determine normal values of finger joints because not only are cold fingers not necessarily a pathological finding, but also because of wide overlap in readings from nonsymptomatic and symptomatic joints observed, even though tender joints tend to be warmer than nontender joints. In the near future, a normal range for finger joint temperatures may be established by the evaluation of finger temperatures from a reference database of normal thermograms of the human body [33, 196].

In chronic inflammation of bone or osteitis deformans, an increased skin temperature over an active site of this disease is frequently observed, of $\sim 4°C$ [198]. In other cases, in almost all areas examined an increase in peripheral blood flow was observed. During the active stage of the disease, the periosteal vascularity is also increased and may lead to a high risk of cardiac failure. In clinical trials conducted in Bath, United Kingdom, on treatment monitoring, it was reported that relapse and the need for retreating could be clearly indicated by thermal imaging [198]. The relation between the degree of bone pain and the level of increased temperature was also shown. In areas where the bone was very close to the skin surface, at the tibia, the most dramatic temperature changes could be observed. With the help of a mathematical model, the increase in temperature measured over the tibia was shown to be primarily derived from osseous (bony) blood flow, instead of metabolic heat, and thus it was categorized as a metabolic bone disease.

In soft tissue rheumatism, pathological conditions such as muscle spasms or myofascial trigger points may become visible as regions of increased temperature [198]. Thermal imaging can

also recognize acute muscle injuries as areas of increased temperature due to inflammation in the early states of trauma. Reduced skin temperatures have been related to osteoarthritis of the hip or frozen shoulder. Sprains and strains, enthesopathies, tennis elbow, golfer elbow, and fibromyalgia can also be diagnosed by IR thermal imaging. In stress fracture of bone, thermography can provide the same diagnostic prediction as bone scans [198].

IR thermal imaging has also been used in the study of peripheral nerve diseases, such as carpal tunnel syndrome, nerve entrapment syndrome, radiculopathy, and thoracic outlet syndrome [8, 198]. When using thermal imaging to diagnose carpal tunnel syndrome, the dorsal side of the hand is reported to be of greater importance than the palmar side of the hand [169]. In addition, IR thermal imaging is regarded as the only technique that can objectively confirm the subjective symptoms of the mild thoracic outlet syndrome and thus was successfully used in the evaluation of the treatment for this pain syndrome [198]. However, thermal imaging did not identify all reasons for temperature deficit shown in patients with several causes for the symptoms of paraesthesia and coldness of the ulnar fingers. In radiculopathies, the diagnostic value of thermal imaging is still under debate. In a review, Hoffman et al. [95] concluded that IR thermal imaging for lumbar radiculopathy should be used only for research and not in clinical routine, based on the evaluation of 28 papers selected from a total of 81 references. Nevertheless, thermography was found to be of high value for the diagnosis of both lumbosacral and cervical radiculopathies in studies by Kim and Cho [117] and Zhang et al. [248]. However, in these studies, healthy control subjects were not mentioned in the study of lumbosacral radiculopathy, the clinical symptoms were not described, and the thermographic diagnostic criteria used were found not reliable. Mabuchi et al. [141], analyzed the underlying physiological condition of the abnormal hypothermal regions in radiculopathy by making comparisons between the abnormal thermal regions with anatomical territories, such as the sensory dermatomes and the shape of muscle, and the regions in which the patients complained of pain or numbness. The results revealed that the hypothermal region, indicated by the developed image-processing method, corresponded to the shape of the muscles innervated by the involved nerve roots rather than to the sensory dermatome of the involved nerve root.

IR thermal imaging has also been reported to facilitate the early diagnosis of the complex regional pain syndrome (CRPS). Early diagnosis of this condition leads to a higher recovery rate [35, 198]. The epicenter of the damaged area is usually hyperthermic and, in some cases, the hyperthermia persists due to permanent damage of the sympathetic nerve fibers. However, IR thermal imaging, like any other test, does not have 100% diagnostic sensitivity due to confusion

and misunderstanding of its parameter changes due to neurovascular instability. CRPS type I is a potentially disabling condition characterized by regional pain that is often disproportionate to or occurs in the absence of an identifiable inciting event [35]. It is usually associated with hyperalgesia, edema, spontaneous pain, abnormal skin color, changes in skin temperature, abnormal sudomotor activity, allodynia, active and passive movement disorders, and trophic changes in nail and hair, and usually develops after minor or major trauma to soft tissue. Functional IR imaging is effective in detecting the thermal signature of vasomotor disturbances, which are an important factor in establishing a diagnosis of CRPS Type I. Early detection of the disease is for the success of the treatment, yet the detection at an early stage of the disease is very difficult due to the similarity of the signs and symptoms with other pathologies. However, several studies have supported the utility of IR thermal imaging in early detection; most have used quantitative homologous side-to-side temperature differences as the sole criterion in establishing the diagnosis.

In advanced stages of diabetic neuropathy, the disease is complicated by neuroinflammatory changes, fractures, and foot ulcers. The changes in thermograms in these patients are the prototypical examples of nerve damage causing irreversible hyperthermia in different degrees.

Finally, IR thermal imaging has also been used as the predictor of early signs of deterioration of ulcers and trophic fracture [35].

2.2.2.2 Headache and Migraine

Migraine is a syndrome diagnosed by a certain combination of signs and symptoms [182]. Poul-Erik [183] defined migraine or hemicrania, meaning unilateral headache, as recurrent attacks of headache associated with gastrointestinal and visual disorders. Migraine can be divided into three types: exploding headache (intracranial pressure), imploding headache (extracranial pressure), and ocular headache (pressure behind the eyeball). In classic migraines, the patient experiences an aura that involves changes in visual perception [182]. In addition, prodromal symptoms with visual disturbances (aura) due to ischemia in the retina are usually observed. The pain usually starts in the eye region and spreads toward the vertex or toward the other eye. It is typically accompanied by nausea, emesis, photophobia, and scintillating scotoma. The forehead, eye sockets, and maxillary sinuses are the areas medicallly essential for headache diagnosis [147]. Migraines affect six million people in the United Kingdom - more than asthma, diabetes and epilepsy combined [49]. However, proper diagnosis has yet to be discovered, which

causes migraines to be mistreated or undertreated [49, 199].

Migraine headaches have typical characteristics, such as unilateral location, pulsating quality (throbbing or varying with the heartbeat at rest or with movement), moderate or severe intensity, and aggravation by routine physical activity in addition to associated features of nausea, photophobia (sensitivity to light), phonophobia (sensitivity to sound), and exacerbation with head movement [199, 137]. This may cause the cerebral blood vessels, which are innervated by sensory fibers of the trigeminal nerve, to dilate. This leads to plasma protein extravasation, neurogenic inflammation, and activation of meningeal nociceptors that cause a pain response to be conveyed to the brain stem. The brainstem and spinal cord centers that are the first to receive the pain impulses from the trigeminal nerve are hypothesized to become sensitized, with a resultant worsening of headache and increased sensitivity to environmental and other stimuli as the migraine progresses [42]. Migraine headaches begin with the brain stem emitting signals to the blood vessels lining the brain, requesting these blood vessels to dilate and expand. The mechanisms within the brain that give rise to the intolerable migraine pain began more than three hundred years ago and include the vascular theory, neurovascular theory and the hypothalamus theory [25]. According to the vascular theory, the throbbing nature of migraine pain has long been regarded as a vascular disorder. However, based on modern imaging, vascular changes are found not to be linked to the migraine pain and therefore migraine should be regarded as a neurovascular headache [7]. So, the exact pathophysiology of migraine is unknown but is believed to be a neurovascular disorder involving dysfunction of the trigeminovascular system [40, 69]. For example, the study reported by David et al. [49, 40] focuses on evidence of physiological activation in the trigeminal system using functional MRI (fMRI).

The main role of the physical examination of migraine is to screen for life threatening conditions, such as intracranial hemorrhage or tumors [182]. Ammer [7] discussed the studies conducted for migraine and headaches using thermal imaging and stated that in the mid-1960s face thermography was used to assess cerebrovascular disease but it was first used in headache patients only in the 1970s. It was shown then that a low temperature on the affected side of the forehead was observed in 80% of patients with acute migraine attacks [131]. Increased blood flow velocities measured by Doppler flow were also found to be correlated with higher temperature in patients successfully treated for cluster headache [127]. A study from Italy found asymmetric facial temperature distribution in 58% of patients during a migraine attack and in 15% between attacks. However, a hot spot at the internal angle of orbita was claimed to be observed more frequent than thermal asymmetry in migraine patients [7, 175]. Ammer [7] stated that the highest inter-

est for thermal imaging as a research tool in headache investigations was during the 1980s with interest starting to decline in the 1990s. Figure 2.4 shows a thermogram of a migraine patient that shows heat in the head and neck caused by a migraine.

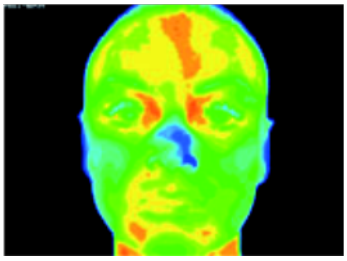


Figure 2.4: A thermogram showing heat (hot spots are represented as red while cold spots are represented as blue) in the head and neck caused by migraine. (Reproduced from [105], with permission.)

Drummond and Lance [50] concluded that in the 1980s, thermal imaging contributed in the findings of dilatation of the superficial temporal artery and its branches, and its role in pain generation in migraine. The authors also described the thermal pattern as an area of low temperature in the affected orbital region, which may spread above and below the eye, down the nose, and to the affected temple in some patients with cluster headache. A typical thermal pattern in patients with cluster headache was also described by Kudrow [127]: two warm vertical lines contralateral to the painful side, mainly between the pain attacks. Drummond and Lance [50] also reported the thermographic findings from 186 patients during 209 separate attacks of headache affecting the anterior part of the head. However, clear relationship between clinical symptoms and temperature changes has not been obtained [7]. Throbbing headaches are associated with low temperatures over the affected fronttemporal region and cheek. Moreover, the supra-orbital region was cooler on the affected side in patients who experienced nausea and on the opposite side in patients who vomited. Edmeads [53] speculated that the utility of thermography might be a marker for vascular headache. Based on the statistical analysis of thermograms from 275 patients and 45 controls without headache, Swerdlow and Dieter [221] concluded that patients with vascular headaches displayed a significantly greater number of cold spots than did the control subjects or patients with secondary headaches. A significantly greater number of cold spots was also displayed by the patients with mixed headaches involving a vascular component, as well as patients with cluster disorders and post-traumatic headaches. Another study conducted with retrospective data including thermograms from 993 patients with various headaches found abnormalities in the thermograms of 855 patients (86.1%) in the form of low temperatures in the supraorbital region [170].

Ammer [7] also presented the current studies dealing with thermal imaging in patients with headaches [73, 218]. Govindan [73] demonstrated clearly that the vasoconstrictive effect can be imaged by IR thermography. The diagnostic utility of thermal imaging for headache in children, which is known to be a difficult issue due to less clear diagnostic criteria, has been evaluated by Wojaczynska-Stanek and Marszal [218]. Evidence showed the existence of different thermal patterns with various forms of headache in children.

In studies for the effectiveness of chiropractic care of headaches and migraines, paraspinal digital IR imaging, which measures cutaneous IR heat emission in a form of thermography was performed as a neurophysiological diagnostic imaging procedure [55]. Thermography showed a high degree of sensitivity (99.2%), specificity (up to 98%), predictive value, and reliability in blind studies conducted comparing thermographic results with those of CAT scan, MRI, EMG, myelography and surgery [70, 228, 239].

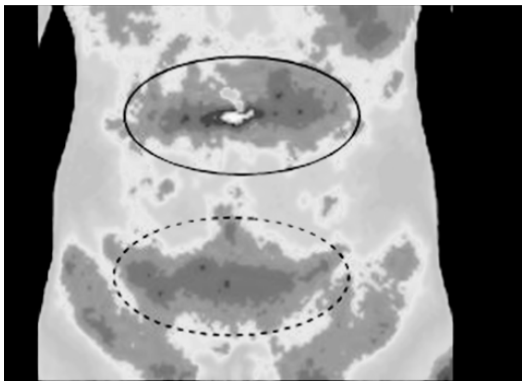


Figure 2.5: Young woman with endometriosis (dotted circle) and colon dysfunction (solid circle). (Reproduced from [138], with permission.)

In women, sometimes migraines are associated with gynaecological problems, such as endometriosis. Ferrero et al. [61] reported that an increased frequency of migraines was observed among women with endometriosis. Endometriosis is a medical condition where womb lining or endometrium cells grow in areas outside the womb, such as on the ovaries, fallopian tubes and the tissues that hold the uterus in place [22]. Thermal imaging (Figure 2.5) is reportedly able to detect endometriosis and to evaluate whether it is the cause of the underlying dysfunction in the female reproductive tract [138].

2.2.2.3 Vascular Related Disorders

A clinical study was conducted to detect peripheral vascular disorders using IR thermal imaging [12]. In this study, the regions of interest were imaged in the anterior, posterior, and lateral views for the corresponding contralateral regions of the patients and of normal controls. The surface temperature profiles of the patients were recorded and analyzed using the IRWIN software (Bagavathiappan et al., [12]). The thermal profile of the area of examination was compared with the counterpart region of the same subject. The same region of a healthy volunteer and the change in temperature in the region of interest was also determined. There were changes in temperature in the affected regions of patients with vascular disorders, which indicated abnormal blood flow in the affected region. The results of thermal imaging were also well correlated with the clinical findings. Certain areas on the affected limbs showed increased temperature profiles, generally by $\sim 0.7^{\circ}$ to 1°C above the normal regions, probably due to inflammation and underlying venous flow changes, since patients with vascular disorders usually had lower temperatures in the extremities due to obstructed arteries. It was concluded that the thermal imaging technique was effective and reliable for detecting small temperature changes in the human body due to vascular disorders.

Deep venous thrombosis (DVT) is a common clinical problem in hospital practice and a frequent cause of emergency medical admission to hospital, either in itself or due to secondary pulmonary embolism (PE) [82]. DVT may also develop in hospital inpatients, particularly in postoperative patients, the elderly, patients with malignant disease (especially pelvic or abdominal malignancy), or severe debilitating illness. Pregnant women and women who use oral contraceptives are at above-average risk of DVT [82]. The need for an accurate method of diagnostic investigation to confirm or exclude DVT in clinically suspected cases is very demanding as clinical diagnosis of DVT has been proven extremely unreliable [82]. This is also due to the expensive treatment of the disease, the time it requires, and the risk it entails, which make it very important to have a reliable investigation method. Thermal imaging is reportedly able to provide this reliability because of its high sensitivity for detecting DVT. Harding [82] presented the investigation of DVT using IR thermal imaging based on a clinical study. Interpretation and recognition of abnormalities in the temperature gradient between the right and left lower limbs, on anterior and posterior views, was undertaken as the main approach. A further investigation usually is required to confirm or exclude DVT using other tools, such as venography and Doppler ultrasound. However, such further investigations could be avoided in over one-third of patients

with suspected DVT by virtue of a normal thermogram [82].

2.3 Data Processing Methods used in the Analysis of Medical Thermograms

Understanding the significance of gray levels is an important requirement in the analysis of an IR image. The gray-level is a measure of the nonlinear response of the IR detector element to the IR radiant power absorbed by it and integrated over all angles. The response also depends on the wavelengths passed by the camera filters and the ambient temperature. Changes in gray levels will follow changes in the surface radiance of the object. Hence, the gray-level is a measure of the skin surface radiance and an integral, rather than the average, of the incident radiation [112].

In the analysis of medical thermograms, two major digital-processing approaches have been explored by many researchers; physical model based approach and image processing based approach. The first, generally known as solving the inverse problem, takes into account the heat exchange processes in the body, the geometry and the anatomy of the skin tissue structure, including the blood vessels, etc.. This approach is useful for the identification of skin's thermal parameters, location of heat source (particularly the vessels), depth of heat source, etc. [3, 11, 29, 47, 149, 171, 172, 173, 174, 243, 241, 244] to compute physiological information, such as localized blood flow, cardiac pulse, and breath rate. This approach necessarily involves the use of the bioheat transfer equation/model, a geometric model, and various assumptions: Some of the parameters are given fixed values from averages over many subjects and other parameters are estimated. Due to the scope of study of this thesis, the approach based on the bioheat transfer equation/model is not included in this chapter. However, it can be found in [106].

On the other hand, the second approach generally involves image processing and analysis based on the heat patterns found in a thermal image. In this section, the review on this approach that relies on extracting indicators from the thermogram images and identifies correlations between observable image characteristics and human physiology without worrying about the physical mechanism that connects them is presented. Many papers have discussed early diagnostic techniques that can detect many diseases based on thermal imaging using this approach [66, 141, 148, 191, 188, 190, 223, 240].

When one tries to identify correlations between observable from the image features and human

physiological parameters, the approach does not involve detailed modeling but rather mostly image-processing techniques. Two major categories in the image-processing approach are followed:

(i) classification of full images;
(ii) extraction of regions of interest (ROI) and their subsequent classification. The automatic identification of ROIs necessitates the use of some sort of segmentation method.
The latter is further discussed in the two following sections.

2.3.1 Extracting Indicators from Thermogram Images

2.3.1.1 Image Segmentation for ROI Detection

ROI detection is done either manually or automatically. The common approaches to perform segmentation include edge-based techniques, threshold-based techniques, and region-growing techniques [57, 58]. Due to the undefined and vague boundary and shape of objects in thermal images, extracting ROIs has become a difficult task for a fully automated segmentation. In some works, manual intervention is preferable [89, 252].

Herry and Frize [89] performed segmentation of ROIs manually or automatically using the results from hot spot and cold spot analysis for pain detection. The analysis of abnormally high and low areas was done based on displays of isothermal regions and intensity profile lines. Noise in the thermograms (assumed to have a Poisson distribution) was first removed using a wavelet technique because it can preserve the sharpness of an image. Then, contour extraction based on edge detection, simple morphological operations, and template matching were performed to classify the thermograms into body parts (e.g., upper/lower back, front legs, face). The contralateral part of the ROI was segmented based on reflection with respect to the left-right symmetry.

Zhu et al. [252] presented another method using manual intervention. They performed extraction of the supraorbital vessels in thermal forehead images using the Open End Snake (OES) segmentation method. In this method, first the vessels were initialized automatically by the top hat and Hough transforms [179]. Then automatic localization of the vessels' central lines was performed by using an active contour model. Finally, using a special operator, fast determination of vessel boundaries was performed to search for the maximum temperature gradient along a vessel's radial direction at each point of the active contour. The method is reported

to be capable of segmenting simulated vessels with high noise level and to outperform other vessel segmentation methods according to two performance parameters: accuracy and Hausdorff distance. However, the method requires both manual indication of the number of vessels in the ROIs by the operator and a skillful operator to select the correct ROI on the forehead. The performance of the method was also found to decrease with decreasing image quality [252].

Koay et al. [124] reported a semi-automated image segmentation and ROI identification method for breast thermograms. In the semi-automated image segmentation, image enhancement was performed using the top hat and bottom hat morphological operators with a five-pixel radius disk as the structuring element. This enhancement method emphasized the contours and the edges in the image that were then extracted using a Canny edge operator followed by some trimmings of all edge contours corresponding to vertical or horizontal lines since they were likely artifacts. The ROI identification was then performed based on an ellipse fitting algorithm using the ellipse that best fitted the contour of the smallest convex region enclosing the remaining extracted edges. The breast nipple was determined based on the value of eccentricity of the region that was closest to 1. The segmented breasts were further divided into four quadrants and statistical parameters were computed for each breast and each quadrant within the breast.

Many researchers have tackled the problem of segmenting ROIs fully automatically. Fully automated segmentation of ROIs could ensure the repeatability and robustness of an algorithm for disease diagnosis and thus enable mass screening of a disease in a clinical trial. User subjectivity in the results of screening could thus be eliminated.

Qi et al. [190] applied the Hough transform [179] to extract four feature curves automatically to segment the left and right breasts in thermograms for breast cancer detection. The four feature curves included the left and the right body boundary curves and two parabolic curves indicating the lower boundaries of the breasts. Unlike the boundaries of the left and the right sides of the breasts, the lower boundaries of the breasts were difficult to detected by an edge operator. Thus, parabolic functions were used to form the lower boundaries of the breasts by using the coordinates of the two highest peaks in the parametric space (accumulator array) of the Hough transform, adapted for the detection of parabolic curves. The Hough transform was found very suitable for extracting the curves that form the boundaries of the breasts [190]. However, based on the resultant images of breast segmentation presented in the paper, some regions of the breast, particularly near the boundaries, were lost; this would jeopardize any automated diagnosis method based on left-right comparisons due to the lack of symmetry [152]. There was

also a possibility that the discarded regions might contain a lesion [152].

In a face recognition study using face thermograms, the face region was segmented based on a number of approaches, such as horizontal and vertical profile analysis, Sobel edge detection, and the ellipse-fitting method [6]. Initially, the face image was extracted from the gray-scale image based on the high contrast between the background and the foreground. Then, using acquired thermal information of the face skin, the face region was segmented. Any segmented neck regions were eliminated based on the analysis of the horizontal and vertical profiles of the segmented image. The horizontal profile was obtained using the sum of the intensities along each column, while the vertical profile was obtained using the sum of the intensities along each row. The analysis of both profiles was conducted to define the ROI around the head. Inside this ROI, Sobel edge detection was used to obtain edge data to be used in fitting an ellipse around the face. The fitted ellipse was then used as a mask to extract the face region (Figure 2.6) [6].



(a) (b)

Figure 2.6: Segmentation of face region in a thermogram. (a) original thermogram; (b) extracted face region. (Reproduced from Akhloufi and Bendada [6], with permission.)

A simple edge detection algorithm was applied by Palfy and Papez [166] to trace the outline of the hand in thermograms for carpal tunnel syndrome (CTSd) analysis. To increase the contrast of the hand with its background, a cooled towel was placed underneath the hand during the acquisition of the hand thermogram. Once the outline had been extracted by simple edge detection, the hand was further segmented into 12 ROIs by calculating the hand's center of mass and determining characteristic points at the hand's edge (i.e., at the fingertips and between the fingers). The distance between each edge point and the center of mass was calculated and the local maxima and minima were extracted to determine the fingertips and points between the fingers, respectively. By connecting these points, different hand segments were defined, including the carpal and wrist parts (Figure 2.7).

In another study involving segmentations of hands and upper arms, a combination of techniques,

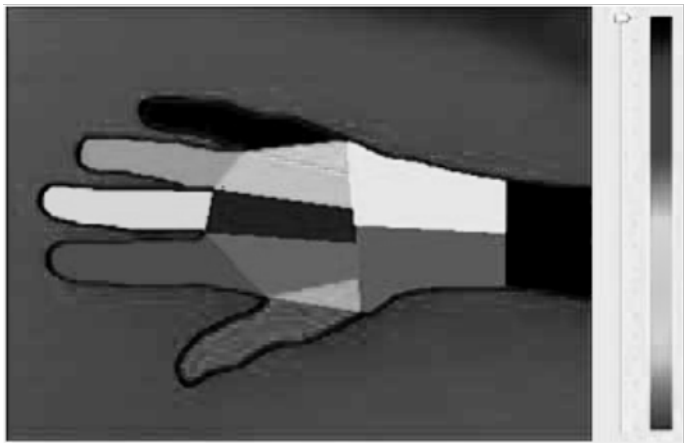
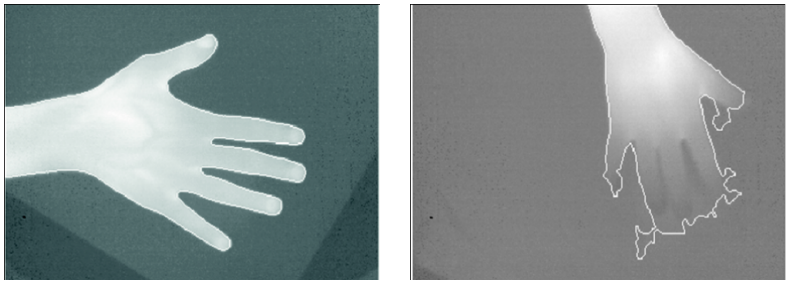


Figure 2.7: Segmentation of the hand in a thermogram. (Reproduced from Papez et al.[169], with permission.)

such as Canny edge detector, Otsu global thresholding, and morphological operations, was applied [91]. Initially, noise in the IR thermal images was removed using a stationary wavelet transform [178] that could preserve fine details in the image. Then, the Canny edge detector was used to extract the outline/boundary of the hand. A binary image obtained by Otsu's thresholding method was then added to the Canny edge–detected image. In the postprocessing of the resultant image, a series of morphological operations, such as opening and closing [178], were conducted to bridge gaps, remove small components and spurious objects, etc. to improve the segmentation result further. Landmarks AQ:19 in the segmented image were then identified using profile lines for the fingers, the junction of the wrist and the thumb for the hand, and the junction of the wrist and the elbow for the upper arm area. The success rate of the segmentation technique, which was tested on 658 thermal images of upper arms (anterior view) and 1216 thermal images of hands (left and right, dorsal and palmar views), was 78.8% [91]. The method, however, had some weaknesses. It tended to extract two fingers together when they were close to each other and had difficulty in finding the contour of a cold finger because the whole finger was very faint (Figure 2.8; [91]).

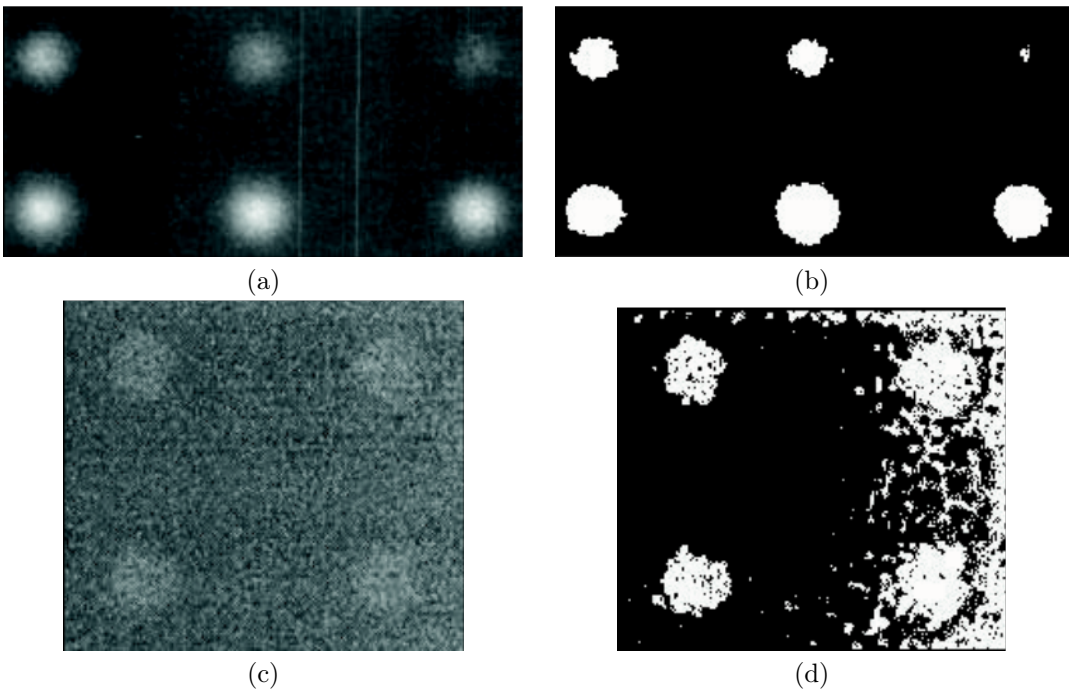
Alternatively, Zhang et al. [249] developed a method that incorporated GA and 2D Otsu thresholding to segment thermograms (Figure 2.9). In this study, the genetic algorithm was initialized with possible solutions that were selected as randomly as possible, with the help of the logistic mapping equation, which allowed the generation of an initial population with maximal diversity. The fitness function was calculated by taking the trace of the dispersion matrix as the distance measurement function between the background class and the object class [249]. The dispersion matrix was formulated based on the threshold calculated by the 2D Otsu thresholding



(a) (b)

Figure 2.8: Segmentation of a hand in thermograms. Examples of (a) a successful segmentation and (b) an unsuccessful segmentation due to low contrast between the fingers and their background. (Reproduced from Herry et al. [91], with permission.)

method. The GA method also used an adaptive mutation rate, based on the maximum value of the fitness function in the current population, to increase the performance of the algorithm. This approach had a faster speed of implementation, better stability, and produced a better segmentation compared with the 2D Otsu method alone [249].



(a) (b)

(c) (d)

Figure 2.9: Image segmentation results by Zhang et al. [249]. (a) Input image with low level of noise; (b) segmented low-noise image; (c) blurred and very noisy input image; (d) segmented blurred and very noisy image. (Reproduced from Zhang et al. [249], with permission.)

Chang et al. [30] incorporated the wavelet transform in their automatic multilevel thresholding approach for its multi-resolution nature. In this transformation, a set of dilated wavelets at different scales was convolved with the histogram of the thermogram. This was followed by identification of the zero-crossings and the local extrema in the set of modified histograms to

identify thresholds and representative gray levels, respectively. The best threshold value for the multilevel image segmentation was determined by minimizing a cost function:

$$C_{func} \equiv kd^{\frac{1}{2}} + (1-k)U \tag{2.1}$$

where

$$d \equiv \frac{\sum_{i=0}^{X-1}\sum_{j=0}^{Y-1}|f(i,j)-g(i,j)|}{XY} \tag{2.2}$$

with k denoting a weighting parameter that can be adjusted, d representing the difference between the original image $f(i,j)$ and the segmented image $g(i,j)$, U indicating the number of thresholds selected for segmentation and $X \times Y$ the size of the image[30]. The results obtained were compared with those obtained by applying the plane curve approach and found to be superior[30]. The plane curve approach uses the curvature of the cumulative distribution function (CDF) of a histogram to locate the potential thresholds for multilevel segmentation [19, 30].

Edge detection and global thresholding methods may result in loss of some information or fine details, mainly at low-contrast regions. Motta et al. [152] recovered undetected low-contrast regions in a segmented image obtained by Otsu thresholding by performing a contour detection on the segmented image in search of the region with the smallest gray-level variance. This was done because the region with the largest contour is normally the region where undetected low-contrast pixels are located. The mean gray-level value in this region was then used as a new threshold value to the input image. The segmentation of the left and right side of a breast in the thermograms was further performed using automatic border detection, mathematical morphology, and curve extraction and interpolation (Motta et al., [152]). Good results were achieved based on the resultant images presented in the paper (Figure 2.10). However, in breast thermogram analysis, this method can be used only for breast thermograms of the frontal view . The validation of the method was done solely by visual inspection by medical specialists.

Selvarasu et al. [206, 207] attempted to compare a combination of edge detection and morphologically based approaches with a region growing–based approach to segment arthritis and stress fractures. In the former approach, the first pixels in the region, which had sharp transitions in intensity (above a threshold value), were determined using Sobel masks and marked as edge pix-

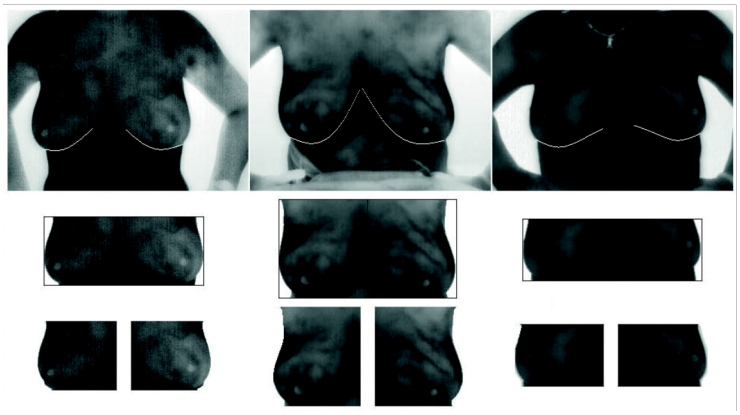


Figure 2.10: Segmentation results of breast thermograms. (Reproduced from Motta et al. [152], with permission.)

els. Morphological operations, such as dilation, region filling, and erosion, were then performed on edge-detected images to produce the abnormality regions. In the region growing approach, the thermogram was segmented into sub-images, with each sub-image composed of pixels with values within a certain range tolerance. The pixel with median intensity was chosen as the seed pixel, and a tolerance value of 0.04 was selected as the similarity criterion to identify the abnormal regions. The region growing approach detected and quantified abnormalities effectively and could be standardized for all types of disease that manifest themselves as hot spots in the thermograms. The approach was also claimed to be parameter independent and fast [206].

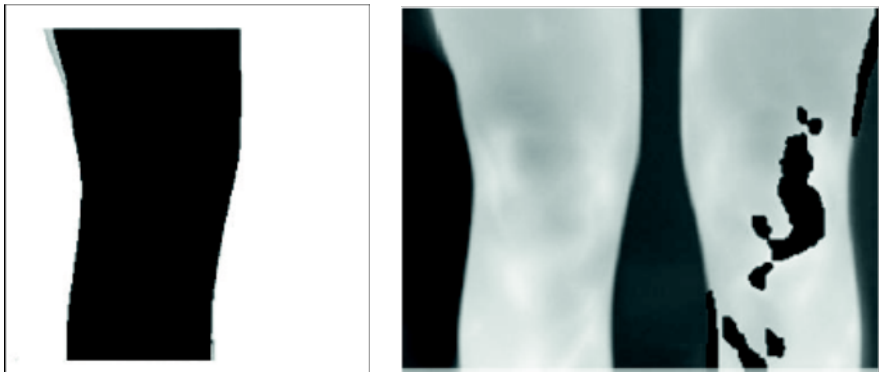
Later, Selvarasu et al. [207] compared the region growing approach with a wavelet-based approach in the segmentation of arthritis and stress fractures using thermograms. In the wavelet-based approach, thermograms were converted from the color domain to the gray scale to reduce processing time and computational complexity. Then, the discrete wavelet transform (DWT), using Haar wavelets, was applied to the gray-scale thermograms to obtain the approximation image, as well as the vertical, horizontal, and diagonal detail images. Since the researchers observed that the abnormality region always appeared as a low-resolution region, the detailed coefficients were set to zero while the approximation image was retained. The thermograms were then reconstructed and hot spots were isolated using thresholding. Each hot spot was then quantitatively characterized. Both techniques were able to identify and quantify the abnormality successfully. It was concluded that the wavelet transform, because of its multi-resolution nature, is very useful if the abnormality is at a different resolution from that of normal tissue (Selvarasu et al., [207]). However, only one level of resolution was used. If all detail coefficients were not equal to 0, as the paper implies, this wavelet-based method amounts only to low-pass filtering the image with a local averaging window.

Herry and Frize [90] identified potential ROIs using fixed dermatomal subdivisions of the body, isothermal analysis, and segmentation techniques. In the ROI segmentation, the background was first extracted from the thermogram based on a method combining an optimal thresholding method, adapted from Tsai's [229] work and additional morphological processing steps. After this steps, landmarks of the body were identified by locating specific reference points on the body, analyzing the contours and profiles across the image using approaches such as edge detection, by defining functions that represent line profiles of various parts of the body, detecting extremity points, and so on. The landmarks of the body, known as dermatomes, were the shoulders and the hips for the chest and back, the buttock cleft for the back, and the area around the knee for the legs. The more specific regions than dermatomes—namely, the hot and cold regions—were determined based on isothermal analysis. Post-processing, such as merging regions, discarding regions smaller than 10 pixels, thresholding, and eliminating artifacts at the boundaries of the segmented ROIs, was performed to obtain the most significant regions [90].

Tang and Ding [223] determined ROIs in breast thermograms using mathematical morphology. In this study, the heat pattern in a thermogram was defined as the set of peaks and ridges on a topographical surface [223]. Based on this definition, the authors performed a sequence of operations to achieve breast segmentation based on morphological operations. In their coarse segmentation stage, first openings and closings with directional structuring elements of different lengths and along different orientations were performed. Then the difference between the maximum and the minimum values of a pixel from the resultant images after openings along different orientations was computed to obtain the so-called positive strength of the pixel. They then did the same for closing to obtain the so-called negative strength of the AQ:3 pixel. When the positive strength of the pixel was larger than the negative strength, this pixel was determined to have positive orientation. The positive orientation of a pixel was used to determine the heat pattern in the coarse segmentation stage (Figure 2.11(a)). In order to refine the coarse segmentation result, a marker image was first obtained by morphological reconstruction, which was carried out by computing the difference between the original image and the image after opening by reconstruction (Figure 2.11(c)). Then a logical "AND" operation between the marker image and the coarsely segmented image was performed to obtain a refined heat pattern (Figure 2.11(d)), where some unwanted heat patterns (along the outer boundaries of the breasts) in the coarsely segmented image were removed. Next, using the extended maxima transformation, another marker image, which consisted of a set of pixels that represented the wanted heat patterns within the breasts area, was obtained (Figure 2.11(e)) based on the temperature differences between the

heat patterns and their background [223]. This marker image was then used to locate the rest of the desired heat patterns in the refined image using a transformation based on morphological reconstruction (Figure 2.11(f)). The segmentation result superimposed on the original image is shown in Figure 2.11(g).

Herry et al. [92] performed segmentation of abnormal regions by a simple translation followed by calculation of the absolute difference between two contralateral knees. Thresholding was then performed on the absolute difference image by using the 90% point of the cumulative distribution function to obtain the cluster of interest showing asymmetry abnormalities. The location of the cluster was then mirrored and translated back to their equivalent location on the contralateral knee (Figure 2.12).



(a) (b)

Figure 2.12: Example of asymmetry analysis: (a) difference image between left and right knee; (b) clusters found by thresholding the difference image. (Reproduced from Herry et al. [92], with permission.)

Most of the developed methods in thermogram analysis discussed in this section were developed for a particular type of disease and require a priori knowledge concerning the ROIs to be extracted. Herry et al. [92] alternatively developed an approach to extract abnormal regions in a wide range of clinical thermogram images. No specific knowledge about the underlying thermal dysfunctions was required. The approach consisted of feature images and an adaptive resonance theory (ART) clustering neural network applied to a thresholded linear composite. The feature images were obtained by a combination of feature detectors—normalized global contrast, entropy filter, and Laplacian of Gaussian (LoG) and Sobel operators.

Alternatively, applied directly onto the body region, the ART segmented clusters of interest using a match-based learning method. The ART network consisted of two layers—the layer of cluster centers/nodes, and a layer that received the input data, feedback from each cluster

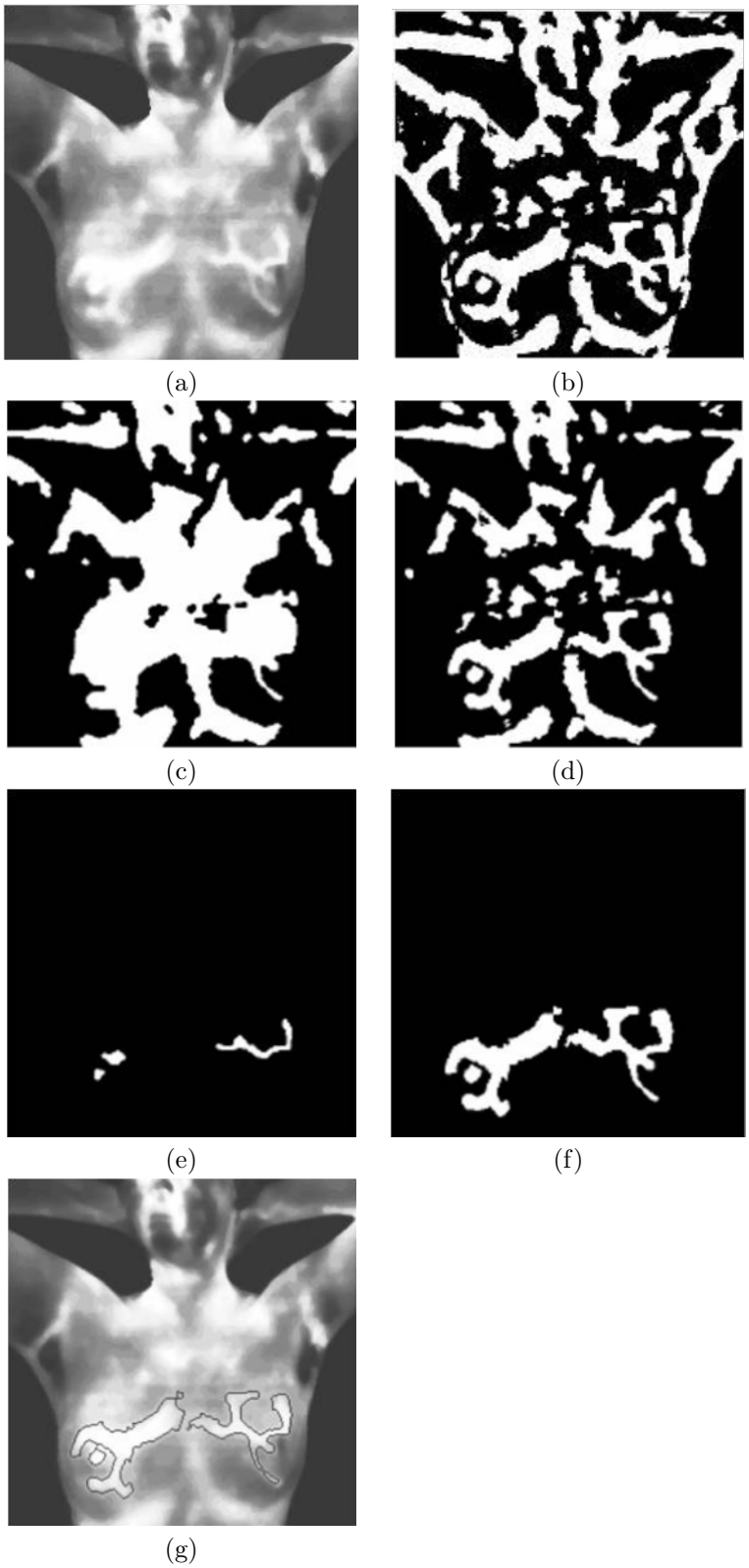


Figure 2.11: Morphological image segmentation process. (a) Original image; (b) coarse segmentation result; (c) marked image through the top-hat transformation by reconstruction at the breast scale; (d) refined result obtained by applying the "AND" operator to (b) and (c); (e) extracted marker through extended extrema transformation; (f) filtered heat patterns; (g) final segmentation result. See text for details. (Reproduced from Tang and Ding [223], with permission.)

and a time-varying bias signal. Based on unsupervised learning, the matching nodes from the existing cluster in the ART network were searched to match the input data to the network. If no matching node was found, a new node was added. In order to perform this process, the signal from the feedback connections and the inputs were compared and then thresholded with a parameter that determined whether to assign the input to an existing cluster or to create a new one [92]. The results obtained from the feature detectors and the ART, which consisted of sets of regions that differed significantly from their surroundings (clusters of interest), were merged through a logical "AND" operation. Experimental results showed that the approach was able to detect abnormalities in thermograms. However, it was tested only on two images with known abnormalities [92].

2.3.1.2 Asymmetry based Features

In medical applications, the thermogram is principally known to be symmetrical in temperature patterns [66, 67, 141, 191]. Small asymmetries in temperature patterns in relatively symmetrical thermograms may be suspected for abnormalities. This is the basic principle in asymmetry analysis for lesion detection in breast cancer studies and in abnormality detection in other parts of the human body [191]. In the case of an asymmetrical thermogram, as shown in Figure 2.13, this asymmetry can serve either as an indicator of a physiological abnormality that can be (1) pathological (including cancer, fibrocystic disease, an infection, or a vascular disease) or (2) an anatomical variant [66, 67, 191, 240]. Since these small asymmetries may be difficult to detect by the human eye, to eliminate human factors, it is very important for difficult, tiring, and repetitive tasks to be fully automated. The other motivation for this type of analysis is the elimination of individual and environmental factors of temperature variations [66, 141] since their effect is canceled when differences within the same image are sought.

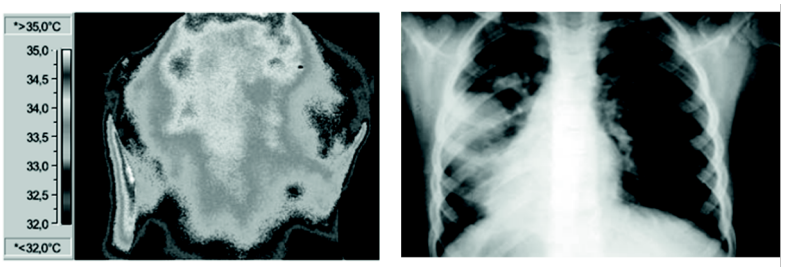


Figure 2.13: Nonsymmetrical temperature distribution for pneumonia with corresponding X ray image. (Reproduced from Wiecek et al. [240], with permission.)

Most asymmetry studies conducted in thermogram analysis compare contralateral images by evaluating the difference in statistical parameters such as first- and second-order statistics. The first-order statistical parameters are obtained by using the image histogram to compute signatures (Figure 2.14), while the second-order statistical parameters are defined from gray-level co-occurrence matrices [240], who reported that by using two second-order parameters—the difference variance and variance—separation of almost all malignant tumor cases was successful, unlike when using first-order parameters.

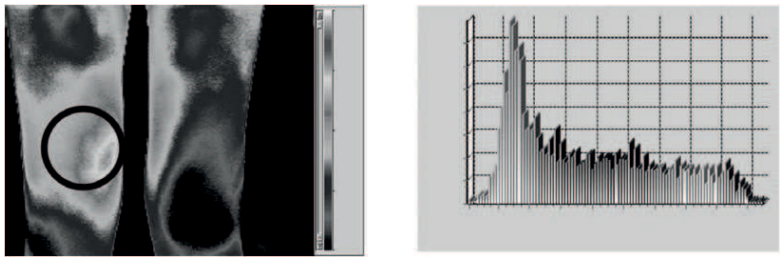


Figure 2.14: Region of interest of a thermal image and its histogram. (Reproduced from [240], with permission.)

A computerized thermographic system (CTS) that performs analysis of thermograms based on asymmetry and a thermographic index was also presented by Fujimasa [66] and Mabuchi et al. [141]. In particular, a five-step procedure, including asymmetry analysis, was proposed for the thermographic analysis by Fujimasa [66] as tabulated in Table 2.2. In these studies, the body region was divided into two symmetrical parts to obtain the affected side and the contralateral healthy side of the body. The two parts were then further divided into the same number of symmetrically located trapezoidal pairs (Figure 2.15). The distribution of temperature differences between the affected side and the contralateral healthy side of the body was then obtained based on the trapezoidal pairs. As there was no standard skin surface temperature, the system measured the body surface temperature of each pixel in the affected area and subtracted from it the body surface temperature of the corresponding pixel in the symmetrically located contralateral healthy area to generate a difference image [66, 141]. To achieve this, the mean temperatures of both the affected area and its contralateral healthy area were calculated and the difference between these mean temperatures was taken. However, several problems were reported with this method. One of the problems was defining the abnormal area, which could be identified as larger or smaller than the true abnormal area [66, 141]. This could change the difference in the mean temperature between the two sides and thus might prevent the detection

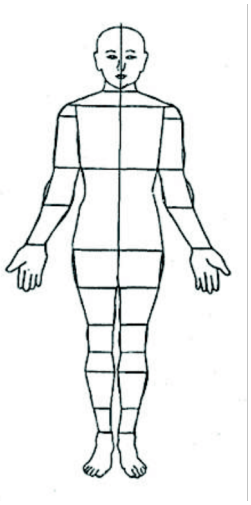


Figure 2.15: Symmetrically located trapezoidal pairs of the affected and contralateral healthy side of a body. (Reproduced from Mabuchi et al. [141], with permission.)

Table 2.2: Five diagnostic steps of clinical thermography.

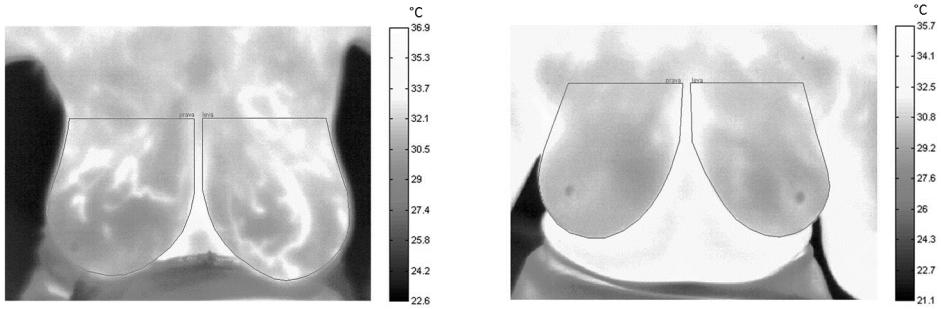
Diagnostic steps	**Image Processing techniques**	**Meaning of processing**
1	Standardized thermograms	Screening for abnormal temperature distribution
2	Precise thermograms with temperature analysis of region of interest (ROI)	Precise temperature analysis of ROI
3	Asymmetry detection thermograms	Detection of true abnormal regions
4	Thermographic index thermograms (TI) and TI histograms of ROI	Determination of the degree of heat accumulation
5	Sequential subtraction of thermograms	Analysis of the thermal dynamics of ROI

Reproduced from Fujimasa [66]

of significant differences.

Zavisek [246, 247] claimed that the differences in vascular patterns and the appearance of hot and cold spots between the left and right breast are the most significant thermopathological features (Figure 2.16). In these studies, several methods, including histogram analysis, temperature cooccurrence matrix (COM), Fourier spectrum analysis, and moment and cluster analysis, were used for feature extraction. For image I, the spatial COM $P(m, n)$ of temperatures m and n was defined as the number of pairs of pixels with temperatures m and n and being in a fixed spatial relative position (a fixed distance apart or a fixed distance along a fixed direction apart). By using the elements of the matrix, textural feature extraction could be performed without being affected by changes in the temperature thermograms and being affected only by changes in the topological relationships of temperatures [246, 247]. Commonly used statistics, such as energy, entropy, contrast, and homogeneity, could also be generated based on the COM for classification

of the veining of breasts [205, 246]. By using points in contralateral images, COM could be modified to become cross COM (X-COM) to assess symmetry and evaluate roughness and orientation of the sought features. Some of the parameters used achieved more than 80% sensitivity and specificity in the classification of thermograms [246]. Zavisek [247] used feature combination to obtain a set of new combined features by using two methods—averaging and weighted relative ranking—with the so-called optimal weights and reduced optimal weights inspired by neural networks. An individual parameter—namely, the homogeneity of X-COM—was the best feature with the highest sensitivity and specificity, equal to about 67%. The new combined features reportedly further enhanced the strength of the individual parameters, where the highest sensitivity achieved by a combined feature was as high as 90%.



(a) (b)

Figure 2.16: (a) Abnormal thermogram with strong veining on the left breast; (b) normal thermogram with both breasts symmetrical without any hot spots or veins. (Reproduced from Zavisek [247], with permission.)

Koay et al. [124] used the first-order parameters derived from histograms as thermal features for asymmetry analysis. The asymmetry based features were also obtained by evaluating the difference of statistical parameters, including mean, standard deviation, median, maximum, minimum, skewness, kurtosis, entropy, area, and heat content, between contralateral breasts. In the asymmetry analysis, the difference statistics were divided into two sets: for the whole breast image and for each quadrant of the breast (Koay et al., [124]). The statistical parameters used for the whole-breast image were the mean difference and the variance difference between the contralateral breasts. For the breast quadrant approach, the parameters were defined as

$$\text{Input Param 1} : Q1_{meanDiff} + Q2_{meanDiff} + Q3_{meanDiff} + Q4_{meanDiff} \tag{2.3}$$

$$\text{Input Param 2} : (Q1_{stdDiff})^2 + (Q2_{stdDiff})^2 + (Q3_{stdDiff})^2 + (Q4_{stdDiff})^2 \tag{2.4}$$

where Qn is the breast quadrant ($n = 1, 2, 3, 4$).

Herry and Frize [89] performed statistical analysis and comparisons of intensity distributions of symmetric or comparable ROIs using low-order, high-order, and Kolmogorov–Smirnov statistics. Using the statistical analysis and comparisons performed, a decision support scheme was used to summarize the results for each thermal image. Tarnawski et al. [224] used a number of statistical thermal features in their asymmetry analysis, such as mean of absolute temperature difference, absolute difference of standard deviation, median temperature and the temperature at 90th percentile, image moments, histogram features (absolute value of the maximum of difference histogram, the number of bins exceeding a certain threshold, the number of zero crossings, energy and the difference of the positive and negative parts of the histogram), COM-based features (homogeneity, energy, contrast and symmetry), and mutual information. The authors further extracted the same features from the same image after contrast enhancement by a Laplacian filter to obtain another subset of features. Each breast thermogram was then categorized using the combination of all the asymmetry-based features extracted: about 38 features in total per breast thermogram, describing the asymmetry between the two sides. Each feature was normalized to the interval of 0 to 1 to arrive at comparable units between descriptors [224].

Qi et al. [190] conducted the asymmetry analysis using the ratio of the extracted features from the left segment to the right segment. The closer the value of the ratio was to 1, the more correlated the features or the less asymmetric the segments. The asymmetry-based features were obtained by evaluating the low- and high-order statistics that consisted of four moments of the intensity image (mean, variance, skewness, and kurtosis), the peak pixel intensity of the correlated image, entropy, and joint entropy. These were defined as

$$\text{Mean, } \mu = \frac{1}{N}\sum_{j=1}^{N} p_j$$

$$\text{Variance, } \sigma^2 = \frac{1}{N-1}\sum_{j=1}^{N} (p_j - \mu)^2$$

$$\text{Skewness} = \frac{1}{N}\sum_{j=1}^{N}\left[\frac{p_j - \mu}{\sigma}\right]^3$$

$$\text{Kurtosis} = \frac{1}{N}\sum_{j=1}^{N}\left[\frac{p_j - \mu}{\sigma}\right]^4$$

$$\text{Entropy, } H(X) = -\sum_{j=1}^{N} p_j \log p_j$$

$$\text{Joint Entropy, } H(X,Y) = -\sum_{i=1}^{N_X}\sum_{j=1}^{N_Y} p_{ij} \log p_{ij} \tag{2.5}$$

where p_j is the value of the jth bin of the normalized histogram, p_{ij} is the joint probability density between the left and right breast segments, computed from the normalized 2D joint histogram of the two segments [177], N is the total number of bins, and N_X and N_Y are the total number of bins of the histogram of image segments X and Y, respectively. The entropy was selected because it could be used to measure the uncertainty of the information in a segmented image. When the entropy is low, less information is contained in the segmented image [190]. Entropy is usually low when the temperature distribution becomes more uniform [190]. This was the case for hot spots. For the joint entropy, an increase in its value shows a decrease in the possibility of existence of tumor (more symmetric). Based on the performance evaluation of the features used, the entropy and the mean values were less useful than the other features used in the asymmetry detection.

Merla and Romani [148] used a quantitative assessment of symmetrical/ asymmetrical temperature distributions using a first-order statistics algorithm based on two parameters: the histogram asymmetry factor and the spatial correlation factor. The former determines the asymmetry factor between two calculated frequency tables of the temperature distributions of the left and right side of contralateral regions. The latter compares homologous contralateral regions through a cross-correlation method. This approach allows the quantitative assessment of regional variations of the temperature distributions, hence permitting the identification of functional asymmetries related to the human posture. The developed quantitative diagnostic application was reported to be used routinely nowadays in clinical settings [148].

Most of the asymmetry-based features were used in the quantitative asymmetry analysis. Tang and Ding [223] included a qualitative analysis as well in their study of asymmetry of breast thermograms. Quantitatively, the authors performed asymmetry analysis of breast thermograms based on extracted features—namely, the skewness, variation, kurtosis, temperature difference, and the maximum ratio between temperature difference and area. They then computed the bilateral ratio of these features. The further the ratio was from 1, the greater the asymmetry. A qualitative analysis was also performed by using the curve of the cumulative histogram, which described the temperature variation with the area of the left and right heat patterns. The steeper the curve of the cumulative histogram, the more abnormal the temperature distribution was inferred to be [223].

Alternatively, Herry and Frize [90], proposed a method to assess the degree of asymmetry between contralateral ROIs using distance measures between histograms of comparable ROIs, based on several distances— Manhattan or absolute distance, Euclidean distance, maximum distance, chi-square distance, Jeffrey divergence distance, and Mallows distance. This approach was used to overcome the limitations of asymmetry analysis based on the difference of statistics that neglects the importance of temperature distribution. The Manhattan, Euclidean, and maximum distances are generated from

$$D(H,G) \equiv \left(\sum_{i=1}^{L} |H(i) - G(i)|^r \right)^{1/r} \tag{2.6}$$

where H and G denote the two histograms, L is the number of histogram bins, and $r = 1$ for the Manhattan distance, $r = 2$ for the Euclidean distance, and $r = \infty$ for the maximum distance. The chi-square distance, the Jeffrey divergence distance and the Mallows distances are defined as

$$D_{chisquare}(H,G) \equiv \sum_{i=1}^{L} \frac{\left(H(i) - \frac{H(i)+G(i)}{2} \right)^2}{\frac{H(i)+G(i)}{2}} \tag{2.7}$$

$$D_{Jeff}(H,G) \equiv \sum_{i=1}^{L} \left\{ H(i) \log \frac{H(i)}{\frac{H(i)+G(i)}{2}} + G(i) \log \frac{G(i)}{\frac{H(i)+G(i)}{2}} \right\} \tag{2.8}$$

$$D_{Mallows}(H,G) \equiv \left(\frac{1}{L}\sum_{i=1}^{L}\left|H_{(i)} - G_{(i)}\right|^2\right)^{1/2} \tag{2.9}$$

Here, $H_{(i)}$ is the sorted sequence $H(i)$ and $G_{(i)}$ is the sorted sequence $G(i)$ [135]. For example, for a 4-bin histogram H, with $H(i)$ bin values $[5,7,1,5]$, and a corresponding histogram G, with bin values $G(i) = [1,7,8,2]$,

$$\begin{aligned} D_{Mallows}(H,G) &= \left(\frac{1}{4}(|1-1|^2 + |5-2|^2 + |5-7|^2 + |7-8|^2\right)^{1/2} \\ &= \left(\frac{1}{4}(|3|^2 + |2|^2 + |1|^2)\right)^{1/2} = \left(\frac{14}{4}\right)^{1/2} = 1.87 \end{aligned} \tag{2.10}$$

From the quantitative assessment conducted using thermograms of normal and pain patients, it was shown that the method based on the Euclidean distance outperformed the other methods considered, including comparisons of statistical parameters such as mean, variance, skewness, kurtosis, and maximum values between contralateral ROIs [90].

2.3.1.3 Other Features

Other features that have been used as indicators for abnormalities in thermograms are vascular/focal pattern (hyperthermic or hypothermic or atypical complexity), abnormal physical contour, localized heat along an abnormal physical contour (edge sign), and the presence or absence of an adaptive response to an autonomic challenge procedure (dynamic imaging) [30, 67, 89, 114]. Acharya et al. [1, 2] working with thermograms for breast cancer detection, used texture features, such as homogeneity, energy, entropy, moments of various orders, angular second moment, contrast, mean, short run emphasis, long run emphasis, run percentage, gray-level nonuniformity, and run length nonuniformity were extracted from the co-occurrence and run length matrices. A run length matrix is a 2D matrix, one element of which is $P_\theta(i,j)$ and records the number of pixels where gray-level i has a run length j contingent in the θ direction. The first dimension of the 2D matrix corresponds to the maximum gray-level, while the second dimension corresponds to the maximum run length. The short run emphasis is a weighted average of the inverse run lengths squared, with the weights being the values of $P_\theta(i,j)$:

$$\text{Short run emphasis} = \frac{\sum_i \sum_j \frac{P_\theta(i,j)}{j^2}}{\sum_i \sum_j P_\theta(i,j)} \tag{2.11}$$

The long run length emphasis is the weighted average of the run lengths squared:

$$\text{Long run emphasis} = \frac{\sum_i \sum_j j^2 P_\theta(i,j)}{\sum_i \sum_j P_\theta(i,j)} \tag{2.12}$$

The run percentage was calculated by dividing the total number of observed runs in an image with the area of the image, A:

$$\text{Run percentage} = \frac{\sum_i \sum_j P_\theta(i,j)}{A} \tag{2.13}$$

The value of gray-level non-uniformity decreases with the increase of uniformity in the distribution of the runs over all gray levels [2]:

$$\text{Gray level non-uniformity} = \frac{\sum_i \left\{\sum_j P_\theta(i,j)\right\}^2}{\sum_i \sum_j P_\theta(i,j)} \tag{2.14}$$

On the contrary, the value of the run length non-uniformity reaches its lowest when the distribution of the run over all run lengths is uniform [2]:

$$\text{Run length non-uniformity} = \frac{\sum_j \{\sum_i P_\theta(i,j)\}^2}{\sum_i \sum_j P_\theta(i,j)} \tag{2.15}$$

However, only four features were finally selected—the first- and the third order moments, the run percentage, and the gray-level nonuniformity— because they were found to be clinically significant compared with the other features [1].

The thermal features, such as the maximum temperature in the eye region and the maximum temperature in the forehead region, were found to be very promising indicators for SARS analysis, headache, migraine, vascular disorders, sleep apnea, etc. [50, 131, 147, 159, 192]. Quek et al. [192] extracted the maximum temperature in the forehead and eye regions using a fuzzy neural network. A hot spot at the internal angle of orbita was observed more frequently than thermal asymmetry in migraine patients [7, 175]. In the analysis of arthritis and stress fracture, thermal

features, such as major axis length, minor axis length, and area, were extracted from segmented hot spot regions for further analysis [207].

In CTSd analysis, the mean temperature of each segment of a hand thermogram and the ambient temperature were measured for classification into healthy and CTSd hands, using an artificial neural network without the need of a cold stress test [169]. For mass screening of fever, Ng and Kee [160] extracted temperature data at the frontal and side profile of a face thermogram. The temperature data then were normalized and statistical analysis was performed to obtain the minimum, maximum, mean, median, and standard deviation of the temperature data. Varga and Hanka [235] selected mean temperature and variances of different disease classes as features that appeared most important for disease classification based on the Kittler and Young [122] feature extraction method.

Selvarasu et al. [207] used the major and minor axis length, the area, and the variance in pixels of extracted hot spots to characterize the nature and severity of the abnormality in thermograms of arthritis and stress fractures. Nurhayati et al. [164] reported that by fitting the curves of skewness, standard deviation, and entropy values as functions of the mean value, they could discriminate between normal and abnormal breast thermograms, especially for early and advanced cases. Furthermore, they found that the normal breast thermograms had the smallest standard deviation and skewness values, unlike the abnormal ones, especially the advanced cases. In contrast to this finding, the normal breast thermograms had the highest mean value, which was different from the advanced and early breast cancer thermograms [164].

Wiecek et al. [240] obtained thermal features for image classification using image histograms, COMs, and wavelet transforms. By using raw data analysis, three of seven original features were selected with the first two derived from the COM (sum of squares and inverse difference moment) and the third based on the wavelet transform (energy for the first scale of analysis and high- and low-frequency sub-bands along the x- and y-axes). Wavelet transformation was performed by low-pass and high-pass image filtering, followed by decimation in all scales until the size of the image was reduced to a single pixel. From the wavelet transformed image, one may work out the gradient of the temperature (obtained from the high-pass filtering), the global temperature distribution (obtained from the low-pass filtering) and the level of temperature, estimated from the energy of the signal. Classification based on these features was then performed using a neural network and was compared with the nearest neighbor (NN) classification.

In a study of facial expression, transient facial thermal features were used in the classification

[118, 120]. In this work, thermal intensity values (TIVs) in thermograms of faces were measured to obtain sample data using CMView Plus software where each thermogram was divided into a grid of squares. The highest temperature value in each square was recorded as the TIV for each square. Then the variation in TIVs was measured based on multivariate analysis and exploratory realignment. These methods were used to identify TIVs with significant thermal changes and to produce 75 squares (using a grid of 128 squares) known as facial thermal feature points (FTFPs). The FTFPs provided the information of facial thermal variations across the face. Before the thermal feature extraction the TIV data were normalized using the mean thermal value. A thermal feature vector, consisting of the projection coefficients on eigenfaces, was then extracted using PCA to be used for the classification process.

For thermogram analysis, Underwood [234] used active appearance models (APMs) containing not only the shape but also texture data of hands, regardless of the pose of the hand. In the modeling of the APMs, in order to obtain parameters able to control both shape and appearance, a set of parameters describing shape and gray-level variations was extracted using methods such as morphing, affine transformation, etc. The parameters of the shape and the gray-level variations were then concatenated and further used in a PCA. Two training approaches were used in parallel to obtain this model: the total approach (using all the images) and the serial approach (using only corresponding points from the various images). Upon training of the models, extraction of the percentage variance explained by each parameter and by the first 20 parameters for each image was performed for further processing [234].

2.3.2 Classification Methods

The classification is performed using features extracted from the image. The most commonly used features are designed to capture asymmetries observed in contralateral parts of the body. When several features are to be used, feature reduction via principal component analysis (PCA) may be used followed by some sophisticated classifier, like a neural network or a support vector machine (SVM).

Artificial neural networks (ANNs), which constitute a supervised learning method, are commonly used in the classification of thermograms [108, 124, 169, 234, 240]. A neural network generally consists of input nodes, hidden layers, and output nodes (Figure 2.17). The number of input nodes is equal to the number of selected image features, whereas the number of neurons in the first hidden layer may be equal to or less than the number of features in the classification.

A user-defined hidden layer may be added as well to allow additional nonlinear processing of the input features [240]. This approach is commonly known as nonlinear discriminant analysis (NDA) and can improve the classification by allowing additional decorrelation and data reduction [240]. An important step in ANN is the training of the network, which can be considered a multivariable optimization problem, typically based on the back-propagation (BP) technique. To avoid generating false solutions, it is better to have a sufficient number of data, especially for the learning phase, and to repeat the training of the network with different initial values of the neuron weight coefficients solutions [240].

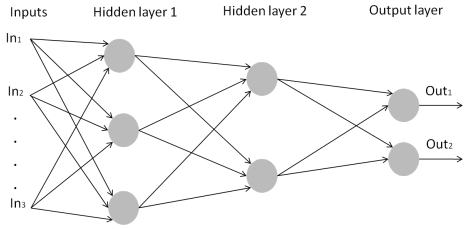


Figure 2.17: A Neural network example with inputs, two hidden layers, and an output layer ([169]).

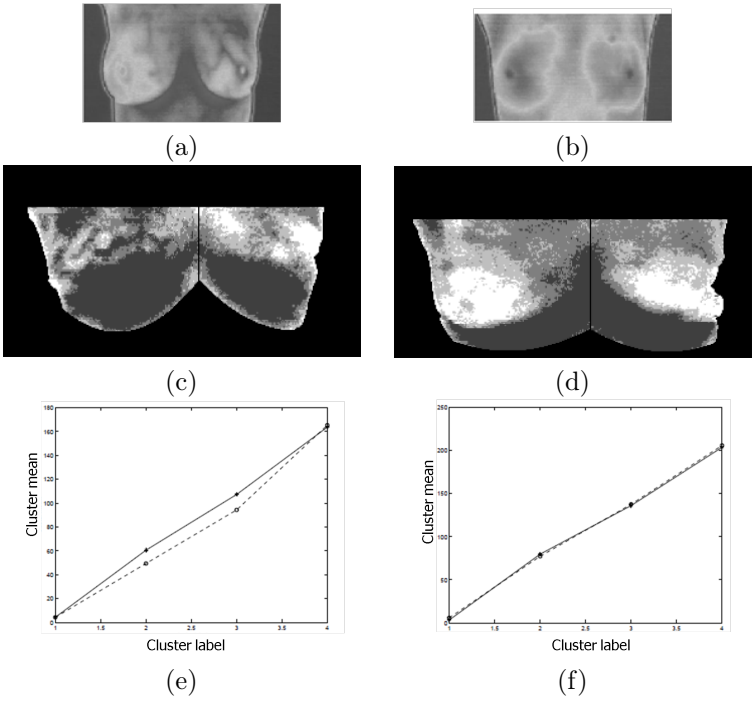


Figure 2.18: Results of k-means clustering. (a) Original Image A; (b) original image B; (c) classified image A in labeled format; (d) classified image B in labeled format; (e) profiles of the mean value of pixels in each cluster for the left and right breast segments of classified image A; (f) profile of the mean value of pixels in each cluster for the left and right breast segments of classified image B. (Reproduced from Qi et al. [190], with permission.)

Koay et al. [124] used a supervised classification method based on a BP neural network for

diagnosis of breast cancer using breast thermograms. The algorithm was implemented with the MATLAB Neural Network Toolbox built-in functions. Initially, based on a correlation analysis of the statistical parameters computed using the Statistical Package for the Social Sciences (SPSS), five parameters were chosen for further analysis: mean, standard deviation, skewness, kurtosis, and heat content. However, due to the small number of datasets, the BP network was trained and used with only one hidden node and two input parameters: the mean temperature difference and the standard deviation difference. Two types of training algorithm were investigated for suitability: the Levenberg–Marquardt and the resilient back-propagation. In the network, all neurons had the tan-sigmoid function as their transfer function and all inputs were normalized between -1 and 1. The BP neural network was able to generate fairly accurate clinical outcomes for both training algorithms. However, both algorithms produced a false-negative outcome because of the small number of patients with cancer [124].

An ANN was also used by Papez et al. [169] for the classification of hand thermograms for CTSd. The mean temperature of each hand segment, as well as the ambient temperature were measured to classify the hand thermograms into healthy and CTSd hands. The ANN was used by the authors as they claimed this classification method is capable of extracting similarities in apparently unrelated data [169]. Their network consisted of an input layer, an output layer, and two hidden middle layers (nine neurons in the first layer and five neurons in the second layer); 80% of the entire dataset was chosen randomly as the training set, whereas the remaining data were used for testing the network. To eliminate the variation factor of hand temperature between different people, normalization of temperature for each individual segment was performed according to the mean temperature of the whole hand. The classification was then conducted for four cases: using data from (1) all images, (2) dorsal images, (3) palmar images, and (4) dorsal images of healthy and severe cases only. A success rate as high as 80% was achieved in most cases. However, a success rate exceeding 83% was achieved using the data of healthy subjects and severe cases of CTSd only. From the results of all classifications conducted, the authors concluded that the proposed ANN method was able to classify thermograms of CTSd hands without the need for a cold stress test [169].

Because of the small number of datasets (6 normal and 18 cancer patients), Qi et al. [190] performed the classification using the bilateral ratio alone (as discussed in Section 2.3.1.2) with the k-means algorithm. The algorithm was applied to classify the pixels in segmented breast regions into a certain number of clusters. The mean value of the pixels in each cluster for each breast segment was then calculated and ranked in increasing order. These values then

formed the so-called profile of each breast. Examples of such profiles for two images are shown in Figure 2.18. Any asymmetric pattern between contralateral breasts could be identified by taking the difference of the corresponding values of the profiles of the left and right breasts [190].

Ng and Kee [161] used an ANN based on a radial basis function Network (RBFN) consisting of three layers using the Neural Network II/Plus software. The maximum temperature of the near-eye regions and the maximum temperature of the forehead regions were selected as input variables for training the ANN because they were found to be the best correlated regions by a biostatistical method called parabolic regression (PR). The PR method was chosen over a linear regression method as it could provide a more accurate and realistic approach in providing the correlation coefficient between two variables: 1 (nonhealthy) or 0 (healthy) and the actual health status (healthy or nonhealthy) of a subject. It was concluded that the proposed approach yielded predictions with a high level of accuracy, sensitivity, and specificity based on the temperature data extracted from the thermograms. Since the correlation with the body core was high, the efficacy and reliability of the proposed approach for mass screening of fever cases were considered proven [160].

Other classification methods that can be found in the classification of thermograms are the k-Nearest Neighbor (kNN) [190, 222], fuzzy classifiers [123, 205, 222, 224], Gaussian mixture models [222] and Support Vector Machines (SVM) [1, 222]. These methods are discussed and detailed out in Izhar and Petrou [106].

2.3.3 Discussion on the Merits and Demerits of the Indicators Extraction Approach in Thermal Image Processing and Analysis

The two approaches—namely, (1) solving the inverse heat transfer problem based on numerical modeling techniques and (2) extracting indicators from thermograms based on image-processing and analysis techniques— have their own advantages and disadvantages in quantifying the relationships between thermal behavior and the underlying physiological/ pathological conditions.

This section only focus on the latter approach. This approach requires understanding of the significance of gray levels in thermograms in correlation with the underlying physiological conditions of the human body. With the improvement of thermal imaging systems, thermogram analysis using this approach is very promising [112]. Abnormalities in medical thermograms exist due

to the underlying physiological/pathological condition that causes alteration in the thermoregulation of the human body [89]. These conditions are often manifested as abnormal vascular and focal patterns, high-/low-temperature regions, asymmetries in temperature distribution, abnormal contours, etc. [89, 114]. By extracting these features as indicators of abnormalities in thermograms, diagnosis from thermograms may be performed with high success rate. The processes involved generally consist of segmentation of ROIs, feature extraction, and subsequent classification of the thermogram into healthy and nonhealthy classes based on the extracted features. In this approach, the segmentation of ROIs could assist in more accurate diagnosis from thermograms and reduce computation time, since analysis is performed only on particular regions instead of the whole image. The thermal features can be extracted from the ROIs using statistical parameters computed directly from the image or after the image has been subjected to some transformation (see Sections 2.3.1.2 and 2.3.1.3). In thermogram analysis using asymmetry-based features, the environmental factors or the internal thermal conditions require no special care. By using asymmetry-based features, environmental factors (e.g., the ambient temperature) and internal thermal conditions (e.g., age, gender, body weight) are eliminated. This may increase the accuracy of the diagnosis [66, 141]. Asymmetry analysis also allows the use of temperature distribution in the disease classification rather than the use of the absolute temperature. Smaller and deeper tumors may also be detected by asymmetry analysis. Other features, such as the presence or absence of an adaptive response to an autonomic challenge procedure (dynamic imaging), which can be extracted effectively by image-processing techniques, can also serve as important indicators for abnormalities in thermograms [67, 89]. They can also characterize, in a meaningful way, the localized regions associated with the underlying pathological condition and thus lead to high accuracy in disease diagnosis [89, 118, 120, 234]. Further processing using classification methods based on ANNs, fuzzy classifiers, SVMs, etc. using the features extracted may lead to accurate and efficient diagnosis from thermograms. However, the segmentation of ROIs may require manual intervention due to the irregular shape and vague boundaries of parts of the body. The results of classification are also less specific on the structure of the tumor (depth, size, and so on) and vessel geometry than the physics-based approaches.

2.3.4 Image Registration

Image registration is found very useful and of vital importance in the analysis of medical images such as in longitudinal studies where there is a need to detect any differences between two or more images of different or same subjects that can be taken at different times and/or angles [79, 143].

It aligns two or more images into one coordinate system prior to integration/comparison between them. Hence, image registration is a very crucial step before any further analysis that involves integration or comparison between two or more image data can be carried out [79, 162].

A simple translation method employed in Herry et al. [92] for difference analysis between two contralateral knees is one form of image registration. In Schaefer et al. [204], thermogram of body parts of morphoea patients and their optical image data are fused together after image registration is performed for further analysis of the disease and monitoring of treatment efficacy. In the feature extraction for analysis of rheumatoid arthiritis, Aretusi et al. also had to perform image registration in order to obtain a uniform interpretation of the segmented features prior to image classification.

In this thesis, image registration methods are discussed further in Chapter 3 and Chapter 4.

2.4 Conclusions

Thanks to the advances in IR thermal imaging technology, image, processing techniques, and the pathophysiological understanding of thermograms, IR imaging is very suitable for use as a first-line supplement to both health monitoring and clinical diagnosis. IR thermal imaging can be very effective in medicine and useful for early screening and detection of a wide range of diseases, ranging from neurology, vascular disorders, rheumatic diseases, tissue viability, oncology (breast cancer in particular), dermatological disorders, neonatal, ophthalmology and pain, to health problems, such as stress, anxiety, sleep disorders, and even for surgery and monitoring efficacy of drugs and therapies [3, 65, 82, 87, 124, 149, 158, 161, 162, 188, 189, 208]. This is achievable because changes in blood perfusion caused by inflammation, infection, injuries, angiogenesis, and tumor growth can be observed as hot or cold spots in thermograms. Hence, the study of the observable abnormalities in thermograms and the study of the heat exchange processes of the human body can provide information on the pathology of the underlying diseases [66, 161, 174, 241]. However, the study of the heat exchange processes in the human body for thermogram analysis is nondirect, difficult to apply, and requires values for several parameters relying on several assumptions, unlike the phenomenological approach, which searches for correlations between health states and observations made from thermograms using image-processing techniques.

In medical applications, thermograms are principally known to be symmetrical in temperature

patterns. Asymmetries induced by the formations of these hot and cold spots in thermograms often serve as indicators of physiological abnormalities. Thus, an asymmetry analysis approach based on image-processing methods seems quite popular for hemilateral disease diagnosis such as breast cancer and hemilateral radiculopathy. The asymmetry approach could also eliminates internal and external variables and allows the detection and evaluation of changes in the body surface temperature in the affected areas even for slight changes and for smaller and deeper tumors. Apart from using asymmetry-based features, other features, such as the mean temperature of the abnormal regions, variation and contours in thermograms, and features obtained by wavelet transform, could also assist in thermogram analysis. Classifiers such as ANNs, k-NN, SVMs, and others can be used to successfully distinguish between normal and abnormal thermograms based on the extracted features. ANNs are widely applied in the classification of medical thermograms due to their ability to identify similarities in apparently unrelated data. However, the result of the classification by this approach can be validated only if the size of the dataset used for training is large or at least sufficient. SVM-based classification methods also show great performance in the classification of medical thermograms [1].

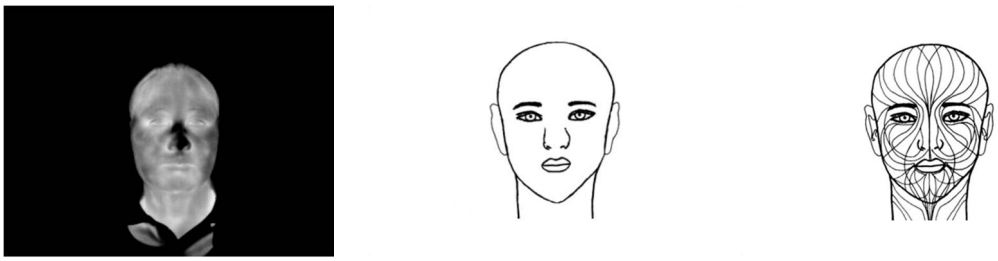
In conclusion, a fast, effective, and robust system based on thermal imaging can be very useful in the analysis of medical thermograms and hence allow mass screening for a disease. This is also supported by its advantages over other imaging modalities, such as being noninvasive, nonintrusive, radiation-free, fast, and cost-effective. Thus, it is necessary to develop image-processing and analysis methods to evaluate changes in the distribution of the body surface temperature for disease diagnosis. However, care must be taken as some of the changes in blood perfusion may occur for a variety of reasons other than inflammation and angiogenesis, such as previous traumas, and therefore they may be nonspecific. Therefore, it is found very useful and important to incorporate information from image taken by different imaging sensors such as visible image, MRI etc. into a thermal image so that information from the thermal image can be accessed more easily and most importantly with better accuracy than from the thermal image alone. In order to achieve this kind of integration between two or more images, image registration is thus inevitable in aligning these images into one coordinate system beforehand. In this thesis, image registration methods developed for medical application purposes based on thermal imaging are presented and discussed in the following chapters.

Chapter 3

Normalized Gradient cross-correlation (NGC) Method in Multimodal Image Registration

In an automated system based on thermal imaging, image registration is of vital importance to assist in the process of disease diagnosis and monitoring (e.g. in morphoea). In this chapter, a rigid or global based image registration is employed prior to integration between face thermograms and a face sketch (with and without the Blaschko's lines) (see Figure 3.1). As described in Chapter 1, it has been the main motivation of this work to utilize the information provided by the Blaschko's lines in not only the diagnosis of morphoea [16, 238], but also in monitoring of the disease progress and its treatment efficacy. On the other hand, apart from using optical image of a face, a face sketch without the Blaschko's lines can also provide important features such as the face outline, eyes, nose, mouth, ear etc. to an ambiguous face thermogram in order to improve its low spatial resolution. By integrating the information from both the images, the ambiguity in the thermogram can be reduced greatly and the access to its information can be enhanced. Hence, the current diagnosis and monitoring system of morphoea and other medical problems based on thermal imaging can be improved.

In recent years, there is an increasing number of applications which involve image analysis tasks that require integration between images from different types of sensors especially in medicine,



(a) (b) (c)

Figure 3.1: (a) Face thermogram as a reference image, (b) a drawing of the face or a face sketch as a target image (Reproduced from [238].) and (c) a face sketch with the Blaschko's lines that represent lesion patterns of linear morphoea (Reproduced from [238].)

remote sensing, computer vision, surveillance systems and image compression [177, 253, 254]. In general, the integration between multimodal images can enhance the amount of available information for a given image scene. For example, in medicine, combining data from different imaging modalities can sometimes be required in order to obtain complete or more information about the condition of a patient, for monitoring of tumor growth, treatment verification, and comparison of a patient's data with anatomical atlases [204, 72]. In remote sensing, a combination of various types of data is used for change detection, image mosaicking, environmental monitoring and multispectral classification. Similar comments apply to other image processing and computer vision problems such as target localization, automatic quality control, multispectral facial recognition and other problems [177, 253, 254]. A wide range of multimodal imaging technologies uses different type of sensors, different instrument modalities and different acquisition techniques to obtain a variety of images that is characterized in different manner in terms of their information [72, 109, 204]. The images of the same scene acquired by different imaging modalities may also differ in terms of contrast, object focus, color properties, texture and spectral characteristics [109]. Extracted information from any given multimodal image can be utilized to complement one source image to another and thus integration between them can be very useful for further analysis [72, 109, 177, 204].

The integration of these data from multimodal imaging systems leads to an important need of a process to transform the different sets of data into one coordinate system. This problem is generally referred to as image registration [79, 96, 181, 194]. In fact, image registration is the key element in all image analysis tasks where the integration of various data sources is the final outcome, such as in image fusion, change detection, multichannel image restoration and multiview analysis. In general, image registration aims to align and overlay two or more images of the same scene taken at different times, from different angles and/or by different sensors such

as from x-ray to near infrared, optical, laser (i.e., ladar, laser Doppler), ultrasound, magnetic resonance (MRI scan), computerized tomography (CT scan), positron emission tomography (PET scan) and particle image velocimetry (PIV). There is an abundance of image registration methods reported in literature. Some of the most popular methods are correlation based methods [13], feature based methods [21, 109, 125], and Fourier transform based methods [36, 39, 129, 194, 231]. In image registration, given a set of two images, one of the images is usually referred to as the reference or source image, while the other is called the target or sensed image [72]. Correlation based methods work by calculating a correlation matrix between the source image and the target image [13]. These methods are highly dependent on the brightness/magnitude of the pixels. On the other hand, feature based methods try to find distinct patterns/features such as lines, contours and shapes which occur in both images [21]. However, in the case of large image size, the computational complexity of the features in the correlation based methods becomes too high [39]. In the Fourier transform based methods, the frequency components in images are utilized. These frequency components can be produced by taking the Fourier transform of the images to be registered. A fast technique developed for implementation of the Fourier transform algorithms known as the FFT algorithm has contributed to the wide use of the Fourier transform based methods [28, 36, 39, 194, 231]. Moreover, the FFT based methods are found to be more resilient to differences in illumination as well as random noise [253]. They are also more favored than the other methods owing to their ability in solving for the best correlation of the frequency domain features [129].

Petrou [177] has outlined the steps that are found in most image registration approaches as follows.

1. A correspondence between two images (a target image and a reference image) is assumed. The correspondence can be represented by points, also known as control points, representing features detected (boundary regions, edges, corners, contours, line intersections, etc.) manually or automatically.

2. A transformation from the target to its reference image is estimated on the basis of the established correspondence.

3. The target image is transformed by applying this transformation model.

4. A similarity measure is computed between the reference image and the transformed target image.

5. The whole process is repeated until the value of the similarity measure is within acceptable limits.

In this chapter, an overview of the methods performed in regards to image registration between a face sketch and face thermograms of normal subject is firstly presented. Section 3.2 then explains the pre-processing steps involved in order to bring the multimodal images to the same image representation; gray edge maps. This is followed by the methodology of a phase correlation (PC) based image registration method in Section 3.3 and the methodology of a modified normalized gradient cross-correlation (NGC) method in Section 3.4. The results and analysis based on the NGC registration method are presented using artificially created image pairs in Section 3.5.1, and using real data in Section 3.5.2, followed by comparison analysis between the PC and the NGC based registration methods presented in Sections 3.5.2.1 and 3.5.2.2 respectively. Finally, conclusions from this chapter are given in Section 3.7.

3.1 Method Overview

The image pre-processing is the first step in the proposed global registration method between face thermograms and the face sketch. It has been known that registration between two different image modalities such as a thermal image and an optical image or a drawing, suffers from the problem of having non-direct relationship in their pixel intensities [109]. To overcome this problem, an edge detection approach can be employed in pre-processing of the two images of different modalities prior to the registration between them. From this process, the gray level edge map for each of the images are obtained in order to have both the images sharing the same meaning in their gray values [36, 177]. The edge information can also give more robustness and accuracy in the registration between two images as compared with intensity information of an image, as an edge map captures the structure of salient image features. Furthermore, problems related to the low-pass nature of a thermal image can also be solved. Besides, edges directly correspond to the sketch lines of drawings of the same object.

Hence, in this work, to register a thermal image with a drawing, edge detection is firstly performed as described in the next section [36, 177, 254]. In general, the features that can be extracted and used in an image registration are such as significant regions (e.g. human face, eyes, nose), lines (region boundaries) or points (e.g. corners, line intersections). In the case

of a face thermogram, the only lines that matter will be those that come from the change of tissues, as different tissues are expected to have different temperatures. However, changes of temperature within the same tissue have to be ignored as they are not always at the same place and they do not correspond to real facial features. The only tissue that is non-skin on the human face is the eyebrows and the eyes. So, the eyebrows are expected to be cold and produce thin line-like features on the face. Also, the nasal region is usually cold, hence the coldest part in the middle of the face will be the nasal region. Finally, the outline of the face can be easily determined because of an abrupt change of temperature between the face and the background.

Then, a phase correlation (PC) method which belongs to the Fourier transform based methods is performed using the edge maps obtained for registration between the two images of different modalities. The PC method is known for its ability to give large performance gains as it uses the FFT algorithm to compute the cross-correlation between two images [36, 194, 231]. It works by taking into account the correlation between two corresponding images and identifying the significant peak/maximum obtained [28, 36]. The peak corresponds well to the relative translation between the two images as it occurs at the position of the displacement coordinates. The property of the phase correlation in regards to its whitening of signals by normalization (global approach) enables the method to be robust to noise [28, 36, 39, 194, 231]. The noise can be associated with the image functions including uniform variations of illumination, offsets in average intensity and fixed gain errors due to calibration [64]. This property also serves as the key factor in the suitability of the method for registration between different spectral bands [64]. For two images that differ not only in translation but also in scaling and rotation, the phase correlation can be extended to the mapping of the Fourier transform of the two images to log-polar coordinates [36, 39, 194, 227, 231]. This is because, in the log-polar domain, the process of solving for the scaling and rotation differences can be simplified to finding a translation using the same PC technique for solving translational difference. The highest peak obtained by the cross-correlation in the log-polar domain corresponds well to the scaling and rotational differences between the two images. Section 3.3 discusses the PC method in details followed by Section 3.4 on a modified PC method known as the normalized gradient cross-correlation (NGC) method.

3.2 Image Pre-Processing

The corresponding points between the face sketch and a face thermogram can be obtained by edge detection applied to the face thermogram [36, 177, 254]. The edge information of an image can be extracted using edge detectors based on image gradient (e.g. Sobel, Canny etc.) or as zero-crossings in the second derivative of the image (e.g. by using filters like Laplacian, Laplacian of Gaussian (LoG)) [179]. The gradient based approaches detect edges by identifying the local maxima and minima in the first derivative of the image [142]. Canny, a gradient based edge detector is known for its great performance in noisy images that outweighs its high and complex computation [142]. On the other hand, a Sobel edge detector which is very sensitive to noise, gives good performance in detecting edges in low noise images [179]. It is also known for its simplicity in detecting edges. The thermograms used in this chapter are captured using a VarioCAM hr head 700 thermal camera with a thermal sensitivity of $30mK$ or $0.03°C$ [104]. With this level of thermal sensitivity it is known that the captured thermogram will have a very high signal to noise ratio as can be observed in Figure 3.1(a) [104, 226]. Hence, a Sobel edge detector which has the advantages of performing well in low noise images as well as being simple in detecting edges is selected to be applied to the face thermograms.

The Sobel operator consists of a pair of 3×3 convolution kernels that are designed to respond maximally to intensity changes running vertically and horizontally relative to the pixel grid. In this work, the commonly used Sobel operators, s_x and s_y, is applied as follows.

$$s_x = 1/8 \begin{bmatrix} 1 & 2 & 1 \\ 0 & 0 & 0 \\ -1 & -2 & -1 \end{bmatrix} \tag{3.1}$$

$$s_y = 1/8 \begin{bmatrix} 1 & 0 & -1 \\ 2 & 0 & -2 \\ 1 & 0 & -1 \end{bmatrix} \tag{3.2}$$

By applying the two directional convolution kernels separately to an image, f, the gradient components in each direction, g_x and g_y, can be obtained as

$$\begin{aligned} g_x &= f * s_x \\ g_y &= f * s_y \end{aligned} \tag{3.3}$$

where * is the process of convolution. By using the gradient component in each direction, g_x and g_y, the absolute magnitude of the gradient, g is computed as

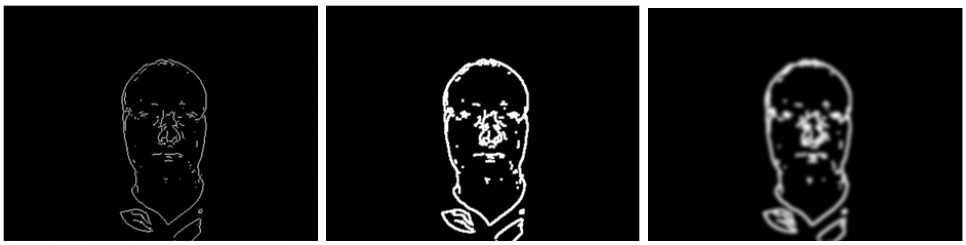
$$g = \sqrt{g_x^2 + g_y^2} \tag{3.4}$$

Then thresholding is applied first in post-processing for the edge detection. The threshold value is chosen automatically such that all amplitude discontinuities of a minimum contrast level are detected as edge pixels while all others as non-edge pixels. It is computed based on the root mean square (RMS) estimation of noise to obtain edge map that contains correctly detected edges from the edge gradients [184]. The noise is estimated by computing the mean of the magnitude of the squared gradient, g^2, as this mean value is considered to be roughly proportional to its signal-to-noise ratio (SNR) [184]. Then by taking the RMS of this estimated SNR value that is multiplied with 4, the threshold value is obtained automatically. The next task in the post-processing is to eliminate noise-induced edges. For this purpose, a morphological majority black operation is used [184]. This morphological operation sets a pixel to 1, if five or more pixels in a 3×3 window are 1, or else it is set to 0 [184]. Finally, a morphological thinning to reduce the width of the edge lines to a one-pixel width line is performed [184]. An example resultant image of such an edge map obtained at this point is shown in Figure 3.2(a).

As the contrast of the background and the face area in the face thermogram is high, it can be observed in Figure 3.2(a) that the outline of the face is effectively detected by the Sobel operator except for the jawline and chin area. This is due to the fact that changes of temperature between these areas and the adjoining neck area are very small. The nasal region is the feature where the most edges are detected (as predicted) even though there are some noise induced edges being detected as well. The edge of the upper lip is seen more often detected than that of the lower lip. Some meaningful edges representing the eyes and the eyebrows are also detectable by the Sobel operator. As for the drawing of the face, edge detection is not applied because the image already consists of outlines of the face. However, the negative of the drawing image is taken to provide the outlines in the image in white pixels as shown in Figure 3.3(a).

Next, the overlapping area between the edge map of the face thermogram and the outlines of

the face sketch has to be increased. This is in order to spread the information conveyed by each image and facilitate the registration process. This can be done by thickening of the edge/outline pixels to a 3 pixel width in size, by dilation with a 3×3 square structuring element. The thickened edge map and drawing outlines are shown in Figures 3.2(b) and 3.3(b) respectively. In order to increase the potential for pixel overlappings between the reference and the target images, the distribution of the thickened lines is spread by a Gaussian smoothing filter [179] of size $(2M + 1) \times (2M + 1)$ with $M = 5$ and with a discontinuity, ϵ of 0.1 at its sharpest cut-off edge, and a σ of 2.33. These settings are chosen as they produce sufficiently smooth distribution of the edge map (thermogram) and the drawing outlines (face sketch). Now, smoother, more distributed and spread edge map and drawing outlines as shown in Figures 3.2(c) and 3.3(c) are obtained to enhance the performance of the image registration based on phase correlation.



(a) (b) (c)

Figure 3.2: Pre-processing of the face thermogram; (a) edge map obtained using Sobel edge detector, (b) edge map after thickening and (c) after the Gaussian smoothing.



(a) (b) (c)

Figure 3.3: Pre-processing of the drawing of the face; (a) inverse of the drawing, (b) after thickening and (c) after the Gaussian smoothing.

Prior to phase correlation, spectral leakage effect that can be caused by the FFT needs to be eliminated or reduced. The FFT always assumes that an image's size is infinite and thus produces some spectral leakage or non-zero values as a result of spreading of energy when there are sharp discontinuities or broad frequency spectra [39, 231]. This effect of spectral leakage can be eliminated or reduced by lowering the discontinuities at the ends of a signal measurement time. This can be done by multiplying the signal data or the image by a function that smoothly

approaches zero at both ends. This process is also known as windowing and the multiplying function is called a 'window' function.

A suitable window function can be chosen with low side lobe amplitudes [84, 144]. In this work, a cosine tapered window, known as Tukey window [18] is used as it sufficiently suppresses leakage error upon FFT processing. This window function can be regarded as a cosine lobe of width $\frac{rL}{2}$ that is convolved with a rectangle window of width $\left(1-\frac{r}{2}\right)L$ [84, 230] as follows:

$$w(x) = \begin{cases} \frac{1}{2}\left\{1+cos(\frac{2\pi}{r}\left[x-\frac{r}{2}\right])\right\} & 0 \le x \le \frac{r}{2} \\ 1 & \frac{r}{2} \le x \le 1-\frac{r}{2} \\ \frac{1}{2}\left\{1+cos(\frac{2\pi}{r}\left[x-1+\frac{r}{2}\right])\right\} & 1-\frac{r}{2} \le x \le 1 \end{cases} \tag{3.5}$$

where L is the size of the Tukey window in the column vector w, x represents any of the L sampling points uniformly spaced along the real axis, in the range $[0, 1]$ and r parameter specifies the ratio of the length of taper section to the total length of the window. At $r \le 0$, this window becomes an L-point rectangular window while at $r \ge 1$, it becomes an L-point Hanning window [18]. A 2D Tukey window function, $w(x, y)$ can be obtained by multiplying a 1D Tukey window function with its inverse as follows.

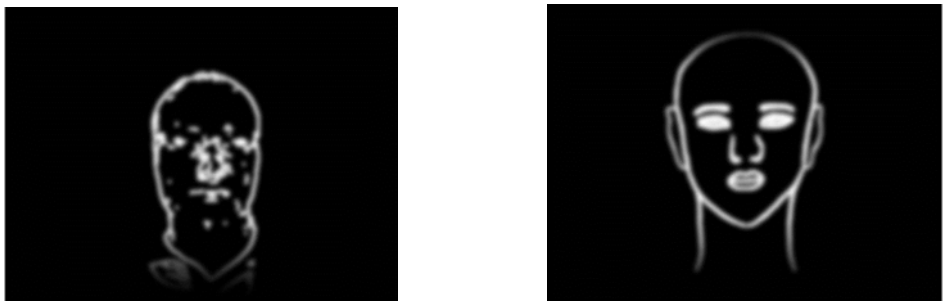
$$w(x, y) = w(x) \times w(y)' \tag{3.6}$$

where $'$ denotes inverse operation. Then, by multiplying an image function $f(x, y)$ by the 2D Tukey window function, $w(x, y)$, element-wise, windowing of the image function can be performed as given by

$$f'(x, y) = f(x, y).*w(x, y) \tag{3.7}$$

where $.*$ represents matrix element-wise multiplication. The resultant images after windowing by a 2D Tukey window for both the edge maps can be seen in Figures 3.4(a) and (b) .

It can be observed that windowing with the Tukey window also helps in excluding (i.e., minimizing the influence of) unwanted regions such as the neckline of a shirt, shoulder etc. in order to improve the perfomance of the registration process between two images. Initially r value is set to 0.6 as this value leads to good registration results between the face thermograms and the face sketch used in this work as unwanted pixels near image border are sufficiently reduced.

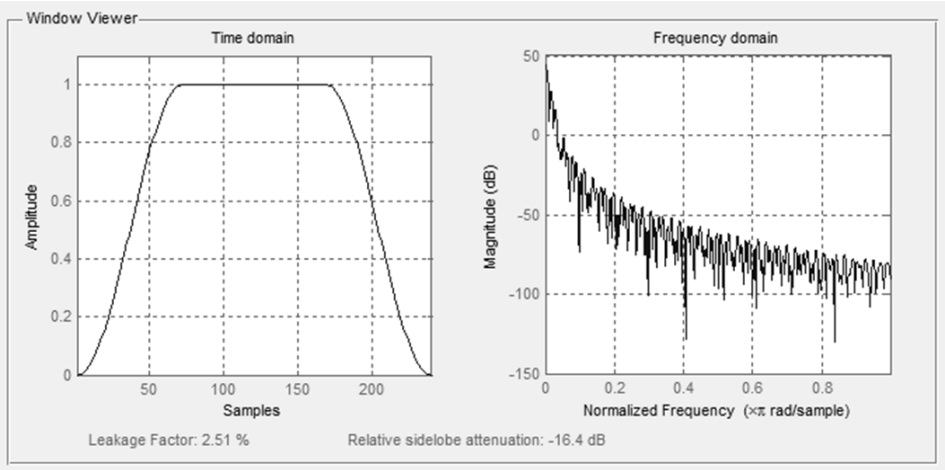


(a) (b)

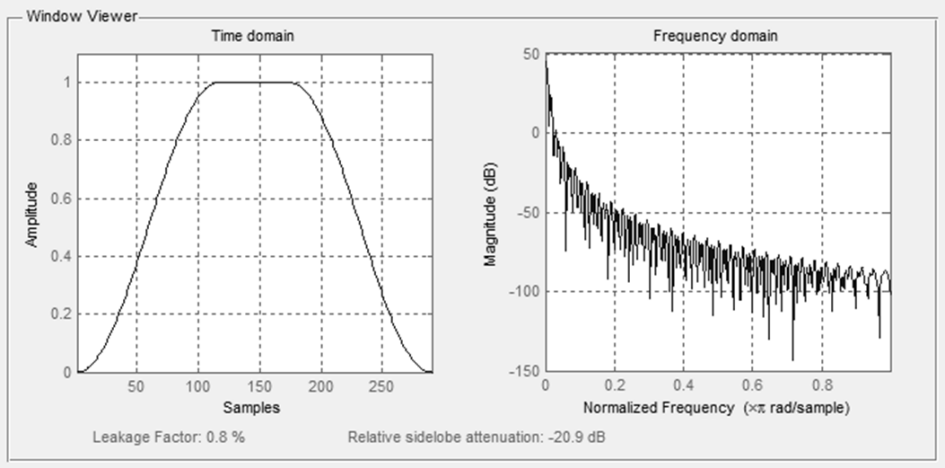
Figure 3.4: Resultant images after windowing using a Tukey window with $r = 0.6$ for (a) edge map of face thermogram and (b) the pre-processed drawing of the face.

However in some small cases where a foreground in a thermogram is small, a higher value of r, around 0.8 is needed to reduce the unwanted pixels near image border in order to achieve good registration result. A value to represent the ratio between image foreground and the size of the image is computed to assist in the windowing process. This value/image ratio is defined by the number of edge pixels (foreground) divided by the total number of pixels in the image. Then, a threshold value of 0.32 is used to determine whether a foreground in a thermogram is considered small or not based on the computed image ratio. The threshold value of 0.32 is chosen experimentally based on its ability to separate between the thermograms based on the size of their foregrounds (image ratio) satisfactorily. Hence, for those thermograms with an edge image ratio smaller than 0.32, a Tukey window with r value of 0.8 is applied (as the area of border pixels being attenuated are wider) while for those with an edge image ratio larger than 0.32, a Tukey window with r value of 0.6 is applied. Examples are shown for 1D Tukey windows of size 240 pixels in width, with the r value of 0.6 and 0.8 in Figure 3.5(a) and Figure 3.5(b) respectively. It can be observed that the Tukey window with $r = 0.8$ has less leakage factor, higher sidelobe attenuation and smaller 3dB bandwidth. However, both the windows show a decrease in the magnitude of its sidelobes which is one of the important features of a window.

Although by windowing both the images to be registered before their FFTs are taken can improve the performance of the registration performed as it reduces spectral leakage, this process can also result in lost of some information at image borders. This is because the pixels that carry information at image border are forced to become zero. However, this is not the case for the data used in this work. As can be seen in Figure 3.1, most of the useful edge information in the thermogram and the face sketch is centered at the middle of the image. Even though there are some edge pixels near the border at the bottom part of the images, these edge pixels are not carrying the information that is of interest in this work. In fact, these edge pixels are actually



(a) Tukey window with length of 240 and r= 0.6



(b) Tukey window with length of 240 and r= 0.8

Figure 3.5: 1-dimensionalTukey windows in time domain and frequency domain for different r values.

unwanted pixels that need to be removed or suppressed. By using the Tukey window, this objective can be achieved as shown in Figure 3.4(a) where it can be observed that these edge pixels are reduced in appearance.

3.3 Phase Correlation (PC)

3.3.1 Phase Correlation (PC) for Translation

The phase correlation (PC) technique is based on the Fourier shift property [13, 27, 129, 177, 194]. According to this property, a shift or translation in the Cartesian coordinates of two functions is a linear phase difference in the Fourier domain. Let $f_1(x, y)$ and $f_2(x, y)$ be two image functions that differ by a displacement or translation of (x_0, y_0):

$$f_2(x, y) = f_1(x - x_0, y - y_0) \tag{3.8}$$

Then their Fourier transforms are related by

$$\begin{aligned}
& F_2(u,v) && = F_1(u,v)e^{-j2\pi(ux_0+vy_0)} \\
\implies\ & F_1(u,v) && = F_2(u,v)e^{j2\pi(ux_0+vy_0)} \\
\implies\ & F_1(u,v)F_2^*(u,v) && = F_2(u,v)F_2^*(u,v)e^{j2\pi(ux_0+vy_0)} \\
\implies\ & F_1(u,v)F_2^*(u,v) && = |F_2(u,v)|^2\, e^{j2\pi(ux_0+vy_0)} \\
& && = |F_1(u,v)|^2\, e^{j2\pi(ux_0+vy_0)}
\end{aligned} \tag{3.9}$$

since $|F_2(u, v)| = |F_1(u, v)|$. The cross power spectrum of the two images is then defined as

$$\frac{F_1(u,v)F_2^*(u,v)}{|F_1(u,v)F_2^*(u,v)|} = e^{j2\pi(ux_0+vy_0)} \tag{3.10}$$

where F^* is the complex conjugate of F. The phase of the cross power spectrum represents the phase difference between the Fourier transforms of the two images [194]. The inverse Fourier transform of the normalized cross power spectrum $\frac{F_1(u,v)F_2^*(u,v)}{|F_1(u,v)F_2^*(u,v)|}$ is then performed. This process is the same as taking the inverse Fourier transform of function $e^{j2\pi(ux_0+vy_0)}$ that results in a Dirac delta function or an impulse that is centered at (x_0, y_0) and is zero everywhere else. Thus,

by choosing its maximum in the real domain, the displacement/translation between the two images can be identified [36, 39, 177, 194, 227, 231].

If the two images differ not only by translation but also by rotation and scaling, the inverse Fourier transform of the cross power spectrum of whitened signals (or normalized cross power spectrum) will not have a single distinct maximum [36, 39, 194, 231, 227]. Hence, the rotation and/or the scaling have to be removed first before retrieving the translation information.

However, using the PC, there is always some insignificant peaks obtained which can be assumed to be distributed over a mean value of zero. The power of these insignificant peaks correspond to the percentage of non-overlapping areas [64].

3.3.2 Phase Correlation (PC) for Scaling and Rotation

For scaling and rotation, the PC algorithm for translation described in the previous section has to be extended to be applied to log-polar mapping of the Fourier transform [27, 36, 39, 194, 227, 231]. This is done to isolate the scaling and rotation effects in the Fourier transform magnitude, since working in the log-polar domain simplifies the scale and rotational differences between the images to simple displacements/translations [36, 39, 227].

The mapping of the points on the Cartesian Fourier transform (u, v) into points in the log-polar grid (ξ, θ) is done using [194]:

$$\begin{aligned} \xi &\equiv \log \rho \\ \theta &\equiv \arctan \tfrac{v}{u} \end{aligned} \tag{3.11}$$

where $\rho = \sqrt{u^2 + v^2}$. The value of *base* for logarithmic conversions in eq. 3.11 has to be chosen to map as many points in the Cartesian grid as possible in the new log-polar grid while maintaining the same number of data points [194]. The following formula can be used to calculate the *base* [39]:

$$base = e^{\frac{\log_e(rmax)}{rmax}} \tag{3.12}$$

where, for a square image of odd dimensions, $(N + 1) \times (N + 1)$, (N is even).

$$rmax = \frac{N}{2} + 1 \tag{3.13}$$

The value of $rmax$ can also be defined as the maximum radius that can fit inside the image. The maximum radius is chosen to reduce the effect of discretization on the interpolation as more pixels are being considered for a given scene [36]. In this work, the edge maps are padded with zeros to a size of 1024×1024. This is done not only to make a different size images become of the same size, but also to ensure that the sizes of the images are of a power of 2, horizontally and vertically. By using eq. 3.13, with $N = 1024$, the $rmax$ calculated is 513. Then by substituting the $rmax$ in eq. 3.12, the value of the *base* calculated is 1.0122. The size of the log-polar grid is set to be $rmax \times rmax$ in order to avoid oversampling during the Cartesian to log-polar conversion [231]. The choice of the *base* using the size of the log-polar grid is also made to ensure that the extrapolated data will span the range $[0, rmax]$.

Now, let $f_2(x, y)$ be a target image that differs from its reference image $f_1(x, y)$ in translation by (x_0, y_0), rotation by θ_0 and scaling by s (along both dimensions). Their Fourier transforms are related as follows [231]:

$$F_2(u, v) = \frac{1}{s^2} F_1 \left(\frac{u}{s} \cos\theta_0 + \frac{v}{s} \sin\theta_0, -\frac{u}{s} \sin\theta_0 + \frac{v}{s} \cos\theta_0 \right) \times e^{-j2\pi\left(\frac{u}{s}x_0, \frac{v}{s}y_0\right)} \tag{3.14}$$

To eliminate the exponential term which is related to the translation, the magnitudes of both Fourier transforms are used. Let M_1 and M_2 be the magnitudes of F_1 and F_2, respectively. They are related as follows [231]:

$$M_2(u, v) = \frac{1}{s^2} M_1 \left(\frac{u}{s} \cos\theta_0 + \frac{v}{s} \sin\theta_0, -\frac{u}{s} \sin\theta_0 + \frac{v}{s} \cos\theta_0 \right) \tag{3.15}$$

It can be seen that the magnitudes of both Fourier transforms are the same except for the fact that one is a scaled and rotated version of the other. By mapping the points in M_1 and M_2 into their corresponding points in the log-polar grid (ignoring the multiplication factor $1/s^2$), change in scale and rotation becomes a shift; solving for the scaling and rotation is reduced to one of estimating a translation [177, 194, 231]. Furthermore, by using the Fourier magnitude representation in log-polar domain, the effect of low-frequency components induced by the areas of constant intensity level can be eliminated. This can further reduce the interpolation error

induced by the conversion from Cartesian to polar/log-polar domain [231]. The magnitudes of the two Fourier transforms in log-polar representation are related by [194]

$$M_2(\log \rho, \theta) = M_1 (\log \rho - \log s, \theta - \theta_0) \tag{3.16}$$

This can be written as

$$M_2(\xi, \theta) = M_1 (\xi - d, \theta - \theta_0) \tag{3.17}$$

where $d \equiv \log s$, $0 \leq \xi \leq rmax$ and $0 \leq \theta \leq rmax$.

Note that eq. 3.17 has the same form as eq. 3.8 and as such, the same PC technique can now be used to find translation, in order to estimate the rotation and scaling parameters θ_0 and d, and from it s. Parameters θ_0 and d can be found by taking the coordinate of the maximum from the inverse cross power spectrum as point of translation, (d, θ_0). The scale factor s can be retrieved by using the *base* (log space) defined earlier and the maximum coordinate d. On the other hand, the rotation angle is recovered as sampling rate in θ direction or degrees per pixel multiplied by $\theta_0 - 1$ which is the amount of displacement in log-polar domain in θ direction. These formulae are shown respectively as follows [194],

$$\begin{aligned} s &= base^{(d-1)} \\ angle &= \tfrac{180}{rmax} \times (\theta_0 - 1) \end{aligned} \tag{3.18}$$

Note that, we have to subtract 1 from the parameters θ_0 and d since MATLAB starts indexing from 1. In Fourier domain, the magnitude of the discrete Fourier transform has a period π and not 2π. This means that it repeats itself after 180 degrees. Hence, in the case of rotation, there is always a 180° ambiguity in the calculated rotation angle [194, 231]. To resolve this ambiguity, it is necessary to compensate for both possible rotations, θ_0 and $\theta_0 + 180°$, compute their correlation functions, and, finally, choose the angle that yields the highest peak (obtained in the inverse cross power spectrum) as the valid solution to the rotation [194, 231]. Using the true angle, the rotation of the target image is corrected and then the translation can be found by the PC technique as described in Section 3.3.1.

However, small differences in the values obtained for the scale and rotation may originate from

the interpolation error introduced during the mapping from the Cartesian grid to log-polar grid [39]. This is because, when log-polar mapping is performed, instead of corresponding directly to another pixel in the Cartesian plane, a pixel in the log-polar plane corresponds to several pixels (the number of which is determined by the interpolation method used: e.g. bilinear, nearest neighbour, cubic, etc.) in the Cartesian plane [39, 168]. Hence, interpolation can cause some loss of resolution. Bilinear interpolation is used in this work as it has been found to give the best results for this application [194, 231].

To summarize, the PC algorithm for scaling, rotation and translation is performed as follows.

Algorithm 3.1 Phase correlation between multimodal images

Given a thermal image $f_1(x, y)$ and a sketch $f_2(x, y)$, in order to correct for the global translation, scaling and rotation, by which they differ, do the following.

1. Perform Sobel edge detection to the thermal image and take the negative of the sketch image in order to have the sketch lines in white pixels. Then, pre-process the negated sketch image and the edge map by dilation with a 3×3 square structuring element and followed by smoothing with a Gaussian filter of size 11×11 and $\sigma = 2.33$ to obtain the gray edge maps of both the images for further registration process.
2. Using the edge maps obtained in step 1, perform windowing using a Tukey window with a size that is the same as the image's size and with $r = 0.6$ or $r = 0.8$.
3. Zero-pad the images to size $N \times N$, where $N = 2^n$ and n is the smallest integer such that N is larger than the larger dimension of the image. Here, $N = 1024$ is used.
4. Compute their Cartesian FFTs, $F_1(u, v)$ and $F_2(u, v)$ and their magnitudes, $M_1(u, v)$ and $M_2(u, v)$.
5. Resample $M_1(u, v)$ and $M_2(u, v)$ to the log-polar domain using bilinear interpolation to obtain $M_1(\xi, \theta)$ and $M_2(\xi, \theta)$.
6. Compute the FFTs for the log-polar magnitudes without zero-padding.
7. Compute its inverse cross power spectrum and estimate the rotation angle and scaling factor, θ and s respectively, based on the location of the maximum peak (d, θ_0).
8. Undo the scale and the rotation of the target image using the estimated scaling factor and rotation angle by bilinear interpolation. Resolve the 180° ambiguity associated with the rotation angle.
9. Repeat steps 2 to 4 with the reformed target image in edge map.
10. Compute the cross power spectrum, then calculate the inverse cross power spectrum and find the location of the highest peak. This location will represent the translational differences between the images.

This methodology has recently been modified to work with the gradient field of an image instead of the gray values and this way it has been made more robust [231]. This modification is discussed next.

3.4 Normalized Gradient Cross-Correlation (NGC)

The greatest phase shift in an image occurs at the edges of the image. The information of the changes in the intensity values of the image pixels can be obtained in the magnitude of its gradients while the orientation of its gradients gives the direction of the change [39, 177, 231]. In this normalized gradient based cross-correlation (NGC) algorithm, image gradients from both the gray edge maps for both the reference and the target images (as obtained in Section 3.2) are derived along the x-axis and the y-axis to obtain gradients along the vertical direction, g_x, and the horizontal direction, g_y, respectively. Using these directional gradients, a complex gradient, g_1 of an image f_1 is given by

$$\begin{aligned} g_1(x,y) &= \tfrac{\delta}{\delta x} f_1(x,y) + j\tfrac{\delta}{\delta y} f_1(x,y) \\ &= g_{1,x} + jg_{1,y} \end{aligned} \tag{3.19}$$

where $j = \sqrt{-1}$. The gradient cross-correlation, GC, between two images can be defined as

$$GC(u,v) = \int\int g_1(x,y) g_2^*(x+u, y+v) dxdy \tag{3.20}$$

where $*$ shows the complex conjugate operation. In frequency domain, eq. 3.20 takes the form

$$GC(u,v) = F^{-1}\big\{G_1(w_1,w_2) G_2^*(w_1,w_2)\big\} \tag{3.21}$$

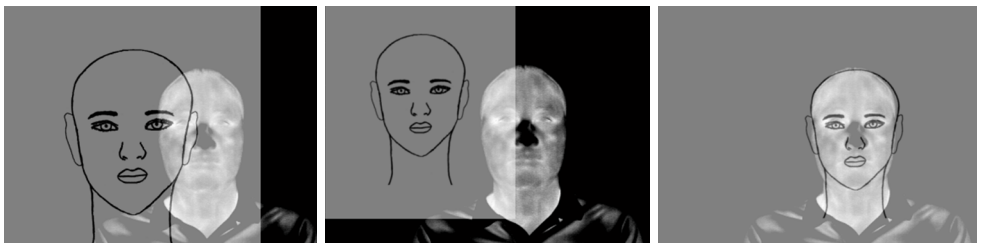
where $G_1$and G_2 are the 2D Fourier transform of g_1 and g_2 respectively and F^{-1} is the inverse FFT function. Now, the normalized gradient correlation (NGC) can be given as

$$NGC(u,v) = \frac{GC}{F^{-1}\big\{|G_1(w_1,w_2)|\,|G_2^*(w_1,w_2)|\big\}} \tag{3.22}$$

It can be seen that the NGC definition is similar to the inverse Fourier transform of the normalized cross power spectrum $\frac{F_1(u,v)F_2^*(u,v)}{|F_1(u,v)F_2^*(u,v)|}$ in the PC method except that the NGC scheme is based on image gradients. In this work, for the FFT computation in Cartesian coordinate (the first FFT), instead of using the complex gradients, the directional image gradients are combined by taking their magnitudes for both the reference and the target image as shown previously in eq. 3.4. However, the complex gradients of both images as shown in eq. 3.19 are used as the im-

age functions for the FFT computation in log-polar coordinate (the second FFT). In recovering for translational differences between the two images once the scale and/or rotation differences are removed from the target image, again the magnitudes of the gradients are used instead of their complex representation as edge magnitude gives pixel locations strong edge responses and suppress the contribution of areas of constant intensity level which do not provide any reference points for motion estimation [231].

The results of image registration based on the NGC method between a face thermogram (reference image) and the face sketch (target image) that differs in scaling and translation are shown in Figure 3.6. Another results obtained for the registration between the two images that differs not only in scaling and translation, but also in rotation, are shown in Figure 3.7.



(a) (b) (c)

Figure 3.6: Image overlay (a) before image registration is performed, (b) after removing of the scaling of the target image and (c) after translation is corrected (fully registered image) using the NGC method, between the face sketch and a face thermogram of Subject S4.

The NGC algorithm as summarized in Algorithm 3.2 for scaling, rotation and translation is similar to the algorithm of the PC method for scaling, rotation and translation (Algorithm 3.1 in Section 3.2) except for the image functions used in the NGC method as described as follows.

1. For step 3 in Algorithm 3.2, the image functions used are obtained by

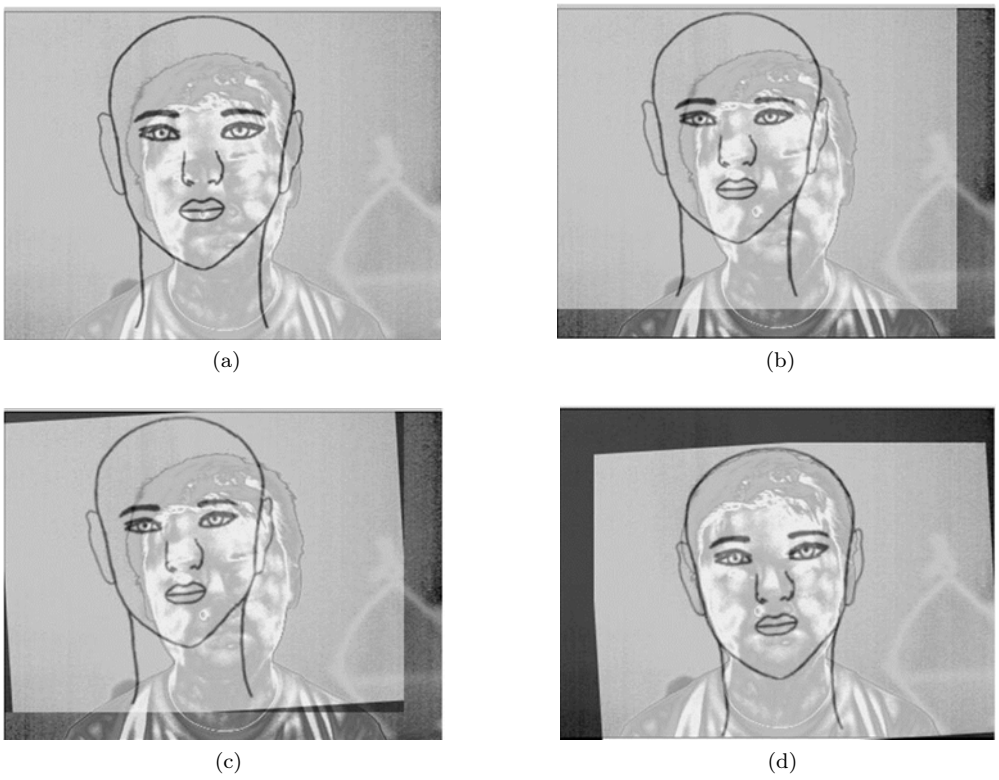
   (a) taking the directional gradients of the images obtained in step 2 by using the Sobel operator along the x-axis and the y-axis and

   (b) combining them by taking the magnitudes of the gradients for both images.

2. For step 6 in Algorithm 3.2, the image functions are obtained by

   (a) taking the directional gradients of the Fourier magnitudes in log-polar coordinates using the Sobel operator along the x-axis and the y-axis and

   (b) combining them in a complex representation for both images.



(a) (b)

(c) (d)

Figure 3.7: Image overlay (a) before image registration is performed, (b) after removing of the scaling from the target image, (c) after removing of the scaling and rotation from the target image and (d) after translation is corrected (fully registered image) using the NGC method, between the face sketch and a face thermogram of Subject S2.

As mentioned earlier, the face sketch used in this registration with thermograms is originally extracted from a sketch of a face with the Blaschko's lines as shown in Figure 3.8(a). Hence the sketches with and without the Blaschko's lines are similar in all aspects except for the Blaschko's line patterns. This enables the same parameters obtained to remove the translational, scaling and rotational differences from the face sketch without the Blaschko's lines to be applied to the face sketch with the Blaschko's lines, in order to register between the face sketch with the Blaschko's lines and its reference image (i.e., face thermogram) as can be seen in Figure 3.8(b).

3.5 Results and Analysis

Performance of the NGC method using artificially created image data is firstly presented in Section 3.5.1. Then, the NGC method is evaluated against the PC method using real data (thermogram) in Section 3.5.2. Fusion of the registered images presented in this chapter is performed by image overlay based on alpha blending by utilizing the alpha data property of

Algorithm 3.2 Normalized gradient cross-correlation (NGC) between multimodal images.

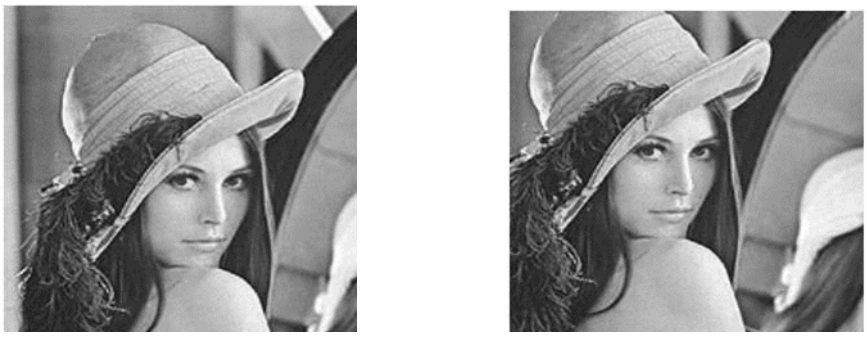
1. Perform Sobel edge detection to the thermal image and take the negative of the sketch image in order to have the sketch lines in white pixels. Then, pre-process the negated sketch image and the edge map by dilation with a 3×3 square structuring element and smoothing by a Gaussian filter of size 11×11 and $\sigma = 2.33$.
2. Using the edge maps obtained in step 1, perform windowing using a Tukey window with a size that is the same as the image's size and with $r = 0.6$ or $r = 0.8$.
3. Compute the directional gradients of the images obtained in step 2 using the Sobel operator along the x-axis and y-axis and combine them by taking the magnitudes of the gradients for both images
4. Zero-pad the images to size $N \times N$, where $N = 2^n$ and n is the smallest integer such that N is larger than the larger dimension of the image. Here, $N = 1024$ is used.
5. Compute their Cartesian FFTs, $F_1(u, v)$ and $F_2(u, v)$ and their magnitudes, $M_1(u, v)$ and $M_2(u, v)$.
6. Resample $M_1(u, v)$ and $M_2(u, v)$ to the log-polar domain using bilinear interpolation to obtain $M_1(\xi, \theta)$ and $M_2(\xi, \theta)$.
7. Compute the directional gradients of the Fourier magnitudes in log-polar coordinates ($M_1(\xi, \theta)$ and $M_2(\xi, \theta)$) using the Sobel operator along the x-axis and y-axis and combine them in a complex representation for both images denote by G_{M_i}.
8. Compute the FFTs for the G_{M_i} without zero-padding.
9. Compute its inverse cross power spectrum and estimate the rotation angle and scaling factor, θ and s respectively, based on the location of the maximum peak (d, θ_0) as described in eq.3.18 .
10. Undo the scaling and/or the rotation of the target image using the estimated scaling factor and/or rotational angle by bilinear interpolation. Resolve the 180° ambiguity associated with the rotational angle.
11. Solve for the translation by using the NGC formula in the spatial Fourier domain (the conventional way).



(a) (b)

Figure 3.8: The face sketch with the Blaschko's lines (a) prior to registration and (b) after registered to a reference thermal image.

any one of the registered images. The alpha data is an $M \times N$ matrix of the same size as the image with each element that can be referred to as alpha values, in the range of $[0, 1]$ indicating the opacity of a pixel [52]; with 0 indicating zero/null image strength to 1 indicating full image strength. An alpha value of 0.6 was used for the reference image as it was found to be able to give sufficient transparency to the reference image in the image overlay with its registered face sketch. Furthermore, to enable the subsequent image display of the reference image added to the registered image regardless of the sizes of both of the images, the current plot and certain axes



(a) (b)

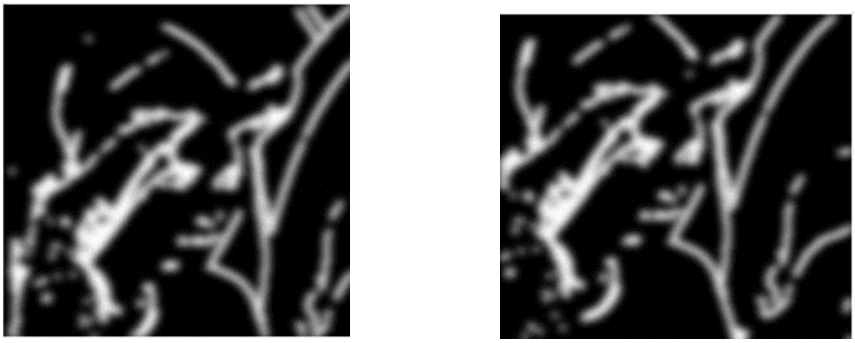
Figure 3.9: Artificially created images (of equal size) to be compared by taking two cropped images from a bigger image with a difference in translation of (20, 20); (a) Reference image and (b) Target image.

properties of the registered image was retained. However for further analysis of the underlying information from the thermograms, it is preferrable to apply the alpha value on the target image (face sketch) alone in the fusion image.

3.5.1 Performance Analysis based on Artificial Image Pair

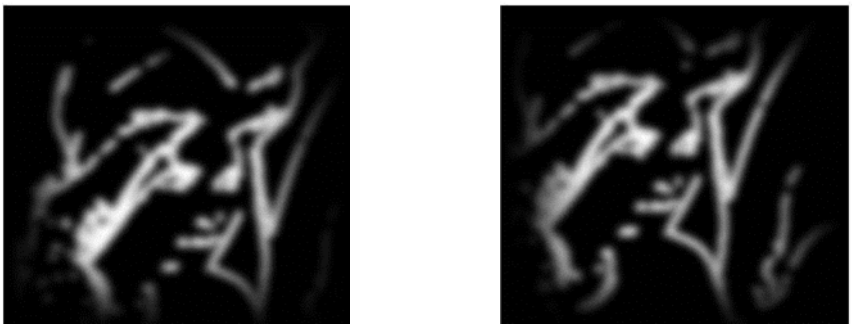
This section presents the performance evaluation for the NGC method using artificially created image pair. The method is evaluated on how accurate it can correct for any translations, scaling and rotations needed for an image to be registered to another image. For translational difference, two images (of equal size) as shown in Figures 3.9(a) and (b) are artificially created with significant overlap between them. The target image in Figure 3.9(b) is translated about (20,20) away from the centre of its reference image (Figure 3.9(a)). Figure 3.10 shows the gray edge maps of the reference and target images respectively that are used as the input image functions for the NGC algorithm. The edge maps will firstly undergo the windowing process with the Tukey window before their FFTs are taken (Figure 3.11). Fully registered images obtained (i.e., after the translation difference in the target image is corrected) by the NGC method are shown by the inverse cross power spectrum in Figure 3.12 and by image overlay in Figure 3.13. It can be observed in Figure 3.12 that the location of the maximum/peak is $(21, 21)$. As we need to subtract 1 from the location of the peak obtained as MATLAB starts indexing from 1, the location of the peak then becomes $(20, 20)$. This shows that the NGC method accurately estimates the translational differences between these images.

Another example using ground truth images where the target image in Figure 3.14(b) is a trans-



(a) (b)

Figure 3.10: The gray edge maps for the (a) reference image and the (b) target image.



(a) (b)

Figure 3.11: After multiplication of the edge maps with a Tukey window for the (a) reference image and the (b) target image.

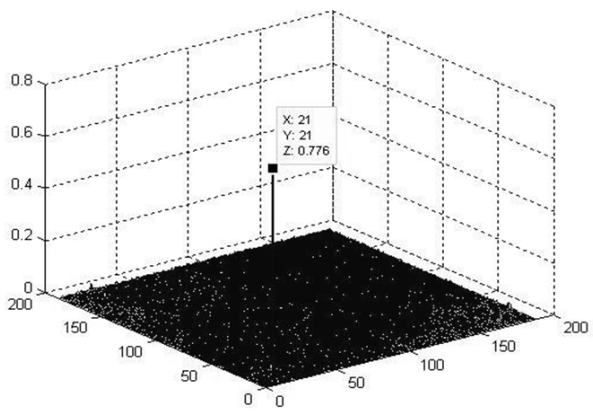


Figure 3.12: The inverse cross power spectrum with a significant peak at the translation between the two images.



Figure 3.13: Image overlay between the reformed target image (by translation) and the reference image.



Figure 3.14: (a) Original image as a reference image, (b) A replica of the original image after scaling, rotation and translation.

lated, upscaled and rotated replica of its reference image (Figure 3.14(a)), with a translational difference of $(20, 30)$, scaling factor of 1.2 and rotation angle of 45° is presented. Figure 3.15 shows the inverse cross power spectrum obtained between the target and the reference images where scale index, d, and the angle index, θ_0, are represented by the peak. Using the *base* value calculated previously, the information of the scale, s, and the rotation angle, θ_0, needed to compensate for the differences in scaling and rotation can be calculated from the location of the peak/maximum (θ_0, d) described as follows. The scale index, d, obtained is 16, hence the computed scale size is as follows:

$$s = \texttt{base}^{(\texttt{d}-1)} = 1.0122^{(16-1)} = 1.2002$$

Similarly for the computation of the recovered rotational angle, 1 is subtracted from the angle index, θ_0 obtained, which is 65, to compute the rotation angle as:

$$\theta \quad = (\theta_0 - 1) \times 360/(N/2) \quad = (65 - 1) \times (360/512) \quad = 45^\circ$$

It can be observed that the scale, s, and the rotational angle, θ, obtained are approximately the same as the actual scaling factor and rotational angle used to obtain the target image. However,

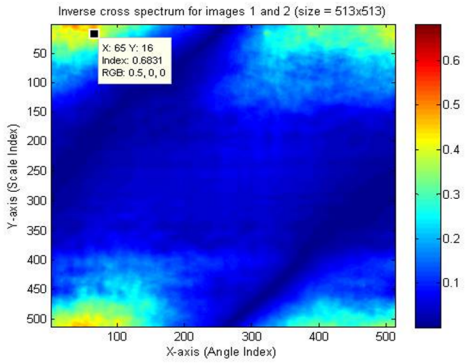


Figure 3.15: The inverse cross power spectrum of the two images and its maximum peak for finding the scale and angle of rotation based on the NGC method.

any small differences in the values obtained for the scale and rotation can be originated from the interpolation error introduced during the mapping from the Cartesian grid to log-polar grid [39]. This is because, when log-polar mapping is performed, instead of corresponding directly to another pixel in the Cartesian plane, a pixel in the log-polar plane corresponds to several pixels (the number of which is determined by the interpolation method (briefly explained in Chapter 4) used: e.g. bilinear, nearest neighbourhood, cubic, etc.) in the Cartesian plane [39, 168]. Hence, interpolation can cause some loss of resolution. Bilinear interpolation method is used in this work as it has been found to give better results for this application compared to the nearest interpolation.

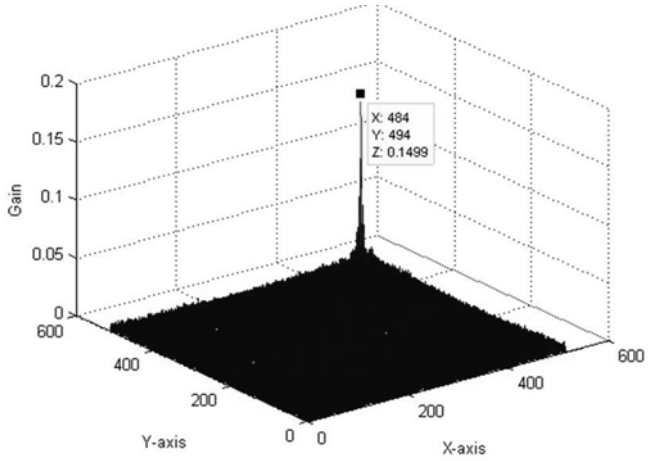


Figure 3.16: The inverse cross power spectrum of the two images and its maximum peak for finding the shift.

To retrieve the shift/translational displacements, it can be seen from Figure 3.16 that the location of the maximum peak is at row 494 and column 484. These row and column values are considered negative shifts as they are above half of the size of $(N/2) + 1$ (as the size of the inverse cross

power spectrum follows the $rmax$, along the vertical and horizontal dimensions respectively). Hence the actual translation is obtained as given by:

$$\begin{aligned} x_0 &= \{(N/2)+1\} - (row - 1); \\ y_0 &= \{(N/2)+1\} - (column - 1); \end{aligned} \tag{3.23}$$

The actual translation along the row thus becomes $513 - (494 - 1) = 20$ while the actual translation along the column becomes $513-(484-1) = 30$. This shows that the actual translation obtained is exactly the same as the translation applied to the target image. It has to be pointed out that the inverse cross power spectrum has small non-zero values at coordinates other than the translation between the two images as shown in Figure 3.16. This is the result of having limited overlapping between the two images as each image has areas where the other image does not possess [39]. Figure 3.17 shows the image overlay between the two input images that differ in scaling and rotation while Figure 3.18 shows the image overlay between the two input images that differ in translation, scaling and rotation.



(a) (b) (c)

Figure 3.17: Result of accuracy analysis; image overlay for the target and reference images (a) before image registration is performed, (b) after down scaling of the target image and (c) after removing the translational difference from the target image (complete registration).

3.5.2 Comparison Analysis between the NGC and the PC Methods

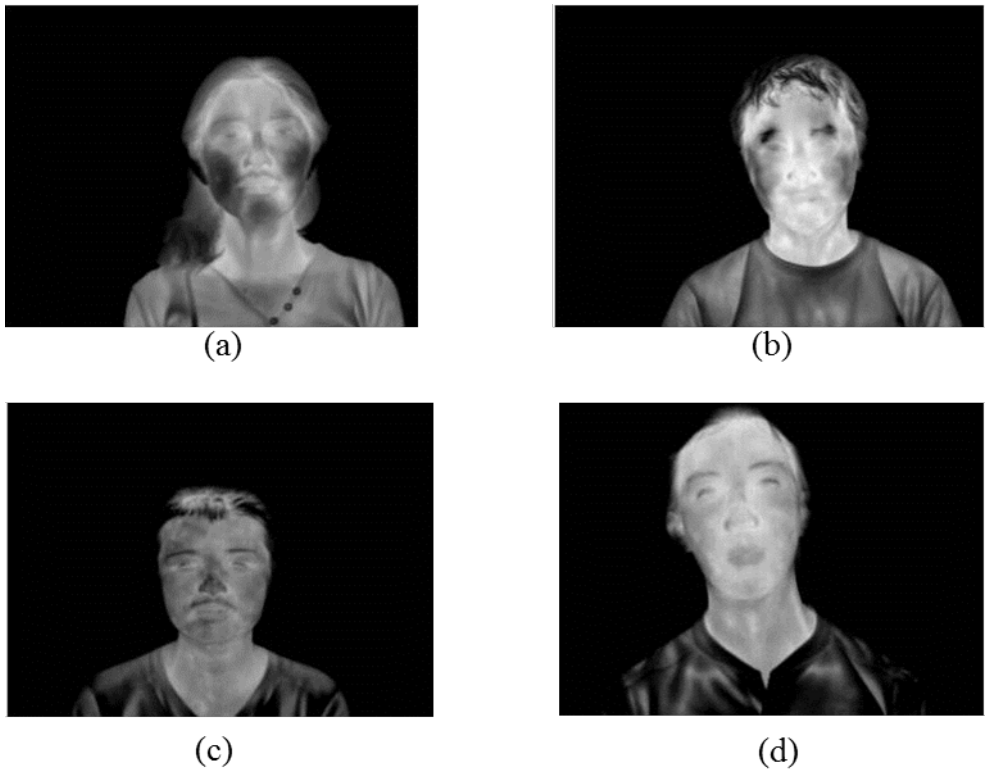
In this section, the results and analysis of registration between face thermograms and the face sketch using the NGC method is compared against the PC method. The face thermograms are acquired from 11 normal subjects at 7 time-points during a day for each subject. The pixel resolution of the face thermograms is 386×290, acquired using VarioCAM hr head 700 by InfraTec with a thermal sensitivity of up to $30mK$ or $0.03°C$. On the other hand, the pixel



(a) (b) (c)

Figure 3.18: Result of accuracy analysis; image overlay for the target and reference images (a) after down scaling of the target image, (b) after undoing the rotation of the target image and (c) after removing the translation difference from the target image (complete registration).

resolution of the face sketch is 348×306. From the 77 thermograms, 21 of them (total from 3 subjects) are used as training data for the development of the NGC algorithm and in fine tuning of its parameters while the rest of the 56 thermograms (from the remaining 8 subjects) are used as test data (as shown in Figure 3.19). The dataset consists mostly thermograms that differ only in scaling and translation with the sketch. However, it is observed that some data are slightly differed in rotation as well.



(a) (b) (c) (d)

Figure 3.19: Some examples of real data used for the multimodal registration; (a) training data of Subject S1 (no rotation needed); (b) training data of Subject S2 (rotation needed); (c) test data of Subject S9 (no rotation needed); (d) test data of Subject S8 (rotation needed).

3.5.2.1 Quantitative Analysis I

In this section, the registrations between the face sketch and the thermogram data are compared between the two presented methods; the PC method and the NGC method. For this comparison purpose, a quantitative analysis is carried out based on the results obtained by both methods (as shown in Figures 3.20-3.24) using performance parameters such as under-detection error, e_u, and over-detection error, e_o. These measures are obtained between the registered face sketch and its reference image based on their edge pixels. The edge pixels of the reference image are extracted manually for the quantitative comparison purpose between the NGC and the PC methods so that unwanted edge pixels from features that are not present in the face sketch are not included in the computation of the performance parameters. The only features that are manually extracted are such as the face outline, eyes, nose, mouth, neck and head as shown in Figure 3.25. The images with the manually extracted edge pixels are then binarized for the analysis purpose.

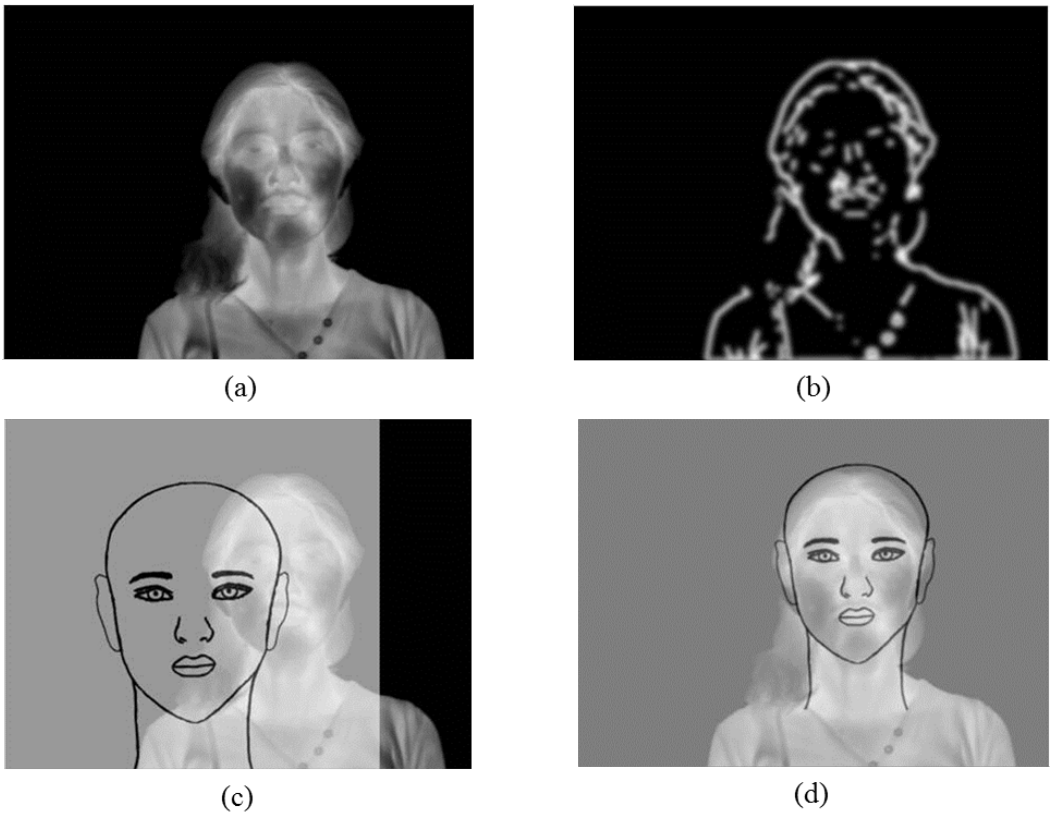


Figure 3.20: Registration result for a training data (Subject S1) using the NGC method; (a) the reference thermogram, (b) its input gray edge map, (c) before registration, and (d) after registration.

Based on the manually extracted edge pixels for each thermogram, $R(x, y)$, and the registered

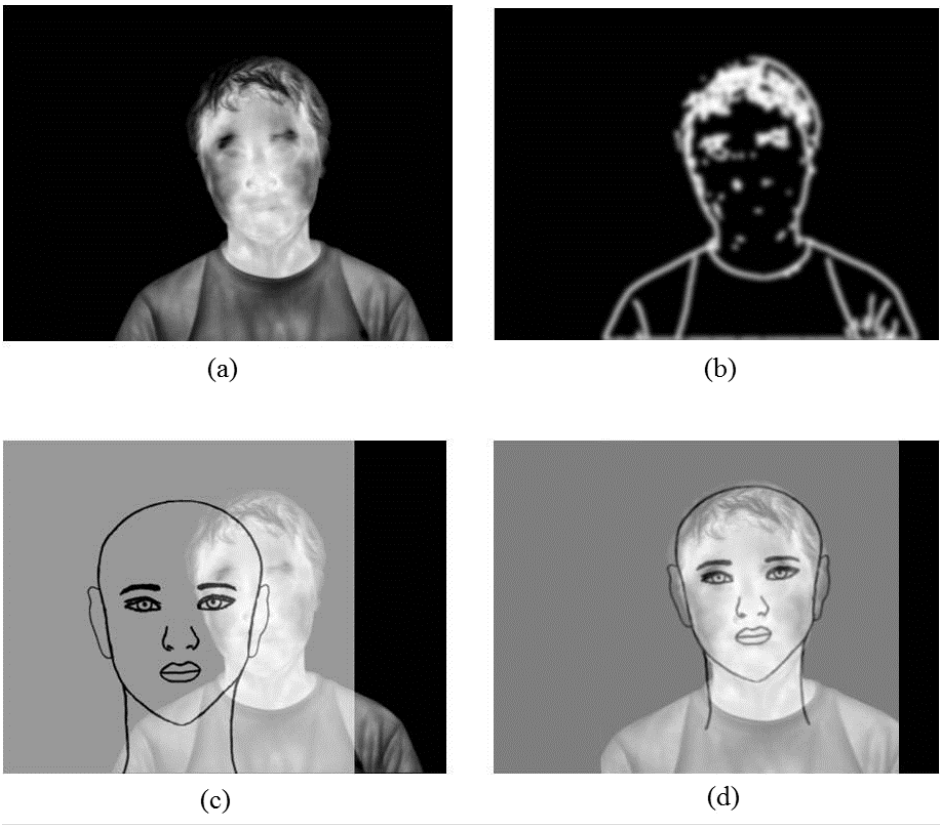


Figure 3.21: Registration result for a training data (Subject S2) using the NGC method; (a) the reference thermogram, (b) its input gray edge map, (c) before registration, and (d) after registration.

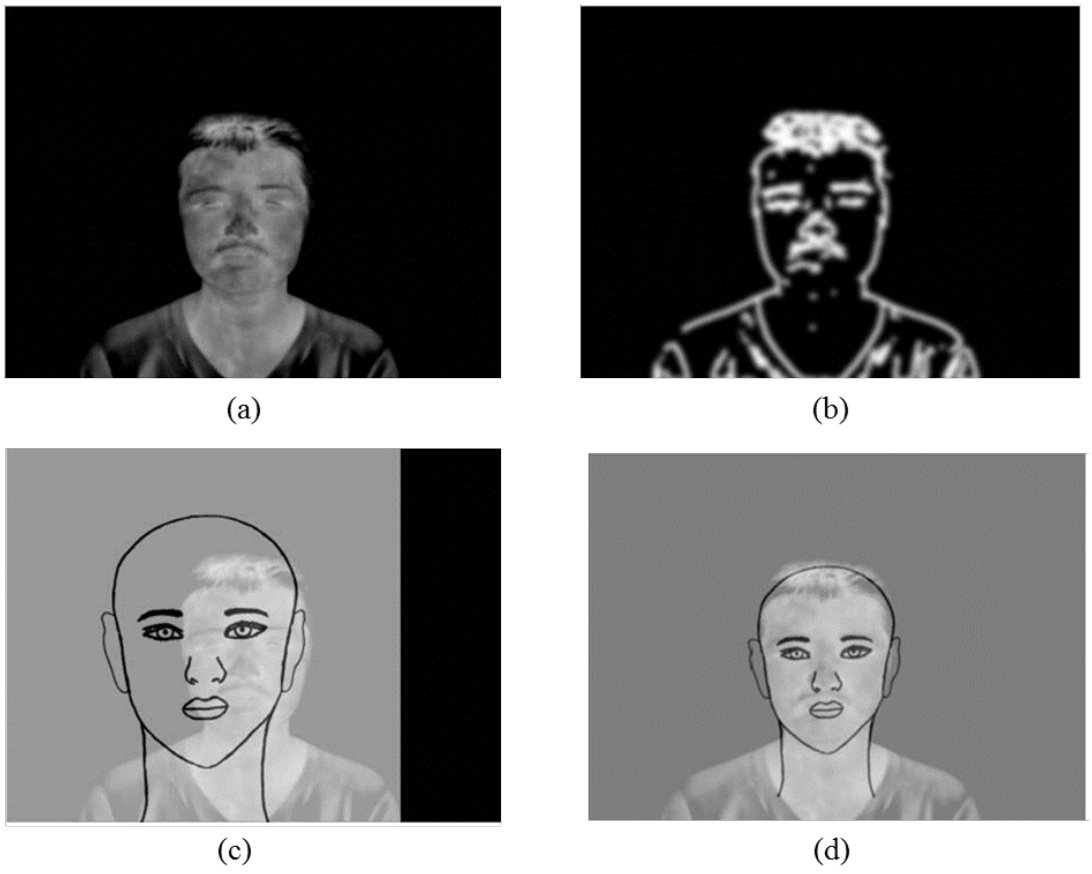


Figure 3.22: Registration result for a training data (Subject S9) using the NGC method; (a) the reference thermogram, (b) its input gray edge map, (c) before registration, and (d) after registration.



Figure 3.23: Registration result for test data S8 using the NGC method (a) the original thermogram, (b) its input gray level edge map, (c) before registration, and (d) after registration.

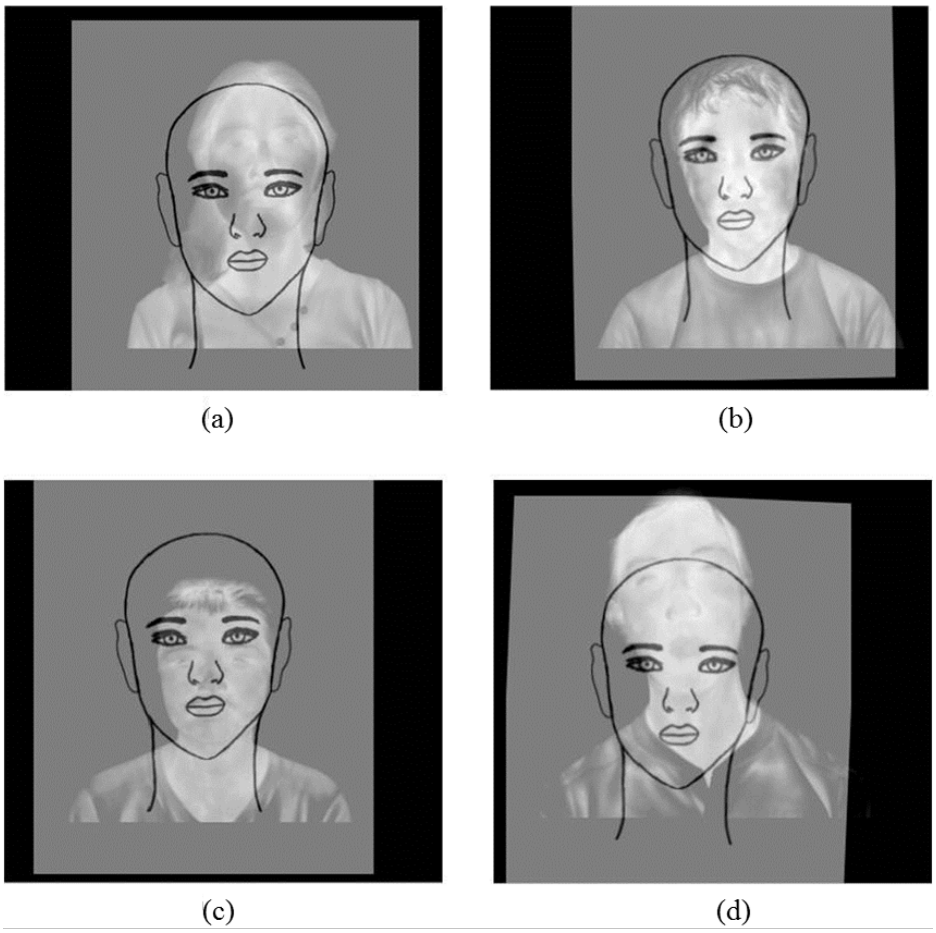


Figure 3.24: Registration results using the PC method for (a) Subject S1 (at 9 am), (b) Subject S2 (at 9 am), (c) Subject S9 (at 10 am) and (d) Subject S8 (at 10 am).

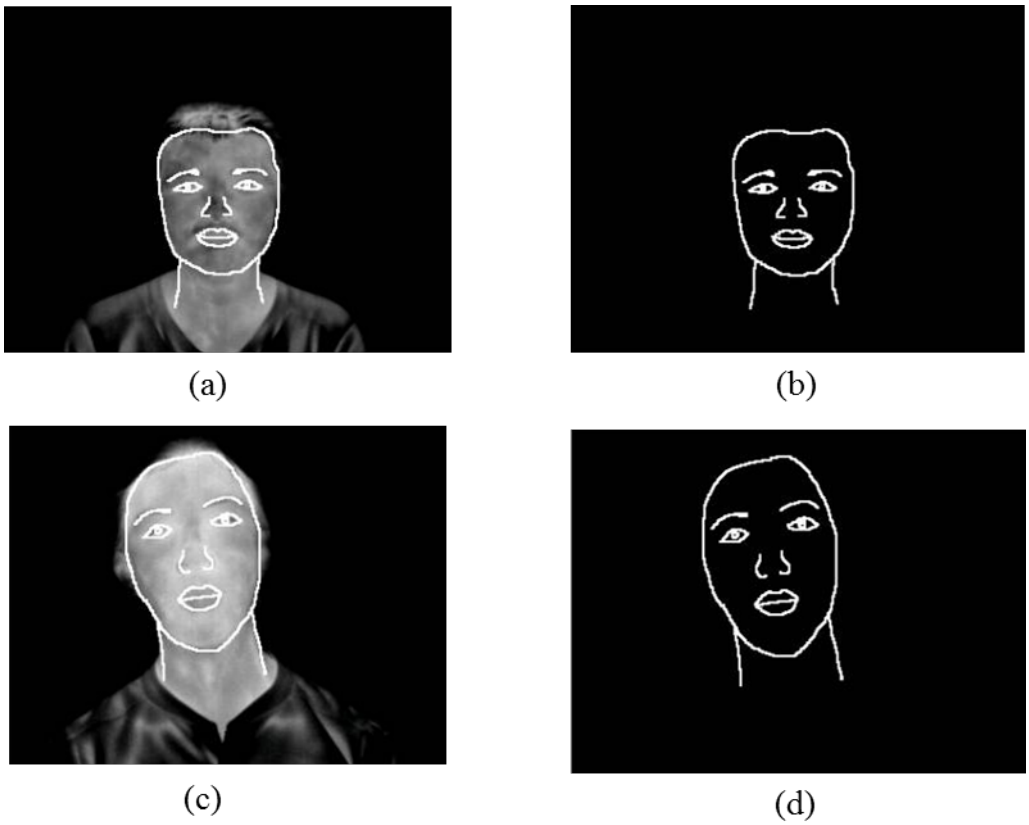


Figure 3.25: (a) Manually traced outlines from a thermogram (Subject S9) and (b) its extracted traced lines; (c) another example of manually traced outlines from a thermogram (Subject S8) and, (d) its extracted traced lines.

face sketch (intensity image), $S(x, y)$, once both images are in registration, to compute e_u and e_o, the followings are performed.

1. For every black pixel (edge pixel) in the registered sketch, $S(x, y)$, with coordinates (i, j), check whether there is an edge pixel with the same coordinates in $R(x, y)$. If yes, count it with a counter A. If no, count it with a counter B. Then, compute the under-detection error, e_u, as follows:

$$A = \sum_{x=i,y=j} [S(x, y) = R(x, y) = \text{Edge Pixel}] \tag{3.24}$$

$$B = \sum_{x=i,y=j} [(S(x, y) = \text{Edge Pixel}) \cap (R(x, y) = \text{Non-Edge Pixel})] \tag{3.25}$$

$$\text{Under-detection error, } e_u = B/(A + B) \tag{3.26}$$

1. For every edge pixel in $R(x, y)$, with coordinates (i, j), check whether there is a black pixel (edge pixel) in the registered sketch, $S(x, y)$, with the same coordinates. If yes, count it with a counter C. If no, count it with a counter D. Then, compute the over-detection measure, e_o, as follows:

$$C = \sum_{x=i,y=j} [R(x, y) = S(x, y) = \text{Edge Pixel}] \tag{3.27}$$

$$D = \sum_{x=i,y=j} [(R(x, y) = \text{Edge Pixel}) \cap (S(x, y) = \text{Non-Edge Pixel})] \tag{3.28}$$

$$\text{Over-detection error, } e_o = D/(C + D) \tag{3.29}$$

The process of computing these parameters is then repeated with a modification to consider the neigbouring 8 positions (3×3 neighbourhood of overlapping points). For example, when we look for a pixel (i, j), if there is a match in the other binary map, we do not just check position (i, j), but also the neighbouring 8 positions. Hence, a count is made as if a match is found if any of the pixels in the 3×3 neighbourhood of (i, j) is marked. The values obtained by this modification are referred to as case B while the ones without this modification as case A (1×1). Table 3.1 shows the comparisons between the performance parameters obtained for the NGC method and

the PC method for all the 11 subjects, each with 7 face thermograms taken at different time. The parameters (e_u and e_o) for both cases A and B are presented based on minimum, maximum and standard deviation (std) obtained from 7 images for each subject. As can be seen in Table 3.1, it can be observed from the overall values that the NGC method outperforms the PC method in terms of lower range of under detection and over detection measures obtained. It can also be observed that, as predicted, by considering 8 neighbouring pixels, the overall error parameters for both the NGC and the PC methods are reduced. The average stds computed for the results obtained for each subjects for all cases using both the methods are small, from 0.011 to 0.32 and comparable.

The average for the minimum, maximum, mean and standard deviation are also computed based on all subjects (a total of 77 images) for the parameters e_u and e_o for both cases A and B as tabulated in Table 3.2. From this table, it can be observed that for case A, in average, the range of values obtained for e_u and e_o for the NGC method are $0.76-0.87$ and $0.46-0.70$ respectively while for the PC method, the range of values are higher, $0.84-0.95$ for its e_u and to $0.59-0.85$ for its e_o respectively. On the other hand, for case B, as predicted, the range of values for both the under-detection error, e_u and the over-detection measure, e_o are reduced/improved; $0.57-0.77$ and $0.32-0.57$ respectively for the NGC method, $0.71-0.89$ and $0.48-0.77$ respectively for the PC method. However, the average errors found in case B for the PC method are still higher than that achieved by the NGC method.

From the mean errors obtained based on the 77 images (see Table 3.2), it can also be observed that both the NGC and the PC methods suffers from under-detection more than over-detection. Using case B, the gap between the two error measures is more significant in the NGC method since the value of over-detection error achieved by this method is reduced greatly. The average standard deviations computed for the results obtained for the 77 images for both cases A and B are small, in the range of $0.004-0.012$ for the NGC method and in the range of $0.11-0.16$ for the PC method. Overall, as expected, the NGC method outperforms the PC methods by having less under-detection and over-detection errors in registration between two multimodal images based on face thermogram and the face sketch.

3.5.2.2 Quantitative Analysis II

Apart from the comparisons performed based on the under-detection and the over-detection errors, a comparison based on the registration parameter such as scaling factor is also carried

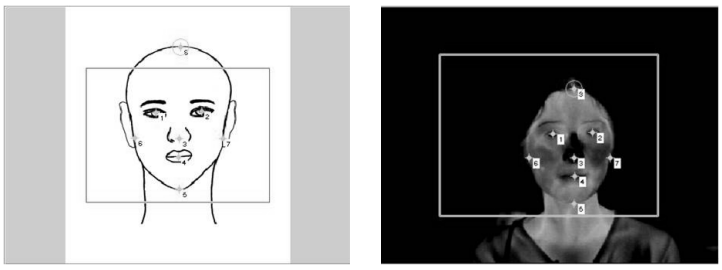
Table 3.1: Performance comparison between the NGC method and the PC method for Case A and Case B based on the under-detection error, e_u, and over-detection error, e_o obtained based on 7 images for each subjects. The best results for each case are shown in bold.

Name	Method	Under detection (Case A)			Under detection (Case B)			Over detection (Case A)			Over detection (Case B)		
		Min	Max	Std	Min	Max	Std	Min	Max	Std	Min	Max	Std
S1	NGC	0.7488	0.9028	0.0500	0.5743	0.7437	0.0590	**0.3849**	**0.5936**	**0.0620**	**0.2497**	**0.4195**	**0.0580**
	PC	0.8325	0.9758	0.0480	0.6831	0.9126	0.0820	0.4890	0.7819	0.1050	0.3650	0.6801	0.1130
S2	NGC	0.8070	0.8464	0.0140	0.6376	0.9755	0.1170	0.4396	0.6357	0.0690	0.2650	0.5216	0.0780
	PC	0.8729	0.9442	0.0240	0.7524	0.8867	0.0460	0.6386	0.8532	0.0630	0.5345	0.7730	0.0710
S3	NGC	0.8148	0.8635	0.0160	0.6241	0.7337	0.0210	0.5183	0.5852	0.0250	0.3898	0.4656	0.0260
	PC	0.8410	0.9042	0.0270	0.7135	0.8183	0.0460	0.4856	0.7571	0.0950	0.3850	0.6610	0.0970
S4	NGC	0.7850	0.8155	0.0110	0.6028	0.6462	0.0170	0.4437	0.6253	0.0666	0.3255	0.4468	0.0480
	PC	0.8269	0.9553	0.0420	0.6740	0.9094	0.0760	0.6478	0.8593	0.0710	0.4798	0.7927	0.0990
S5	NGC	0.7377	0.9224	0.0600	0.5298	0.8598	0.1100	0.4789	0.8482	0.1190	0.3145	0.7877	0.1540
	PC	0.7757	0.9530	0.0670	0.6185	0.9025	0.1060	0.6130	0.9662	0.0960	0.4978	0.7746	0.1070
S6	NGC	0.7791	0.9472	0.3200	0.5858	0.8899	0.2900	0.4832	0.8875	0.2910	0.3102	0.8120	0.2880
	PC	0.8607	0.9602	0.0418	0.7408	0.9213	0.0760	0.7033	0.9225	0.0897	0.5699	0.8686	0.1250
S7	NGC	**0.7197**	**0.8713**	**0.0480**	**0.5043**	**0.7443**	**0.0740**	0.5009	0.7276	0.0800	0.3215	0.5979	0.0920
	PC	0.8640	0.9446	0.0300	0.7555	0.8886	0.0500	0.6484	0.8672	0.0700	0.5585	0.7778	0.0700
S8	NGC	0.7610	0.8486	0.0310	0.5594	0.7075	0.0530	0.3690	0.6362	0.0990	0.2211	0.5355	0.1060
	PC	0.8290	0.9623	0.0460	0.6780	0.9240	0.0850	0.6121	0.8780	0.0900	0.4729	0.8219	0.1220
S9	NGC	0.7708	0.8188	0.0178	0.5809	0.6480	0.0230	0.4672	0.6417	0.0670	0.2938	0.4881	0.0688
	PC	0.9093	0.9548	0.0180	0.8335	0.9368	0.0380	0.6591	0.8814	0.0800	0.5852	0.8382	0.0900
S10	NGC	0.7609	0.8935	0.0500	0.5710	0.7833	0.0850	0.4986	0.7488	0.1170	0.3272	0.6420	0.1250
	PC	0.9268	0.9601	0.1400	0.8595	0.9260	0.0260	0.7001	0.8613	0.0590	0.5801	0.7954	0.0750
S11	NGC	0.7574	0.9108	0.0540	0.5699	0.8254	0.0940	0.5463	0.8276	0.1070	0.3885	0.7405	0.1370
	PC	0.7759	0.9378	0.0720	0.6036	0.8716	0.1220	0.3770	0.7759	0.1560	0.2720	0.7046	0.1720

Table 3.2: Performance comparison between the NGC method and the PC method for Case A and Case B based on the under-detection error, e_u, and over-detection error, e_o obtained based on 77 images from 11 subjects.

Performance parameters	Average Range		Mean		Std.	
	NGC	PC	NGC	PC	NGC	PC
e_u (Case A)	0.76-0.87	0.84-0.95	0.81	0.89	0.0447	0.1140
e_u **(Case B)**	**0.57-0.77**	**0.71-0.89**	**0.61**	**0.79**	**0.1000**	**0.1612**
e_o (Case A)	0.46-0.70	0.59-0.85	0.63	0.76	0.1183	0.1265
e_o **(Case B)**	**0.32-0.57**	**0.48-0.77**	**0.43**	**0.72**	**0.1265**	**0.1581**

out. For this comparison purpose, a ground truth of the scaling parameter needed for the sketch to be aligned to the thermograms are obtained from a semi-automated feature based registration approach. This semi-automated method performed using some of the MATLAB built-in functions which involves human intervention in the selection of the control points among features such as the centers of each eyes, the tips of nose, the center of lips etc. as points of correspondences to register between the two images as shown in Figure 3.26. In this approach, once the control points have been selected and obtained, they are then used to infer a spatial affine transformation between the sketch and the thermogram based on non-reflective similarity that includes rotation, scaling and translation. In this type of transformation, shapes and angles are preserved while parallel lines remain parallel and straight lines remain straight. As this approach involves human intervention in the selection of the points of correspondences between the two images, the transformation parameters (i.e., scaling factor, rotation angle, translation) obtained using this semi-automated method to register between the sketch and the thermograms are considered as the ground truth. Once the ground truth for scaling factor used to register between the face sketch and its reference thermogram is obtained, it is used for comparison with the scaling factor found by the NGC method. This process is performed for all the 77 thermograms and the results based on the average error between the scaling factors obtained for both the NGC and the PC methods are compared in Table 3.3.



(a) (b)

Figure 3.26: An example of the procedure of selecting points of correspondences for both the (a) face sketch (target image) and (b) a face thermogram (reference image)

Table 3.3: The average error between the scaling factor obtained by the semi-automated registration method and by the methods being compared; the NGC and the PC methods from 11 subjects (7 images for each subjects). The lowest and the highest average scale error for each method are shown in bold.

Image	Average Error for Scale	
	NGC	PC
S1	0.09	0.28
S2	0.03	0.20
S3	0.03	0.20
S4	0.09	0.30
S5	0.04	0.23
S6	**0.10**	**0.60**
S7	0.05	0.44
S8	0.03	0.28
S9	0.07	0.16
S10	**0.02**	0.26
S11	0.04	**0.03**

Table 3.3 shows the average error for each method in retrieving the actual scaling factor based on the ground truth obtained for each thermogram by the semi-automated registration approach. It can be observed that the NGC method achieved a scaling error of as small as ± 0.02 to as high as ± 0.10 while the PC method achieved a scaling error of as small as ± 0.03 to as high as ± 0.60. The average and standard deviation (std) of the errors calculated for all 11 subjects are ~ 0.06 and ~ 0.029 respectively for the NGC method while a higher value is obtained by the PC method; ~ 0.27 and ~ 0.148 respectively for the average and the std errors. Furthermore, the scaling factor that can be recovered by the PC method for the registration between the sketch and the face thermograms ranges from 1 to 1.4939 unlike the NGC method where a scaling factor of up to 1.7713 is achieved.

In the PC based registration method, most of the time, due to the inability of the method to recover the scale difference between the images to be registered accurately, the method suffers a poor retrieval of the displacement parameters for translational differences between the images to be registered. In terms of rotational angle, both the registration methods are able to retrieve a sufficient amount of angle to reduce the rotational difference between the images. Furthermore, the difference between the recovered angles by both the methods is small; from 0.13 to 10.87 in degrees. Since there is only little to none rotational difference present between most of our thermogram data and the face sketch, performance comparison based on the angle retrieved by the semi-automated approach is not carried out.

In another aspect, it should also be reported that the NGC method works best with thermograms

that has a good contrast between the face features and the skin area as well as between the face area and its adjacent area; especially the neck area; between the jawline, chin and the neck. A very low contrast between the jawline and the chin area, and the neck, that separates the face area from the neck, may affect the performance of the NGC method especially in recovering translational differences. This is usually the case when it involves thermograms with a shirt collar that is high in contrast and in position in the image, and very similar in shape as the jawline of the face sketch. Two examples of registration outcomes that suffered from inaccurate retrieval of the global transformation parameters needed especially for the shift or translation are shown in Figures 3.27 and 3.28. For these two cases, the NGC method fails to accurately correct for the translational differences in the final registration process, where it can be observed that the jawline of the face sketch is registered alongside the shirt collar. This problem may be solved by cropping the thermogram in order to have the collar area near the bottom periphery of the image prior to the registration process. However, to have a fully automated global registration method, this solution is not of interest. It is found that by replacing the final registration part of the NGC method where translational differences are solved based on the NGC formula (3.22) in the spatial Fourier domain with an iterative based normalized cross-correlation coefficient (NCC) technique performed in the spatial domain, the performance and robustness of the NGC method can be greatly improved. Further details on the improved hybrid NGC algorithm are described and presented in the next section.

On the other hand, the PC method is found to perform quite badly in recovering the scale factor as compared to the rotational angle and translational displacements in registering between the multimodal images (that are not from the same scene or subject) as shown in Figure 3.24. It also failed to solve for the 180° ambiguity in a number of occasions.

3.6 A Hybrid NGC

It is found that some misregistrations suffered from the NGC registration method are mostly caused by inaccurate translational differences being recovered by the NGC in the spatial Fourier domain usually in the cases where the jawline and the chin are not being represented in the edge map of a thermogram due to the very low contrast between this area and the adjacent neck area. Hence, performing the NGC with the NCC technique to recover translational differences in the spatial domain is investigated and found to be able to improve the registration results.

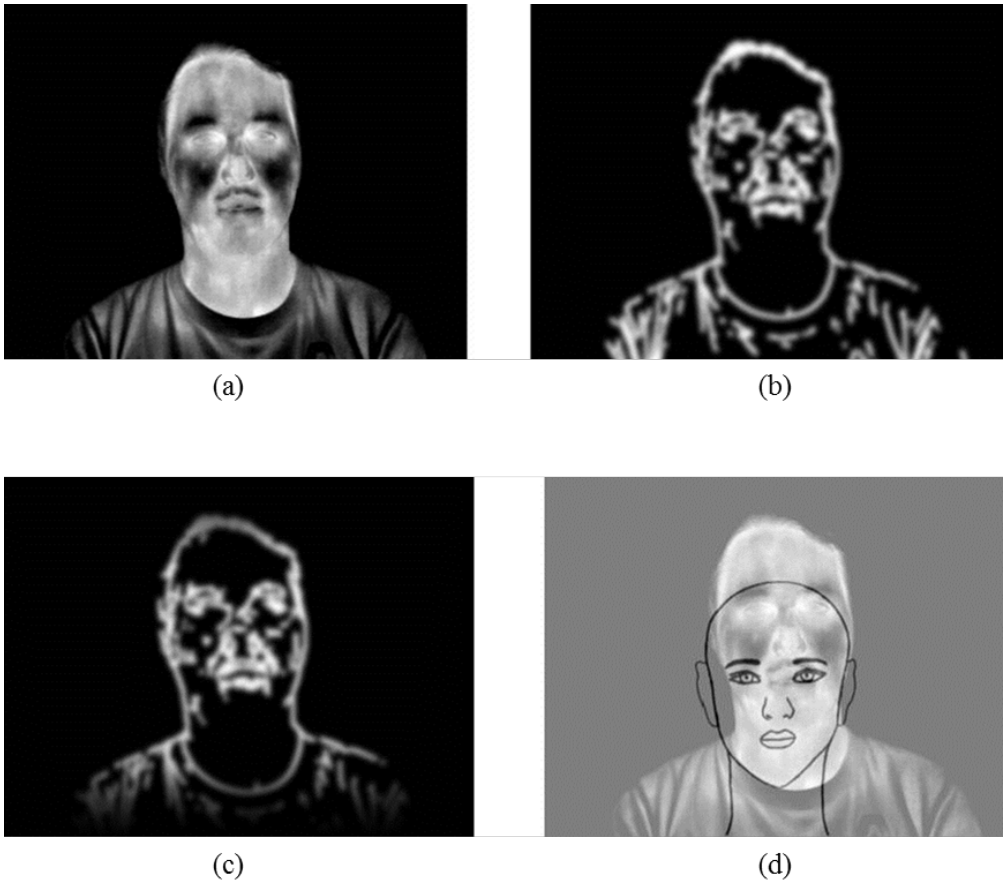


Figure 3.27: An example of a bad registration result; (a) the original thermogram (Subject S6), (b) its input gray edge map, (c) after windowing and (d) overlay result between the registered sketch and the thermogram.

For this purpose, a fast normalized cross-correlation (NCC) algorithm developed by Lewis [134] is employed using image gradients. In this algorithm, the NCC is defined as

$$\gamma(u,v) = \frac{\sum_{x,y}(f(x,y) - \bar{f}_{u,v})(t(x-u,y-v) - \bar{t})}{\sqrt{\sum_{x,y}(f(x,y) - \bar{f}_{u,v})^2 \sum_{x,y}(t(x-u,y-v) - \bar{t})^2}} \tag{3.30}$$

where $f(x,y)$ is the reference image and t is the target image, $\bar{f}_{u,v}$ denotes the mean value of $f(x,y)$ in the region under the t, while $\bar{t}$ denotes the mean value of the target image, t. The $\bar{f}_{u,v}$ is computed by

$$\bar{f}_{u,v} = \frac{1}{N_x N_y} \sum_{x=u}^{u+N_x-1} \sum_{y=v}^{v+N_y-1} f(x,y) \tag{3.31}$$

where N_x and N_y are the total number of pixels in the x-axis and the y-axis of a target image,

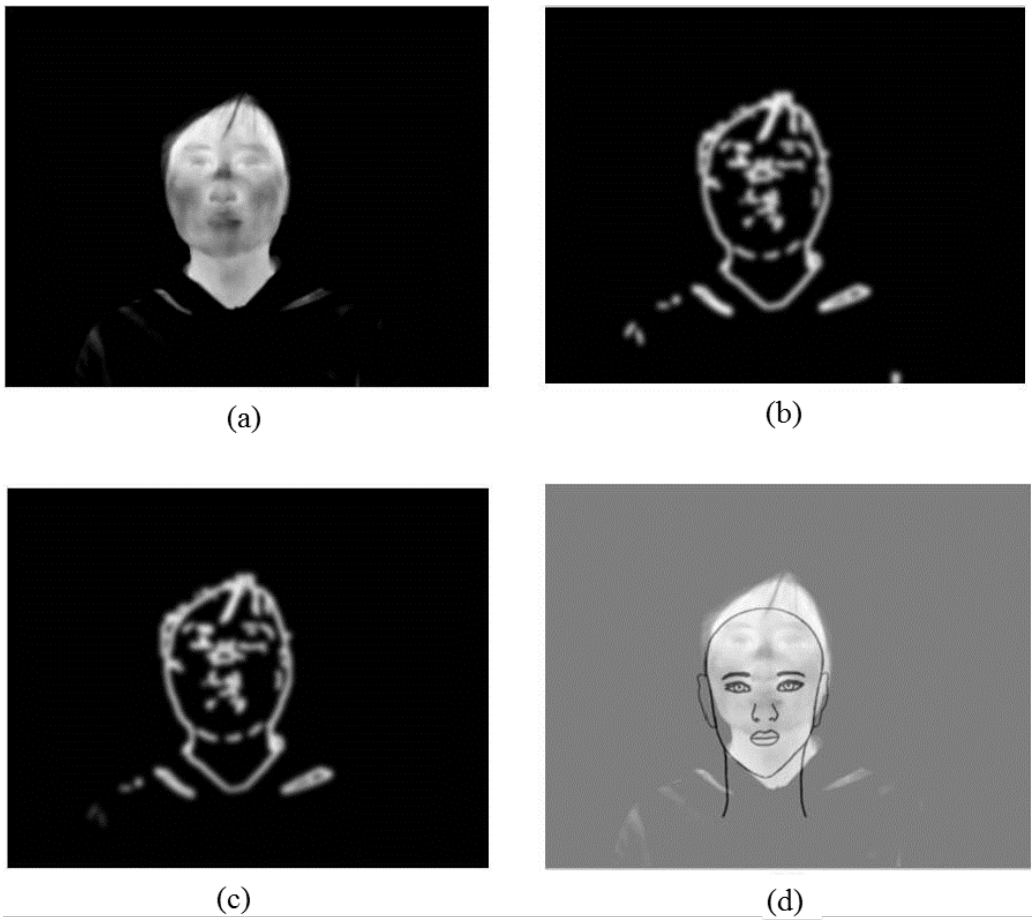


Figure 3.28: An example of a bad registration result; (a) the original thermogram (Subject S11), (b) its input gray level edge map, (c) after windowing and (d) overlay result between the registered sketch and the thermogram.

t, respectively. In this work, this method is employed in the spatial domain to give estimation of translational difference once the scale and/or angle differences from the target image is removed by the NGC method explained earlier. Hence, this new approach that combines the NGC method performed in the Fourier domain for the retrieval of scaling factor and/or rotational angle with the NCC algorithm performed in the spatial domain for the retrieval of translational difference, known as the hybrid NGC is proposed.

Magnitude of the gradients (as shown in eq. 3.4) of both the reference and the rescaled and/or rotated target image are used instead of their complex representation as edge magnitude gives pixel locations strong edge responses and suppress the contribution of areas of constant intensity level which do not provide any reference points for motion estimation [231]. Replacing both the images with their gradient magnitudes, eq. 3.30 takes the form

$$NCC(u,v) = \gamma(u,v) = \frac{\sum_{x,y}(g_1(x,y) - \bar{g_1}_{u,v})(g_2(x-u,y-v) - \bar{g_2})}{\sqrt{\sum_{x,y}(g_1(x,y) - \bar{g_1}_{u,v})^2 \sum_{x,y}(g_2(x-u,y-v) - \bar{g_2})^2}} \tag{3.32}$$

The translational differences (u, v) is found by taking the maximum value of $\gamma(u, v)$. The two functions in the denominator in eq. 3.30 are the variance of the zero mean image function and the shifted zero mean template function respectively. The normalization contributed to invariant of the metric to changes in brightness or contrast of the image, which are related to the mean value and the standard deviation. However, the calculation of the NCC is fairly expensive. Hence a number of researchers have developed fast algorithms in computing the NCC including Lewis [134]. Lewis proposed an efficient way to calculate the denominator of the NCC by the use of sum table scheme where the local sums are calculated by precomputing running sums. Using a fast algorithm such as designed by Lewis [134] for the NCC, makes the method becomes more attractive to be used for image matching, feature detection and opens up other new applications [134].

Figure 3.29 shows improvements in the registrations for the two different subjects where the NGC method has failed in recovering for the correct translations. For the first subject as shown at the top row, the hybrid NGC is able to reduce the under-detection eror, e_u, and over-detection error, e_o**,** obtained by the NGC method by 9.2% and 73.7% respectively. For the second subject as shown at the bottom row, the errors are reduced to 7.3% and 77.4% for both the e_u and e_o respectively. The hybrid NGC algorithm for scaling, rotation and translation is given as summarized in Algorithm 3.3.

3.7 Discussion and Conclusions

Overall, based on the first quantitative analysis conducted using the under-detection and over-detection errors, it is shown that the NGC method outperforms the PC method by lower range of values achieved for both the error measures using both case A and case B. This demonstrates that by using the gradients of the gray edge maps, the performance of the PC based image registration method can be improved. This is due to the property of the gradients that consists of pixels that strongly correlates with the amount of information that each pixel in both images carries. However, it is found that windowing is still needed in the registration based on the NGC method to remove or suppress the edge pixels near the border at the bottom part of the images

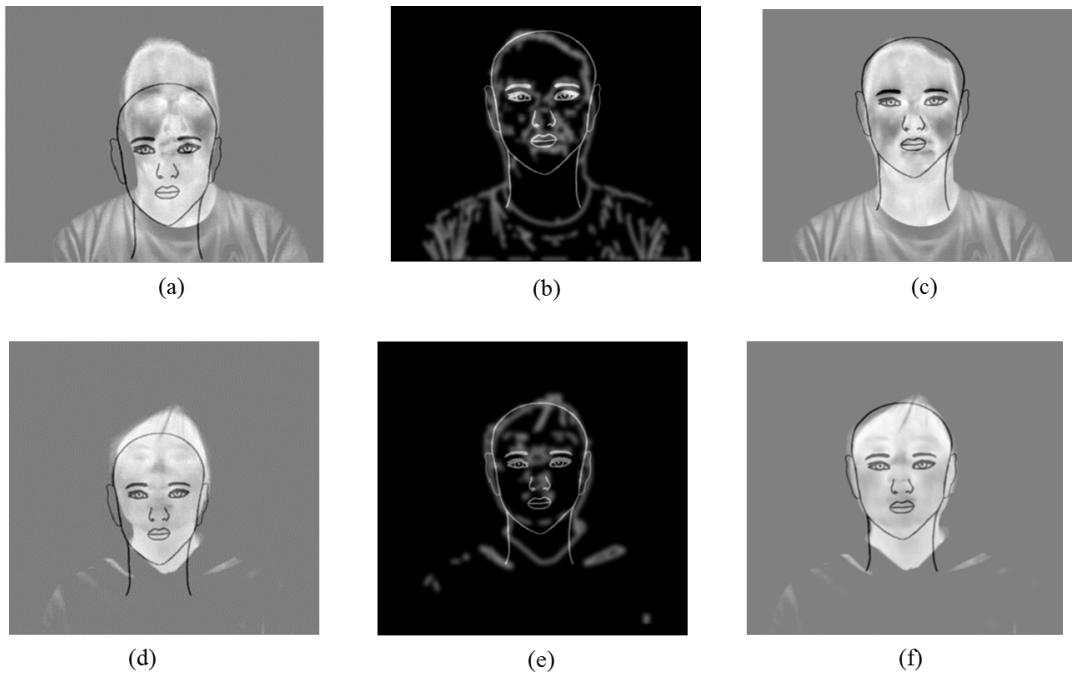


Figure 3.29: Improved registration results obtained by the NGC performed in the spatial domain for recovering the translational difference based on the NCC algorithm. (a),(d) Initial registration results. After translation recovery performed in the spatial domain; improved registration results in (b),(e) edge maps and (c),(f) in intensity image.

especially for the reference image. The overall registration results for the NGC method are fairly good even though the average under-detection range for case A is found to be quite high; above 0.7. It is observed that a value of e_u of up to as high as 0.8 for the under-detection error still display an acceptable registration result while a value of above 0.9 indicates a poor registration result. On the other hand, for the over-detection measure, a value of below 0.4 shows fairly good registration results while a value of over 0.7 indicates poor registration results. Hence, the measure based on the value of e_0 is more reliable in demonstrating the performance of the NGC method. These outcomes may be caused by the fact that the target image (the sketch) and the reference image are not taken from the same image source or subject. Even though the features such as the face outline, the nose and the eyes between the face sketch and the thermograms are already in good registration, as the shape or line patterns of the features are not identical or exactly the same, this has considerably affected the accuracy of the computed error measures. Therefore, it is found that the error measures computed based on 8 neighbouring pixels or known as the case B display the performance of the registration method more agreeably than the values obtained in the case A as it took into consideration this issue by considering more neighbour pixels. This problem may be minimized by replacing the face sketch with an atlas image of a face generated using optical images of the same 11 subjects integrated by groupwise based

Algorithm 3.3 Hybrid based normalized gradient correlation (hybrid NGC) between multi-modal images.

1. Perform Sobel edge detection to the thermal image and take the negative of the sketch image in order to have the sketch lines in white pixels. Then, pre-process the negated sketch image and the edge map by dilation with a 3×3 square structuring element and smoothing by a Gaussian filter of size 11×11 and $\sigma = 2.33$.
2. Using the edge maps obtained in step 1, perform windowing using a Tukey window with a size that is the same as the image's size and with $r = 0.6$ or $r = 0.8$.
3. Compute the directional gradients of the images obtained in step 2 using the Sobel operator along the x-axis and y-axis and combine them by taking the magnitudes of the gradients for both images, $g_1$and g_2 respectively.
4. Zero-pad the smoothed $g_1$and g_2 to size $N \times N$, where $N = 2^n$ and n is the smallest integer such that N is larger than the larger dimension of the image. Here, $N = 1024$ is used.
5. Compute their Cartesian FFTs, $G_1(u, v)$ and $G_2(u, v)$ and their magnitudes, $M_{G_1}(u, v)$ and $M_{G_2}(u, v)$.
6. Resample $M_{G_1}(u, v)$ and $M_{G_2}(u, v)$ to the log-polar domain using bilinear interpolation to obtain $M_{G_1}(\xi, \theta)$ and $M_{G_2}(\xi, \theta)$.
7. Compute the directional gradients of the Fourier magnitudes in log-polar coordinates ($M_{G_1}(\xi, \theta)$ and $M_{G_2}(\xi, \theta)$) using the Sobel operator along the x-axis and y-axis and combine them in a complex representation for both images denote by G_{M_i}.
8. Compute the FFTs for the G_{M_i} without zero-padding.
9. Compute its inverse cross power spectrum and estimate the rotation angle and scaling factor, θ and s respectively, based on the location of the maximum peak (d, θ_0) as described in eq.3.18 .
10. Undo the scaling and the rotational differences from the target image using the estimated scaling factor and rotational angle by bilinear interpolation. Resolve the 180° ambiguity associated with the rotational angle.
11. Solve for the translation by using the NCC formula in the spatial domain based on the magnitudes of gradients of both the transformed target image and the reference image.

registration as this atlas image may resemble a face feature that is much similar to the face feature of subjects involved in the study than the face sketch. Furthermore, by performing the NGC in the so-called hybrid approach, it is shown that the registration errors are reduced up to 9.2% for under-detection and as high as 77.4% for over-detection based on two subjects where the NGC has failed to recover for the correct translations.

However, as the NGC method is a global affine transformation based registration approach, there are still some limitations in achieving an accurate registration between the face sketch and a thermogram that can be observed. Since the target and the reference images involved in this work are not of the same nature (i.e., between an artificially created data (face sketch) and a real data (face thermogram)), the registration between these images can be quite challenging. Thus, a need for the registration between these type of images to be approached not only by global or rigid transformation based method alone but also by a local or non-rigid transformation based method is found inevitable. In the next two chapters, the non-rigid registration approach for further registration between two images that are already globally in registration is presented and

discussed.

Chapter 4

A Stochastic based Non-Rigid Affine Registration (NRAR) Method

This chapter describes a parametric based non-rigid affine registration (NRAR) algorithm using a stochastic approach to reduce small local displacements that are still present between globally registered images to further improve the alignment between them. Like the rigid registration method, a non-rigid registration method can be applied for registration between images taken with different imaging modalities (i.e., multimodal registration), or from different viewpoints or at intervals of time [72, 96, 119, 200, 201, 202, 214, 217]. However this method is preferable to the rigid one for registration between images of different subjects especially those of soft-tissues (i.e., human body) due to the presence of local displacements between these types of images [34, 79, 115, 119, 126, 143, 202, 242]. Nevertheless, since applying local and varying deformations in aligning two images can be a slow process, there is still a need to reduce the large geometrical differences between the images beforehand. Hence, in this work, prior to the NRAR method, a global registration method based on the NGC global registration method as presented in Chapter 3 is employed to reduce large displacements between two images.

In this chapter, a brief introduction to non-rigid registration methods is given in Section 4.1. A section after that explains and discusses the methodology of the proposed NRAR method that includes affine transformation, Delaunay based image interpolation, dissimilar criterion based on similarity measures and selection of its parameters. This is followed by Section 4.3 where the performance analysis of the method is presented based on four types of artificially created image

pairs, each pair with a unique registration problem between them. Then, some results using real data for potential detection and monitoring of morphoea are also discussed. Finally in Section 4.4, some discussions and conclusions from this chapter are given.

4.1 Introduction

Global affine transformation models are not able to entirely recover the displacements or alignment differences between different shapes and contours in particular, especially small and varying differences between two images of different subjects (e.g. between face thermogram and a face sketch as presented in Chapter 3) and acquired by different imaging modalities (e.g. between thermogram and visual image, between PET scan and MRI) [9, 93, 113, 133, 200, 204]. A non-rigid registration method is thus very essential in applying small deformations to a globally registered image in order to increase the alignment/registration accuracy between the globally registered image and its reference image. Unlike a global/rigid registration method, a non-rigid registration method performs deformations that vary across an image and is able to map straight lines to curve [96]. This method is very favoured in medical applications especially in registration of anatomies that are considered as soft-tissues as this method is able to deform them based on the nature of soft-tissues [34, 119, 143]. As a result, this enables localized image differences to be distinguished and analyzed. Furthermore, comparison and cross-examination of medical knowledge between different anatomies can also be carried out for either medical treatment or surgery [9, 34, 59, 119].

A non-rigid registration is also known as a local registration as it performs registration based on local deformations as opposed to a global or rigid registration which involves registration on an entire image. Local deformations of pixels can be performed via image features that can be derived from image characteristics such as anatomical structures (i.e., curves, contour, landmarks, edge, point of correspondences, surfaces and so on) that utilize geometrical information, or via intensity values where only pixel intensity values are considered in order to find the transformation of interest, or via both geometrical information and intensity value (also known as a hybrid approach in order to get the best of both) in order to align between two images especially of different subjects and imaging modalities[115, 153, 242]. As explained previously, in a local registration, the deformations performed vary across pixels in an image. It is usually performed onto a globally registered image as large pixel displacements in this image in regards

to its reference image have been reduced to a considerable amount. This will enable small local displacements that may still present between the globally registered image with its reference image to be further reduced to improve the alignment between them. In non-rigid registration methods that also include a global registration method such as the free-form deformation (FFD) based registration method [202], the process of global registration is very crucial in developing a fully automated local registration as it could solve the problem in initial positioning of the images to be matched locally/non-rigidly as the deformation process is always done iteratively.

In general, a local registration process involves a minimum of two images; a reference image or source image, A, and a target image or moving image, B. The best transformation of a point at B that associates to its corresponding point in A is the one that optimizes a dissimilar criterion/similarity measure, S, between the transformed target image, $B^{'}$, and the reference image A. In literature, local registration methods vary in terms of the deformation models (e.g. physical based model and function representations), similarity/dissimilarity criterion (i.e., based on sum of absolute differences (SAD), correlation coefficient (CC), mutual information (MI) and others), interpolation approaches, and optimizing techniques applied [72, 79, 93, 96, 113, 181, 217, 253].

4.1.1 Deformation Models

A deformation model or transformation model is usually used to relate the target image space to the reference image space. The mostly used transformation models for global registration are the ones that includes linear transformations such as rotation, scaling, translation, and other affine transforms. On the other hand, non-linear transformation models which are also known as deformation models allow non-rigid or local deformations of a target image to match its reference image [72, 96, 143, 253]. This type of deformation model can be categorized into physical-based model (e.g. elastic, fluid flow) and functions representations. A physical-based deformation model imitates various physical processes such as the notions of stress and strain of an object/a body/fluid where a body's internal force is subject to an external force that can cause it to deform [96]. In applying this physical model in image registration, the forces are derived by a similarity measure or a similarity/dissimilarity criterion (a set of similarity measures). In Bejo et al. [213, 214] and Kovalev et al. [126], an elastic registration that comprises of four mathematical models has been developed. Each mathematical model operates differently in

terms of the elasticity model imposed to the object such as shrinkage operator, growth operator, translation operator and parabolic flow front operator. A dissimilar criterion that comprises correlation coefficient or mutual information, a geometric term that defines amount of distortion desired as well as a term that defines the maximum overlap desired is expressed and used as the driving force in the elastic registration method [126, 213, 214].

In a local mapping function, an image can also be treated as a composition of patches or sub-images and the function parameters depend on the location of their support in the image. This approach also belongs to the interpolating method group as it leads to the tessellation of the image, usually a triangulation. In this approach, the parameters of the mapping function for each patch are defined separately. In Karamitrou et al. [113], affine transformation is employed locally by a windowing approach. This means that each image patch is transformed differently by an affine transformation model in order to achieve a non-rigid transformation which is found to be a very simple approach but yet serve the purpose of a deformable transformation model.

However, elasticity based image registration can only cater for small deformation. In order to increase the ability to cater for large deformation, a deformation model based on viscous fluid flow can be employed especially for intersubject registration [96, 143, 217]. Physically, fluid is very flexible as it can be deformed easily and largely in so many ways. However, it can be too flexible resulting in misregistration the higher the flexibility is; e.g. anatomically incorrect alignment of different but closely aligned structures. To overcome this limitation, some constraints in its mapping are needed. This method also suffers from blurring during the registration process. On the other hand, a more controlled non-rigid deformations can be achieved by finite element (functions based) models such as a free-form deformation model based on thin-plate splines (TPS), B-Splines or radial basis functions [202, 200, 253]. A free-form deformation model is based on a regular grid of control points that are distributed across the image at an arbitrary mesh resolution. This is to achieve smoothness, flexibility in controlling deformation precision and efficiency [96, 202, 217]. Even though the TPS and the B-splines based free-form registration methods achieve good results, their computation complexities are high and thus can be time consuming especially if the number of control points is high but can be utilized not only for 2D image registration but also for 3D image registration [202]. Reviews and more details on these methods can be found in [72, 96, 253].

Since simple computation to cater for small deformations in improving our NGC based global registration result is needed and of interest, the approach based on elastic registration devel-

oped by Bejo [213, 214], Kovalev et al. [126] and Karamitrou et al. [113] are followed in the determination of non-rigid transformation model developed in our work.

4.1.2 Registration Metrics

Registration metric is defined by the value returned that indicates how well two or more images are aligned. It can be classified into a feature based registration metric or an intensity based registration metric. For a feature-based registration metric, the similarity measure defined is used to evaluate the quality of the transformation based on the distance between corresponding pairs of features/landmarks extracted from the images to be registered that can be anatomical features or fiducial markers (i.e., invasive method as it can be rigidly attached to bone [54]). For intensity-based registration metric, the quantitative measure of the image alignment achieved can be further categorized into monomodal (intermodality) registration, and multimodal (intramodality) registration. For registration between the same image modality (monomodal), the intensity characteristics are very similar thus quantitative value between them can be computed based on the pixel/voxel intensities generally known as similarity/dissimilarity/proximity measure or distance measure (briefly discussed in Section 4.1.2.1); e.g., sum of absolute differences (SAD), sum of squared difference (SSD), correlation coefficient (CC) and others [79, 143, 216]. However, for registration between images of different modalities (multimodal), the intensity characteristics between these images are different thus quantitative measures based on information theory are alternatively used (briefly discussed in Section 4.1.2.2); e.g., mutual information (MI) and normalized mutual information (NMI) [79, 113, 126, 214]. In this work, a registration metric that includes a dissimilarity measure suitable for monomodal registration is used since the reference and the target images are already brought into the same image representation (smooth gray edge map) as explained in the previous chapter. Further discussions on the registration metric used for the NRAR method can be found in Section 4.2.2.

In the next two sections, more details on the intensity and the information based similarity measures are given.

4.1.2.1 Similarity Measure Using Raw Image Intensities

The SSD is the optimal choice of similarity measure for images that differ only by additive Gaussian noise [79, 93]. It is also frequently used to assess the degree of similarity between two images [165]. It is a very simple similarity measure between two images as defined by

$$SSD = \frac{1}{N} \sum_{x,y \in T} (I_1(x,y) - I_2(x,y))^2 \tag{4.1}$$

where T is the overlap domain of the images and N is the number of pixels in T. SSD is reported to be sensitive to a small number of voxels that have very large differences in intensity between the images. The effect of these voxels with large differences can be reduced by using the sum of absolute difference (SAD) instead [79]. This is why in some cases, the SAD is sometimes used instead of SSD as given by

$$SAD = \frac{1}{N} \sum_{x,y \in T} \|I_1(x,y) - I_2(x,y)\| \tag{4.2}$$

On the other hand, the correlation coefficient (CC) assumes that corresponding intensities in the images have a linear relationship. It is the most commonly used similarity measure in aligning two images in a fast and simple way [121, 145]. It is also called normalized cross correlation but often referred to as correlation coefficient as defined as follows:

$$CC = \frac{1}{\sigma_1 \sigma_2} \frac{1}{n} \sum_{x,y \in T} (I_1(x,y) - \bar{I_1}) \cdot (I_2(x,y) - \bar{I_2}) \tag{4.3}$$

$$= \frac{\sum_{(x,y \in T)} (I_1(x,y) - \bar{I_1}) \cdot (I_2(x,y) - \bar{I_2})}{\sqrt{\sum_{(x,y \in T)} (I_1(x,y) - \bar{I_1})^2} \cdot \sqrt{\sum_{(x,y \in T)} (I_2(x,y) - \bar{I_2})^2}} \tag{4.4}$$

where $\bar{I_1}$ and $\bar{I_2}$ are the mean intensity values of the images $I_1$and I_2, respectively while the denominator is the product of the standard deviations of the two images, both computed over the overlapping part. The CC is one of the best similarity measures for the case of monomodality image registration [121].

4.1.2.2 Information based Similarity Measure

The information based quantitative measures are very suitable for multimodality image registration as intensities are not involved directly in the computation as they use the intensity range instead (probabilities, entropy etc.) [181, 200, 201]. This type of measure is known as the information based similarity measure as it is computed based on the statistical dependence between the intensities of two images. The mutual information, MI, is one of the information based simi-

larity measures that is widely used in multimodal registrations which is proposed independently by Collignon et al. and the MIT group [79]. It is defined by the image entropies. Entropy of a difference image of a pair of images that match each other is zero as the difference image should contain no information [79]. The joint entropy between two images is thus used to measure the amount of combined information between two images as follows:

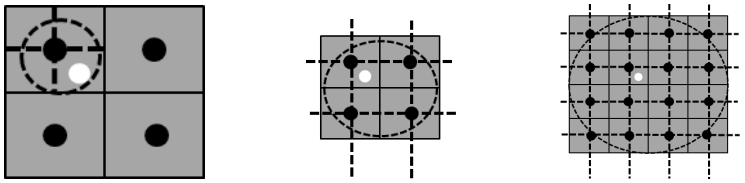
$$H(I_1, I_2) = \sum_a \sum_b p_{I_1 I_2}(a, b) \cdot \log p_{I_1 I_2}(a, b) \tag{4.5}$$

where $p(a, b)$ is the joint intensity probability, also known as the probability distribution function (PDF). It represents a 2D joint histogram. Each values in the joint probability, $p(a, b)$, shows the occurrence of the intensity a in the first image and intensity b in the second image at the same respected positions. If two images are totally misregistered, the joint entropy will be the sum of entropies of the individual images. For two similar images, the joint entropy between these images is equivalent to the individual entropies of the images (i.e., marginal entropies), $H(I_1, I_2) = H(I_1) = H(I_2)$. The resulting joint histogram or PDF is peak when two images are well aligned as their corresponding areas overlap [79]. This resulted in high mutual information between the images. The mutual information between two images, $MI(I_1,I_2)$, is defined by the individual entropies and their joint entropy as follows [79, 93].

$$MI(I_1,I_2) = H(I_1) + H(I_2) - H(I_1, I_2) = \sum_a \sum_b p_{I_1 I_2}(a, b) \cdot \log \frac{p_{I_1 I_2}(a, b)}{p_{I_1}(a) p_{I_2}(b)} \tag{4.6}$$

The MI not only considers the amount of information in the combined image, but also in the information contributed to the overlapping region by each image. In maximizing the MI, the joint entropy is minimized and the marginal entropies are maximized. Drawback with the MI is it does not take into account any spatial information such as pixel location. However, in recent years, the MI is improved by incorporating intensity and one to three spatial parameters [133]. Another way in improving the robustness to the overlapping region is by normalizing the mutual information with respect to the joint entropy [79]. The normalized mutual information, $NMI(I_1, I_2)$, is given by [79, 93]

$$NMI(I_1,I_2) = \frac{H(I_1) + H(I_2)}{H(I_1, I_2)} = \frac{MI(I_1, I_2)}{H(I_1, I_2)} + 1 \tag{4.7}$$



(a) (b) (c)

Figure 4.1: Neighbour based interpolation methods; (a) nearest neighbour interpolation, (b) bilinear neighbour interpolation and (c) bicubic neighbour interpolation. In these illustrations, black circles represent original pixel positions while white circles represent moved pixels at new non-integer locations.

4.1.3 Resampling and Transformation

The intensity values at pixel positions that are vacated after a neighbourhood of pixels are moved to a new location can be computed based on image interpolation. Image interpolation performs computation of new pixel values based on the intensities of neighbouring pixels specified. In this work, an interpolation method which is very suitable and well known for scattered and irregularly spaced data known as the natural neighbour interpolation method [132, 155, 212] is employed. This section explains the natural neighbor interpolation method used after some brief overview are given on the commonly used neighbour based image interpolation methods such as the nearest, bilinear and bicubic interpolation methods.

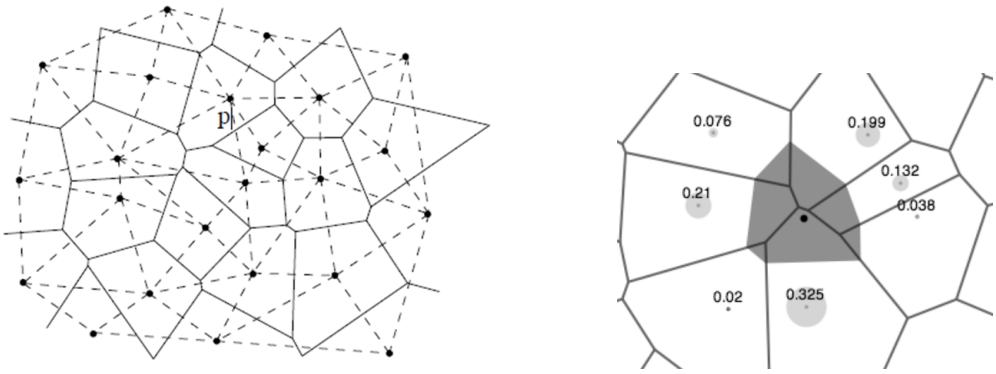
4.1.3.1 Neigbour Interpolation Methods

The most simple and the least expensive interpolation method for 2D images is the nearest neighbour interpolation method. It computes the intensity value from the closest pixel to the transformed/moved position as illustrated in Figure 4.1(a). This enables the intensities of the image to be preserved. Hence, the histogram of the image before and after the interpolation is very similar. For example, in scaling an image to twice its original size in the x and y directions, the new output pixels created between the original pixels will have brightness equal to those of their adjacent neighbors [75]. The nearest interpolation process does not blur image but it could produce aliasing effects such as pixelated effect or jagged/step-like effect due to repetition of some pixel values [72]. These effects are also known as artifacts. This method can also result in distortion of straight edges in images of high resolution and loss of apparent resolution [71]. Satisfactory result may be achieved using this interpolation method if small scale resizing and small geometry changes are involved or when an image contains low number of intensities.

In bilinear interpolation method, the linear interpolation along two orthogonal axes is combined to compute the destination pixel. In other way, bilinear interpolation takes a weighted average of the brightness of the four pixels surrounding the pixel location of interest [75]. Although smoother results are produced if compared to the nearest neighbour method, the results for sharp transitions are not ideal. The lost of brightness values in the interpolated pixels is as a result of value averaging based on four pixel values. Figure 4.1(b) shows the concept of the bilinear interpolation based on the four nearest neighbour pixels (black dots) to the moved pixel (white dot).

In order to have a smoother and sharper interpolated image, the number of input pixels in the calculation of the output pixel value can be increased to sixteen pixels that are adjacent to each other by two pixels in each direction within a neighbourhood [136]. This interpolation method is known as the bicubic convolution method as it uses two cubic interpolation polynomials, one for each plane direction. Not only the interpolated image obtained is sharper than that obtained by the bilinear method, the disjointed appearance observed in the results of the nearest neighbour method can also be eliminated. The bicubic interpolation computes each designated pixel (in white) by interpolation from the nearest sixteen mapped source pixels (black dots) as illustrated in Figure 4.1(c) and thus produces the best result in comparison to the other two neighbour interpolation methods. A good balance between accuracy in preservation of the details and smoothness for resized and rotated images is yielded by this method [233]. This bicubic interpolation is mostly employed for large sampling or when large geometric change of an image is involved. However, contrary to the nearest and bilinear interpolation methods, the bicubic interpolation method requires more computation time and causes more data to be altered [26].

On the other hand, the natural neighbour interpolation method developed by Robin Sibson [132, 212] is closely related to the concepts of the Voronoi diagram and the Delaunay triangulation [45, 132] which are explained further in the next section. This interpolation method is found very suitable for interpolation of scattered and irregularly spaced data. Like the other neighbour based image interpolation methods explained earlier, this method is also a weighted average intensity method but the difference is in the use of the Delaunay triangulation for the input points (scattered data) in finding the interpolated points. Figure 4.2(a) illustrates a point p in a Voronoi cell that has seven natural neighbours. If a point x is inserted into a Voronoi cell, the cell will modify itself by including some volume from the Voronoi cells of its considered natural neighbours (Figure 4.2(b)) [132]. The value for the interpolation point x, is estimated using weighted values of the closest surrounding points in the triangulation. As shown in Figure 4.2(a),



(a) (b)

Figure 4.2: Natural neighbour interpolation. (a) Voronoi diagram and Delaunay triangulation (dashed lines) in 2D (Reproduced from [132]. (b) The colored circles which represent the interpolating weights, w_i , are generated using the ratio of the shaded area to that of the cell area of the surrounding points. The shaded area is due to the insertion of the point to be interpolated into the Voronoi tessellation. (Reproduced/Excerpted from [156])

the natural neighbours are the ones the interpolation point would connect to if inserted into the triangulation. This method which is considered as a triangulation-based method that has an area-of-influence weighting associated with each sample point, is an improvement over linear interpolation method and works well with larger datasets that have uneven sampling [132, 212]. Hence, it has advantages over simpler methods of interpolation, i.e., nearest neighbour, by providing a smoother approximation to the underlying true function [132, 212]. In general, the natural neighbour interpolation finds the unknown intensity from the intensities of the neighbouring pixels as given by

$$G(x,y) = \sum_{i=1}^{n} w_i f(x_i, y_i) \tag{4.8}$$

where $G(x,y)$ is the estimate at (x,y), n is the number of natural neighbour pixels or the closest nodes that form a convex hull around the interpolated point (x,y), w_i are the weights and $f(x_i,y_i)$ are the known data at (x_i,y_i). In the natural interpolation, the weights w_i, are calculated by finding how much each of the surrounding areas is involved in the tessellation as depicted in Figure 4.2(b). The value of w_i for any given x will be in the range of $0-1$; 0 when a point p_i is not a natural neighbour of x, and 1 when p_i is exactly at the same location as x. Hence, the distance from x to p_i and the spatial distribution of the p_i around x both give influence to the natural neighbour coordinates [132].

4.1.3.2 Triangulation of a Scattered/Irregular Point Set

When a set of pixels are moved by a transformation, the new locations will not be at integer positions and the image can no longer be represented as a grid. The scattered and irregular set of points in the image consists of the moved pixels that carry with them their original intensity values and leaving behind their original integer positions vacant. In order to assign new intensity values to these vacant integer locations, image interpolation is therefore necessary. In this work, the scattered and irregular data is represented as a surface made up by triangular patches (Delaunay triangulation) [45]. The value at any point inside a triangle is fully defined by the values at the vertices of the triangle [44]. This is the Delaunay interpolation, because it allows you to find the value at integer positions and thus represent the image by a grid. In this section, the Delaunay triangulation is further described.

The Delaunay triangulation method which is named after Boris Delaunay [45] for his work in this topic is a coordinate based triangulation method commonly used for scattered and irregularly spaced data [113, 245, 251]. It can construct a scattered data into triangulation structure and new value for any point in the diagram will be computed based on the nearest triangular vertex that is surrounding the point [45, 44, 251]. The Delaunay triangulation of a set of points is a triangulation such that the unique circle circumscribed about each triangle contains no other points in the set as illustrated in Figure 4.3 [45, 132]. The convex hull of a set of points is the smallest convex set containing all points of the original set. The Delaunay triangulation will identify triangles composed of three pixels that encompass each of the original integer pixels. The Delaunay triangulation has two very important properties; the empty circle property and the largest minimum angle property [45, 132]. The empty circle property is such that the circumcircle of each triangle contains no other points in a set of points in Euclidean plane. The latter property means that the minimum angle in the triangle of Delaunay triangulation is the largest in the triangular network formed by a set of points. This makes the triangulation based on Delaunay triangulation the closest to the regularization network of triangulation. These properties also ensure even distribution between scattered data points is obtained in order to achieve an optimal triangulation i.e., the closest to equiangular or equilateral triangulation. This is very important in meeting both global and local optimization of triangulation.

The calculation of interpolated values based on the Delaunay triangulation can be done via neighbour interpolation method such as described in the previous section. In this work, the natural based interpolation method is applied in the plane equation that these three vertices (of

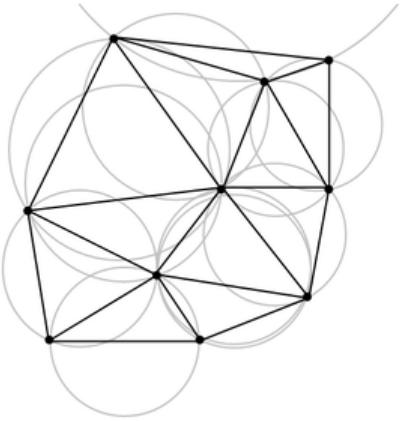


Figure 4.3: Empty Circle (Sphere) Property: No other vertex is contained within the circumcircle (circumsphere) of any triangle (tetrahedron) (Reproduced/Excerpted from [46])

a triangle) form yielding the corresponding new gray value. The process involved in the assigning of new values to the vacant pixel locations is described further in Section 4.2.3.

4.1.4 Stochastic Approach for Optimization

Sophisticated optimization algorithms are normally employed to search for the optimal maxima or minima respectively in a registration method that involves transformations with high degrees of freedom or complex similarity measures or both [119, 202]. A number of optimization algorithms such as Gauss–Newton numerical minimization algorithm, gradient descent optimization method, Levenberg–Marquardt optimization method etc. are commonly employed in image registrations and more details about these optimization methods can be found in most of the survey papers on image registration [96, 115, 143, 217]. In literature of image registration, optimization methods are commonly employed either for transformation parameters to be assigned or searched for [72, 96, 143, 217].

In the proposed NRAR method, the transformation parameters involved are assigned randomly from a specified range of values. The optimization algorithm used is of the type stochastic greedy [113]; for every possible local transformations/changes performed, the algorithm only accepts the changes that improve the solution hence the term 'greedy'. This also means that after every proposed change is performed, the measure of similarity between the images to be registered needs to be computed. In a stochastic greedy optimization approach, the transformation parameters are chosen at random to allow exploration of as much the solution space as possible. Using this approach, a similarity measure can be maximized or a dissimilarity measure can be minimized. The latter is chosen for the proposed NRAR algorithm where the dissimilarity between two im-

ages given a certain transformation is minimized i.e., if the dissimilarity measure between the images after possible changes are performed is found lower than the current dissimilarity measure, the changes performed are accepted and the value of the dissimilarity measure is updated, else the changes are rejected and a new search is repeated for the next transform window with a new set of affine transformation parameters that are randomly reassigned. Furthermore, as only small deformations are needed to improve on the registration accuracy between two globally registered images, it is preferable to have less computational complexity in the algorithm in terms of the type of optimization method used as can be offered by the stochastic greedy optimization method. Hence this method is chosen to optimize the proposed NRAR method.

4.2 Stochastic Non-rigid Affine Registration

4.2.1 The Methodology

This section explains the proposed stochastic based parametric non-rigid affine registration (NRAR) method as summarized in Figure 4.4. The objective of a non-rigid image registration is to correct for small local differences. As mentioned before, in this work, the NRAR method is developed to refine already registered images by the NGC method (Figures 4.5 and 4.6). In the NRAR registration process, a target image is deformed by applying to its randomly selected transform window, affine transformations with parameters chosen at random. If the deformation is accepted then the image for the next deformation is created from the previously created image. Hence, the current image is more similar to the reference image than the previous one. A decision on whether a deformation is accepted or not is based on the dissimilarity measure between the deformed target image and its reference image. In this work, a dissimilar criterion (DC) is employed as the dissimilarity measure and is presented in Section 4.2.2. Prior to the computation of DC, the gray values for vacant pixels in the transform window are computed based on the natural neighbour interpolation method by the Delaunay triangulation approach. If the DC of the imposed deformation improves, the transformed pixels are accepted. If it does not, the transformation made is rejected and the process starts again with randomly reassigned affine parameters and with a new transform window where the pixel next to the previous central pixel is selected as the new central pixel. The whole process stops when either one of the termination criteria used is met. This is explained further in Section 4.2.4. In this section, the details about the processes involved in the proposed NRAR method are elaborated further.

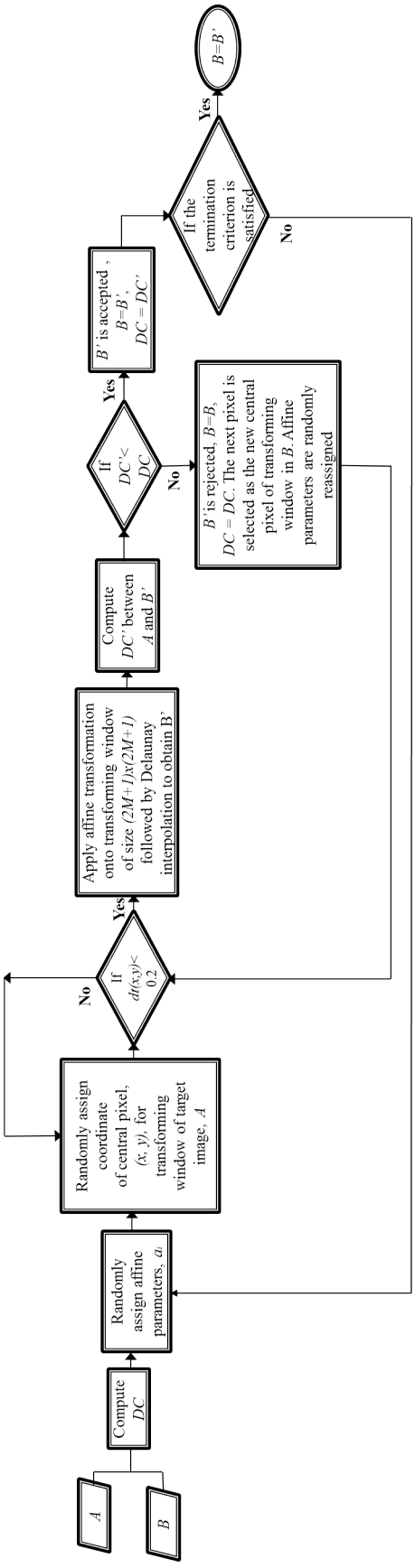


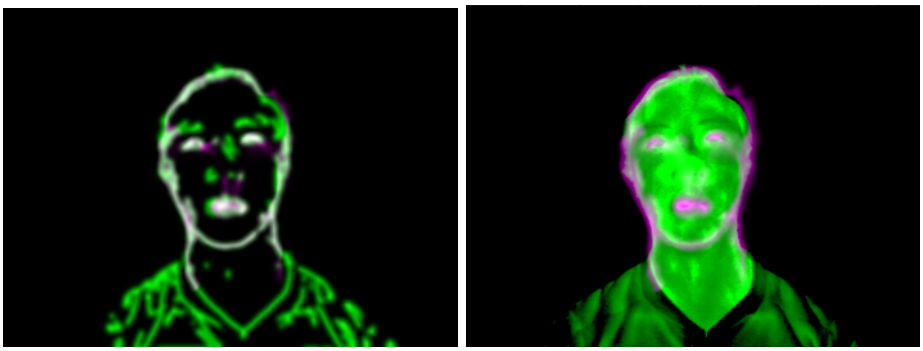
Figure 4.4: A flowchart of the NRAR method with input edge maps, A and B.

As explained in the previous chapter on the NGC global registration method, the reference and the target image used in this work have been brought to the same image formations by the Gaussian smoothing of gray edge maps to produce smoothed and more distributed gray edge maps. Thus, the amount of elements to be distorted in the target image is reduced to a considerable amount for a random stochastic method to handle and may also be more robust to intensity variations. Furthermore, the computational complexity can also be greatly reduced [59]. In the NRAR method, the stochastic approach is employed by (1) a random selection of affine parameters for small deformations to take place and by (2) a random assignment of coordinates of central pixel for the transform window at the start of the registration process and every time after a change is accepted. The affine parameters for scaling, rotation and translation are being selected randomly from a small range of values to ensure only small distortions are applied. Along with the affine parameters, the central pixel of the transform window to be processed in each iterations is also randomly selected at the beginning of the process and each time after a transformation is accepted. However, if a transformation is rejected, a random selection is only performed to generate the affine parameters for new transformation of a new neighborhood of pixels (new transform window) with its central pixel is the pixel next to the previous central pixel. This whole process is repeated until a termination criterion is satisfied (explained in Section 4.2.4).



(a) (b) (c)

Figure 4.5: Overlays between registered face thermogram (reference image) and the face sketch (target image) using only the NGC method shown (a) in gray edge maps and (b) in intensity image; (c) in intensity image with the Blaschko's lines.



(a) (b)

Figure 4.6: Overlays between a registered target image and its reference image after the proposed NRAR method is performed; (a) in gray edge maps and (b) in intensity images.

The size of the transform window used in this work is given by $(2M+1)\times(2M+1)$ with M that can be selected based on the largest displacement present between the images to be registered. In this work, as large displacements should be reduced by the NGC global registration method, $M = 7$ is selected as the most suitable default value as this value is not too small nor too large. Hence window size of 15×15 becomes the default size of the transform window used in the NRAR method. Furthermore, if the size of M is bigger than 7 it will cost unnecessary computation time and can result in blurring of the registered image. On the other hand, $M < 7$ may result in under-registration as deformations that can be performed may not be sufficient in reducing the displacements between the two images.

As mentioned earlier, the local registration between two intensity images (a target image and a reference image) in this work is performed based on their edge maps. As the edge maps of the target image and its reference image have already been brought to registration by the NGC based global/rigid registration method (discussed in the previous chapter) by correcting for large scaling, translation and/or rotation, now only small local displacements mainly on edge pixels need to be corrected to improve the alignment between the globally registered images. This is also to ensure that the information underlying the non-edge pixels (surface area) are minimally affected. This is achieved by applying a locally affine transformation; if (x, y) are the coordinates of a pixel, the pixel is moved to a new location $(x^{'}, y^{'})$ by

$$\begin{pmatrix} x^{'} \\ y^{'} \end{pmatrix} = \begin{bmatrix} a_{11} & a_{12} \\ a_{21} & a_{22} \end{bmatrix} \begin{pmatrix} x \\ y \end{pmatrix} + \begin{bmatrix} t_x \\ t_y \end{bmatrix} \tag{4.9}$$

However, we want to have different deformations in different locations in the image, i.e., the

transformation affine parameters $a_{11}, a_{12}, a_{21}, a_{22}, t_x$ and t_y will be different in different parts of the image. The range of the transformation parameters used is set to $[-0.1, 0.1]$ for a and $[-0.8, 0.8]$ for t respectively to ensure only small deformations are achieved during a transformation. Note that the range of t is bigger than the range of a as it is observed experimentally that most of the local registration differences that will be removed are caused by motion. This can be explained by the decrease of time the algorithm takes to converge to an optimal solution by increasing the value of t found experimentally. This varying local deformations produce gaps between the different parts of the image that transforms differently. In order to reduce the gaps between different parts of the image that transforms differently to ensure smoothness of the deformations, the above eq. 4.9 (a global affine) needs to be modified to include a smoothing operator, e^{-sd}, as given by [113, 126, 213]

$$\begin{aligned} x^{'} &= e^{-sd}\left(a_{11}x + a_{12}y + t_x\right) + x \\ y^{'} &= e^{-sd}\left(a_{21}x + a_{22}y + t_y\right) + y \end{aligned} \tag{4.10}$$

In eq. 4.10, a pixel (x, y) is moved to a new location $(x^{'}, y^{'})$, not far from the original one in an affine way, but the transformation dies away as d increases in the exponential. The parameter s controls how fast the transformation decays with d and is known as a springiness parameter that controls the severity of distortion subject to pixel location in the transform window. If a pixel is away from the central pixel, the amount of distortion is less than the amount of distortion if a pixel is near to the central pixel. For this purpose, s is denoted as $\frac{-\ln g}{M}$, where g is some positive constant in the range of $0 - 1$. This enables the pixels at the periphery of the window to be very minimally affected by the distortion as the exponential operator will be very small, $e^{-sd} \rightarrow 0$. To have this effect, we set g to be 0.1. This will result in a smooth transition of pixels in the transform window with the surrounding pixels. The value d denotes the Euclidean distance between the central pixel, (x_0, y_0), and any pixel (x, y) inside the transform window computed as follows.

$$d = \sqrt{(x - x_0)^2 + (y - y_0)^2} \tag{4.11}$$

Besides the application of the smoothing operator e^{-sd}, another criterion is included prior to the transformations. This criterion is based on the distance transform image/function, dt, of the target image. The value of dt is composed of distance values i.e., distance of every pixel from its nearest edge pixel; 0 for edge pixel, > 0 for non-edge pixel. In order to ensure that the deformations are performed mostly onto edge pixels based on its gray edge map, this criterion

based on dt (i.e., a constraint parameter) is used; if the central pixel of the transform window is an edge pixel or within a specified range, the transformations based on eq. 4.10 are applied to the transform window or else no transformations are to be carried out and a new central pixel is randomly reselected. In this work, a central pixel is considered as an edge pixel or within a specified range if the value of dt of the central pixel is between $0-2$. The value two is considered to be the most suitable cut-off value for pixels to be considered for the transformations based on experimental results obtained. This criteria is also included to not only ensure that the information underlying non-edge pixels are minimally affected during the process but also to reduce the unnecessary time taken for deforming non-edge pixels that would not improve the registration between the two edge maps. The dt is computed based on the geodesic time [103, 215]. The basic equations for geodesic time along a path in an image, I, is given by

$$\begin{aligned} dt_I &= \sum_{i=1}^{l} \frac{I(p_{i-1})+I(p_i)}{2} \\ &= \frac{I(p_0)}{2} + \frac{I(p_l)}{2} + \sum_{i=1}^{l-1} I(p_l) \end{aligned} \tag{4.12}$$

where l is the length of a path from an initial point p_0 to an end point p_l. The geodesic time function is computed using discrete and Euclidean metrics based on a priority queue algorithm to obtain a distance transformed image. An example of a distance transform image obtained by gray-weighted distance transform of grayscale image using edge pixels as seed pixels is shown in Figure 4.7. Using this distance measure as a parameter dt, it can be assured that edge pixels will have full transformation while the pixels away from the edge pixels will have minimum transformation. Figure 4.8 (a) illustrates the deformation field where the transformed pixels are represented by the deformed grids. These deformed grids are mainly among the edge pixels (or feature lines) as can also be observed in Figure 4.8(b) when the same deformations are applied to the face sketch with the Blaschko's lines. Figure 4.9 simplified the processes involved before a deformation takes place in the NRAR algorithm as described previously.

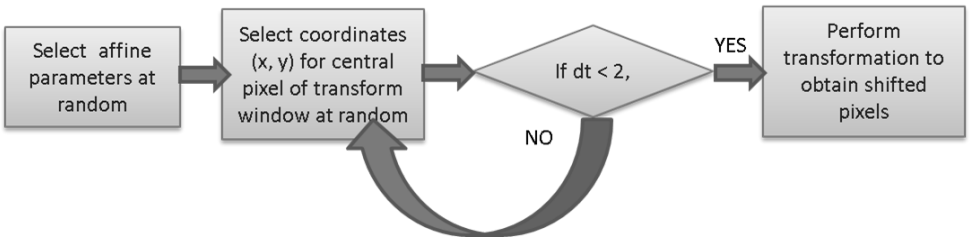
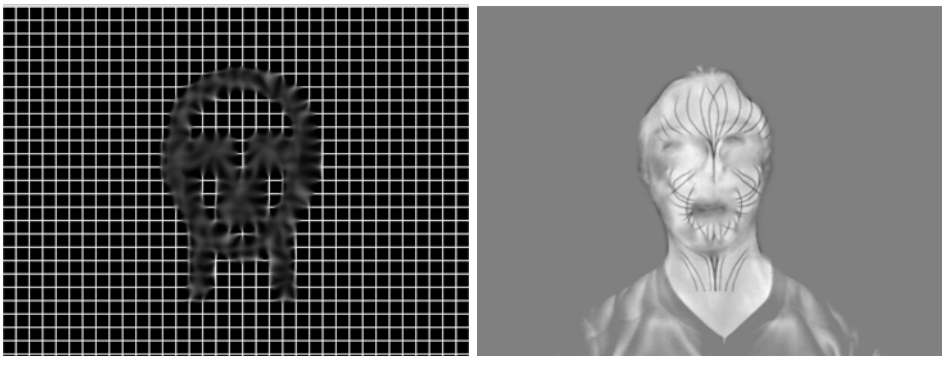


Figure 4.9: The processes involved prior to transformation/deformation of pixels in the randomly selected transform window in the NRAR method.



Figure 4.7: A distance transform image of the target image (i.e., the face sketch). Black pixels represent edge pixels while gray to white pixels represent non-edge pixels.



(a) (b)

Figure 4.8: (a) The deformation field obtained after the registration with the NRAR method. (b) The same deformations are performed for the face sketch with the Blaschko's lines and overlayed with the face thermogram.

Once the pixels in the transform window are shifted to their new positions (non-integer/subpixel coordinates) in accordance to the eq. 4.10, in order for the pixels to not be coinciding with the center of any pixel of the new image, some interpolations are necessary. Image interpolation is carried out to obtain image B' prior to the computation of the new DC (Section 4.2.2) between the reference image, A, and the deformed image, B', after each transformation has taken place on a randomly selected neighbourhood of pixels. This task is performed to give new intensity values to the initial pixel location (vacant pixels) based on the intensity values of the moved pixels and a set of border pixels around the transform window (peripheral pixels). This makes the size of the neighbourhood window involved in the interpolation process becomes $(2M+3)\times(2M+3)$. The inclusion of the peripheral pixels in the interpolation process is made to reduce any disconnections between the transform window and its neighbour pixels. More detailed explanation on this process is given in Section 4.2.3.

If a transformation performed is able to minimize the value of the current DC, the transformed set of pixels will be accepted and the whole process is repeated with a new randomly chosen central pixel. However, if the current DC is not minimized, the pixel next to the current central pixel is selected as the new central pixel and this whole process is repeated until one of the termination criteria defined is met. The termination criteria is further discussed in Section 4.2.4).

4.2.2 Dissimilar Criterion (DC)

In the proposed NRAR method, the DC is calculated at the start of the registration process and after each transformation on the transform window takes place thereafter. The DC employed is a modified version of the similarity functions used in [126, 213]. The so-called DC integrates a dissimilarity measure, E_1, a geometric function as a regularizer, E_2, and a third function to measure pixel overlap, E_3, given by

$$DC = E_1 + \beta E_2 + \alpha E_3 \tag{4.13}$$

where β and α are the parameters that give weighting to the level of influence/importance of their corresponding terms in the DC. The integration of the two other terms besides the similarity measure is introduced to avoid any physically meaningless transformations based on similarity measure alone [200]. For the first term in the cost function, where $E1 \equiv 1 - S(A,B)$, the

$S(A, B)$ is defined by a similarity measure that is expressed by the correlation coefficient (CC). As the images used in the process of registration are both in the same form, which is the gray edge map, it is found sufficient and more suitable to use the CC than the MI as the smimilarity measure. Furthermore, as our developed method is based on adaptive patch-based manner, it is more reliable to use the CC than the MI. Moreover, CC is claimed to be more robust and computationally more efficient than that of MI especially for intensity based registration [9]. The CC is defined as

$$CC(A, B^{'}) = \frac{\sum_m \sum_n (A_{mn} - \overline{A})(B^{'}_{mn} - \overline{B^{'}})}{\sqrt{\left(\sum_m \sum_n (A_{mn} - \overline{A})^2\right)\left(\sum_m \sum_n (B^{'}_{mn} - \overline{B^{'}})^2\right)}} \tag{4.14}$$

where, m and n are the row and column of the transform window, A and $B^{'}$ represent the reference and the transformed images respectively, and $\overline{A}$ and $\overline{B^{'}}$ are their mean images respectively. The double sums indicated are taken over the rows and columns of the two images and A_{mn} and $B^{'}_{mn}$ are the pixel values of images A and $B^{'}$ at row m and column n, respectively. It has been reported that for a transformation that is small enough, by maximizing the CC, the least-mean-square of the difference in the intensity values of A and B can be minimized [195]. Moreover, this statistical measure has the property that it measures correlation on an absolute scale ranging within $[-1, 1]$ [195]. A value of 1 for the CC shows perfect correlation that can be achieved by two similar images, while a value of -1 shows zero correlation between two images i.e., an image with its inverse image.

The second term E_2, in the dissimilar criterion (eq. 4.15) is introduced to act as a regularizer or a smoother in order to obtain a meaningful solution. A regularizer actually allows any a priori knowledge of the physical properties of the underlying anatomical structure to be introduced and enables the solution to escape from possible local minima. As we expect the deformations or distortions applied are as little as possible, a regularizer based on a geometric function adapted from [126, 213] is employed. However, unlike the geometric function term used in their work which is a purely geometric term, the one employed in this work is an intensity based. This modification to intensity base is made to avoid having large differences in intensity between the moved pixels and their surrounding pixels that can cause uneven gray value distribution (surface) especially near the borders. As a sought solution for the particular image registration that requires minor intensity deformations, the intensity based geometric function is defined as given by

$$E_2 \equiv \frac{1}{N_{A,B'}} \sum_{k \in T_{A,B'}} |x_k(i,j-1) - x_k(i,j) - r| + |x_k(i,j+1) - x_k(i,j) - r| + ...$$
$$... + |x_k(i-1,j) - x_k(i,j) - r| + |x_k(i+1,j) - x_k(i,j) - r| \quad (4.15)$$

where the term E_2 defines the small level of distortion that is allowed in the transformation involving pixel values in the calculation. Here, $N_{A,B'}$ is the number of overlapping pixels in $T_{A,B'}$(between images $B^{'}$ and A). The parameter r is the difference in intensity between the coordinates along the x axis as well as the y axis, in two neighbouring pixels aligned along the axes respectively. In a regular grid (before any distortion is imposed), r is assumed to be as small as 0.01. After an iteration takes place, the intensities of the two pixels may shift with respect to each other, so their intensity difference along their axes may have changed. The difference between this intensities and the initial value of r expresses the distortion of the intensities of moved pixels.

The final term E_3, used in the dissimilar criterion is defined as

$$E_3 \equiv 1 - \frac{N_{A,B'}}{N} \quad (4.16)$$

where N here represents the total number of edge pixels in the reference image instead of the total number of pixels in the image as employed by Bejo [213] and Kovalev et al. [126], and $N_{A,B'}$ is the number of overlapping edge pixels between the images $B^{'}$ and A. This term is employed to ensure a maximum overlap is achieved between image A and transformed image $B^{'}$.

If the dissimilar criterion DC, is minimized by a local transformation in a single iteration, then the changes made to the transformed pixels are accepted but if the DC is maintained or increased, the changes made are not accepted and will be rejected. If a deformation is accepted, the process is then repeated with a new randomly assigned central pixel or else the pixel next to the current central pixel is selected as a new central pixel of the transform window. All accepted changes are also applied simultaneously to the globally registered image in its intensity form (Figures 4.13 and 4.14).

4.2.2.1 Explatory Runs for Parameters α and β in the Dissimilar Criterion (DC)

Explatory runs are conducted in this work to select the best values for the parameters α and β used in the DC (eq. 4.13) using model images of Case 4 (Figure 4.22) since the complexity in the registration between these images is the highest among four pairs of model images designed for performance analysis of the proposed NRAR method presented in Section 4.3. This task is very important as the performance of our local registration method between two images that are globally registered to each other is driven by the DC that consists of three terms (explained in Section 4.2.2). The explatory runs are conducted for various parameter settings. In the initial stage of the explatory runs, both parameters will be given values from the set $[0.0001, 0.0005, 0.001, 0.005, 0.001, 0.05, 0.01, 0.5, 0.1]$, where all possible combinations of these values are used. Then using 3 different similarity measures such as the CC, SAD and MI, the quality of registration obtained for each combination of parameter values is evaluated. The set of parameter values that achieved the highest similarity measures will be identified and further explorations of the parameter space around the identified values are performed to refine the parameter values.

The results obtained after 7000 tries for each pair of α and β based on the values of CC, SAD and MI are shown in Table 4.1. It can be observed that the highest value for both CC and SAD is achieved for $\alpha = 0.1$, $\beta = 0.001$. On the other hand, the highest value of MI is also achieved for $\beta = 0.001$ but with $\alpha = 0.0005$. Since the highest performance value for CC, SAD and MI is achieved when $\beta = 0.001$, in the second explatory runs to refine these parameter values, the value of β is also investigated for 0.002, 0.003 and 0.004. On the other hand, for the value of α, we compared the performance between the values 0.0005 (as identified by using MI) and 0.1 (as identified by using CC and SAD). However, for this investigation, the analysis based on intensity form of the model images using CC and MI is considered. This is because it is found that for high value of similarity measures, even though the registration achieved between the images in gray edge maps is fairly good, the registration achieved between the images in their intensity forms may not be as good. An example shown in Figure 4.10 shows this condition; these results are obtained when the method achieved a CC of 0.9117 for edge maps and a CC of 0.8391 for its intensity form. It can be observed that even though the shape of a sphere is well transformed into a C shaped, the filling of the C shaped object is not evenly constructed. Hence, it is best to not only choose the pair of parameters that can achieve high value for edge maps alone but also for its intensity forms. From Table 4.2, it is found that values of CC of above 0.9 is obtained



(a) (b)

Figure 4.10: Registration results between a C shaped object (reference image) and a ring shaped object (target image); (a) Registered target image in edge map and (b) in its intensity image

for both the edge maps and its intensity image for $\alpha = 0.1$, $\beta = 0.004$. To further ensure the high performance of this set of parameters, these values are investigated further by comparing it with the two initial pairs, $\alpha = 0.0005$, $\beta = 0.001$ and $\alpha = 0.1$ and $\beta = 0.001$ with five runs of 7000 tries each for each pair. Then, the average of the results obtained for the five runs for each set is computed and compared in Table 4.3.

It can be observed that the average value of CC based on the edge maps is the highest for $\alpha = 0.0005$, $\beta = 0.001$ with a difference of 0.0067 with the second highest value of CC obtained for $\alpha = 0.1$, $\beta = 0.004$, and with an std of 0.006. On the other hand, based on its intensity form, the highest value of CC is obtained for $\alpha = 0.1$, $\beta = 0.004$ with a difference of 0.01 with the second highest value of CC obtained for $\alpha = 0.0005$, $\beta = 0.001$, and with an std of 0.009. However, for MI, the highest value for both edge maps and its intensity image is obtained for $\alpha = 0.1$, $\beta = 0.004$. Since 3 out 5 performance parameters used (CC for its intensity image, MI for edge maps and MI for its intensity image) achieved the highest value for $\alpha = 0.1$, $\beta = 0.004$ and with only small difference from the CC for $\alpha = 0.0005$, $\beta = 0.001$ obtained for its edge maps, this pair of parameters is employed in our DC.

Table 4.1: Results of the first explatory runs for the selection of parameters α and β for the DC used. The best result for each similarity metric is shown in bold.

α	Similarity metric	β							
		0.0001	0.0005	0.001	0.005	0.01	0.05	0.1	0.5
0.0001	CC Edge	0.9093	0.9057	0.8963	0.8865	0.8996	0.8816	0.8817	0.8529
	SAD Edge	453	458	453	465	446	468	473	536
	MI Edge	0.704	0.756	0.754	0.7586	0.7533	0.7469	0.7415	0.7286
0.0005	CC Edge	0.9086	0.8975	0.9091	0.8908	0.907	0.8821	0.8859	0.8514
	SAD Edge	466	449	438	472	440	467	473	538
	MI Edge	0.7579	0.7656	**0.7673**	0.7628	0.7562	0.7613	0.7473	0.7168
0.001	CC Edge	0.9051	0.9039	0.8999	0.8998	0.904	0.8783	0.8728	0.8584
	SAD Edge	445	457	453	456	444	472	482	529
	MI Edge	0.7578	0.7642	0.7564	0.7496	0.7505	0.7506	0.7234	0.7151
0.005	CC Edge	0.9111	0.9003	0.8963	0.8928	0.9013	0.8856	0.884	0.8623
	SAD Edge	455	461	448	454	443	471	471	515
	MI Edge	0.7632	0.7576	0.7633	0.7477	0.766	0.7647	0.7447	0.7314
0.01	CC Edge	0.8931	0.9081	0.9164	0.89	0.8966	0.8887	0.8775	0.8698
	SAD Edge	463	454	439	457	451	472	484	510
	MI Edge	0.7636	0.7484	0.7537	0.7609	0.7498	0.7494	0.7357	0.7329
0.05	CC Edge	0.9126	0.9	0.9023	0.8973	0.9048	0.8891	0.8886	0.8662
	SAD Edge	439	445	450	461	448	456	466	515
	MI Edge	0.7545	0.7628	0.7593	0.7551	0.7523	0.7531	0.7483	0.7214
0.1	CC Edge	0.9014	0.8933	**0.9243**	0.9079	0.8994	0.891	0.8809	0.8731
	SAD Edge	452	465	**434**	440	453	459	478	509
	MI Edge	0.7474	0.7509	0.7573	0.7642	0.7525	0.7498	0.7357	0.7278
0.5	CC Edge	0.9022	0.8929	0.8943	0.9037	0.8997	0.8987	0.8857	0.8637
	SAD Edge	450	459	455	449	460	444	465	523
	MI Edge	0.7466	0.7537	0.7497	0.7603	0.7487	0.7522	0.7625	0.7377

Table 4.2: Results of the second explatory runs (narrower range forβ) for the selection of parameters α and β for the DC. The best parameter β is shown in bold.

α	Similarity metric	β		
		0.002	0.003	**0.004**
0.0005	CC Edge	0.8947	0.907	0.8959
	CC Int	0.9415	0.8753	0.9408
	SAD Edge	460	452	470
	MI Edge	0.7509	0.7538	0.7582
	MI Int	0.5424	0.5136	0.5413
0.1	CC Edge	0.8954	0.8959	0.9041
	CC Int	0.8674	0.8953	0.9388
	SAD Edge	458	454	448
	MI Edge	0.753	0.7551	0.7549
	MI Int	0.5138	0.5209	0.5375

4.2.3 The Delaunay based Image Construction

Once a transformation is accepted, all the moved pixels remain at their new sub-pixel/non-integer coordinates with their original intensity values. However the vacant integer pixel coordinates's

Table 4.3: Average results for 5 runs for 3 pairs of parameters ($\alpha = 0.0005$ and $\beta = 0.001$, $\alpha = 0.1$ and $\beta = 0.001$, and $\alpha = 0.1$ and $\beta = 0.004$). The best parameters are shown in bold.

(a) Average results for 5 runs (7000 tries each) for $\alpha = 0.0005$ and $\beta = 0.001$

Similarity metric	α=0.1, β=0.001					Average	Std.
	1	2	3	4	5		
CC Edge	0.8945	0.8931	0.8962	0.9089	0.8979	0.8981	0.0062
CC Int	0.9372	0.872	0.8686	0.9416	0.8433	0.8925	0.0442
SAD Edge	468	470	454	449	448	457.800	10.4976
MI Edge	0.7511	0.7514	0.7514	0.7611	0.7531	0.7536	0.0043
MI Int	0.5399	0.5111	0.5112	0.538	0.503	0.5206	0.0169

(b) Average results for 5 runs (7000 tries each) for $\alpha = 0.1$ and $\beta = 0.001$

Similarity metric	**α=0.1, β=0.004**					Average	Std.
	1	2	3	4	5		
CC Edge	0.9041	0.8964	0.8865	0.9043	0.9109	0.9004	0.0093
CC Int	0.9388	0.9408	0.9329	0.9418	0.938	0.9385	0.0035
SAD Edge	448	453	468	446	439	450.8	10.8489
MI Edge	0.7549	0.7548	0.7623	0.7674	0.7578	0.7594	0.0054
MI Int	0.5375	0.54	0.5364	0.5424	0.5381	0.5389	0.0024

(c) Average results for 5 runs (7000 tries each) for $\alpha = 0.1$ and $\beta = 0.004$

Similarity metric	α=0.0005, β=0.001					Average	Std.
	1	2	3	4	5		
CC Edge	0.9001	0.9097	0.9086	0.9153	0.902	0.9071	0.0061
CC Int	0.8773	0.9407	0.9418	0.9427	0.9386	0.9282	0.0285
SAD Edge	452	449	451	442	447	448.2	3.9623
MI Edge	0.754	0.7521	0.7525	0.7696	0.7617	0.7579	0.0075
MI Int	0.515	0.5395	0.5356	0.5408	0.5388	0.5339	0.0108

are left with no intensity values. In this section, the processes involved in the computation of new gray values for the vacant integer pixel locations are explained. As mentioned earlier, new gray values are assigned based on the values of the moved pixels and their neighbour pixels by the Delaunay triangulation based natural interpolation method (as explained in Section 4.1.3.2)[45, 44]. To ensure that the image after interpolation achieves a smooth transition of intensity values especially around the transform window, as explained earlier, one-pixel width of border pixels around the transform window are included resulting in a selected window of a size of $(2M + 3) \times (2M + 3)$ will be involved in the computation of new values [113]. Hence, the Delaunay triangles are created from the border/peripheral original pixels and the moved central pixels. This resulted in having the vacant pixels lying inside these triangles. In estimation of the value for each of the vacant pixels, the interpolation process takes into account the three vertices (pixels) that compose the nearest triangle where the plane surface equation formed by these three vertices is extracted. Then, the corresponding gray value can be obtained by substituting the specific coordinates in eq. 4.8. However, the intensity values of the border pixels remain

unchanged after the interpolation. Only the pixels at integer locations in the initial transform window will be affected after the interpolation. Since the intensity values of the set of border pixels are maintained, the disconnection between this window with the surrounding pixels can be minimized. The values of the border pixels are only used for the calculation of the new gray values for the integer pixels based on the natural interpolation method as illustrated in Figure 4.11.

A MATLAB's 2D Delaunay function that adopted the Computational Geometry Algorithms Library (CGAL) algorithm is used in finding the optimum Delaunay triangulation with more robust, faster, and memory-efficient solutions [44]. An example of a non-rigidly transformed image using the Delaunay triangulation based natural neighbour interpolation is shown in Figure 4.12.

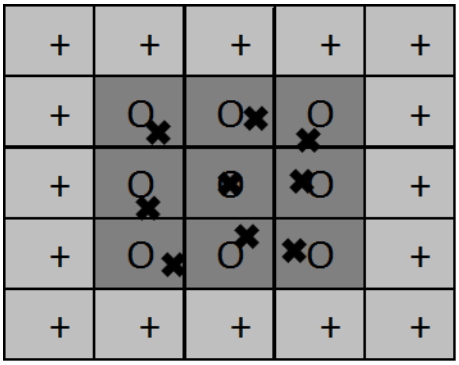


Figure 4.11: An example showing a neighbourhood of 'o' pixels which are the old integer positions that are subjected to local transformations, '+' pixels that are only considered during interpolation and 'x' pixels with new pixel positions. New gray values are needed to be assigned to the old integer positions 'o' of the 8 moved pixels (central pixel is excluded). Delaunay triangulation is performed between the '+' and 'x' pixels followed by natural based interpolation to give new gray values to 'o' pixels [113].

4.2.4 Termination Criterion

The value of the *DC* is used as the driving force for the algorithm to achieve optimal deformations for registration between the images in this work. It is found that if the value of *DC* is not improved after 7000 accepted changes, there is not much improvement that can be achieved beyond that. Hence, this value is used as a threshold value for the algorithm to terminate itself for the registration between the type of data used in this work. A threshold for the



(a) (b) (c)

Figure 4.12: (a) Target image, (b) reference image and (c) deformed target image after the NRAR method is performed between the target image and the reference image based on their gray edge maps.

allowable maximum rejected changes (800 rejections) before a change is accepted is also included. Therefore, the algorithm will be terminated once one of these two criteria is met.

4.3 Performance Analysis with Ground Truth Models

Performance of the NRAR method is investigated for the following model image pairs.

Case 1 A pair of model images of similar shapes but with a small translational difference between them. Image size of 70×70 pixels. See Figure 4.13 for their edge maps and Figure 4.14 for their intensity images.

Case 2 A pair of model images of different shapes with a small translational difference between them. Image size of 70×70 pixels. See Figure 4.16 for their edge maps and Figure 4.17 for their intensity images.

Case 3 A pair of model images of similar shapes with one of them having small distortions at its border. Image size of 120×158 pixels. See Figure 4.19 for their edge maps and Figure 4.20 for their intensity images.

Case 4 A pair of model images with large differences in shape and contour (between a C-shaped object and an ellipse). Image size of 155×202 pixels. See Figure 4.22 for their edge maps and Figure 4.23 for their intensity images.

Performance analysis based on only the NRAR method for each case above is investigated since

it is assumed that the image pairs have already been globally registered. For this purpose, the model image pairs are created to have only small geometrical and local displacements between them as large geometrical differences should already be reduced by the global registration method (as discussed in Chapter 3). However, for the model image pair in Case 4 (Figure 4.22), the local differences between the pair are designed to be a little complex for the purpose of investigating the flexibility and elasticity of the NRAR method.

The input images fed to the NRAR method are in the form of gray edge maps for both the reference and the target images. Once a transformation is accepted, the same transformation parameters are applied simultaneously to the intensity form of the target image.

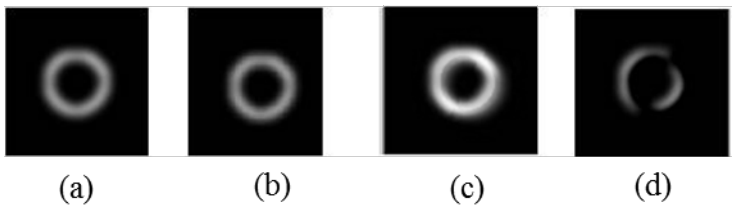


Figure 4.13: Image pair of Case 1; gray edge maps of the (a) reference image of a circle and (b) target image (translated version of the reference image). (c) Overlay between the reference image and the target image, (d) an absolute difference image between them.

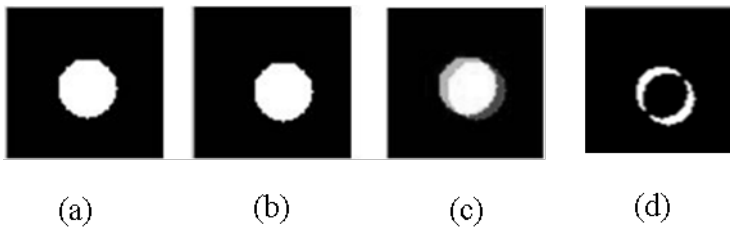


Figure 4.14: Image pair of Case 1; intensity images of the (a) reference image of a circle and (b) target image (translated version of the reference image). (c) Overlay between the reference image and the target image, (d) an absolute difference image between them.

In Case 1, a model image of a circle as a reference image (Figure 4.13(a), Figure 4.14(a)) and its translated version as a target image (Figure 4.13(b), Figure 4.14(b)) are considered. The initial centroid of the reference image is $[36, 36]$. With a translation parameter of $[2, 4]$, the reference image is moved to a new centroid of $[38, 40]$ producing the target image. The displacements between these images can be viewed in their image overlays (Figures 4.13(c), 4.14(c)), and in their difference images (Figures 4.13(d), 4.14(d)). These displacements are reduced to a good extent by the NRAR method. The registration results can be observed in Figure 4.15.

The registration results based on image overlays between the reference and the registered target

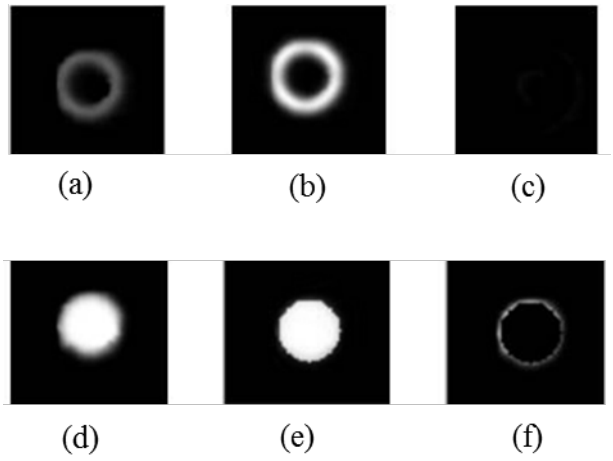


Figure 4.15: After the NRAR method is performed between the image pair of Case 1. Based on the gray edge map for (a) the registered target image, (b) overlay between the reference image and the registered target image, (c) its corresponding difference image. Based on the intensity image for (d) the registered target image, (e) overlay between the reference image and the registered target image and (f) its corresponding difference image.

image in both edge maps and intensity images (in Figures 4.15(b) and 4.15(e)) demonstrate sufficiently good improvement in alignment achieved between them. However, from the absolute difference image obtained between the registered images in intensity image as shown in Figure 4.15(f), it is found that there is intensity leakage at object's border despite the good alignment achieved. This may be due to some extrapolations of intensities of the moved pixels along the object's border.

On the other hand, the registration error for the results obtained can also be shown in terms of the distance of centroids between the reference and the target image before and after the registration is performed. It is found that the centroids of the circle in the registered target image is $[36.7, 36.4]$ for the edge map and $[36.5, 36.7]$ for the intensity image. This shows that the initial displacement of $[2, 4]$ between the circles in the target image and the reference image before registration is performed is greatly reduced to $[0.7, 0.4]$ and $[0.5, 0.7]$ respectively for the edge map and the intensity image. From these observations, it can be inferred that the registration's limitation associated with the registration results based on the model images of Case 1 are mainly caused by the intensity based interpolation performed in the method rather than the geometrical aspect of the registration. The registration results presented for Case 1 is achieved after 269 of accepted tries/changes. The SAD and CC for both before and after NRAR method is performed are computed. It is found that the SAD between the pair of images for Case 1 is reduced from 229 to 108 while the CC is increased from 0.6509 to 0.9840 for the edge maps.

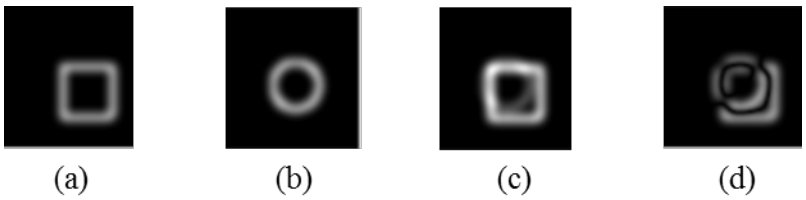


Figure 4.16: Image pair of Case 2; gray edge maps of the (a) reference image of a square and (b) target image of a circle, (c) overlay between the reference image and the target image, (d) an absolute difference image between them.

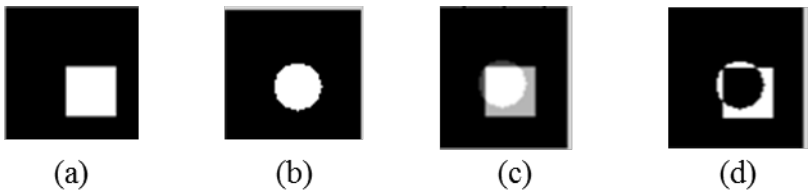


Figure 4.17: Image pair of Case 2; intensity images of the (a) reference image of a square and (b) target image of a circle, (c) overlay between the reference image and the target image, (d) an absolute difference image between them.

In Case 2, a translational difference between two images with different shapes of objects is considered; a reference image of a square object and a target image of a circle object. Both the edge maps and the intensity images of the reference and the target images are shown in Figures 4.16(a) and (b), and Figures 4.17(a) and (b), respectively. Small deformations to match between these images are applied based on the developed NRAR method. The registration results are displayed by image overlays (Figures 4.18(b) and 4.18(e)), and absolute difference images (Figures 4.18(c) and 4.18(f)) that are compared with the ones before registration in Figures 4.16(c), 4.17(c) and Figures 4.16(d), 4.17(d) respectively. Similarly to the result achieved for Case 1, the translational differences between the image pair for Case 2 are also able to be greatly reduced by the NRAR method. Furthermore, the NRAR method has also demonstrated its ability to deform between objects of different shapes in order to match between them. This proves that this method can apply deformations non-homogeneously or elastically and this ability is investigated further by using the model images in Case 4 which will be discussed later in this section. However, from the difference image in Figure 4.18(c), it can be observed that geometrically, the target image is registered well with the reference image but suffered from small reduction in intensities among the transformed pixels. This is the cost that the method has to bear due to the interpolation method employed that is performed based on pixel intensity rather than control points. Figure 4.18(f) also demonstrated this condition where the pixels at the border of the moved object in the registered target image suffer from under-detection mostly at the bottom corner of the square and represents some leakages/reductions of intensity along

the sides of the squares.

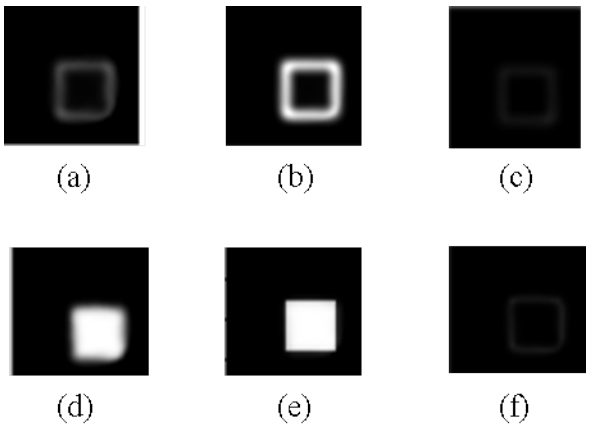


Figure 4.18: After the NRAR method is performed between the image pair of Case 2; Based on the gray edge map for (a) the registered target image, (b) overlay between the reference image and the registered target image, (c) its corresponding difference image. Based on the intensity image for (d) the registered target image, (e) overlay between the reference image and the registered target image and (f) its corresponding difference image.

As for Case 3, two model images of similar shapes with small distortions in the contour of the object in the target image are considered. For this purpose, a reference image of a circle (Figures 4.19(a), 4.20(a)) and a target image (Figures 4.19(b), 4.20(b)) of the same circle but reduced a little in size and with some small distortions at the top part of the circle are used. For this particular case, the deformations applied through the NRAR method should be able to not only correct for the distortions but also to be able to increase the size of the object in the target image to match the size of the circle in the reference image as shown in Figure 4.21. The differences in the contours and sizes can be seen in Figures 4.19(c) and 4.19(d), and Figures 4.20(c) and 4.20(d) by image overlays and image differences between them in both edge maps and intensity images respectively. The results after the NRAR method is performed as displayed in Figure 4.21 clearly show how well the small distortions in the target image are reduced and the size is increased to match the circle in the reference image. However, as expected, similarly to the results obtained for the previous cases, the registered intensity image suffered from extrapolation of pixels and some reduction in intensities along the object's border that can be observed from the difference image taken between the reference image and the registered intensity image even though good registration is achieved geometrically as shown in Figure 4.21(f).

Finally, using the model images in Case 4, the performance of the developed NRAR method in deforming a ring shape object into a C shaped object is investigated. This type of model is firstly introduced by Christensen [63] to investigate fluid registration. For this purpose, a C shaped

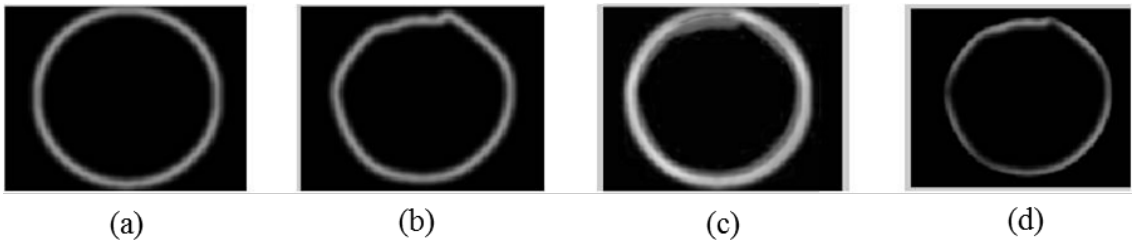


Figure 4.19: Image pair of Case 3; gray edge maps of the (a) reference image of a circle and (b) target image of a circle with some distortions at the top part of the circle, (c) overlay between the reference image and the target image, (d) a difference image between them.

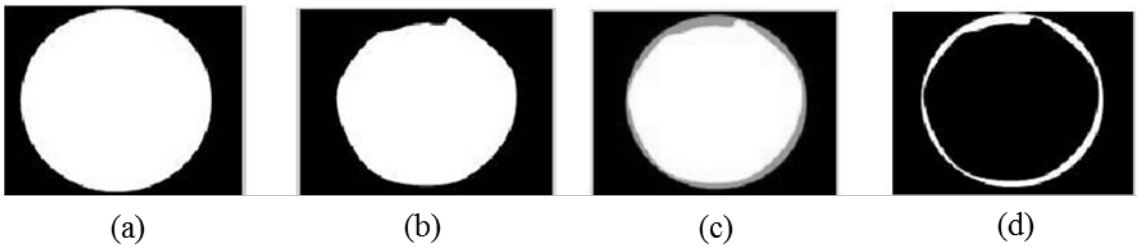


Figure 4.20: Image pair of Case 3; intensity images of the (a) reference image of a circle and (b) target image of a circle with some distortions at the top part of the circle, (c) overlay between the reference image and the target image, (d) an absolute difference image between them.

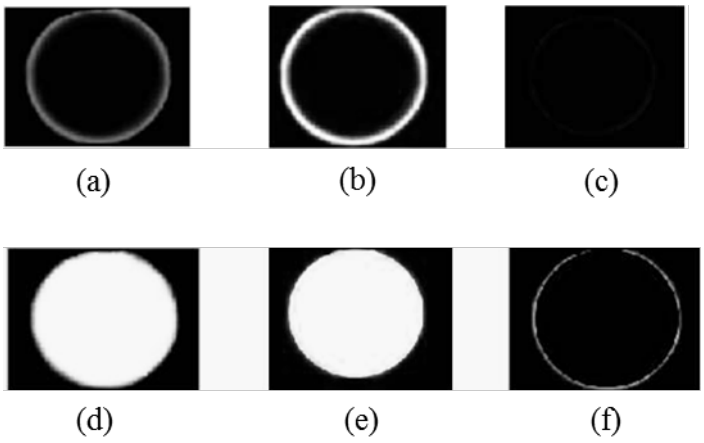


Figure 4.21: After the NRAR method is performed between the image pair of Case 3; Based on the gray edge map for (a) the registered target image, (b) overlay between the reference image and the registered target image, (c) its corresponding difference image. Based on the intensity image for (d) the registered target image, (e) overlay between the reference image and the registered target image and (f) its corresponding difference image.

image is treated as a reference image (Figures 4.22(a), 4.23(a)) whereby an image of a ring shaped object is treated as the target image (Figures 4.22(b), 4.23(b)). The geometrical differences between these images are illustrated by image overlays (Figure 4.22(c) and Figure 4.23(c)) and difference images (Figure 4.22(d) and Figure4.23(d)). The results obtained after the developed NRAR method is performed are shown as in Figure 4.24. The ability of the method to perform the task in matching and adapting the ring/ellipse to a C shaped object shows further that the NRAR method is able to elastically deform an object to match between different shapes and contours [63]. Even though the NRAR method has achieved fairly good results in correcting for small local differences between two images including local contour distortions, the transformed pixels may not achieve sufficient smooth appearance and the regularity of the shape may not be maintained due to intensity leakages at border pixels.

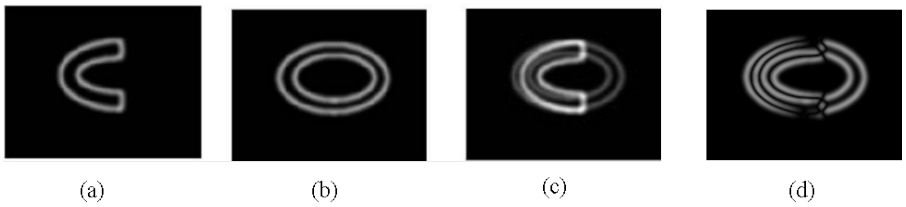


Figure 4.22: Image pair of Case 4; gray edge maps of the (a) reference image of a square and (b) target image of a circle, (c) overlay between the reference image and the target image, (d) an absolute difference image between them.

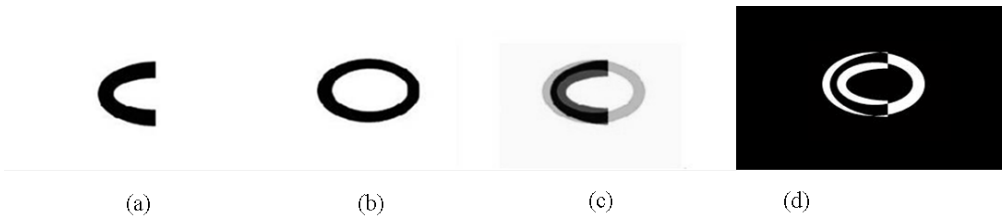


Figure 4.23: Image pair of Case 4; Intensity images of the (a) reference image of a C shaped object and (b) target image of a ring/ellipse, (c) overlay between the reference image and the target image, (d) an absolute difference image between them.

The NRAR method is investigated further by comparing the method with another non-rigid registration method for the same pairs of images. For this purpose, the performance of the NRAR method is evaluated against a free-form deformation (FFD) method developed by Rueckert et al. [202]. However, the method developed by Rueckert et al. consists of both global transformation and local transformation to cater for a 3D registration of breast MRI images. The global motion model employed is a rigid transformation model which is parametrized by six degrees of freedom for a 2D registration and twelve degrees of freedom for a 3D registration. On the other hand, its local transformation model is based on a multi-resolution scheme with a core B-spline free-form

deformation (FFD) model. This approach is the pioneer in non-rigid image registration method that involves the use of MI as the similarity measure in its dissimilar criterion. The dissimilar criterion to be minimized employed by this method is represented by a combination of the cost associated with the smoothness of the transformation and with image similarity [202].

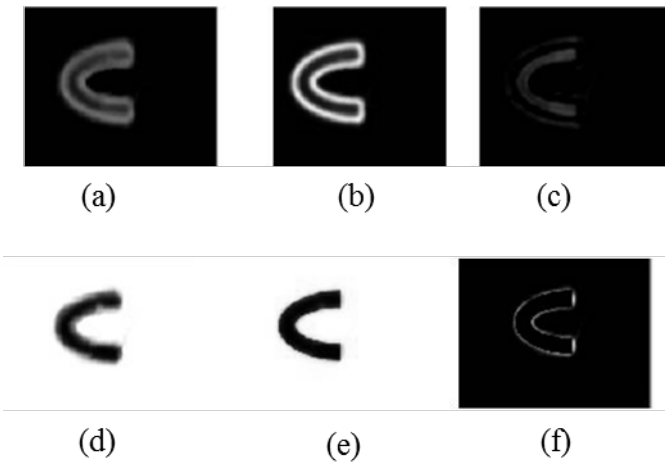


Figure 4.24: After the NRAR method is performed between the image pair of Case 4; Based on the gray edge map for (a) the registered target image, (b) overlay between the reference image and the registered target image, (c) its corresponding difference image. Based on the intensity image for (d) the registered target image, (e) overlay between the reference image and the registered target image and (f) its corresponding difference image.

In this comparison, the FFD method is performed with varying sizes of transformation grid from 9×9, 13×13, 20×20, 30×30 to 50×50 while the NRAR method is performed with varying sizes of M ($M = \{5, 7, 9, 11\}$). This is due to the optimal size of the transformation grid to be set for the FFD method cannot be chosen based on the image size alone but may also based on the complexity of the geometrical differences between the images to be registered. Trial and error is needed to determine the optimal size of the grid for the FFD method; hence the varying sizes of control point grid used for this comparison purpose. For performance evaluation, the CC between the reference and the registered target image for each case achieved using both methods are measured. Then, the average values of CC for all image pairs, for each M size for the NRAR method and for each control grid size for the FFD method are computed and tabulated in Table 4.4. In this table, the highest average CC for both methods based on edge map and intensity images are shown in bold.

Overall, it can be observed from the average CC obtained in Table 4.4 that our method performs fairly well for all the four image pairs with varying sizes of M (in average CC of above 0.92 is achieved) and seems to be comparable to the FFD method. Based on the best average CC

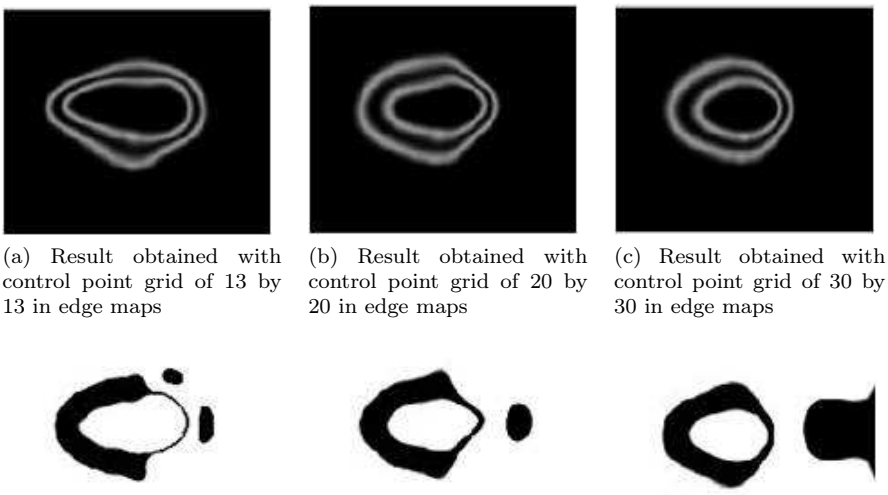
Table 4.4: Registration result in average for all the 4 cases of registration problems, based on varying sizes of M for the NRAR method and varying sizes of control point grid for the FFD method.

Registration parameters	Average CC	
	Edge Map	Intensity image
M=5	0.89	0.88
M=7	**0.94**	0.92
M=9	0.94	**0.95**
M=11	0.93	0.94
FFD (9,9)	0.86	**0.95**
FFD (13,13)	0.88	0.90
FFD (20,20)	**0.95**	0.90
FFD (30,30)	0.93	0.88
FFD (50,50)	0.92	0.85

obtained, even though the FFD method slightly outperforms the NRAR method for the edge maps, the FFD registration method seems to have difficulties in solving for the registration problems associated with the model images of Case 4 where differences between the shapes and contours of the objects to be registered in Case 4 are quite complex. This can be observed from Figure 4.25 where the ring shaped object is unable to be registered or adapted to the C shaped object by the FFD method as successfully obtained by the NRAR method (Figure 4.24). Due to this poor performance of the FFD method, a low average CC in the range of $0.46 - 0.84$ for the edge maps, and in the range of $0.44 - 0.88$ for the intensity images is achieved for the image pairs in Case 4. On the other hand, the NRAR method obtained a fairly high average CC in the range of $0.83 - 0.91$ and $0.71 - 0.92$ for the edge maps and intensity images respectively for the same image pairs. Furthermore, it can also be seen from Figure 4.26(f), for the result using model images of Case 3 (for the intensity images) based on the FFD method, the small distortion on the top part of the circle is still visible in the registered target image.

In terms of robustness, the NRAR method seems to be more robust than the FFD method as the range of average CC obtained for each case model for varying sizes of M is smaller than that shown by the FFD method with varying sizes of control point grid. As for example, in Case 3 (between a square and round shaped object), the FFD method (with different sizes of control grid) achieved an average CC in the range of $0.74 - 0.97$ while the NRAR method (with varying sizes of M) achieved an average CC in a smaller range of $0.92 - 0.95$. By taking all the 4 cases into consideration, it can still be observed from Table 4.4 that the differences in the average CCs obtained is small between the varying sizes of M compared to the differences in the average CCs obtained for between the varying sizes of control points in the FFD method. This further indicate that the NRAR method is robust in regards to the size of transform

window used. However, since most large displacements between the images to be registered by the NRAR method should already been reduced to small local displacements and in order to speed up the registration process, $M = 7$ is chosen as the default M size for the transform window. This size is also selected to reduce intensity leakages at object's border pixels due to pixel extrapolations caused by artefacts produced during interpolation process as larger window can result in more artefacts being produced. Furthermore, since the average CCs obtained by the proposed NRAR method are also high $(0.89-0.95)$, the reliability of the method in achieving good local registration result is as high.



(a) Result obtained with control point grid of 13 by 13 in edge maps

(b) Result obtained with control point grid of 20 by 20 in edge maps

(c) Result obtained with control point grid of 30 by 30 in edge maps

(d) Result obtained with control point grid of 13 by 13 in intensity form

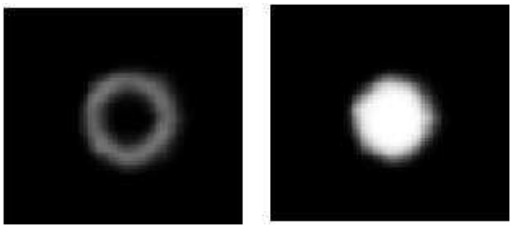
(e) Result obtained with control point grid of 20 by 20 in intensity form

(f) Result obtained with control point grid of 30 by 30 in intensity form

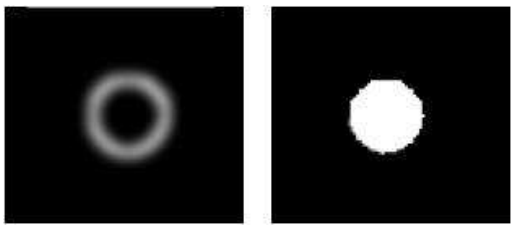
Figure 4.25: Resultant images for Case 4 using the FFD method.

Nevertheless, for the cases where the FFD method outperforms our method, as can be seen in Figure 4.26, the transformed images maintain their smoothness and regularity in shapes and contours unlike in the results obtained by the NRAR method. This is because the interpolation technique used in the NRAR method is an intensity based whereas in the FFD, an interpolation based on transformation/control point grid using the B-spline interpolation method is employed. The B-spline interpolation method can yield a very high degree of freedom depending on the resolution of the control points grid. Its B-spline parametrization uses this control point grid as parameters and interpolates in between with the B-spline basis functions [153]. This has contributed to the smoothness achieved by the FFD method. However, as a consequence, the computational complexity will be increased. But for a large number of control points, this interpolation method is reported to be very computationally efficient due to its locally controlled

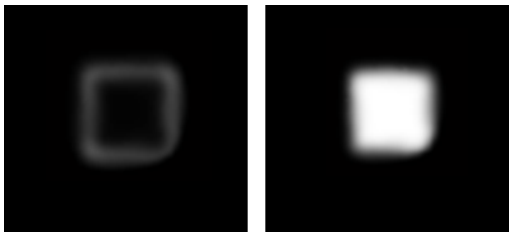
ability [48, 79].



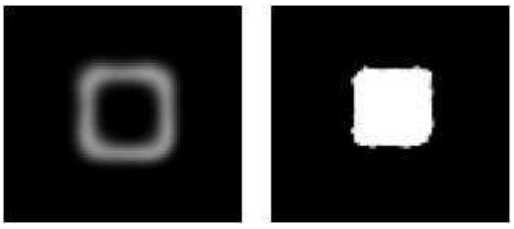
(a) After registration using the developed method for Case 1 with in edge map (left), in intensity image (right).



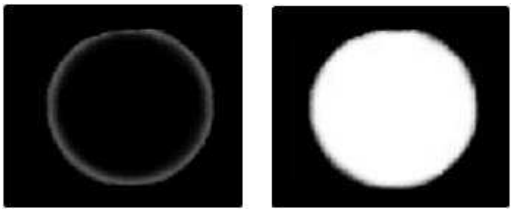
(b) After registration using the FFD method for Case 1 with control point grid 9 by 9 in edge maps (left), in intensity form (right).



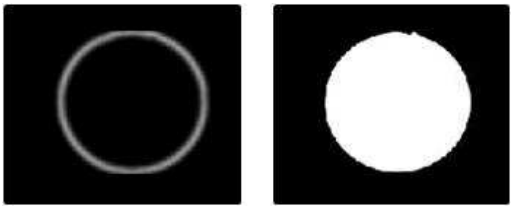
(c) After registration using the developed method for Case 2 in (Left) edge map and in (Right) intensity image.



(d) After registration using the FFD method for Case 2 with control point grid 9 by 9 in (Left) edge map and in (Right) intensity image.



(e) After registration using the developed method for Case 3 in (Left) edge map and in (Right) intensity image.



(f) After registration using the FFD method for Case 3 with control point grid 9 by 9 in (Left) edge map and in (Right) intensity image.

Figure 4.26: Comparison of results obtained by the developed method (left) and the FFD method (right) for image pairs of cases 1 to 3.

4.4 Potential Application in Morphoea

In this section, using real data, the performance of the NRAR method employed to further improve the alignment between the globally registered images obtained by the NGC global registration method as presented in Chapter 3 is discussed. One of the final outcomes that is sought in this thesis is the integration between a face thermogram and the face sketch to improve the low spatial resolution of a thermal image (for the morphoea application) that causes features captured in a thermal image to be quite ambiguous. This type of image integration has been pre-

sented in Chapter 3. In this section, another outcome that is sought for the morphoea application is presented and discussed. For the purpose of diagnosis and monitoring of treatment efficacy of morphoea, an integration between a thermogram and the face sketch with the Blaschko's lines is proposed. The outcomes of this type of integration based on normal healthy subjects are shown as in Figure 4.27. As patient data for the morphoea is not accessible for this study, in this section, only results based on the normal, healthy subjects are presented. It can be seen from Figure 4.27(b) that the NRAR method has successfully improve the alignments between the globally registered images (as shown in Figure 4.27) to a good extent. The improvements can be observed especially from the alignment along the jawlines and chin. However, since the face thermograms include the hair, the top part of the face sketch could not differentiate the border that separates the hair from the forehead. Hence, the top part of the face thermogram including the hair is considered as the head as can be observed especially in Figures 4.27(b) and (d). However in Figure 4.27(c), it is shown that the NRAR method is able to move the right side of the top part of the face sketch with the Blaschko's lines downwards towards the forehead of the face thermogram.

If morphoea data is available, apart from the original thermogram, the Blaschko's lines can also be integrated with segmented thermogram patterns based on either temperature information or gray level/color property that represents abnormalities/inflammations. It is reported in [238] that pixel area with a difference of $0.5°C$ with its neigbouring pixel area indicates the area of interest (inflamed area) in morphoea. It is also reported that the morphoea lesions are considered positive to thermogram when a substantial area of more than 0.5°C warmer than the matching opposite limb or body area site was visible or when it is 0.5°C warmer than surrounding skin if bilateral sites were involved or when comparison was impossible for technical reasons [238]. The pixels that meet these criteria can be extracted to become thermal signatures for morphoea lesions. When integration between these thermal signatures and the Blaschko's lines is obtained, the correlation between them can be investigated and diagnosis and monitoring of morphoea and its treatment efficacy can be performed based on the degree of correlation. This proposed method for potential detection and monitoring of the morphoea using morphoea data is further described in Chapter 6. Using this type of integration based on a computerized system for diagnosis and monitoring of treatment efficacy of morphoea, the subjectivity in the current diagnosis system can be reduced greatly and thus may improve the system's reliability and accuracy. This is mainly because the process of identifying lesions and their borders in thermograms in the initial

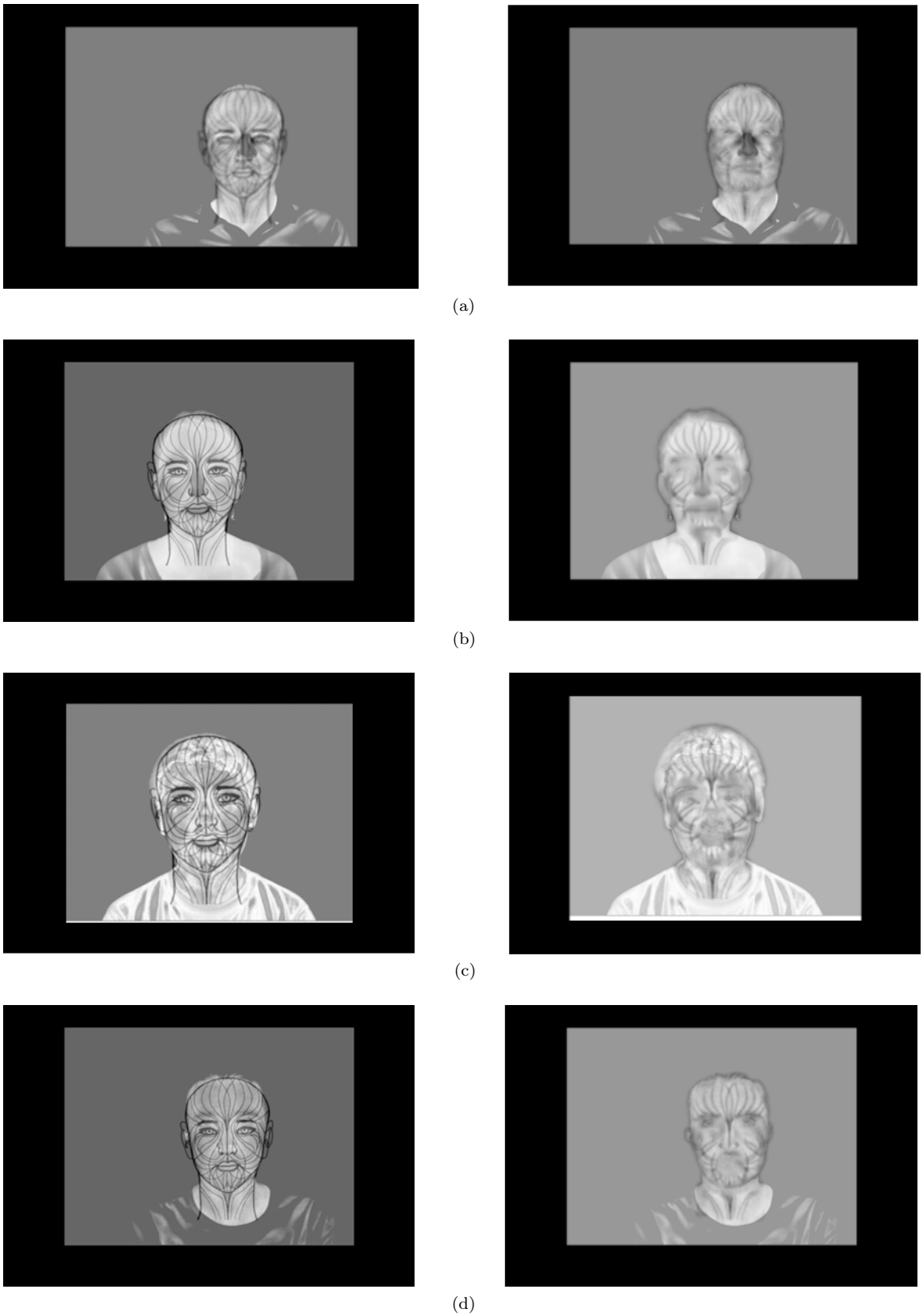


Figure 4.27: (a),(b),(c),(d) Integrations between the face sketch with Blaschko's lines and face thermograms, (Left) before NRAR and (Right) after NRAR is performed.

screening and in repeat screening by human can be removed.

4.5 Discussion and Conclusions

The NRAR method is an adaptation and modification of non-parametric elastic registration methods as proposed by Bejo et al. [213, 214] and Kovalev et al. [126], and an affine parametric based elastic registration method developed by Karamitrou et al. [113]. These elastic registration methods are specifically developed for geophysical studies/problems such as landslide monitoring and geophysical measurements. On the other hand, the proposed NRAR method in this work has shown to be useful in improving global registration result achieved by the NGC registration method for medical applications. This stochastic greedy, window based local registration method applies only small range of deformations to reduce any local displacements present between two images that already being globally registered. The process involves small local distortions being applied based on the gray edge maps of the globally registered images in order to align between their two globally registered intensity images. The edge maps are used to enable two images of different imaging modalities such as between a thermal image and a visual image to be registered by the proposed NRAR method and also to increase registration performance. Each time a transformation using edge maps is found to minimize the dissimilar criterion, DC, similar local changes are also made to the intensity image of the target image simultaneously.

The optimization algorithm used in the NRAR registration method is of the type stochastic greedy which means that the algorithm accepts only changes that can optimize the measure of similarity/dissimilarity between the two images to be registered. Since the affine deformation parameters are assigned randomly, no differential equations need to be solved for unknown deformation parameters that require complex optimization technique subjects to the degree of freedom of the parameters. This resulted in less computation complexity involved in solving for the local, varying registration problems and may lead to less computation time than using . An obvious advantage of this approach is in its simplicity in formulating and optimizing local transformations that contribute to the global elastic transformation without delimiting its ability to refine the alignment between two globally registered images.

In this chapter, investigations on the performance of the developed NRAR method using 4 pairs/cases of model images artificially designed with varying level of registration problems to be solved are presented. The first three pairs of model images used are designed with small geometrical differences and displacements between them while the last pair accommodates large

distance, non-linear deformations. In average, for all cases, it is found that the NRAR method is seen to be able to achieve fairly good registration results based on the high measure of similarity between the registered images with a CC of more than 0.9 (for both edge maps and intensity images) and with small std of below 0.1. In comparison to the FFD method using the same image pairs, the NRAR method is found to be comparable in terms of reductions of small and varied local displacements between two globally registered images. However, the proposed NRAR method is found to be more flexible than the FFD method in terms of the large distance, non-linear deformations that it could perform. This is demonstrated by its ability to adapt to different contours and shapes of objects as shown in the results obtained for the image pair of Case 4 where the FFD method has failed. Hence, it can be considered that in terms of registration between an image pair with large distance and non-linear deformations between them (between shapes and contours that are quite complex), the NRAR method is found to outperform the FFD method.

However, the registration results achieved by the method suffer from reduction of intensities among edge pixels as well as intensity leakages along the edge pixels. These effects are the result of having an intensity based interpolation method in the local deformations made by the NRAR method. Nevertheless, this limitation does not hinder the application of interest i.e., where only small displacements/distortions between images exists, as the pixels of concern in the application are the non-edge pixels which are minimally affected by the transformation. It is known that one of the limitations of a non-rigid registration is that it can affect the local topology of a deformed image in an incorrect manner. In order to avoid this, the NRAR method takes an approach to perform deformations onto edge pixels alone as not only small distortions among these pixels need to be corrected since large displacements between them are already reduced by the NGC method, but also to minimize any unwanted changes to the local topology.

Chapter 5

Thermal Analysis for Cooling Study of Cryotherapy Techniques

Cooling treatment on body areas subjected to trauma through injury or surgery can reduce swelling and bleeding, metabolic rate of injured tissue and activity pain of receptors [14, 150, 151, 193]. However, it can also cause negative effects such as disturbance of lymphatic drainage for temperature below $15°C$, disruption of the micro-circulation for temperature below $10°C$, and disruption of nerve function that could cause ischemia damage to tissues for temperature that reach below $5°C$. These negative effects can be found in cooling treatment using ice packs [17, 101]. Recent innovations in medical treatments after surgery or for injured areas using cryotherapy techniques (the use of low temperatures in medical therapy) such as water-circulating cooling mask (hilotherapy) by Hilotherm, have made it highly desirable to investigate the benefits of the mask over traditional method such as the ice packs in achieving all the positive effects of cooling treatment without the negatives [14, 17, 100, 150, 151, 193].

In order to achieve only the positive effects of cooling without the negatives, the hilotherapy cooling mask system is designed to operate by cold fluid (i.e., water) delivered at a controlled temperature (from $+10°C$ to $+30°C$) using masks to parts of the body area that are treated [94, 100]. The hilotherapy is invented to ease and simplify the process involved in a cooling treatment. Even though the system has been widely accepted in practice, there is still a lack of concrete evidence on its benefit over the ice pack. However, more and more studies have been conducted to investigate this [14, 150, 151, 193, 100]. As it is reported that maximal skin

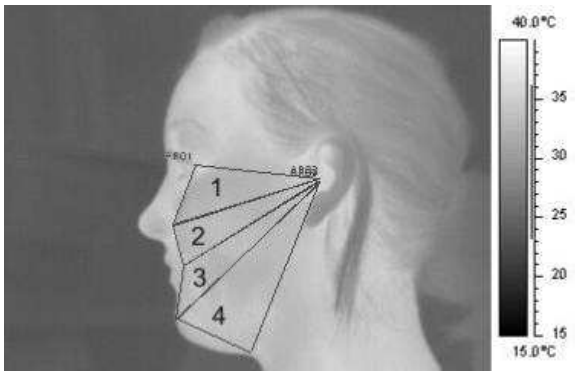


Figure 5.1: Four regions of interest for extracting temperature data from the thermograms. (Reproduced from [100].)

vasoconstriction occurs at a skin temperature of $5°C$, by regulating the mask's temperature at $15°C$, it is assumed that this will be more effective than standard cryotherapy (using cold packs) in reducing swelling and pain after facial surgery [193]. In an early study, Howard and Collier [100] investigated the hilotherapy system in comparison to the ice pack system in facial cooling of 3 healthy control subjects based on thermal imaging. In this study, the cooling efficacy of both the cooling methods was not investigated based on temperature change alone but also based on actual skin temperatures and speed of cooling achieved across the cooling area. The results obtained in the study are presented in the form of statistical information achieved at six time-points based on minimum, maximum and median temperature values measured from each of four anatomical regions of interest (ROIs) as shown in Figure 5.1. Based on this study, it is reported that the use of thermography in the evaluation of facial cooling treatment for the reduction of pain and swelling after maxillofacial surgery is found to be very promising. Their pilot data also proved that the hilotherapy cools facial skin more effectively than an ice compress.

In this chapter, the same cooling study as reported in Howell and Collier [100] is conducted but with a different approach that is based on image-processing methods and analysis. The efficacy of the hilotherapy cooling system over the conventional ice pack in facial cooling treatment based on normal subjects is investigated using a computerized thermal analysis. The analysis approach consists of image registrations and image segmentation based on the Otsu's thresholding method and a seed-based region growing technique (SRG) [57, 71]. The thermogram data used in this investigation is obtained from a collaboration study that also involves investigation on facial cooling using the hilotherapy and ice pack in healthy volunteers based on thermal imaging. This collaboration is between two medical institutions, the Royal Free Hospital and the Chelsea and Westminster Hospital, an industrial partner, and the Imperial College London.



(a) (b) (c)

Figure 5.2: Thermograms of the face of Subject 4 taken at 10 minutes during the hilotherapy cooling procedure in 3 views, (a) anterior, (b) left lateral, (c) right lateral.

5.1 Thermogram Data Acquisition for Cooling Study

The thermogram data acquired from healthy control subjects for both cooling with the hilotherapy system and ice pack are considered for the cooling study presented in this chapter as maxillofacial post-surgery thermogram data is proved difficult to be obtained for this study. Each subject avoided smoking, hot food, alcohol and caffeinated drinks for one hour prior to the investigation, and rested in the thermography laboratory for 15 minutes at a room temperature of $23°C$ prior to imaging. Thermography was performed using an A320G Thermacam imager (FLIR Systems, West Malling, UK) with an Ethernet connection to a personal computer running FLIR Thermacam Researcher software. The A320G is an uncooled focal plane array imager sensitive across the 7-14 μm waveband. The thermal imager was recently quality-assured against a black-body source traceable to the International Temperature Scale of 1990 [211]. No camera readings differed from the source temperature by more than $0.3°C$ across the range of facial skin temperature. Prior to measurement, the thermal imager was operated for one hour to ensure the microbolometer detector gave stable temperature readings. For each subject, the hilotherapy mask was applied to the face and set to cool in continuous mode at a temperature of $15°C$. Anterior, left lateral and right lateral thermograms of the face were recorded (in two formats; intensity and temperature) prior to cooling and 5, 10, 20 and 30 minutes after the commencement of the cooling procedure as shown in Figure 5.2. The mask was briefly removed from the face to allow thermograms to be captured at each measurement time-point. A further set of thermograms was recorded 5 minutes after the cooling procedure had ended. After a 30-minute restabilisation period, the cooling process was repeated in some of the subjects using the ice compress as shown in Figure 5.3.



(a) (b) (c)

Figure 5.3: Thermograms of the face of Subject 4 taken at 10 minutes during the cooling procedure by ice compress in 3 views, (a) anterior, (b) left lateral, (c) right lateral.

5.2 Image Processing Approach

Monitoring of changes throughout a cooling treatment is important in a cooling study to better understand performance of cooling techniques/treatments used. As described in the previous section, the thermogram data involves in this study consists of thermograms taken from healthy control subjects who received facial cooling treatment using the hilotherapy mask and ice pack in a duration of 30 minutes in each cooling session. The thermograms acquired in the study are represented by both the intensity and the temperature data respectively. In this image processing based cooling study, both image representations are used. The patterns of increase and decrease of values obtained from both image representations are the main subject of investigation in this cooling study. For this purpose, important statistical parameters such as median, minimum and maximum values from both the intensity and the temperature data are extracted from identified cooling area. In this section, the image processing approaches developed for the cooling study of the cryotherapy techniques is presented.

Prior to the extraction of the statistical parameters, the cooling areas or areas that are affected by the cooling procedure are identified and segmented using image processing techniques including the image registration approaches developed as presented previously. For accuracy in the measurements obtained from the identified and segmented cooling areas, image registration is thus of vital importance to first align between these images to reduce any displacements or differences (mostly due to motion) between them. This is very crucial in ensuring that further processing of the images for the identification and segmentation of the cooling area could be carried out correctly and accurately.

There are two types of analysis involved in the cooling study; intrasubject analysis (between the same subject/person) and intersubject analysis (between different subject/person). A global registration method is usually sufficient for intrasubject analysis. On the other hand, for intersubject analysis, there is a need for a local registration method to improve on the globally

registered images. However, in medical, due to the nature of soft tissues, local registration may also be needed for intrasubject analysis like in some cases found in some of the subjects involved in this study. For the registration purpose of the cooling study, the proposed NGC method (as discussed in Chapter 3) and the NRAR method (discussed in Chapter 4) are employed to assist in this longitudinal intensity and temperature study of cooling treatments. In the next section, explanations are given on how the registration methods will enable us to:

(a) propagate manually drawn mask (based on the Hilotherm mask applied) from a constructed atlas image to each subject at all time-points in order to extract statistical information from the area that coincides with the mask that involves intensity/heat changes (the manual mask approach), and

(b) match between each subject's baseline images (before cooling) and their follow-up images (during and slightly after cooling) prior to image differencing to extract areas that are affected by the cooling procedure facilitated by a seed-based region growing method (SRG) performed semi-automatically (the semi-automated mask approach).

The methodologies for these two approaches are defined and explained in the next section.

5.3 Determination of Cooling Areas (ROIs)

For the hilotherapy cooling mask system, as it is based on the use of a cooling mask as shown in Figure 5.4(b), the cooling area involved during a cooling treatment by this technique can be clearly defined by the hilotherapy mask applied. On the other hand, for cooling treatment with ice pack/compress, no clear definition of the cooling area covered by ice pack can be obtained due to the change in the shape of ice pack during cooling procedure as the ice melts away. Taking this difference into account, two types of approaches are proposed for the cooling study especially in determination of cooling areas; the manual mask approach and the semi-automated mask approach. Both the approaches involve the use of image registration methods prior to determination of cooling areas and extraction of statistical information. The two approaches are different in terms of the way the so-called cooling areas or region of interests (ROIs) are determined which are further explained in Sections 5.3.1 and 5.3.2.

5.3.1 Manual Mask Approach

The first approach is based on the cooling mask used in the hilotherapy system. Since the hilotherapy cooling system is applied by the use of mask, heat changes (i.e., cooling) on the face will mainly affect the regions under the mask for all the subjects. Hence, in this approach, a mask is manually drawn on the baseline image of Subject 1 (randomly chosen) to represent the cooling area of interest or the ROI. As shown in Figure 5.4(c), the manually drawn mask (in white) that is resembling the hilotherapy cooling mask applied as can be seen in Figure 5.4(b) is placed on the baseline image of Subject 1, taken prior to cooling (Figure 5.4(a)). The baseline image of Subject 1 and the manually drawn mask region form our atlas image (Figure 5.4(c)). The whole process of obtaining the atlas image can take about 15 to 30 minutes to complete. The atlas image is obtained to define a common coordinate system for the registrations involved in the cooling study, such as to become the baseline image for all the images in the study. A flowchart to explain the processes involved in obtaining the atlas image is shown in Figure 5.5.



(a)



(b)



(c)

Figure 5.4: (a) Baseline image of Subject 1, (b) During a hilotherapy cooling mask treatment procedure, and (c) Manually segmented mask on the baseline image of Subject 1 to form an atlas image

Once the atlas image is formed, to determine the ROIs for the follow-up images of Subject 1 in this approach, firstly the baseline image of the atlas image will be aligned to its follow-

up images based on the NGC method. Once the baseline image is aligned with a follow-up image, automatically the mask from the atlas image is also aligned to the follow-up image. This procedure is summarized in Figure 5.5. Once the mask is registered to its follow up image as shown in Figure 5.7, statistical information from the area that coincides with the mask can be extracted.

However in determination of ROIs for follow-up images of other subjects, registration between the baseline image of Subject 1 and the baseline image of other subjects is first performed. Once the mask of the atlas image of Subject 1 is aligned to the baseline image of other subjects, image registration is then performed between the other subjects's baseline image and their follow-up images in order to register the mask onto their follow-up images for determination of ROIs. This is done in this way to avoid from having to manually draw a mask on each follow up image or each of the baseline image. This approach also minimizes the computation time needed for the determination of ROIs in other subjects as registration between sequences of thermograms of the same subject (intrastudy) may only be performed based on the NGC method alone if found sufficient. Thus, the need of using the local registration based on the NRAR method can be reduced to save time. A flowchart describing the processes involved to obtain a new atlas image for a different subject based on the atlas image of Subject 1 is shown in Figure 5.6. This also means that each subject in this study will have their own atlas image constructed from the baseline image of each subject with a globally and (or) locally registered mask from the atlas image of Subject 1. This process mostly involves both the global (NGC) and the local registration method (NRAR) as the registration is between two different subjects. A local registration method based on the NRAR will only be performed when the NGC method alone is unable to achieve a sufficiently good registration. Currently, this decision is made manually. Another example of the mask from the atlas image after being globally and locally registered to a new baseline image (of different subject) to form a new atlas image is shown in Figure 5.8. The same deformation field that registered the baseline image of the initial atlas image (of Subject 1) to the baseline image of the different subject is also used to register the mask to the baseline image of the different subject to form a new atlas image for that subject. Once a new atlas image for a different subject is obtained, the cooling analysis for that subject can be carried out based on mostly the NGC method alone. In this way, computation time can be reduced further by avoiding the need of using the NRAR method for cooling study based on intrasubject. Then extraction of statistical information can be carried out from the determined cooling area (i.e., area that is covered by the mask).

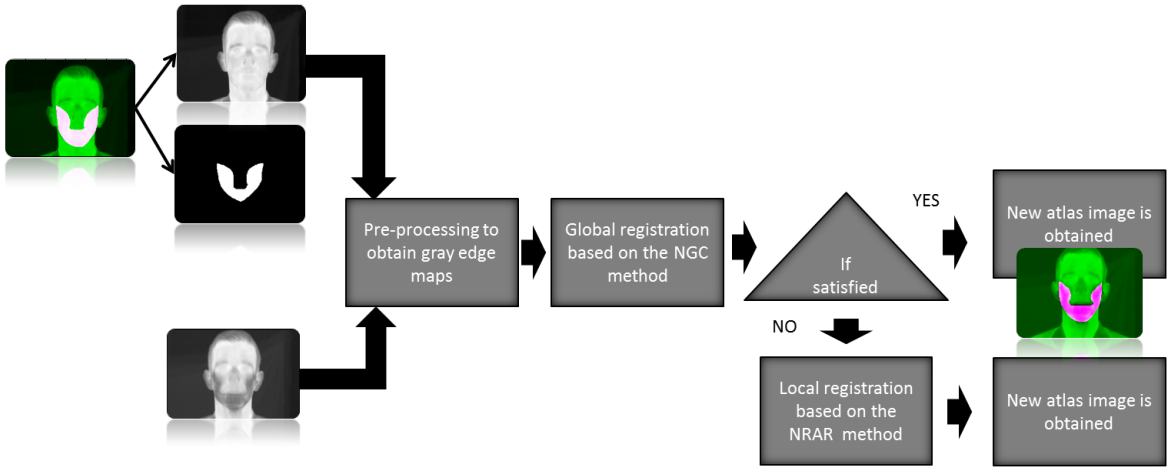


Figure 5.5: An example of intrasubject (same subject) analysis in the manual mask approach

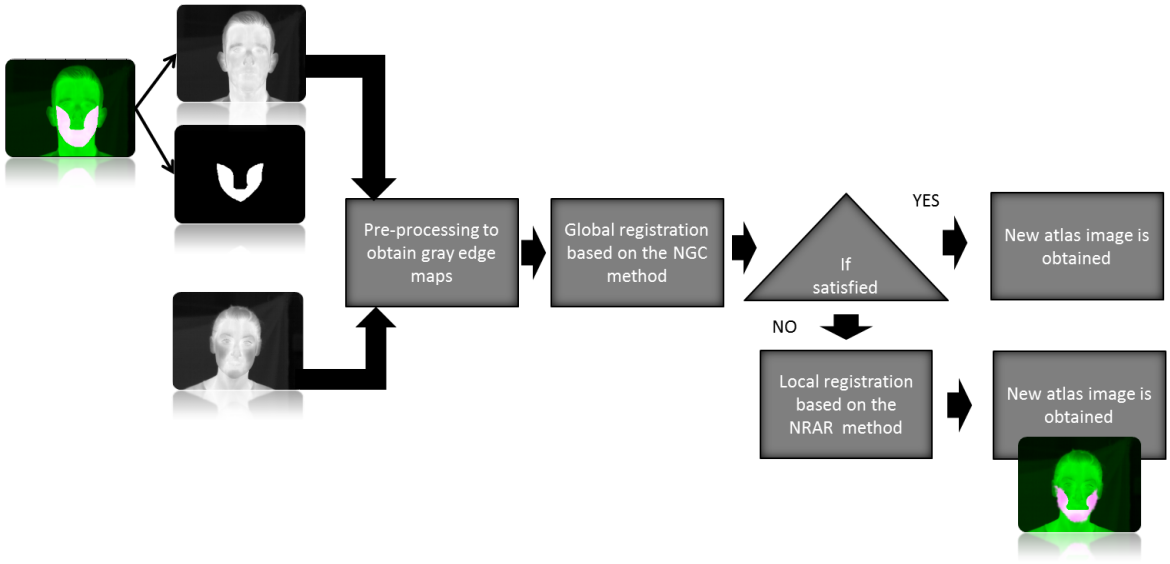
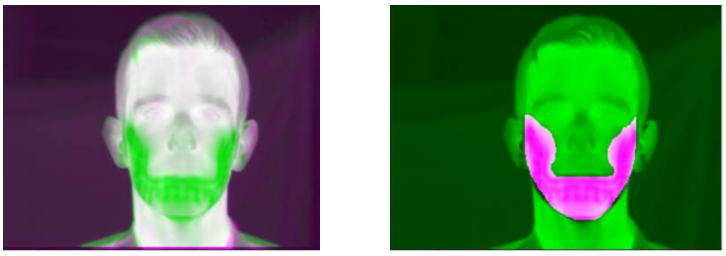
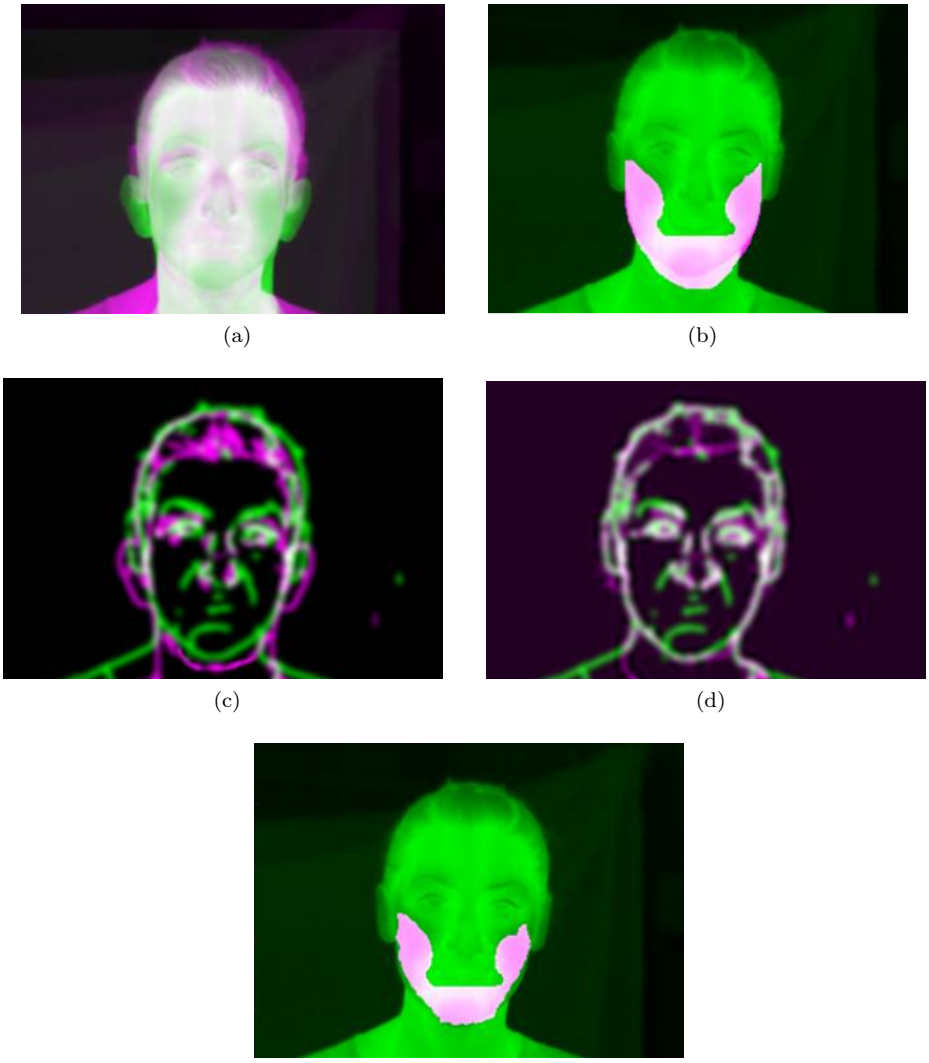


Figure 5.6: A flowchart of the processes involved in the construction of a new atlas image for other subject (intersubject).



(a) (b)

Figure 5.7: Manual mask approach (for same subject (Subject 1)); (a) overlay result between globally registered atlas image and a follow-up image, (b) globally registered mask overlaid on the follow-up image.



(a) (b) (c) (d) (e)

Figure 5.8: An example of obtaining a new atlas image for a different subject based on the atlas image of Subject 1 using the manual mask approach (between different subjects);(a) Overlay result between reference image (image to be analyzed) and target image (baseline image) after the NGC is performed and (b) overlay result between the reference image and the globally registered mask; In gray edge maps, (c) overlay result after the NGC method is performed, (d) overlay result after the NRAR method is performed to the globally registered target image; (e) Overlay result between the target image and a globally and locally registered mask to form a new atlas image for the new subject.

5.3.2 Semi-Automated Mask Approach

In our second approach, a mask is not predefined prior to identification and segmentation of cooling area. In this approach, the cooling area or ROIs will be identified and selected based on the area where changes in intensity are present by utilizing the intensity data. The procedure for this approach is explained in the diagram given in Figure 5.9 and can be explained as follows.

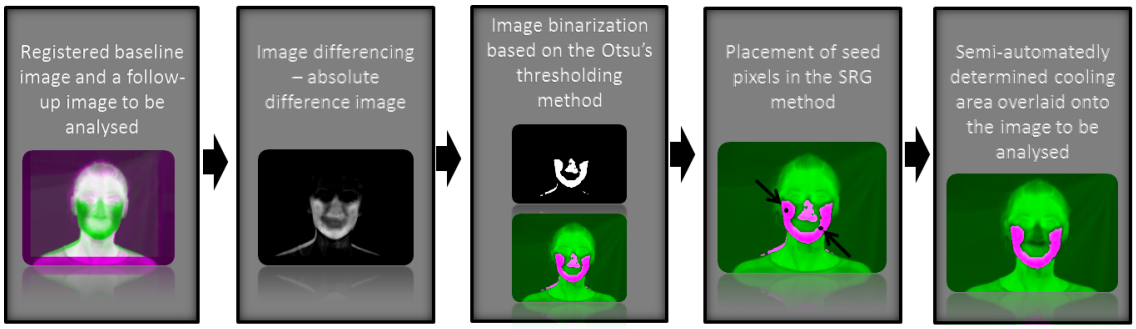


Figure 5.9: A flowchart of the processes involved in the semi-automated mask approach.

1. Firstly, the NGC global registration is performed to reduce large displacements between a baseline image (image taken before cooling procedure is performed) and a follow-up image (image taken during the cooling procedure) based on their gray edge maps.

2. Next, if some small displacements are still present between the globally registered images, using the NRAR method, local registration is performed between the globally registered images to improve the alignment between them based on the globally registered gray edge maps. The same accepted deformations are also applied onto the intensity image of the target image simultaneously. The baseline image is considered as the target image.

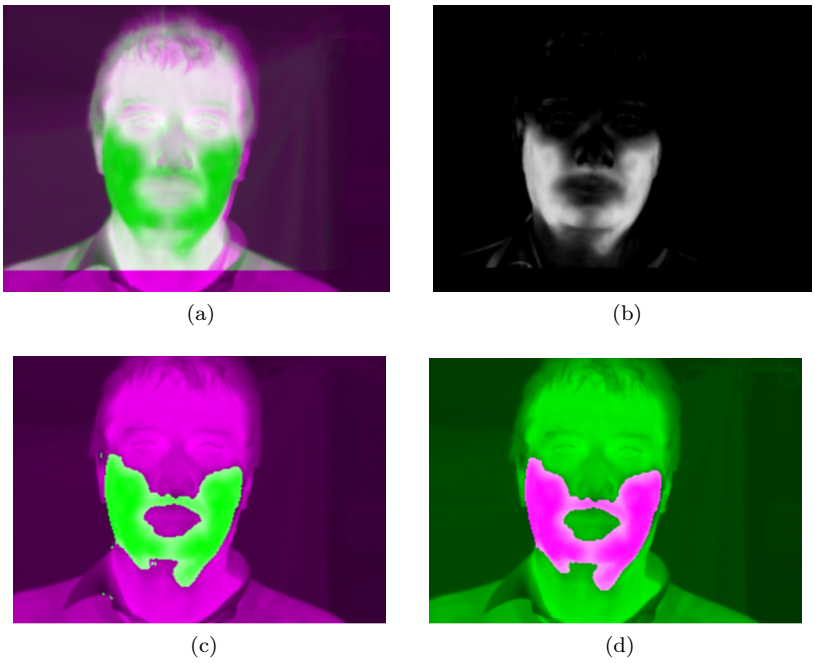
3. Once the two images are in good registration, the absolute difference between the registered baseline image and the reference image is obtained (as shown in Figure 5.10(a)) in order to identify the areas where intensity changes are present. The areas that were covered by the hilotherapy mask usually will be distinguished from its surrounding area in the absolute difference image due to the presence of changes in intensity as the temperature changes. However there are some small artifacts that are highlighted as well in the resultant image that may originate from small parts of the subjects such as the ear or hair due to some very small local displacements between the images that are still present.

4. In order to minimize these unwanted areas, a binarization/thresholding is performed onto the difference image based on the Otsu's intensity thresholding method to identify and extract the desired cooling areas (Figure 5.10(c)).

5. Finally, a post processing is performed based on the SRG method. This is found necessary as in some cases, unwanted areas as explained earlier can also be extracted in the binarized image as shown in Figures 5.10(c) and 5.11. These failures mostly occurred with images taken at 5 minutes after the cooling procedure has ended (i.e., minute 35). This is because for the image taken at this time-point, as the temperature started to rise, the difference in intensity between this image and the baseline image is getting smaller and less variations of intensity distribution in the cooling area are present as compared to the other follow-up images. Hence the SRG is employed to identify and select the correct cooling areas obtained from step 4 above to ensure that no unwanted areas are included in the area to be analyzed (semi-automated mask) (Figure 5.11).

Howell et al. [100] also reported the same findings for the images taken at minute 35 where the thermograms suffered from having small variations in the region affected by the mask and the surrounding region due to the underlying metabolic process. The same scenario can also be observed from cooling analysis with ice pack due to presence of small/little changes/variation in the intensity/temperature between the regions affected by the ice pack and the surrounding region (see Figure 5.12(c)). Figure 5.12 shows comparisons between ROIs determined by the manual mask approach and the semi-automated mask approach for the hilotherapy and the ice pack data.

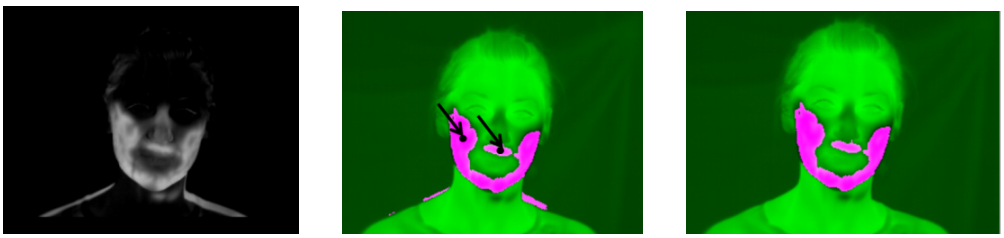
Once the ROIs are obtained, the statistical parameters (i.e., median, mean, minimum and maximum) are extracted from both the temperature and the intensity data based on the ROIs for all time-points for each subject. The cooling patterns established by these parameters are known in this chapter as change of actual intensity for intensity data and change of actual temperature for temperature data. The statistical parameters are also extracted from absolute difference images (as described in Section 5.3.2.2) to give cooling patterns that are based on absolute temperature and intensity changes. The cooling patterns established by these parameters are known in this chapter as absolute intensity change for intensity data and absolute temperature change for temperature data.



(a) (b)

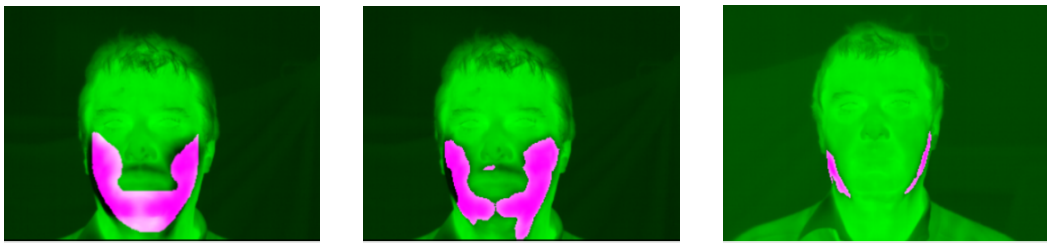
(c) (d)

Figure 5.10: Example of results obtained after image differencing and SRG are performed in the semi-automated mask approach;(a) Registration result between the baseline image of the subject and its follow-up image after 30 minutes of cooling treatment. (b) The resulting difference image between the two globally registered images. (c) Semi-automatically determined cooling areas before SRG is performed. Some unwanted regions can be seen as well. (d) Result after SRG is performed to give true ROI for cooling study.



(a) (b) (c)

Figure 5.11: Applying the SRG in selection of true cooling areas/ROIs in the semi-automated mask approach; (a) an absolute difference image, (b) the extracted ROIs obtained by thresholding of image (a). The arrows show the seed pixel placements for the SRG to select true ROIs from the extracted ROIs, and (c) the selected true ROIs overlayed onto the image to be analyzed (a follow-up image).



(a) (b) (c)

Figure 5.12: Cooling areas/ROIs determined based on (a) the manual mask approach and (b) the semi-automated mask approach for cooling with Hilotherm and (c) for cooling with the ice pack.

5.3.2.1 Seed-Based Region Growing (SRG)

Region growing technique is a well-known technique to extract foregrounds from a noisy background effectively [57, 71]. In a seed-based region growing technique (SRG), the initial seed-pixels (size of 1 pixel by 1 pixel each) are chosen manually among neighbouring pixels of the region to be extracted. In the SRG process as defined in eq. 5.1, if the difference in intensity between a seed-pixel, $S_{(x,y)}$ and the neigbouring pixels, $I_{(x,y)}$ is smaller than a tolerance value, T_{val} at a particular point, the seed pixel is considered to be intensity homogeneous to the region of interest and is part of the region. Otherwise, it is considered part of the surrounding region. The process continues recursively until all pixels have been considered. The resultant image consists of the seed-grown region and the surrounding region.

$$|S_{x,y} - I_{x,y}| \leq T_{val} \tag{5.1}$$

The SRG method is not a fully automated method. However, the SRG method can ensure that only true ROIs are selected for further processing. This method is applied by manually placing one or more seed pixels on each true ROIs in the binarized/thresholded image. In this work, a tolerance value of 0.1 is used for the SRG in the determination of cooling areas in this study. This value is found by experimenting with tolerance values less than 0.4. The value 0.1 is found to be the best value that fits the requirements to include as much the region of interest as possible without expanding or growing unwanted regions. An example of the seed placements in SRG and its resultant image are shown in Figure 5.11.

5.3.2.2 Image Differencing

Apart from analysis based on actual intensity or temperature, analysis based on their change (value of difference) across the cooling area is also explored. The change can be obtained by image differencing. Image differencing is performed by subtracting an image from another image on a pixel-by-pixel basis, to generate a third image composed of the numerical differences between the pair of images (Figure 5.10(a)) [71]. In this work, numerical absolute difference is computed. For this purpose, a difference image, z, is obtained by taking the absolute difference between a baseline image, x', that is already registered to its follow-up image, y. This will produce an image that is constructed based on temperature/intensity change/drop defined as

$$z = \mid x' - y \mid \tag{5.2}$$

5.4 Results and Analysis

Thermogram data from 12 normal subjects are analyzed for the cooling study based on the hilotherapy system and 10 subjects for the ice pack. The data of each subject consists of face thermograms that are taken at six time-points (prior to cooling, 5, 10, 20, 30 and 5 minutes after cessation of cooling procedure) in multiple views; anterior (front), left lateral and right lateral views. Therefore, a total of 216 thermograms of face are analyzed for the cooling study based on the hilotherapy system alone. For data acquisition of cooling with the ice pack, a 30-minute restabilisation period between cooling with hilotherapy and cooling with the ice pack is involved. Results of the cooling studies are presented in cooling patterns (actual intensity and temperature analysis, and absolute intensity and temperature change analysis) obtained by our image processing based approaches as explained previously. Based on these results, comparison studies are performed between

1. the two cooling analysis approaches used; the manual mask approach and the semi-automated mask approach,
2. the two types of cooling treatments; the hilotheraphy cooling mask system and ice pack,
3. the multiple view data; anterior, left lateral and right lateral views,
4. the chosen cooling analysis approach and a clinical assessment.

The following sections on result and analysis are organized based on this order. Section 5.4.1 presents the anterior view analysis that discusses the results obtained based on comparisons between the two cooling analysis approaches developed (the manual mask approach and the semi-automated mask approach) and between the hilotherapy system and the ice pack. Section 5.4.2 presents the left lateral view analysis that discusses the cooling study results based on the left view data of the 12 subjects. Section 5.4.3 presents the right lateral view analysis that discusses the cooling study results based on the right lateral view data of the 12 subjects. Section 5.4.4 discusses the comparisons between the cooling study results obtained for all the multiple view data and finally, Section 5.4.5 that discusses the comparisons between the results obtained by the proposed cooling analysis approach and a clinical assessment.

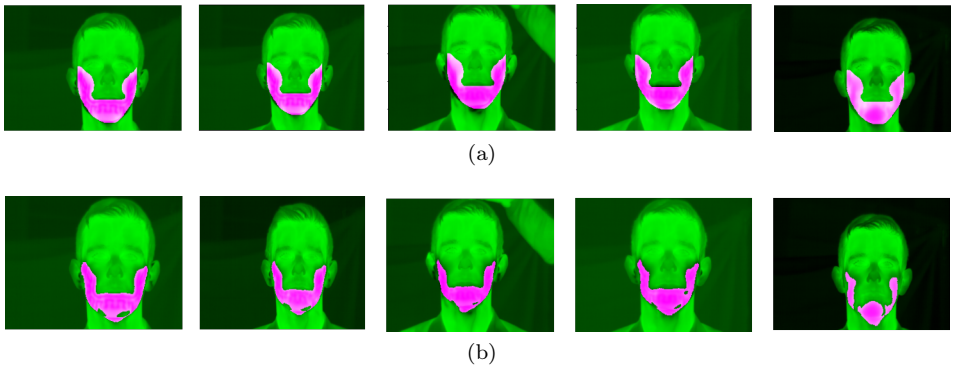
5.4.1 Anterior View based Cooling Study

Based on the anterior view data, the cooling studies for both the hilotherapy system and the ice pack are compared and presented in this section. The comparisons between both the cooling analysis approaches used in this study are also discussed.

5.4.1.1 The Hilotherapy System

For the cooling study using hilotherapy system based on the anterior view data, the cooling patterns obtained are presented based on the first 4 subjects followed by the other 8 subjects and finally for all the 12 normal and healthy subjects. The term cooling pattern used here represents the increase and decrease of intensity and temperature values/change during a cooling procedure. This is deliberately done in this way to investigate whether the size of data considered in each cooling study conducted has any influence in the cooling patterns achieved. If the same cooling pattern or behaviour of cooling of a small number of subject can be achieved when the number of subject is increased, it can be inferred that the cooling treatment performed is reliable, repeatable and effective to be used for after surgery cooling treatment. Furthermore, more importantly, this can also demonstrate the reliability and repeatability of the image processing based approach in the determination of cooling area and cooling patterns for the cooling study. Figures 5.13(a) and (b) present the cooling areas determined by the manual mask approach and the semi-automated mask approach respectively for the anterior view analysis.

Figures 5.14 - 5.16 display results of the cooling studies for the first 4 subjects based on the the



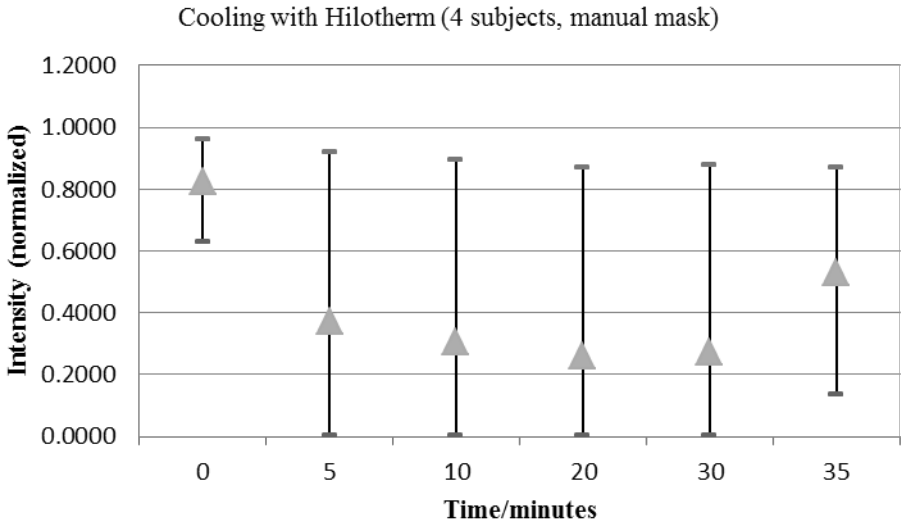
(a)

(b)

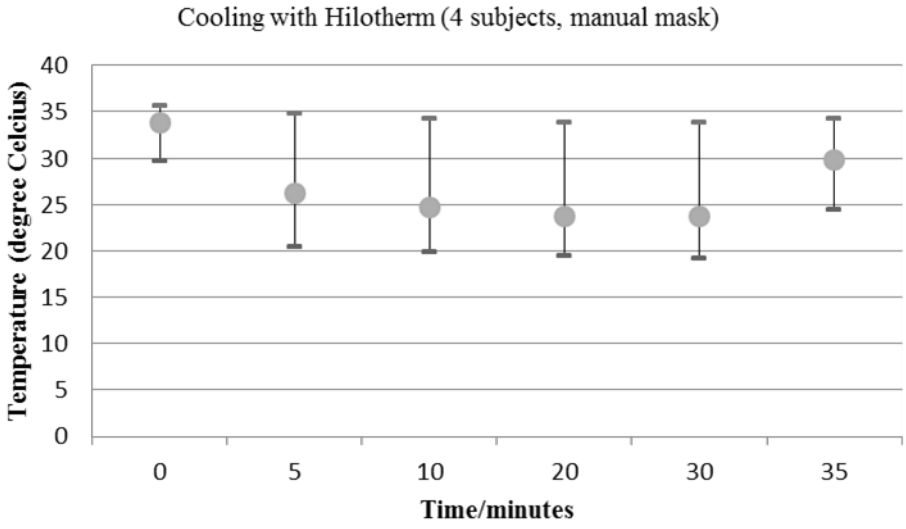
Figure 5.13: Resultant image overlays for follow-up images (at minutes 5, 10, 20, 30 and 35) of Subject 1 for hilotherapy mask. (a) Overlays between each follow-up image and its determined cooling area obtained using the manual mask approach; (b) Overlays between each follow-up image and its determined cooling area obtained using the semi-automated mask approach

two cooling analysis approaches; the manual mask approach and the semi-automated mask approach. The cooling patterns obtained from both the approaches are plotted based on the average values at each time-points computed for median, minimum and maximum intensity/temperature extracted from the determined cooling areas. For the intensity based analysis, the cooling patterns achieved by the manual mask approach is shown in Figure 5.14(a) while the cooling patterns achieved by the semi-auto mask approach is shown in Figure 5.15(a). For the temperature based analysis, the cooling patterns achieved by the manual mask approach is shown in Figure 5.14(b) while the cooling patterns achieved by the semi-auto mask approach is shown in Figure 5.15(b). The change of actual temperature as depicted in Figures 5.14(b) and 5.15(b) conforms with the results reported by Howard et al. [100] in which the average lowest median skin temperature was recorded after 20 minutes of cooling. Howard et al. reported that this cooling pattern is observed for 3 out of 4 ROIs used for the cooling studies conducted [100]. For the manual mask approach, the lowest average median skin temperature recorded was $24.24°C$. It is also found that at the same time-point, the average lowest median gray value of 0.15 was also recorded. However, much lower average values for the median skin temperature and median gray value were recorded after 20 minutes of cooling by the semi-automated mask approach; $\sim 20.21°C$ and a gray value of ~ 0.1037.

On the other hand, Figures 5.16(a) and 5.16(b) show the cooling patterns plotted based on average values of statistical parameters extracted from absolute difference images (as explained in Section 5.3.2.2). The ROIs used for this analysis are obtained by the semi-automated mask approach. It can be observed that the cooling patterns obtained based on the absolute difference values that represent absolute temperature or intensity change/drop, are exact inverse of the

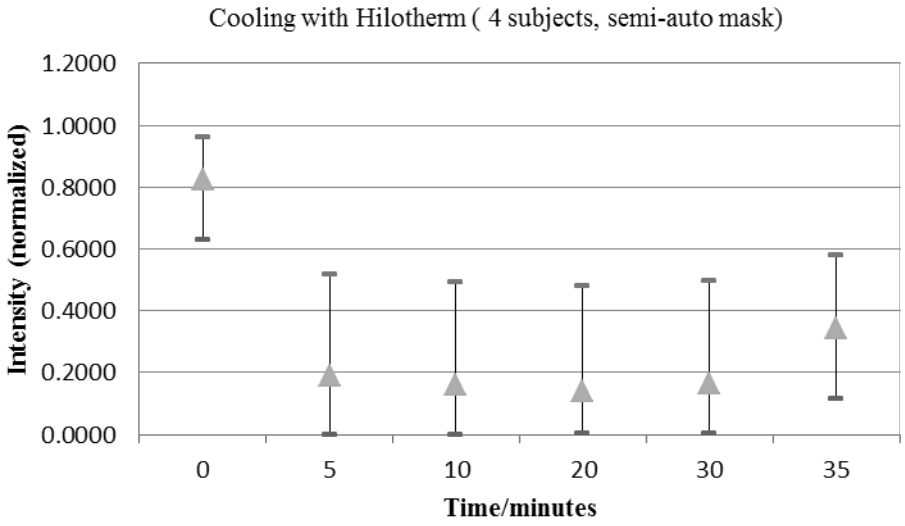


(a)

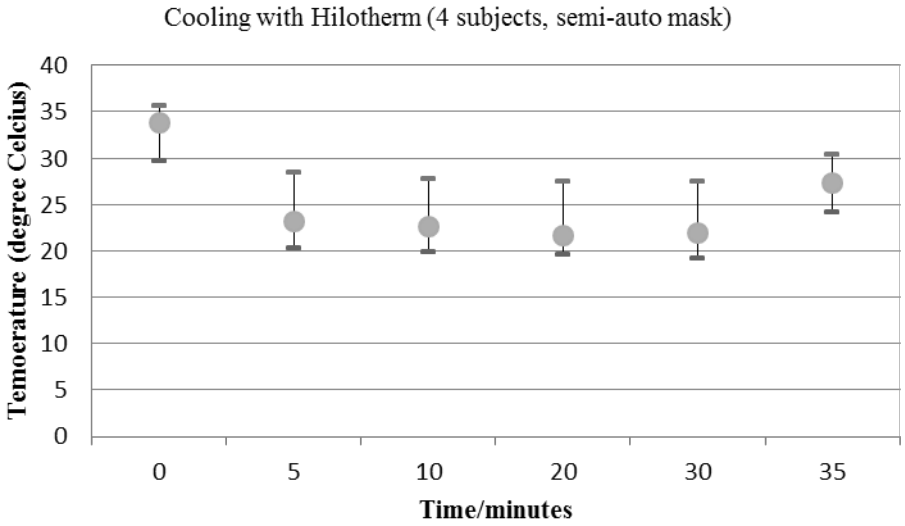


(b)

Figure 5.14: Cooling patterns achieved by the manual mask approach for the first 4 subjects who underwent cooling with hilotherm, based on the change of (a) actual intensity and (b) actual temperature during the cooling procedure.

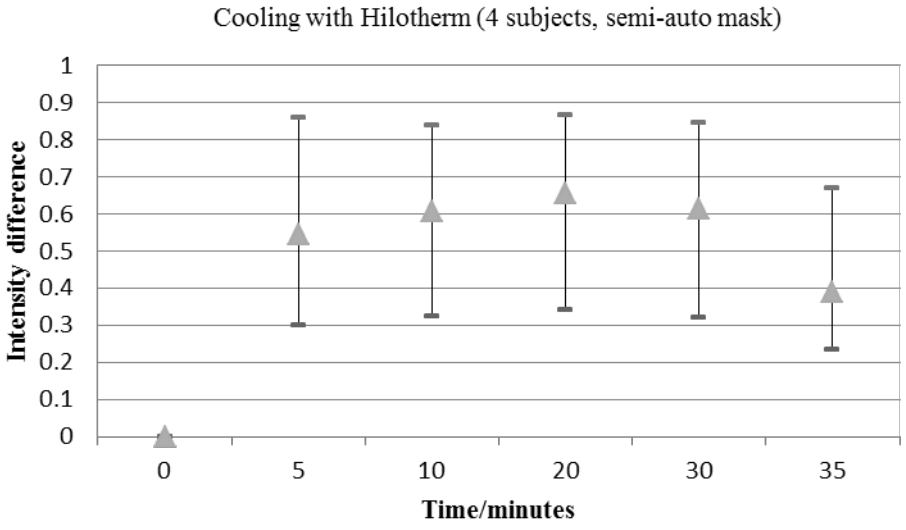


(a)

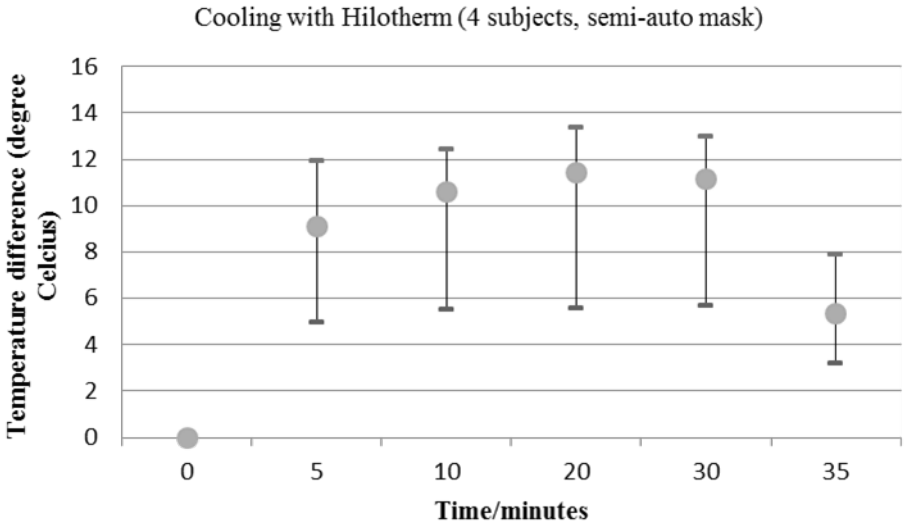


(b)

Figure 5.15: Cooling patterns achieved by the semi-automated mask approach for the first 4 subjects who underwent cooling with hilotherm, based on the change of actual (a) actual intensity and (b) temperature values.



(a)



(b)

Figure 5.16: Absolute change analysis; cooling patterns achieved by the semi-automated mask for the first 4 subjects who underwent cooling with hilotherm, based on the absolute (a) intensity and (b) temperature changes.

cooling patterns achieved based on the change of actual temperature or actual intensity throughout the cooling procedure. It can also be observed that the absolute intensity and temperature changes between the baseline image of each subject with their follow-up images increases until 20 minutes of cooling and started to decrease a little at 30 minutes of cooling and furthermore at 5 minutes after cessation of cooling. Hence, the largest intensity and temperature change are recorded at 20 minutes after cooling has commenced and starts to decrease after that in these cooling patterns. These demonstrate that the cooling patterns achieved based on the absolute intensity/temperature change by the semi-automated method agrees with the cooling pattern achieved based on the changes of intensity/temperature throughout a cooling procedure. As compared to the value at baseline ($t = 0$), in average, the largest median value of the absolute change recorded for the 4 subjects is found to be $11.5°C$ in temperature and 0.65 in intensity.

Nevertheless, even though the cooling patterns obtained by the temperature data and the intensity data for the 4 subjects are similar, it can be observed that by using the temperature data, the average range of value for each statistical parameter (i.e., minimum, median and maximum) at each time-points is smaller than that of the intensity data. This may demonstrate that the cooling analysis achieved by the temperature data is more accurate and sensitive compared to that by the intensity data. However, the intensity data is still very essential in the cooling study as it carries a certain weight especially in providing the information needed in order to obtain semi-automatically extracted mask based on the region where changes of intensity are present.

A lower range of temperature (or intensity) indicates a better cooling effect obtained in a cooling study. Using the cooling patterns plotted in Figures 5.14 and 5.15, the results obtained by both the cooling analysis approaches (the manual mask approach and the semi-automated mask approach) in regards to the parameter values achieved based on the temperature and intensity data are compared. For example, in the analysis based on the intensity data, in average, lower range of actual intensity values especially for the maximum parameter (from minute 5 to minute 35) are able to be extracted by the semi-automated mask approach (around $0.48 - 0.6$), compared to that extracted by the manual mask approach (around $0.86 - 0.92$). The same findings are also observed for the analysis based on the temperature data where the semi-automated mask approach achieved yet another lower range of values in average for its maximum actual temperature values captured (around $27°C$ – $31°C$) compared to that captured by the manual mask approach (around $33°C$ - $35°C$). Another two graphs are also plotted to clearly describe the findings above by alternatively comparing the average median values obtained for both approaches for the intensity data (Figure 5.17(a)) and the temperature data (Figure 5.17(b)). From the observations

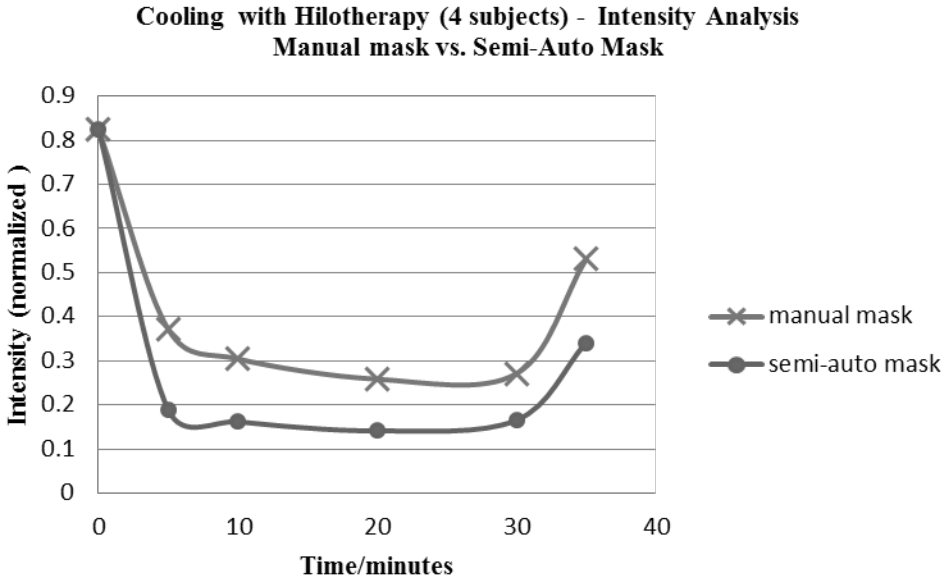
on the cooling studies conducted for the first 4 subjects as discussed above, the semi-automated mask approach is found to be able to produce more reliable results as the changes in actual intensity and actual temperature values captured by the approach are found to be lower and hence more sensitive to that of the manual mask approach. This is due to the more accurate and concentrated ROIs obtained by the semi-automated mask approach. Hence, for the remaining cooling studies for the other 8 subjects and for all the 12 subjects using the anterior data, the semi-automated mask approach alone is investigated.

In the cooling study for 8 subjects conducted based on the semi-automated mask approach, using the temperature data, the lowest median temperature was also achieved at 20 minutes after cooling with an average temperature of $21.59°C$. This is however not the case for the intensity data where the lowest average median intensity was recorded at 30 minutes after cooling (Figure 5.18). However, it can be observed that the difference between the average median intensities obtained at minute 30 and minute 20 for the intensity data is very small; only ~ 0.01.

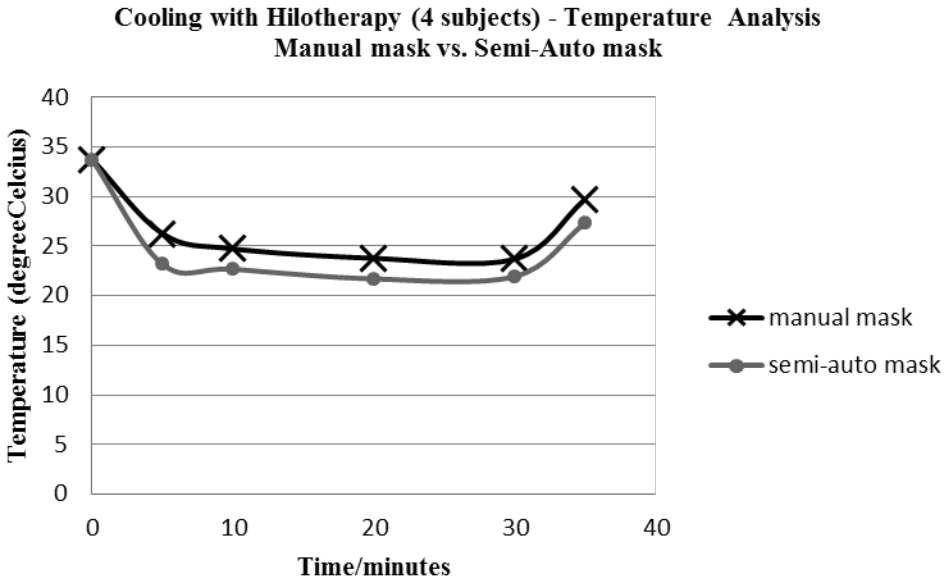
Similarly, based on the absolute change analysis, in average, the largest median value recorded for the 8 subjects is $\sim 11.23°C$ at minute 20 for the temperature data and 0.65 at minute 30 for the intensity data. It is shown from the cooling patterns based on the 8 subjects in Figure 5.19 that the temperature data yet again present a more consistent and desired pattern of cooling (as obtained in [100]) even with larger number of data.

Next, the results obtained by the semi-automated mask approach for both the 4 subjects and the 8 subjects are combined and the cooling patterns obtained for the total 12 subjects based on the average values of each statistical parameters are shown in Figure 5.20. In average, the lowest median of actual temperature value recorded was $20.33°C$ and the lowest median of actual intensity value recorded was 0.14. Both values are recorded at 20 minutes after cooling. On the other hand, for the absolute change analysis, as can be observed in Figure 5.21, in average, the largest median value recorded for the 12 subjects was $10.20°C$ at minute 20, and 0.58 (absolute intensity change) at minute 30. However, the difference between the absolute intensity change achieved at minute 30 and minute 20 is very small.

As predicted, it can be seen that the values in the cooling patterns are gradually becoming smaller/better with the increase number of data. It can also be observed that the cooling behaviour obtained for all the 12 subjects is similar to the one obtained for the first 4 subjects (for both intensity and temperature data) and for the 8 subjects (for only temperature data).



(a)



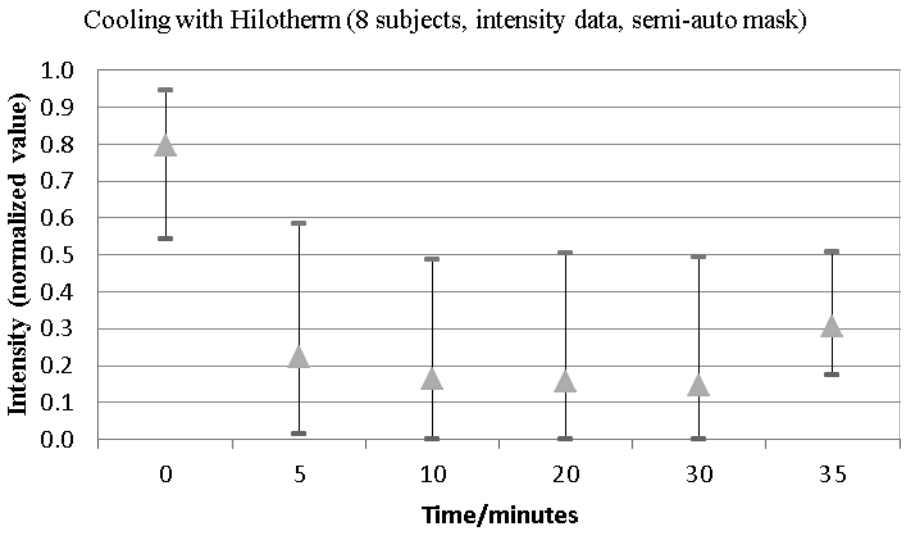
(b)

Figure 5.17: Comparisons between the cooling patterns obtained for cooling with the hilotherapy by the manual mask approach and the semi-automated mask approach for 4 subjects based on both the change of actual (a) intensity and (b) temperature values.

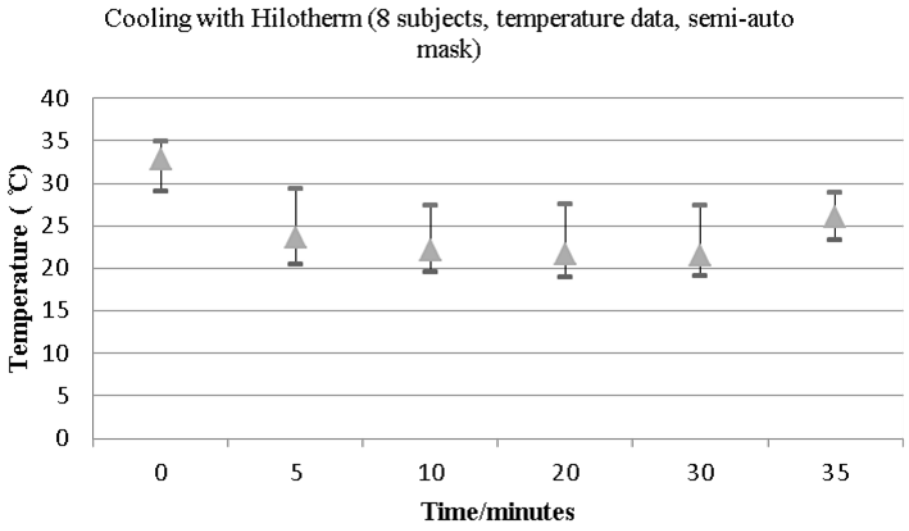
Since the desired cooling patterns achieved for the 4 subjects and 8 subjects (temperature data only) can be reproduced when the number of data is increased to 12, it can be inferred that the hilotherapy cooling system is a reliable and reproducible cooling therapy system and the use of the semi-automated mask approach for the cooling study analysis is also as reliable and reproducible.

5.4.1.2 Cooling with the Ice Pack

Two of the subjects from the first 4 subjects also underwent cooling with the ice pack. The analysis for cooling with the ice pack for the two subjects alone is firstly discussed in this section. Only the semi-automated mask approach is investigated for the cooling study of the ice pack cooling treatment as in the anterior view analysis of hilotherapy cooling data discussed previously, it is shown that this approach gives lower range of values for all the parameters that may indicate better accuracy and sensitivity to changes than the manual mask approach. The cooling areas determined by the semi-automated mask approach for the first two subjects are presented in Figure 5.22 while the cooling patterns are shown in Figure 5.23. As can be observed in Figures 5.23(a) and 5.23(b), based on the actual value analysis, the lowest average value for both the median intensity (0.28) and the median temperature ($\sim 25^{\circ}C$) was recorded in the first 5 minutes of the cooling procedure before they started to rise. However, based on the absolute change analysis, in average, the largest median value was recorded at minute 20 for both intensity and temperature data; ~ 0.2 in absolute intensity change and $\sim 4.4^{\circ}C$ in absolute temperature change respectively which are very small compared to that achieved by the hilotherapy system for 12 subjects (0.58 for absolute intensity change and $10.15^{\circ}C$ for absolute temperature change). This indicates that the cooling with ice pack is only able to give small reduction in temperature unlike the hilotherapy cooling system. For the cooling study with ice pack, the cooling patterns obtained using the change of actual intensity and actual temperature values are also found to be not in keeping with the desired cooling patterns as achieved by the cooling patterns obtained using the absolute intensity and temperature change. Furthermore, the time-points for the best cooling achieved in the analysis based on the change of actual intensity and temperature values (recorded at minute 5) and the best cooling achieved by the absolute intensity and temperature change (recorded at minute 20) are not correlated to each other. This finding can be observed in Figures 5.23(c) and 5.23(d). However, the behaviour of cooling with ice pack based on absolute change of temperature/intensity analysis where the best cooling is recorded at minute 20 is similar to the desired cooling pattern. This may indicate that the analysis based on the absolute

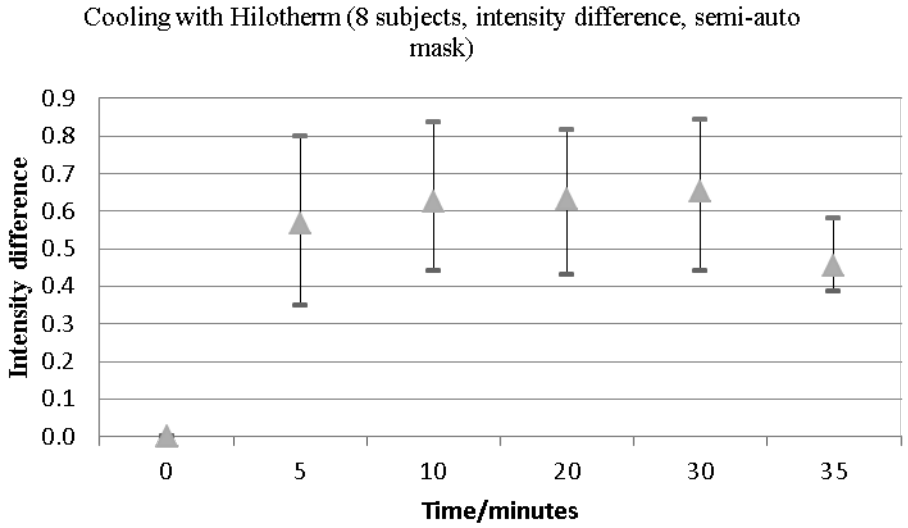


(a)

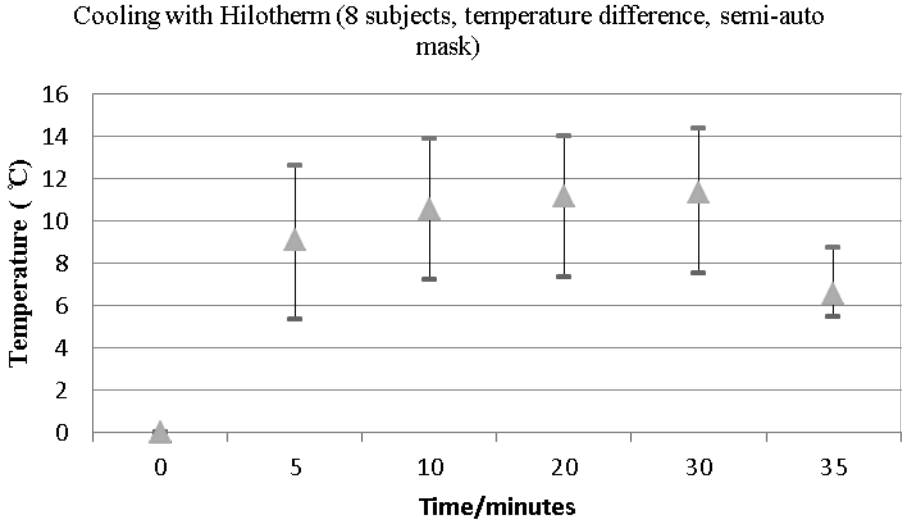


(b)

Figure 5.18: Cooling patterns achieved by the semi-automated mask approach for 8 subjects for cooling with the hilotherapy based on the change of actual (a) intensity and (b) temperature values.

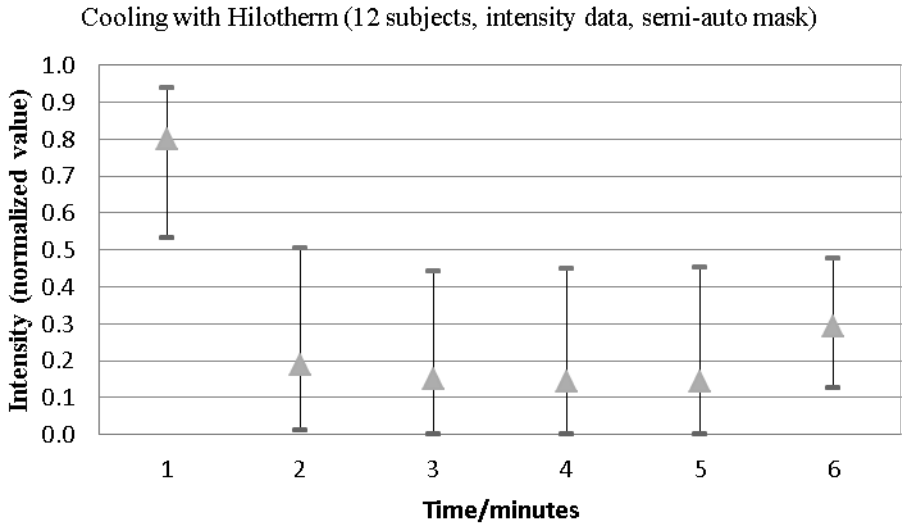


(a)

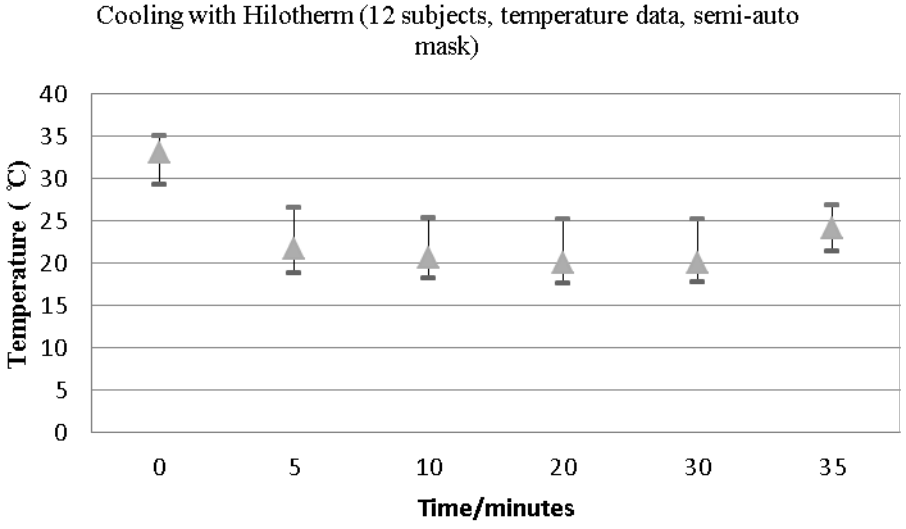


(b)

Figure 5.19: Absolute change analysis; cooling patterns achieved by the semi-automated mask for 8 subjects who underwent cooling with the hilotherapy, based on the absolute (a) intensity and (b) temperature changes.

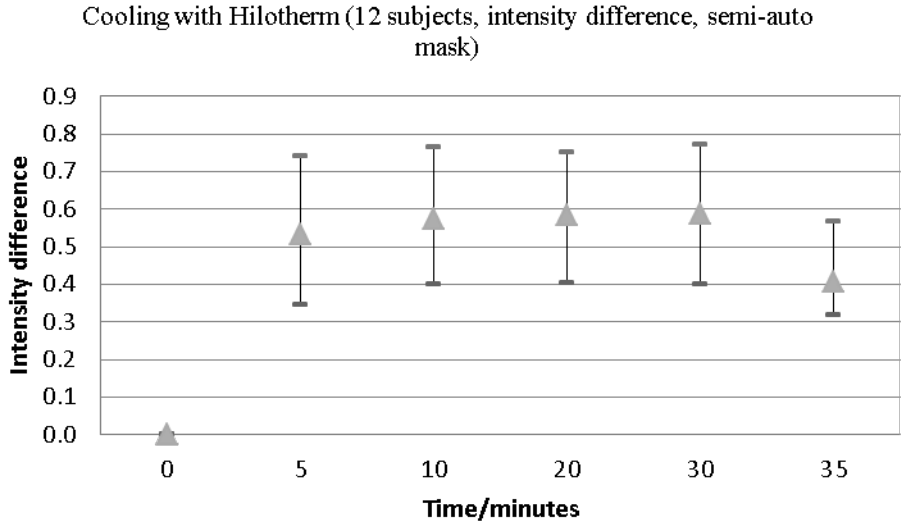


(a)

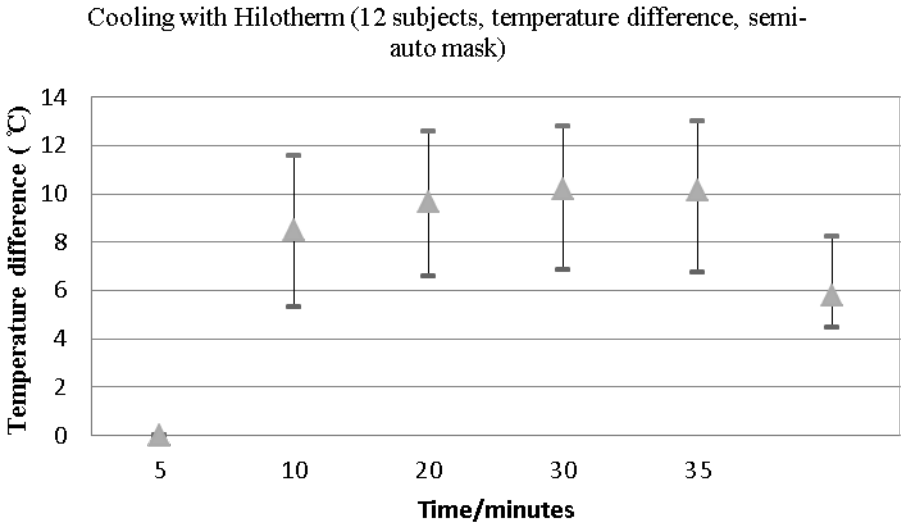


(b)

Figure 5.20: Cooling patterns achieved by the semi-automated mask approach for 12 subjects for cooling with the hilotherapy, based on the change of actual (a) intensity and (b) temperature values.



(a)



(b)

Figure 5.21: Absolute change analysis; cooling patterns achieved by the semi-automated mask approach for 12 subjects who underwent cooling with the hilotherapy, based on the absolute (a) intensity and (b) temperature changes.



Figure 5.22: Resultant image overlays for follow-up images (at minutes 5, 10, 20, 30 and 35) of the anterior view data of Subject 3 for the ice pack cooling study; (Left to right) The determined cooling areas obtained using the semi-automated mask approach for each of the follow-up image.

change is more reliable for the cooling study with ice pack than using the actual intensity and temperature values.

The inconsistencies of the results obtained for the cooling study with ice pack may be due to the small area of cooling achieved by the ice pack during the whole cooling period. This can be observed by the non-even distribution of cooling effects that resulted in small area being cooled that leads to small cooling area being identified as shown in Figures 5.12(c) and 5.22.

Now, let us look at the analysis performed with more data for cooling with ice pack as presented in Figures 5.24 using 10 normal subjects that includes the two subjects analyzed previously. Figure 5.24 presents the cooling patterns obtained from both intensity and temperature data. With more data, it can still be observed that the largest drop of temperature and intensity is recorded at 5 minutes after cooling based on the average median value. It can also be observed that the average median values obtained at 5, 10, 20 and 30 minutes of cooling are not so far apart for both the temperature data and the intensity data. Again, in contrast to the cooling patterns based on the change of actual intensity and temperature values, the cooling patterns based on the absolute intensity and temperature changes achieved the desired cooling pattern where the largest change of temperature is observed at 20 minutes after cooling (see Figures 5.24(a) and 5.24(b)). Since the same findings can be observed with a larger size of data for the absolute change analysis, this may imply that the cooling study based on the absolute change is more suitable for the cooling study with the ice pack due to the small and uneven cooling area achieved by this cooling method. It is also found that the ranges of values obtained for the cooling with ice pack suffered from large deviations from the median values except for the ones obtained based on the temperature data (Figures 5.23(b) and 5.24(b)).

On the other hand, in comparison with the cooling with hilotherapy, the lowest average of median temperature achieved by ice pack is $4.77°C$ higher. Furthermore, it is also found that an average minimum of $2.1°C$ drop in temperature is achieved by ice pack for 10 subjects while a higher/better minimum value of about $4.5°C$ (maximum of $10°C$) drop in temperature is

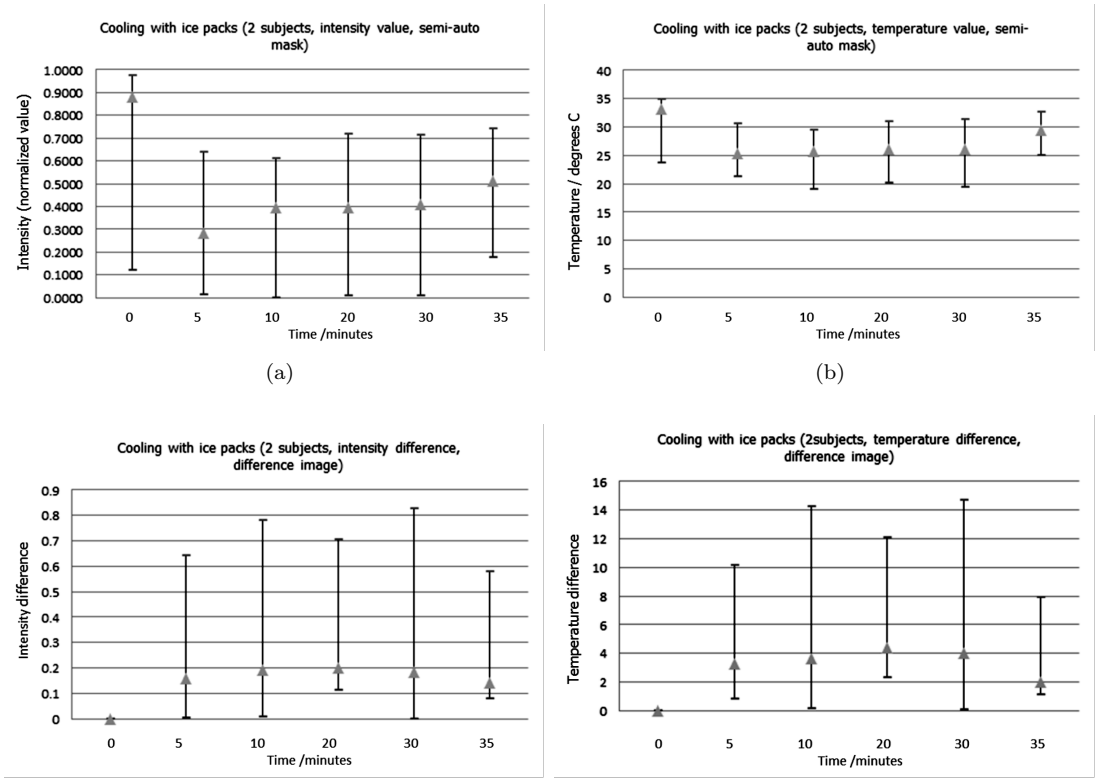


Figure 5.23: Cooling patterns achieved for the cooling with ice pack for 2 subjects based on the change of actual (a) intensity and (b) temperature, and based on the absolute (c) intensity and (d) temperature changes.

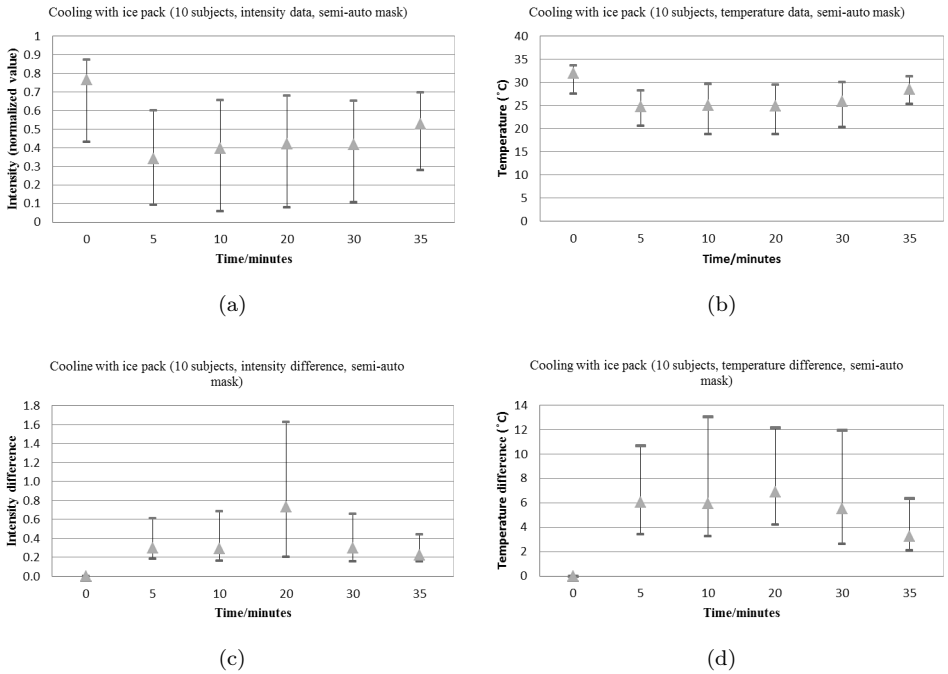
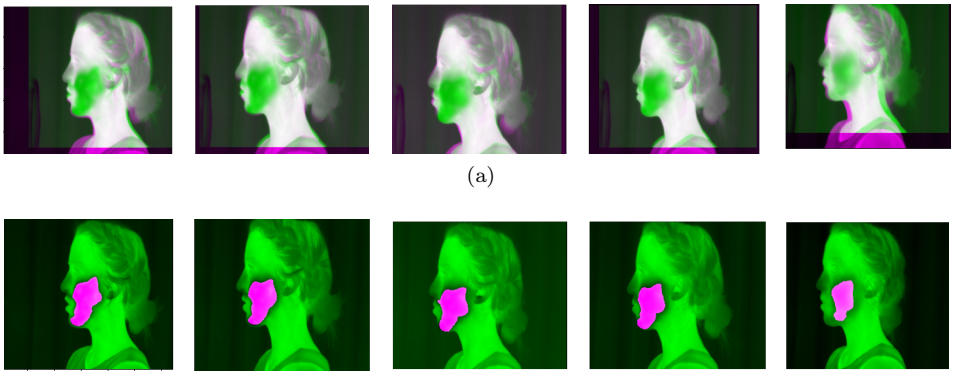


Figure 5.24: Cooling patterns achieved for the cooling with ice pack for 10 subjects based on the change of actual (a) intensity and (b) temperature, and based on the absolute (c) intensity and (d) temperature changes.

achieved by the hilotherm cooling system (Figure 5.20(d)).

As explained previously, the cooling with ice pack does not achieve an even distribution of cooling and only able to cover small facial area especially near the ears, hence resulted in low contrast and small variation in the cooling areas being determined. This demonstrates that the ice pack cooling treatment is found to be not consistent and ineffective in the cooling effect and that the spread/distribution of the cooling achieved appears to be very minimal. Similarly in Howell and Collier [100], the cooling with ice pack is reported to be less effective than cooling with the Hilotherm as the area effected by ice pack cooling is very small and more concentrated near the ears. This may also be the factor that leads to the large deviations in the ranges of values obtained at most time-points (Figures 5.23(a), 5.23(c) and 5.23(d)). All in all, based on the proposed semi-automated mask approach, cooling with ice pack is shown to be not achieving the desired cooling effect by the inconsistencies in the cooling behaviours and small distributions of the cooling effects achieved in the facial areas involved in the cooling treatment.

Taking into account the findings above, the remaining cooling studies for the left lateral and right lateral view data of the same 12 subjects are investigated only for cooling with the hilotherapy system using only the semi-automated mask approach. The objective of comparing between the



(a)

(b)

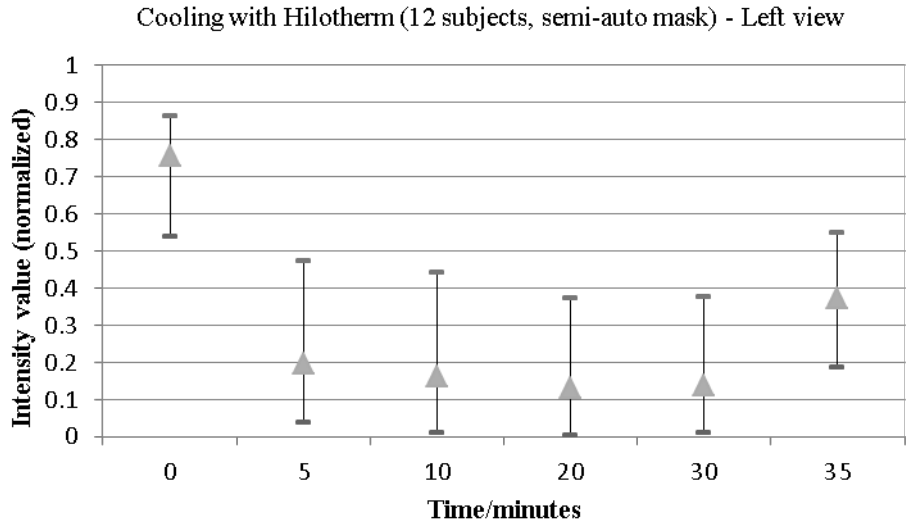
Figure 5.25: Resultant image overlays for follow-up images (at minutes 5, 10, 20, 30 and 35) of the left lateral view data of Subject 7; (a) overlay between registered baseline image and its follow-up images for each time-point, (b) the determined cooling area based on the semi-automated mask approach for each follow-up images.

cooling studies achieved by the multiple view data is to investigate any similarities or differences between them; not only between the two lateral sides but also between the lateral sides and the front view. Furthermore, the performance of the semi-automated mask approach can also be investigated for lateral view face thermograms. The results and discussions are presented in the following sections.

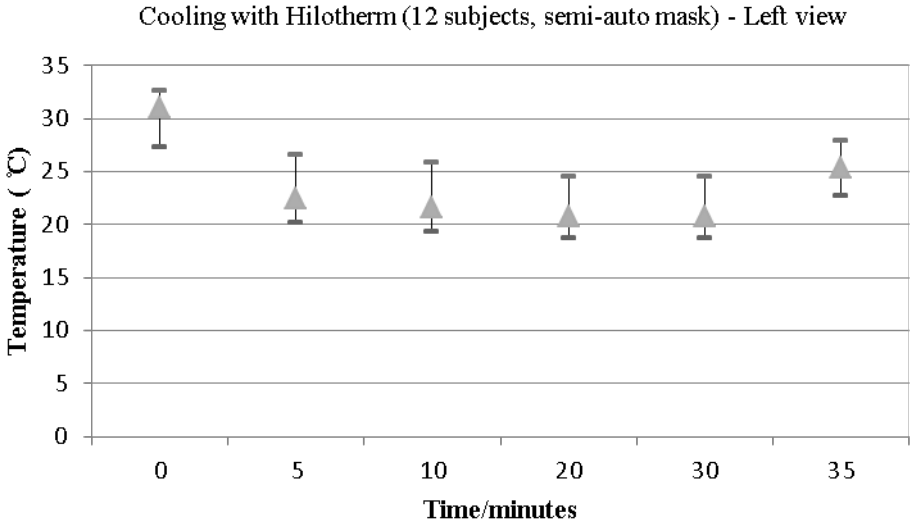
5.4.2 Left Lateral View based Cooling Study

The semi-automated mask approach is performed to conduct the cooling study for the lateral left view data as the results achieved by this method for the anterior view data that is found to be more sensitive to the changes present during a cooling treatment than that achieved by the manual mask approach. Figure 5.25 depicts the registration results and determined cooling areas based on the semi-automated mask approach. It can be observed that the semi-automated mask approach has also shown good performance in the determination of cooling area using the left lateral view data.

Table 5.1 presents the average values obtained for each statistical parameters extracted at each time-point for both change of actual intensity and temperature of the total 12 subjects based on their left lateral view data. On the other hand, Table 5.2 presents the results based on the values obtained from absolute difference images (between baseline images and their follow-up images). Both tabulated results are plotted for analysis of the cooling patterns obtained for the left lateral view data of the 12 subjects as shown in Figures 5.26 and 5.27.

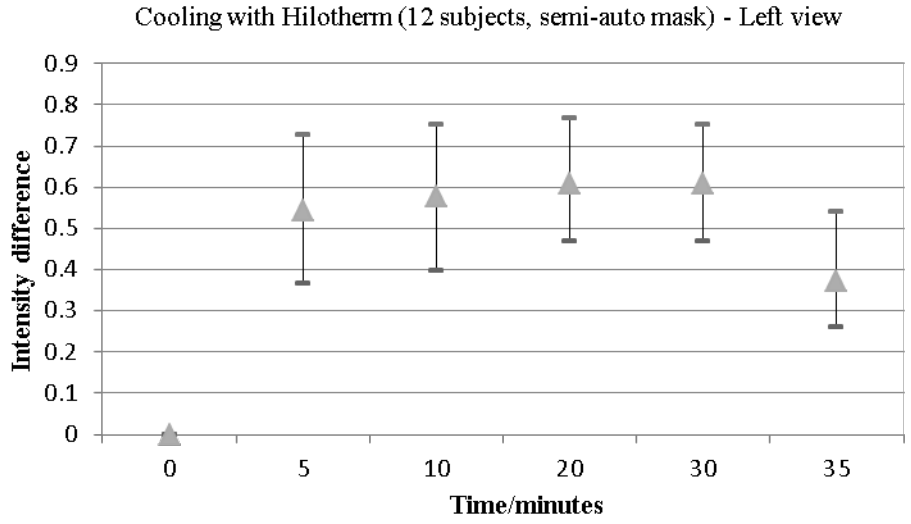


(a)

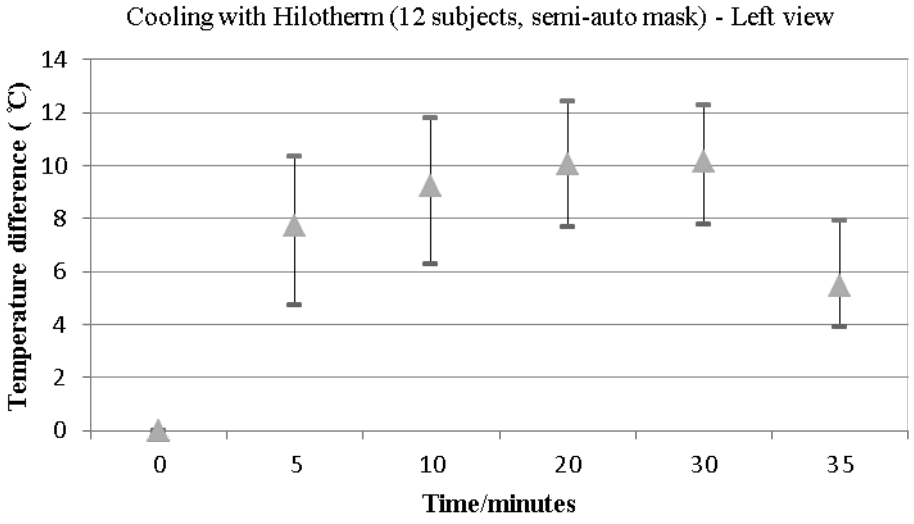


(b)

Figure 5.26: Cooling patterns of the left lateral view data for 12 subjects based on the change of actual (a) intensity and (b) temperature values.



(a)



(b)

Figure 5.27: Absolute change analysis; cooling patterns obtained from analysis of the left lateral view data based on the absolute (a) intensity and (b) temperature changes.

Table 5.1: The average maximum, minimum and median values based on the change of actual intensity and temperature values at 6 time-points obtained for the cooling study of the 12 subjects based on the left lateral view data.

Minute	Maximum		Minimum		Median	
	Intensity	$^{\circ}C$	Intensity	$^{\circ}C$	Intensity	$^{\circ}C$
0	0.87	32.59	0.54	27.33	0.75	31.03
5	0.47	26.59	0.04	20.19	0.19	22.42
10	0.44	25.81	0.01	19.29	0.16	21.59
20	0.37	24.54	0.002	18.75	**0.13**	**20.73**
30	0.38	24.48	0.008	18.74	0.14	20.74
35	0.55	27.92	0.19	22.65	0.37	25.38

Table 5.2: The average maximum, minimum and median values based on the absolute intensity and temperature changes at 6 time-points obtained for the cooling study of the 12 subjects based on the left lateral view data.

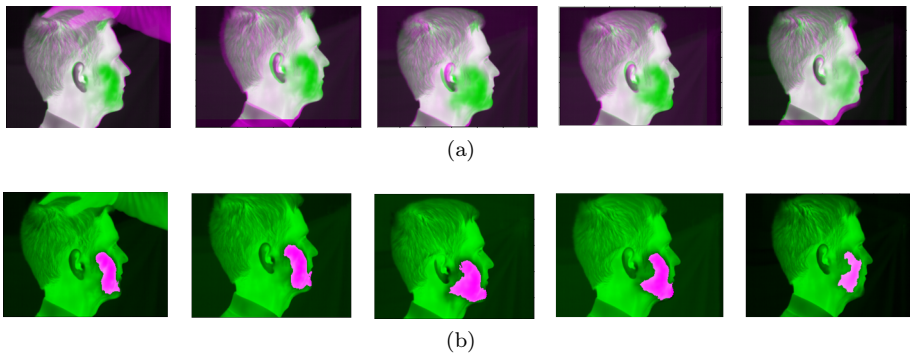
Minute	Maximum		Minimum		Median	
	Intensity	$^{\circ}C$	Intensity	$^{\circ}C$	Intensity	$^{\circ}C$
0	0	0	0	0	0	0
5	0.73	10.35	0.37	4.73	0.54	7.74
10	0.75	11.77	0.39	6.29	0.58	9.23
20	0.77	12.44	0.47	7.66	**0.61**	10.06
30	0.75	12.28	0.47	7.79	**0.61**	**10.15**
35	0.54	7.91	0.26	3.89	0.37	5.46

From the values and cooling patterns presented for the analysis based on the change of actual values, it is observed that the best cooling for both intensity and temperature were achieved at 20 minutes after cooling with considerably small differences with that achieved at 30 minutes after cooling. Similarly, for the absolute change analysis, the best/largest drop in both intensity and temperature values can be observed at minute 20 with considerably small differences with that (median value) achieved at minute 30.

5.4.3 Right Lateral View based Cooling Study

Similarly using the right lateral view data, the semi-automatic mask approach is employed for the cooling studies of the 12 subjects. Figure 5.28 depicted the registration results and the determined cooling areas for Subject 1. Table 5.3 presents the average values obtained for each of the statistical parameters obtained at each time-points in the cooling procedure based on both change of intensity and change of temperature. Results based on the absolute change are also tabulated as in Table 5.4. The cooling patterns for each analysis are shown in Figures 5.29 and 5.30.

From the cooling patterns presented in both Figures 5.29 and 5.30, the same cooling behaviours



(a)

(b)

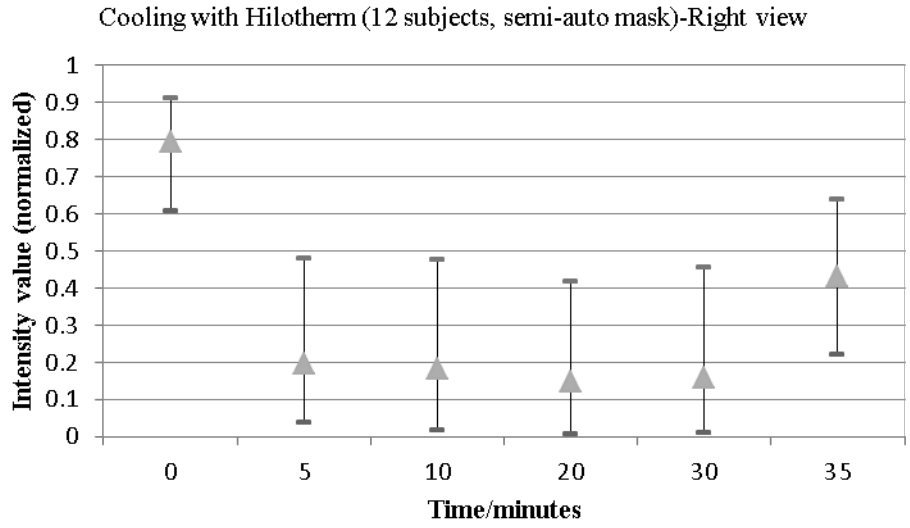
Figure 5.28: Resultant image overlays for follow-up images (at minutes 5, 10, 20, 30 and 35) using the right lateral view data of Subject 1; (a) Overlay between registered baseline image and its follow-up images for each time-point; (b) The determined cooling area based on the semi-automated mask approach for each follow-up images.

Table 5.3: The average maximum, minimum and median values based on the change of actual intensity and temperature values at 6 time-points obtained for the cooling study of the 12 subjects based on the right lateral view data.

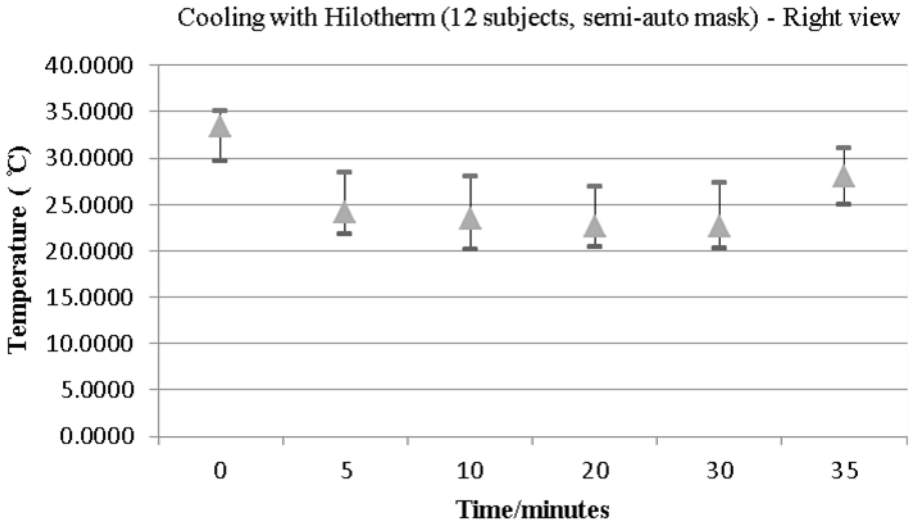
time-points	Maximum		Minimum		Median	
	Intensity	$^{\circ}C$	Intensity	$^{\circ}C$	Intensity	$^{\circ}C$
0	0.911	35.06	0.61	29.72	0.79	33.35
5	0.4804	28.39	0.04	21.76	0.19	24.12
10	0.4769	28.01	0.02	20.09	0.18	23.51
20	0.4156	26.88	0.004	20.38	**0.15**	22.67
30	0.4561	27.35	0.008	20.20	0.16	**22.56**
35	0.6393	30.99	0.22	25.00	0.43	27.98

Table 5.4: The average maximum, minimum and median values based on the absolute intensity and temperature changes at 6 time-points obtained for the cooling study of the 12 subjects based on the right lateral view data.

time-points	Maximum		Minimum		Median	
	Intensity	$^{\circ}C$	Intensity	$^{\circ}C$	Intensity	$^{\circ}C$
0	0	0	0	0	0	0
5	0.76	11.51	0.42	6.21	0.59	9.15
10	0.78	12.38	0.42	6.64	0.61	9.82
20	0.79	12.92	0.48	7.69	**0.65**	**10.66**
30	0.79	13.09	0.44	7.23	0.63	10.63
35	0.57	7.66	0.26	3.77	0.37	5.42

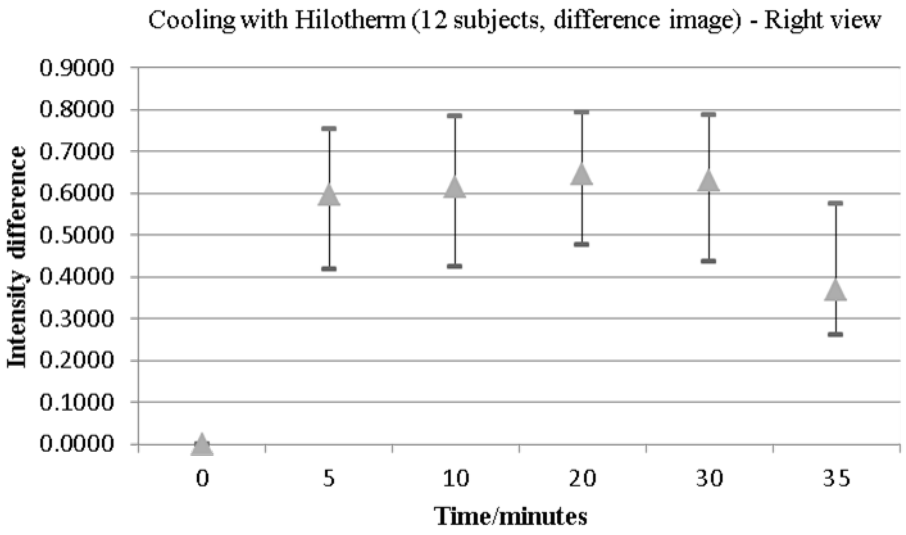


(a)

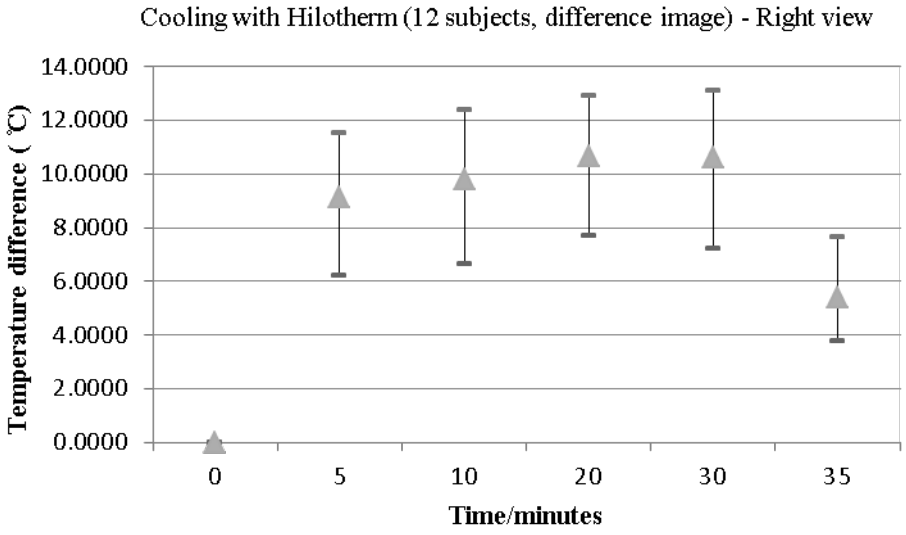


(b)

Figure 5.29: Cooling patterns obtained from analysis of the right lateral view data based on the change of actual (a) intensity and (b) temperature value.



(a)



(b)

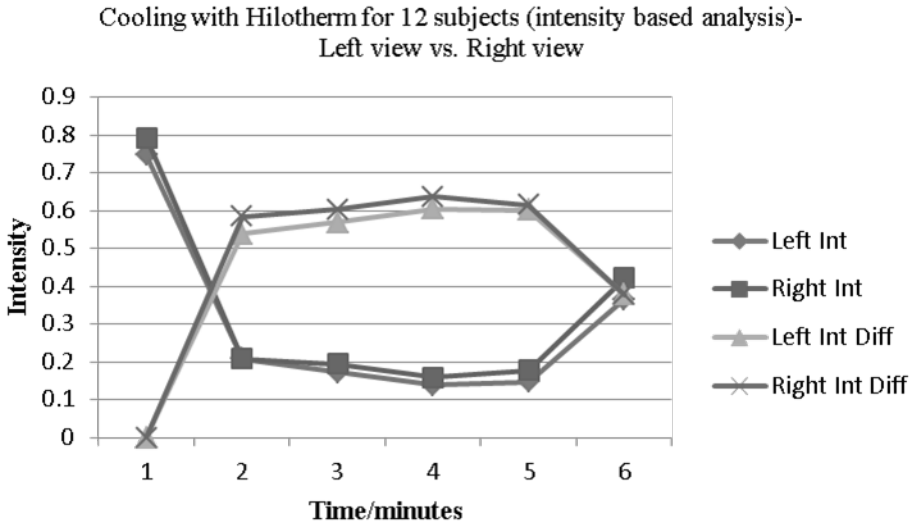
Figure 5.30: Absolute change analysis; cooling patterns achieved for the cooling study with the hilotherapy mask for 12 subjects using the right lateral view data based on the absolute (a) intensity and (b) temperature changes .

can be observed between the analysis based on the change of actual intensity and temperature and the analysis based on the absolute intensity and temperature changes using the right lateral view data. It can also be observed that the best cooling in average (based on the median value) for both the two types of analysis is achieved at minute 20. In the next section, a comparison study between the results obtained for all the three views are presented.

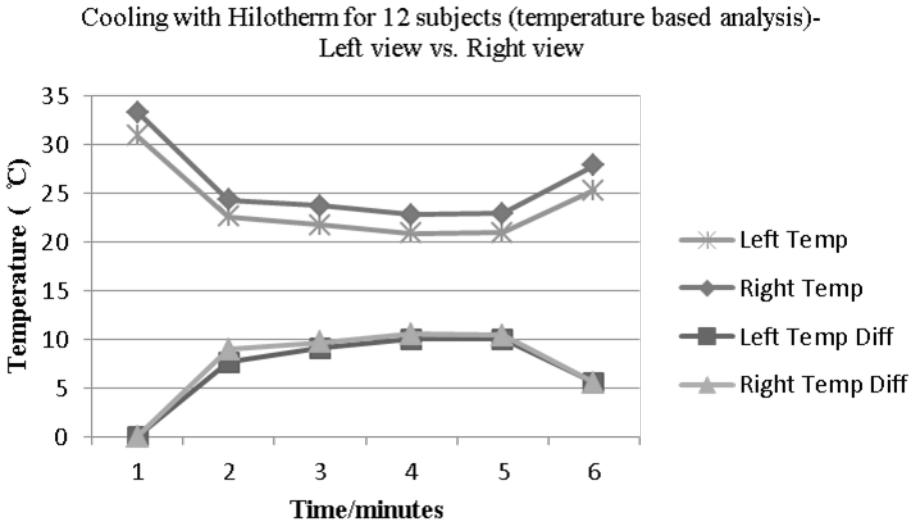
5.4.4 Left Lateral View vs. Right Lateral View vs. Anterior View

It is assumed that for a normal, healthy subject, temperature patterns between the left and the right sides of the face are alike or have very small differences between them. Hence, when cooling is performed to both sides of the face with a cooling mask controlled at the same temperature, the cooling effects achieved by the two lateral sides should be quite similar in both the pattern or behaviour and the value (should not be far apart). On the other hand, it is also assumed that by using the anterior view, the measurements of the cooling effects achieved should be more accurate, sensitive to changes and reliable as the cooling areas involved in this type of analysis covered both the right and the left sides of the face. In this section, the results obtained by the semi-automated method are investigated for the multiple view data analysis; comparisons in terms of similarities and differences between the anterior and the lateral views are presented. For this purpose, firstly, the cooling patterns obtained for both the lateral sides of 12 subjects are presented in the same graph to further compare between them as shown in Figure 5.31. Figure 5.31(a) shows the comparisons between the lateral views data based on the change of actual intensity (at the bottom part of the graph) and based on the absolute intensity change (at the upper part of the graph). On the other hand, Figure 5.31(b) shows the comparisons between the lateral views based on the change of actual temperature (at the upper part of the graph) and based on the absolute temperature change (at the bottom part of the graph). It can be observed from these figures that the cooling patterns obtained for all the four types of analysis for both the lateral views are similar. However, in the analysis based on the change of actual intensity and actual temperature during the cooling procedure, it is observed that the ranges of values obtained for the right lateral data are slightly higher (i.e.,warmer) than that observed for the left lateral data even at the time before cooling treatment is performed (i.e., at $t = 0$ minute).

Next, the cooling patterns obtained for all the three views (left, right and anterior/front) are compared and presented in Figures 5.32 and 5.33. The cooling patterns in Figure 5.32(a) shows



(a)



(b)

Figure 5.31: Comparison analysis between the two lateral view data of 12 subjects; (a) Intensity based analysis (the cooling patterns at the upper part represents absolute change analysis while the ones at the bottom represents actual intensity analysis), and (b) temperature based analysis (the cooling patterns at the upper part represents actual temperature analysis while the ones at the bottom represents absolute change analysis).

the comparisons between the anterior view and the two lateral view data based on the change of actual intensity (at the bottom part of the graph) and based on the absolute intensity change (at the upper part of the graph). On the other hand, Figure 5.33(b) shows the comparisons between the anterior view and the two lateral view data based on the change of actual temperature (at the bottom part of the graph) and based on the absolute temperature change (at the upper

part of the graph). It is found that for all the four types of analysis performed, the cooling patterns achieved by the anterior view are also similar to the cooling patterns achieved by the lateral views. In the analysis based on the change of actual temperature, among the three views, the front view data achieved the lowest average range of median values (best cooling pattern) throughout the cooling period even though it can be seen that the average median temperature at its baseline is the same as the right data (Figure 5.32(a) (upper part of the graph)). On the contrary, based on the absolute difference value, the right lateral data achieves the largest temperature drop at all time-points but only with small differences with the temperature drop obtained by the other two views data; in the range of $0.36°C - 1.45°C$. However, the cooling ranges obtained by the front view data and the left view data are very similar/close to each other compared to the right view data. In the analysis based on the intensity data as shown in Figure 5.33(b), the results obtained by the left lateral and the right lateral views demonstrate the similarity between them in terms of the cooling patterns achieved. However, in terms of the values achieved at all time-points, the left lateral view seems to be more closer to the anterior view than the right lateral view. Overall, the results obtained for the right lateral view based on the ranges of values obtained for the change of actual temperature and intensity values seems to be on the highest side which means the warmest/worst of all three. Nevertheless, the differences in the values along the 6-time points for both analysis based on actual values and absolute changes between the anterior and the two lateral views are small (≤ 1.2 in intensity, $\leq 3°C$ in temperature).

To further investigate the differences between the cooling achieved by the three types of views, four comparison parameters are used; average intensity (actual), average intensity change, average temperature (actual) and average temperature change. These parameters are computed by taking the average of the difference values computed between the results achieved by two types of views (i.e., between the left and the right views, the front and the left views, and the front and the right views) for both the temperature and the intensity data. These values are compared in Table 5.5. Overall, the average difference values obtained based on the four comparison parameters used are small. However, it can be observed that the values of the four parameters for the comparison between the anterior data and the left lateral data are the smallest (the most similar) while the largest is observed between the anterior and the right lateral data (the most dissimilar). These findings conform to the previous comparison analysis based on the cooling

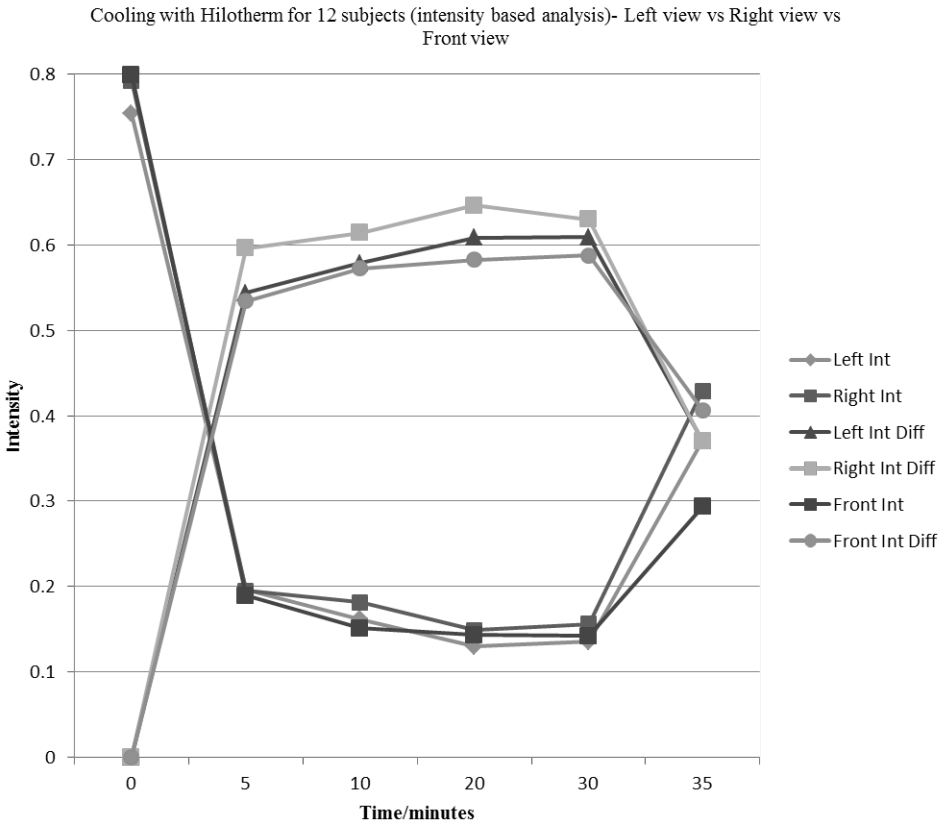


Figure 5.32: Comparison analysis between the lateral views and the anterior view data of 12 subjects based on intensity (the cooling patterns at the upper part represents absolute change analysis while the ones at the bottom represents actual intensity analysis).

Table 5.5: Comparison analysis between two different views.

Comparison Parameter	Difference Value between Two Different Views		
	Left vs Right	**Front vs Left**	Front vs Right
Average Actual Intensity	0.029	**0.027**	0.029
Average Absolute Intensity Change	0.025	**0.018**	0.039
Average Actual Temperature	2.095	**0.964**	2.349
Average Absolute Temperature Change	0.468	**0.241**	0.471

patterns achieved (Figures 5.32 and 5.33).

5.4.5 Comparison Analysis based on the Clinical Assessment

The cooling patterns achieved by the extraction of statistical values from the cooling areas identified by the image registration and segmentation techniques (the semi-automated mask approach) are shown to be correlated with the cooling patterns achieved in Howell and Collier [100] as presented in the previous sections. However, in [100], the results were only based on three subjects. To support our cooling study analysis based on the proposed semi-automated mask

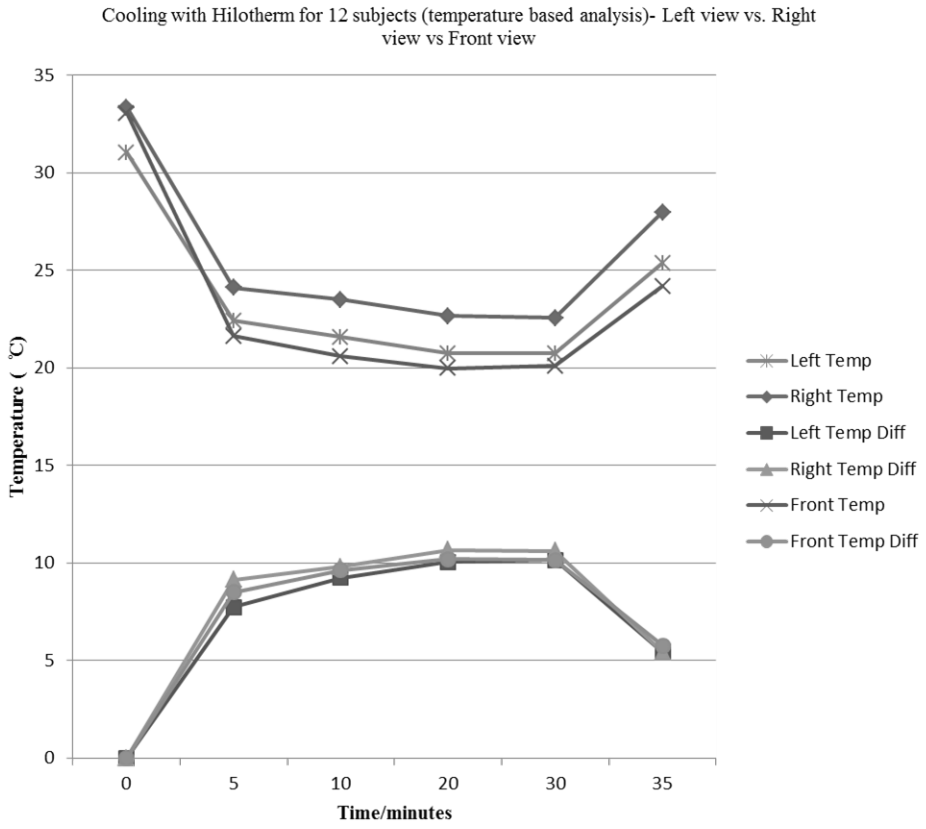


Figure 5.33: Comparison analysis between the lateral views and the anterior view data of 12 subjects based on temperature (the cooling patterns at the upper part represents absolute change analysis while the ones at the bottom represents actual intensity analysis).

approach, the results are also compared with the results obtained by a clinical assessment (i.e., a manual way) for the same thermogram data. In this clinical assessment, the measurements for the cooling study were performed manually using the FLIR's Thermacam Researcher software by a final year medical student and closely monitored and validated by a medical doctor and a clinical scientist. This current clinical method for the cooling study based on thermal imaging is found quite tedious as it takes about 30 minutes to draw the regions of interest (ROIs) on the face for the whole sequence of images for one subject. Then, it is followed by plotting of the cooling patterns in Microsoft Excel once the software exports the temperatures.

The results from the clinical assessment are obtained for only 9 subjects from the total of 12 subjects. As similar as in [100], the process of extraction of the statistical parameters such as the minimum, maximum, median, average and standard deviation are performed on region-by-region basis where our ROIs are considered for both the lateral views data only. They have also computed temperature change/drop for each time-point based on the change of temperature obtained earlier. However, no analysis are performed for the anterior view data in the clinical

Table 5.6: Clinically obtained results for cooling with hilotherapy mask based on the change of actual temperature values for the left lateral data.

Statistical parameters	Cooling temperature ($^{\circ}C$) at each time-point					
	0	5	10	20	30	35
Mean	33.33	24.98	24.02	23.44	23.32	28.09
Median	33.47	24.77	23.47	22.97	22.67	27.90
Std	0.73	2.01	1.85	1.73	1.75	1.88
Maximum	34.30	28.50	27.40	26.03	26.83	32.10
Minimum	32.23	22.57	21.47	21.27	21.40	26.00

assessment as the ROIs for this view are not decided as yet.

In order to compare the results obtained by the proposed semi-automated approach with the results obtained by the clinical assessment, it is thus necessary to compute the average value of each parameters obtained clinically across the four ROIs at each time-point as presented in Table 5.6 and Table 5.7 for the change in actual temperature for the left and the right lateral data respectively, and in Table 5.8 and Table 5.9 for the temperature change for the left and the right lateral data. Next, comparisons between the cooling patterns achieved clinically for the two lateral views are carried out by plotting the median values from Table 5.6 and Table 5.7 side by side as depicted in Figure 5.34 for analysis based on the change of actual temperature. The median values from Table 5.8 and Table 5.9 are also plotted side by side in Figure 5.35 for comparison analysis based on the temperature change. As shown in Figure 5.34, it can be observed that the cooling patterns achieved in the clinical assessment for the right lateral view displays a lower range of temperature value across the cooling period compared to that displayed by the left lateral view data. This may be due to the lower value of the baseline temperature of the right lateral data than the baseline temperature of the left lateral data. The cooling patterns exhibited by both the lateral views seem to be very similar to each other. However, in terms of the amount of change in temperature as shown in Figure 5.35, the left lateral view is shown to demonstrate a higher value of temperature reduction than that of the right lateral view. As compared to the results obtained by our proposed method for the lateral views (Figure 5.31(b)), it can be seen that the differences of values at all time-points between the left and the right lateral views are much lower than that displayed by the clinical assessments. This may infer that the proposed method is more reliable and accurate in measuring the temperature across the cooling areas than the clinical assessment approach.

Further investigations are carried out for the comparisons between the clinically achieved cooling patterns and the cooling patterns achieved by the proposed semi-automated approach. Fig-

Table 5.7: Clinically obtained results for cooling with hilotherapy mask based on the change of actual temperature values for the right lateral data.

Statistical parameters	Cooling temperature ($^{\circ}C$) at each time-point					
	0	5	10	20	30	35
Mean	24.94	19.06	18.25	17.87	17.64	21.24
Median	24.95	18.63	17.85	17.75	17.43	20.80
Stdev	0.54	1.40	1.33	1.01	1.20	1.39
Max	25.60	21.65	20.83	19.58	20.35	24.35
Min	24.13	17.45	16.75	16.43	16.35	19.85

ures 5.36 and 5.37 depict the cooling patterns achieved by the semi-automated approach and the clinical assessment approach for all the three views based on the median values obtained for both the change of actual temperature analysis and the temperature change analysis. From Figure 5.36, it can be observed that the cooling patterns achieved by the proposed semi-automated approach for the anterior, left and right lateral views and the cooling patterns achieved by the clinical assessment for the left lateral view are very close to one another (identical with the right lateral view obtained by the proposed method). On the other hand, the cooling pattern for the right lateral view obtained by the clinical assessment seems to be quite distant from the others. It can also be observed that even though the cooling patterns determined by the clinical assessment for the lateral left and right views are similar in terms of the behaviour however, the change of actual temperature values are quite large in difference (up to $\sim 9.5^{\circ}C$). As the data for this study is acquired from healthy control subjects, the values of thermal patterns between the left and the right side of the face should be similar or small in difference as displayed by the cooling patterns achieved by the proposed semi-automated mask approach. From this point of view, it may be inferred that the proposed semi-automated mask approach may be more reliable in terms of sensitivity and accuracy of cooling patterns achieved than the manual clinical approach.

Table 5.8: Clinically obtained results for cooling with hilotherapy mask based on the temperature change for the left lateral view data.

Statistical parameters	Temperature change ($^{\circ}C$) at each time-point					
	0	5	10	20	30	35
Mean	0	8.35	9.31	9.89	10.01	5.24
Median	0	8.33	9.30	9.83	10.33	5.67
Std	0	1.90	1.68	1.38	1.57	1.54
Max	0	5.03	6.13	7.87	6.70	1.43
Min	0	11.03	12.27	12.13	12.50	6.47

Table 5.9: Clinically obtained results for cooling with hilotherapy mask based on the temperature change for the right lateral view data.

Statistical parameters	Temperature change ($°C$) at each time-point					
	0	5	10	20	30	35
Mean	0	5.88	6.69	7.07	7.30	3.70
Median	0	6.10	6.98	7.00	7.58	4.08
Std	0	1.46	1.37	0.97	1.25	1.19
Max	0	3.40	4.33	5.50	4.85	0.85
Min	0	7.88	8.50	8.53	8.70	4.90

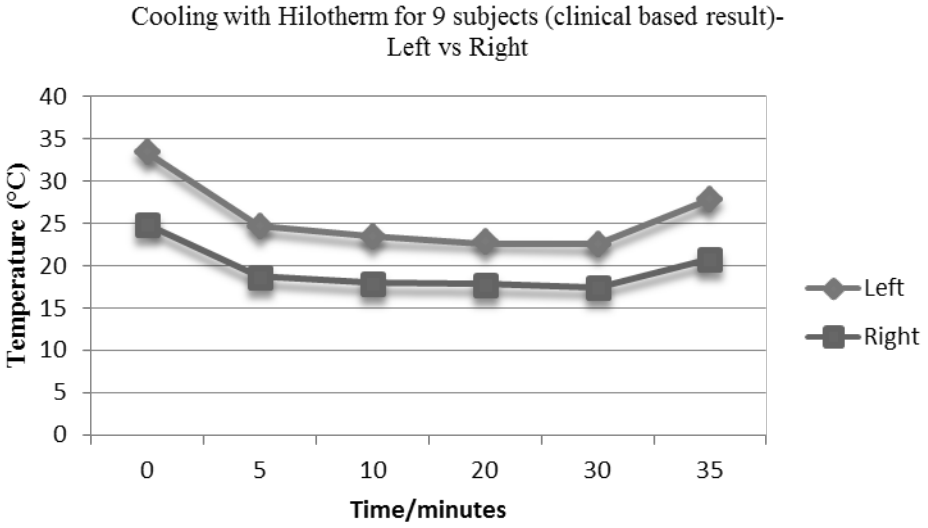


Figure 5.34: Comparison analysis for cooling with hilotherm (9 subjects) between the left lateral view and right lateral view data using the clinical assessment approach based on the change of actual temperature.

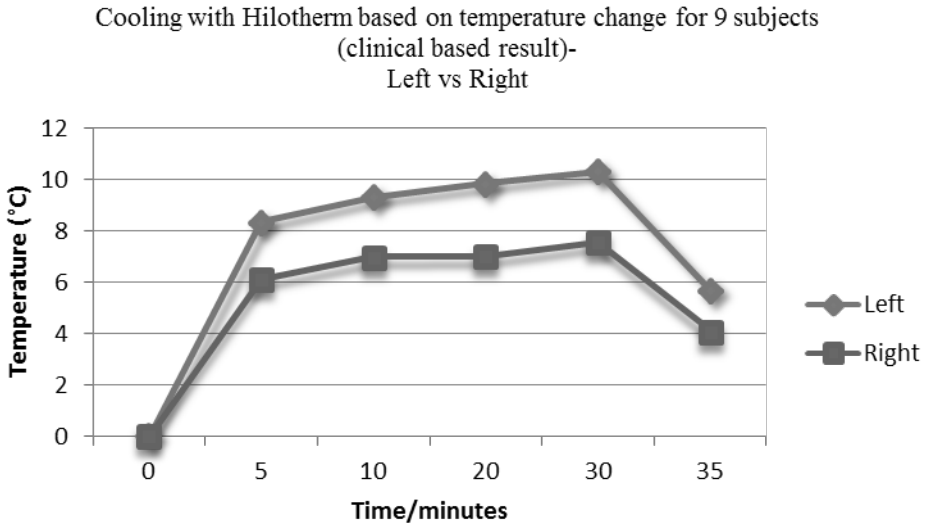


Figure 5.35: Comparison analysis for cooling with hilotherm (9 subjects) between the left lateral view and right lateral view data using the clinical assessment approach based on the temperature change.

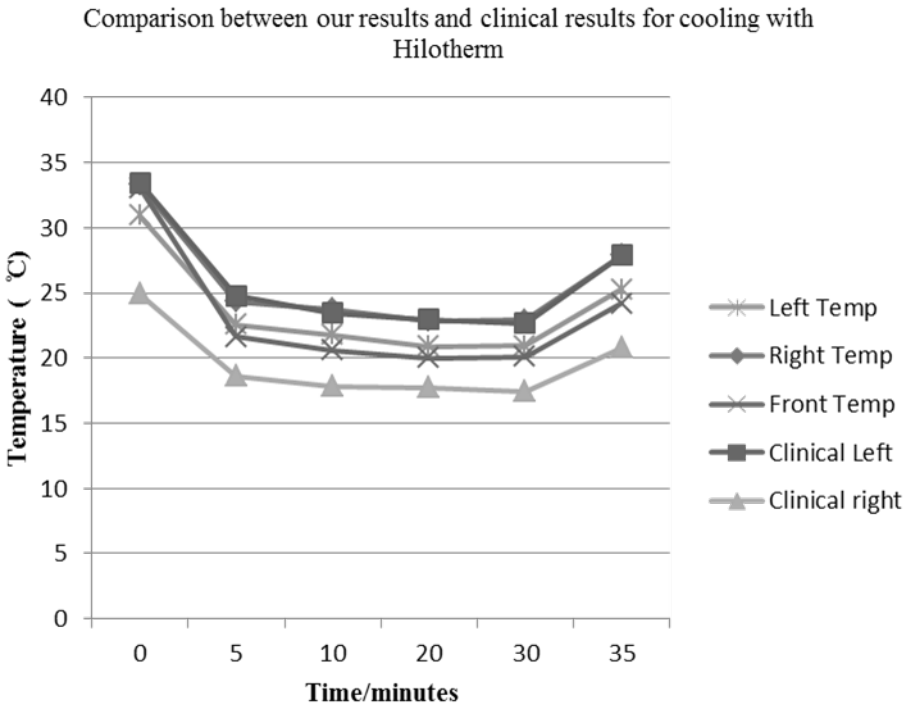


Figure 5.36: Comparison analysis for cooling with hilotherm between the proposed semi-automated method (12 subjects, all the three views) and the clinical assessment approach (9 out of the 12 subjects, lateral left and right views) based on the change of actual temperature.

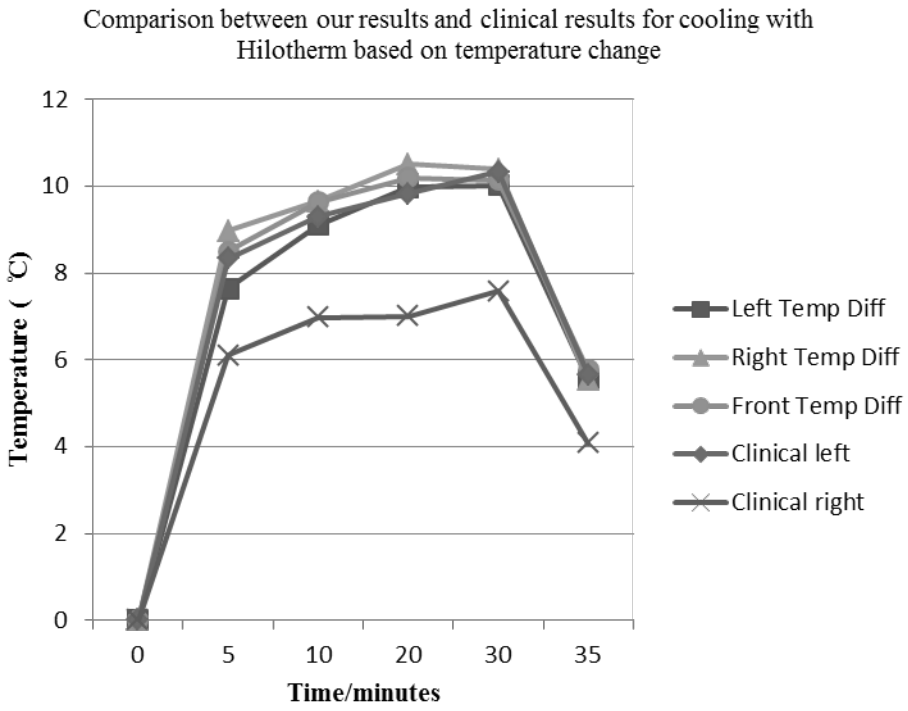


Figure 5.37: Comparison analysis for cooling with hilotherm between the proposed semi-automated method (12 subjects, all the three views) and the clinical assessment approach (9 out of the 12 subjects, lateral left and right views) based on the temperature change.

5.5 Discussion and Conclusions

The proposed semi-automated method has shown to be successfully being employed in the thermal analysis for both the hilotherapy cooling system and ice pack. This is based on the cooling patterns achieved by the proposed method that are in keeping with the desired cooling patterns as described in Howell and Collier [100], for most of the cases presented in this chapter. The proposed method is also able to show that the hilotherapy cooling system is more effective than ice pack as also supported by [100], by the analysis performed based on the cooling areas determined and the cooling patterns achieved for both the cooling treatments. In this work, the claim that the hilotherapy system serves the purpose of a cooling treatment much better than the ice pack is made based on the following findings obtained by the proposed semi-automated method.

- The wide and evenly distributed cooling areas/effects achieved,
- the consistencies in the cooling effects produced that can be presented by both temperature and intensity data from the start of cooling until around 20 minutes after cooling compared to only around the first 5 minutes for the ice pack, and
- the lower range of average median temperature achieved from 5 minutes after cooling until 30 minutes after cooling ($16°C$ - $22°C$), compared to that achieved by the ice pack ($24°C$ - $26°C$).

Furthermore, the cooling patterns achieved by the proposed method is found to be similar to the cooling patterns achieved by the clinical assessments. However, the differences in the cooling ranges between the three views are smaller for the proposed method (less than $3°C$ for the actual temperature analysis and less than $1°C$ for the absolute temperature change analysis) than the cooling ranges obtained by the clinical assessment for the lateral views (in the range of $4°C$ - $9.5°C$ for actual temperature analysis and in the range of $2°C$ - $4°C$ for absolute temperature change analysis). As the lateral sides of the healthy subjects are assumed to be having no large differences in their temperature values based on thermal symmetry property of a healthy subject, the lower the differences of the cooling ranges obtained between the lateral sides are, the more accurate and reliable the method of analysis used is. Hence, from the thermal symmetry point of view, it can be deduced that the semi automated method slightly outperforms the clinical assessment method. This may be due to the accurate and concentrated cooling areas that can be extracted by the semi-automated mask approach based on the changes in intensity in the

thermograms.

On the other hand, based on the multiple view results obtained by the semi-automated mask approach, it can also be inferred that any of the views can be used to represent a cooling study due to the similarities in the cooling patterns achieved and the small differences in the cooling ranges obtained among them. However, as it is found that the cooling patterns achieved by the anterior view data gives the best representation of cooling pattern as not only the cooling behaviour follows the optimal cooling behaviour (largest drop at 20 minutes), but the ranges of values extracted from this data based on the change of temperature are also found to be the lowest of all the three views. Thus using the anterior view data can increase the level of accuracy of the cooling patterns achieved as sensitivity in detecting changes in intensity and temperature present in the cooling study is slightly increased. This may be mainly because the anterior view data contains information from both the lateral sides that enables the ranges obtained for each statistical parameters to be extracted from a larger and evenly distributed cooling area that contributes to the increase in the accuracy of the cooling study conducted. With the image processing based approach, the task to identify the cooling area of interest in a manual drawing way can be removed. This enables the cooling study to be conducted with less time, less tedious and reduced subjectivity in the analysis.

Overall, the proposed semi-automated cooling analysis approach based on the semi-automated mask approach has shown to be robust and reliable in the cooling study of normal subjects for the hilotherapy system for all the three view data, and the ice pack. This is proven by the cooling patterns achieved by this approach that is in keeping with the cooling pattern achieved in the clinical study performed by Howell and Collier [100]. The behaviour of the cooling patterns produced for all the multiple view data by the proposed analysis approach is also found to be comparable to the clinical assessment. However, as the differences between the ranges of values obtained for the multiview data by the proposed approach are much smaller than that obtained between the lateral views by the manual clinical approach, it can be considered that the proposed method slightly outperforms the clinical approach based on accuracy and reliability of the determination of cooling patterns. The results of cooling study achieved by the proposed semi-automated approach have been validated by the same medical doctor and clinical scientist who are involved in the cooling study reported in [100].

Based on the comparability and reliability shown by the semi-automated approach, it is therefore very promising and useful for the proposed method to be used as a semi-automated tool for

cooling study of cryotherapy techniques based on thermal imaging. Furthermore, the approach is also potentially employed in investigating the optimal cooling configuration for maxillofacial surgery patient based on the hilotherapy system.

Chapter 6

Conclusions and Future Work

In this thesis, image processing algorithms were proposed to improve the accuracy and scalability of diagnosis and monitoring of morphoea and to investige the effectiveness of a cooling mask treatment intend for maxillofacial post-surgery treatment based on thermal imaging. However, since access to the morphoea and the maxillofacial post-surgery data is proved difficult to be obtained, the proposed algorithms for these two medical applications are investigated based on healthy control subjects. The algorithms developed were focused on two different fields, one was to incorporate the Blaschko's lines from a face sketch into a face thermogram as accurate as possible and the other was to identify cooling areas for cooling pattern analysis to better understand the hilotherapy cooling system and ice pack cooling, as well as to assist in finding the optimal cooling configuration for maxillofacial post-surgery treatment based on image processing techniques.

6.1 Potential Diagnosis and Monitoring of Morphoea based on the Blaschko's Lines

The image registration approaches developed for this purpose are presented in two separate chapters where each chapter describes a registration approach that is solving for different types of registration problems; (1) the global displacements between two images, and (2) the local, varying displacements between two images. The first part of the image registration approach is described in Chapter 3. In this chapter, a normalized gradient cross correlation (NGC) method is

shown to greatly reduce large displacements between face thermogram and the face sketch based on the edge map representations of the two multimodal images as an edge map does not only provides salient information of an image but also enables two multimodal images to carry the same meaning in their intensities. A hybrid NGC method is also proposed to overcome limitation in the NGC method on misregistration due to inaccurate retrieval of translational diferences. However, since the face is regarded as soft tissues, small local displacements between the globally registered images by the hybrid NGC method are therefore still present especially from motion, shape and contour. Hence, a non-rigid registration approach based on a stochastic non-rigid affine registration (NRAR) method is proposed to improve further the golbally registered images as presented in Chapter 4. Nevertheless, the results of the NGC or the hybrid NGC method is very crucial as an initial positioning of the images to be matched by the NRAR method as a time saving first step for a successful local based registration to be achieved.

The NRAR method has successfully demonstrated its capability in reducing the local displacements that exist between two globally registered images in an efficient manner based on; (i) ground truths, (ii) between the face sketch and face thermograms, and (iii) between face thermograms of the same subject and of different subjects taken at intervals of time (Chapter 5). Furthermore, the NRAR method is found to be comparable to the FFD method for registration between images with small local displacements. In the case where large and complex differences in shapes and contours are present between two images, the NRAR method is found to outperform the FFD method. The NRAR method has shown more flexibility than the FFD method by successfully adapting/transforming a ring-shaped object into a C-shaped object where the FFD method has failed. This shows that the NRAR method is able to register not only between two convex shape of objects, but also between a convex and a concave shape of objects. However, the FFD method is found to produce smoother registration results compared to the NRAR method. This can be explained by the interpolation method employed in the FFD method that involves control point grid rather than pixel intensities as employed in the NRAR method. However, this is not a serious issue in this work as the transformed pixels are mainly edge pixels while the pixels that are of interest are the ones that lie on the skin surface or non-edge pixels. Overall, the simple computation, stochastic based affine non-rigid registration (NRAR) method proposed is found to be fairly elastic, robust and reproducible.

For a future work, based on registered face thermograms of morphoea patients, lesion patterns can be segmented as thermal signatures using the information of abnormal heat changes in the thermogram. Apart from using its temperature information, segmentation of abnormal heat

patterns can also be performed by utilizing the intensity information from the RGB image channels of a thermogram. Using these segmented abnormal heat patterns, correlation with the lines of Blaschko can be investigated and used as an indicator for not only the presence or absence of morphoea disease but also for treatment efficacy.

The stochastic approach in the NRAR method can result in a slow convergence of the algorithm to the optimal solutions when M is larger than 7 or for a large size image. A future work can be carried out to perform the NRAR method based on a multiresolution approach that is also known as a pyramid scheme. In this scheme, the algorithm can be initially performed at their coarse resolution. Then using the results obtained in the coarse resolution, the algorithm will continue the search for new deformations to align between two images in a resolution finer than the previous one. This process can be repeated for three or more different levels of image resolution. In this way, any local displacement that could not be found in a particular resolution can be found in another resolution.

6.2 Cooling Pattern Identification and Analysis for Cooling Study based on Thermal Imaging

Both the NGC and the NRAR methods have shown in this thesis to be useful for another medical application which is the study of effectiveness of a cooling mask (hilotherapy) over the ice pack based on the cooling patterns achieved through a semi-automated approach using thermal imaging technique on healthy control subjects. The semi-automated system proposed has successfully obtained cooling patterns as similar to the ones reported in a clinical study; a decreasing pattern of temperature/intensity until it reaches its peak (maximal cooling) at minute 20 and an increase pattern after that until minute 35 [100]. The system is also able to show that the cooling with hilotherapy achieves better reduction in temperature (more effective) than cooling with the ice pack as similarly reported in a clinical study conducted by Howell and Collier [100]. It is also found that by using the thermograms' temperature data, more accurate cooling patterns can be produced than using the intensity data. However, the intensity data is very useful for determination of the ROIs in the cooling study based on the semi-automated approach. The results achieved also show high correlations with the clinical assesments.

Using the proposed approach that involves image registration and image segmentation tech-

niques, the time taken for a cooling study can be reduced to a fraction of that taken by the clinicians (more than 30 minutes per subject). Not only the time to assess these data can be reduced, the approach is also proven to be robust, reliable and reproducible for a study of the effectiveness of a cooling treatment even for maxillofacial post-surgery patients. These claims are made based on the consistencies achieved by the desired cooling patterns obtained across a small number of subjects as well as a larger number of subjects. The semi-automated approach proposed is also found to be able to demonstrate clearly the effectiveness of the hilotheraphy system over the ice pack based on the consistencies in achieving better temperature reduction and the desired cooling patterns. The cooling patterns obtained in the cooling studies conducted using the semi-automated approach are in keeping with the clinical findings of Howell and Collier [100]. However to investigate the optimum cooling configuration for maxillofacial surgery patients by the hilotherapy system based on the proposed semi-automated approach, patient data is thus necessary.

In the future, it is useful to fully automate the semi-automated system proposed by incorporating a region growing method based on automatic seed pixel placement.

Bibliography

[1] U. R. Acharya, E. Y. K. Ng, J. H. Tan and S. V. Sree, "Thermography Based Breast Cancer Detection Using Texture Features and Support Vector Machine", *J Med Syst*, 1-8, 2010.

[2] U. R. Acharya, E. Y. K. Ng, J. H. Tan, S. V. Sree and K. H. Ng, "An Integrated Index for the Identification of Diabetic Retinopathy Stages Using Texture Parameters", *J Med Syst*, 1-10, 2011.

[3] J. P. Agnelli, A. B. Cristina and V. Turner, "Tumor Location and Parameters Estimation by Thermography", *Mathematical and Computer Modelling,* 53(7–8):1527–1534, 2011.

[4] R. C. Allen, B. M. Ansell, R. P. Clark, M. R. Goff, R. Waller and S. Williamson, "Localized Scleroderma: treatment response measured by infrared thermography", *Thermology 1987*, 2:550–553.

[5] J. Arrillaga, N. R. Watson, *Power System Harmonics*, John Wiley and Sons, 2003, pp. 41.

[6] M. A. Akhloufi and A. Bendada, "Infrared Face Recognition using Distance Transforms", in *Image and Vision Computing, WASET 2008. International Conference*, 30:160-163, 2008.

[7] K. Ammer, "Does Thermal Imaging Provide Extra Information in Patients Suffering from Headache?", *Thermology International - Editorial (Austrian Society of Thermology, Vienna, Austria)*, 45-48, 2006.

[8] M. Anbar, "Clinical Thermal Imaging Today - Shifting from Phenomological Thermography to Pathophysiologically based Thermal Imaging", *IEEE Engineering in Medicine and Biology*, 25-33, 1998.

[9] A. Andronache, M. von Siebenthal, G. Sze´kely and P. Cattin, "Non-rigid registration of multi-modal images using both mutual information and cross-correlation", *Medical Image Analysis*, 12: 3-15, 2008.

[10] Y. Avnon, M. Nitzan, E. Sprecher, Z. Rogowski and D. Yarnitsky, "Autonomic Asymmetry in Migraine: augmented parasympathetic activation in left unilateral migraineurs", *Brain (2004)*, 127(9):2099-2108, 2004.

[11] S. Bagavathiappan, T. Saravanan, J. Philip, T. Jayakumar, B. Raj, R. Karunanithi, T. Panicker, M. P Korath and K. Jagadeesan, "Investigation of Peripheral Vascular Disorders using Thermal Imaging", *British Journal of Diabetes & Vascular Disease*, 8(2):102-104, 2008.

[12] S. Bagavathiappan, T. Saravanan, J. Philip, T. Jayakumar, B. Raj, R. Karunanithi, T. Panicker, M. P Korath and K. Jagadeesan, "Infrared Thermal Imaging for Detection of Peripheral Vascular Disorders", *J Medical Physics*, 34(1):43-47, 2009.

[13] D. I. Barnea and H. F. Harvey, "A Class of Algorithms for Fast Digital Image Registration", *IEEE Transactions on Computers*, C-21(2):179-186, 1972.

[14] E. Belli, G. Rendine and N. Mazzone, "Cold therapy in maxillofacial surgery", *J Craniofac Surg.*, 14:878–880, 2009.

[15] N. Birdi, A. Shore, P. Rush, R. M. Laxer, E. D. Silverman and B. J. Krafchik, "Childhood linear scleroderma: a possible role of thermography for evaluation", *J Rheumatol*, 19(6):968-73, 1992.

[16] Blaschko A. Die Nervenveteilung in der Haut in ihrer Beziehung zu den Erkrankungen der Haut. In: Beilage zu den Verhandlungen der Deutschen Dermatologischen Gesellschaft: VII. Congress zu Breslau, Mai 1901 (W. Braunmu¨ ller, ed.), Vienna: Braunmu¨ ller, 1901.

[17] C. Bleakley, S. O'Connor, M. A. Tully, L. C. Rocke, "The PRICE study (Protection, Rest, Ice, Compression, Elevation): design of a randomised controlled trial comparing standard versus cryokinetic ice applications in the management of acute ankle sprain", *BMC Musculoskeletal Disord 2007*, 8:125, 2007.

[18] P. Bloomfield, *Fourier Analysis of Time Series: An Introduction*, Wiley-Interscience, New York, 6:69, 2000.

[19] S. Boukharouba, J. M. Rebordao and P. L. Wendel, "An Amplitude Segmentation Method based on the Distribution Function of An Image", *Computer Vision, Graphics, and Image Processing*, 29(1):47-59, 1985.

[20] Breast Cancer Care, "England Health Check Breast Cancer in England Survey 2008: summary and recommendations". Retrieved from `http://www.breastcancercare.org.uk/upload/pdf/England_Health_check_08_Recommendations.pdf`. (Accessed in January 2011).

[21] L.G. Brown, "A survey of image registration techniques", *ACM, Computing Surveys*, 24:326-376.

[22] Bupa, Health information team, "Endometriosis", May 2009. Retrieved from `http://www.bupa.co.uk/individuals/health-information/directory/e/endometriosis`. (Accessed in September 2010).

[23] S. B. Burns, J. L. Burns, "Hydrotherapy", *J Altern Complement Med.*, 3:105-107, 1997.

[24] R. Burstein, D. Yarnitsky, I. Goor-Aryeh, B. J. Ransil and Z. H. Bajwa, "An Association between Migraine and Cutaneous Allodynia", *Annals of Neurology*, 47:614-624, 2000.

[25] M. V. Carlos, C. David, F. V. Luis, D. V. Peter and R. S. Pramod, "Migraine: pathophysiology, pharmacology, treatment and future trends", *Current Vascular Pharmacology*, 1:71-84, 2003.

[26] J. B. Camphell, *Introduction to Remote Sensing*, Taylor and Francis, 3rd edition, 2002.

[27] D. Casasent and D. Psaltis, "Position, rotation, and scale invariant optical correlation", *Applied Optics*, 15:1795-1799, 1976.

[28] E. De Castro and C. Morandi, "Registration of Translated and Rotated Images Using Finite Fourier Transforms", *IEEE Transactions on Pattern Analysis and Machine Intelligence*, 5:700-703 , 1987.

[29] M. P. Cetingul and C. Herman, "A Heat Transfer Model of Skin Tissue for the Detection of Lesion: sensitivity analysis", *Physics in Medicine and Biology, IOP Science*, 55(19):5933-5951, 2010.

[30] J. S. Chang, H. Y. M. Liao, M. K. Hor, J. W. Hsieh and M. Y. Chern, "New Automatic Multi-Level Thresholding Technique for Segmentation of Thermal Images", *Image and Vision Computing, Elsevier*, 15(1):23-34, 1997.

[31] M. J. Cohen, D. L. McArthur and W. H. Rickles, "Comparison of Four Biofeedback Treatments for Migraine Headache: physiological and headache variables", *J Psychosomotic Medicine*, 42(5):463-480, 1980.

[32] A. J. Collins and J. A. Cosh, "Temperature and Biochemical Studies of Joint Inflammation", *Annals of the Rheumatic Diseases*, 29(4):386-392, 1970.

[33] A. J. Collins, E. F. Ring, J. A. Cosh and P. A. Bacon, "Quantitation of Thermography in Arthritis using Multi-Isothermal Analysis", *I. The Thermographic Index. Annals of the Rheumatic Diseases*, 33(2):113-115, 1974.

[34] O. Commowick, V. Arsigny, A. Isambert, J. Costa, F. Dhermain, F. Bidault, P.Y. Bondiau, N. Ayache and G. Malandain, "An Ecient Locally Ane Framework for the Smooth Registration of Anatomical Structures", *Biomedical Imaging: Nano to Macro, 3rd IEEE International Symposium.*, 478-481, 6-9 April 2006.

[35] T. D. Conwell, J. Giordano and S. J. Gulevich, *Functional Infrared Imaging in the Evaluation of Complex Regional Pain Syndrome, Type I: Current Pathophysiological Concepts, Methodology, Case Studie, Clinical Implications*, Medical Infrared Imaging Book, Edited by N. A. Diakides and J. D. Bronzino, CRC Press, Taylor and Francis Group, Chap 18:1-26, 2008.

[36] C. E. Costa and M. Petrou, "Automatic registration of ceramic tiles for the purpose of fault detection", *Machine Vision and Applications*, 11: 225-230, 1999.

[37] S. Craig and F. Evan, "Egan's Fundamentals of Respiratory Therapy", *St. Louis, Mosby Year Book*, 1999.

[38] "Cutaneous Receptor", *Wikipedia*. Retrieved from `http://en.wikipedia.org/wiki/Cutaneous_receptor`. (Accessed in June 2011).

[39] D. Dini, "FFT based Image Registration", *Final Year Project Report*, Department of Electrical and Electronic Engineering, Imperial College London, 2009.

[40] B. David, B. Rami and B. Lino, "Functional Imaging of the Human Trigeminal System: opportunities for new insights into pain processing in health and disease", *Wiley InterScience*, 61(1):107-125, 2004.

[41] M. B. David, "Cervicogenic Headache: a review of diagnostic and treatment strategies", *JAOA Supplement 2*, 105(4):16-22, 2005.

[42] B. David, B. Rami, M. Eric and B. Lino, "Functional Imaging of Migraine and the Trigeminal System", *Headache: American Head Society, Blackwell Publishing*, ISSN 0017-8748, S32-S38, 2006.

[43] A. P. Davis and A. H. Lettington, *Principles of Thermal Imaging*, In: S. C. Burnay, T. L. Williams and C.H. Jones, Editors, Applications of Thermal Imaging, Adam Hilger, Bristol, Philadelphia, 1:1-34, 1988.

[44] CGAL, Computational Geometry Algorithms Library. Retrieved from `http://www.cgal.org`. (Accessed in October 2012).

[45] Delaunay B., *Sur la sphère vide, Izvestia Akademii Nauk SSSR, Otdelenie Matematicheskikh i Estestvennykh Nauk*, 7:793-800, 1934

[46] Delaunay triangulation image. Retrieved from `http://en.wikipedia.org/wiki/Delaunay_triangulation`. (Accessed in October 2013).

[47] Z. S. Deng and J. Liu, "Mathematical Modelling of Temperature Mapping Over Skin Surface and Its Implementation in Thermal Disease Diagnostics", *Comp. in Biology and Medicine*, Elsevier, 34(6):495-521, 2004.

[48] T. M. Deserno, *Biomedical Image Processing*, Springer, 5:137, 2011.

[49] A. Dowson, "Cracking Pain: one expert helps to solve the mystery of migraine", *An article by the Director Of Headache Services, King's College Hospital London.* Retrieved from `http://www.dailymail.co.uk/health/article-1245522/Cracking-pain--expert-helps-solve-mystery-migraine.html`. (Accessed in September 2010).

[50] P. D. Drummond and J. W. Lance, "Extracranial Vascular Changes and the Source of Pain in Migraine Headache", *Annals of Neurology*, 13(1):32-37, 1983.

[51] P. D. Drummond and J. W. Lance, "Facial Temperature in Migraine, Tension-Vascular and Tension Headache", *Cephalalgia*, 4(3):149-58, 1984.

[52] S. Eddins, "Image Overlay Using Transparency", *The MathWorks News & Notes*. Retrieved from `http://www.mathworks.com/tagteam/6044791790v00Tips&Tricks-NN09.pdf`. (Accessed in October 2009).

[53] J. Edmeads, "Is Thermography a Marker for Vascular Headaches?", *Headache*, 26:47, 1986.

[54] G. Eggers, J. Mühling and R. J. Marmulla, "Template-based registration for image-guided maxillofacial surgery", *Oral Maxillofac Surg.* , 63(9):1330-6, 2005.

[55] E. L. Elster, "Upper Cervical Chiropractic Care for A Patient with Chronic Migraine Headaches with an Appendix Summarizing and Additional 100 Headache Cases", *J Vertebral Subluxation Research*, August 3, 2003.

[56] M. J. M. English, "Physical Principles of Heat Transfer", *Focus on: perioperative hypothermia, Current Anaesthesia & Critical Care, Harcourt Publishers Ltd*, 12:66-71, 2001.

[57] M. H. A. Fadzil, I. I. Lila, P. A. Venkatachalam and T. V. N. Karunakar, "Extraction and Reconstruction of Retinal Vasculature", *J Medical Engineering Technology*, 31(6):435-442, 2007.

[58] M. H. A. Fadzil and I. I. Lila, "A Non Invasive Method for Analysing the Retina for Ocular Manifested Diseases", *International Bureau Patent*, Pub. No:WO/2010/030159, 2010.

[59] S. Periaswamy and H. Farid, "Elastic Registration in the Presence of Intensity Variations", *IEEE Transactions on Medical Imaging*, 22(7):865-874, 2003.

[60] J. Fei, I. Pavlidis and J. Murthy, "Thermal Vision for Sleep Apnea Monitoring", *MICCAI 2009*, Springer-Verlag Berlin Heidelberg Part II, LNCS 5762:1084-1091, 2009.

[61] S. Ferrero, S. Pretta, S. Bertoldi, P. Anserini, V. Remorgida, M. Del Sette, C. Gandolfo and N. Ragni, "Increased Frequency of Migraine among Women with Endometriosis", *Human Reproduction*, 19(12):2927-2932, 2004.

[62] N. Fett and V. P. Werth,"Update on morphea, Part II. Outcome measures and treatment", *J Am. Acad. Dermatol.*, 64(2):231-242, 2011.

[63] B. Fischer and J. Modersitzki, A unified approach to fast image registration and a new curvature based registration technique*, Linear Algebra and its Applications*, 380:107–124, 2004.

[64] H. Foroosh, J. B. Zerubia and M. Berthod, "Extension of phase correlation to subpixel registration", *IEEE Trans. Image Processing*, 11(3):188-200, 2002.

[65] M. Frize, C. Herry and R. Roberge, "Processing of Thermal Images to Detect Breast Cancer: comparison with previous work", *Proceedings of the Second Joint EMBSBMES Conference Houston, USA*, 2:1159-1160, 2002.

[66] I. Fujimasa, "Pathophysiological Expression and Analysis of Far Infrared Thermal Images", *IEEE Engineering in Medicine and Biology Magazine*, 17(4):34-42, 1998.

[67] I. Fujimasa, T. Chinzei and I. Saito, "Converting Far Infrared Image Information to other Physiological Data", *IEEE Engineering in Medicine and Biology*, 19(3):71-76, 2000.

[68] M. Garbey, A. Merla and I. Pavlidis, "Estimation of Blood Flow Speed and Vessel Location from Thermal Video", *Proceedings of the 2004 IEEE Computer Society Conference on Computer Vision and Pattern Recognition (CVPR'04)*, 1:356-363, 2004.

[69] P. J. Goadsby, R. B. Lipton, and M. D. Ferrari, "Migraine. Current Understanding and Treatment", *N Engl Journal Medical*, 346:257-270, 2002.

[70] G. Goldberg, "Thermography and Magnetic Resonance Imaging Correlated in 35 cases", *Thermology*, 1:207-211, 1986.

[71] R. Gonzalez R. and R. Woods, *Digital Image Processing*, Second Edition, Prentice Hall, 2002.

[72] A. Goshtaby, "2-D and 3-D Image Registration for Medical, Remote Sensing, and Industrial Applications", *Wiley Press*, 2005.

[73] S. Govindan, "Imaging the Effect of Sumatriptan in Migraine Treatment", *Thermology International*, 16:61-64, 2006.

[74] J. Green, "Neurothermography", *Seminars in Neurology*, 7(4):313-316, 1987.

[75] A. B. Gregory. *Digital Image Processing.* John Wiley and Sons Inc. 1994.

[76] M. W. Grenn, J. Vizgaitis, J. G. Pellegrino and P. Perconti, "Infrared Camera and Optics for Medical Applications", *Medical Infrared Imaging Book*, Edited by N. A. Diakides and J. D. Bronzino, CRC Press (2008), Taylor and Francis Group, (5):1-14, 2008.

[77] A. C. Guyton, *Medical Physiology*, Philadelphia, PA: WB Saunders Co, 1991.

[78] P. Haehnel and M. Gautherie, "Long-term Assessment of Breast Cancer Risk by Thermal Imaging", *Biomedical Thermology*, 279-301, 1980.

[79] J. V. Hajnal, D. L. G. Hill and D. J. Hawkes. *Medical Image Registration*, The Biomedical Engineering Series, CRC Press, 2001.

[80] Handbook: "The Ultimate Infrared Handbook for R&D Professionals-Resource Guide for Using Infrared in the Research and Development Industry", *FLIR Systems, AB.* Retrieved from `http://www.flir.com/uploadedFiles/Thermography/00_Landing_pages/Direct_Sales_Landing_pages/RD-Handbook.pdf`. (Accessed in June 2010).

[81] Haralick, M. Robert and L. G. Shapiro, *Computer and Robot Vision*, Addison-Wesley, (I):28-48, 1992.

[82] J. R. Harding, "Investigating Deep Venous Thrombosis with Infrared Imaging", *IEEE Engineering in Medicine and Biology*, 17(4):43-46, 1998.

[83] J. Hart, B. Omolo, W. R. Boone, C. Brown, and A. Ashton, "Reliability of three methods of computer-aided thermal pattern analysis", *J Canadian Chiropractic Association*, 51(3):175–185, 2007.

[84] F. J. Harris, "On the use of Windows for Harmonic Analysis with the Discrete Fourier Transform", *Proceedings of the IEEE,* 1978. 66(1): 51–83. doi:10.1109/PROC.1978.10837. Article on FFT windows which introduced many of the key metrics used to compare windows.

[85] R. Happle and A. Assim, "The lines of Blaschko on the head and neck", *J Am Acad Dermatol,* 44:612–15, 2001.

[86] R. A. Harway, "Precision Thermal Imaging of the Extremities", *Orthopedics*, 9(3):379-382, 1986.

[87] J. F. Head, F. Wang and R. L. Elliot, "Breast Thermography Is a Noninvasive Prognostic Procedure That Predicts Tumor Growth Rate in Breast Cancer Patients", *Annals of the New York Academy of Sciences,Breast Cancer: from Biology to Therapy, Pisa Symposia in Oncology* , 698:153-158, 1993.

[88] A. L. Herrick, H. Ennis, M. Bhushan, A. J. Silman and E. M. Baildam, "Incidence of childhood linear Scleroderma and systemic sclerosis in the UK and Ireland", *Arthritis Care and Research, American College of Rheumatology*, 60(2):213-218, 2010.

[89] C. L. Herry and M. Frize, "Digital Processing Techniques for the Assessment of Pain with Infrared Thermal Imaging", *Proceedings of the 24th Annual International Conference of the IEEE Engineering in Medicine and Biology Society*, 2:1157-1158, 2002.

[90] C. L. Herry and M. Frize, "Quantitative Assessment of Pain-related Thermal Dysfunction through Clinical Digital Infrared Thermal Imaging", *Biomedical Engineering Online*, 3:19, 2004. Retrieved in Jun 2010 from `http://www.biomedical-engineering-online.com/content/3/1/19`. (Accessed in June 2010).

[91] C. L. Herry, M. Frize and R. A Goubran, "Segmentation and Landmark Identification in Infrared Images of the Human Body", *Proceedings of the 28th IEEE EMBS Annual International Conference*, 957-960, 2006.

[92] C. L. Herry, M. Frize and R. A. Goubran, "Search for Abnormal Thermal Patterns in Clinical Thermal Infrared Imaging", *MeMeA 2008 -IEEE International Workshop on Medical Measurements and Applications*, 9-10 May:61-65, 2008.

[93] D. L. G. Hill and D. J. Hawkes: *Across-modality registration using intensity-based dissimilar criterion*, Handbook of Medical Imaging: Processing and Analysis, Academic Press, pp. 537–553, 2000.

[94] Hilotherapy information folder. Retrieved from `http://www.hilotherm.si/files/Hilotherm/hilotherapyinformationfolder_en.pdf`. (Accessed in May 2013).

[95] R. M. Hoffman, D. L. Kent and R. A. Deyo, "Diagnostic Accuracy and Clinical Utility of Thermography for Lumbar Radiculopathy. A meta-analysis", *Spine (Phila Pa 1976)*, 16(6):623-628, 1991.

[96] M. Holden, "A Review of Geometric Transformations for Nonrigid Body Registration", *IEEE Transactions on Medical Imaging*, 27(1):111-128, 2008.

[97] H. Hooshmand, M. Hashmi and E. M. Phillips, "Infrared Thermal Imaging as a Tool in Pain Management - An 11 Year Study, Part II:Clinical Applications", *Thermology International*, 11:1-13, 2001.

[98] K. J. Howell, G. Martini, K. J. Murray, R. E. Smith and C. M. Black, "Infrared thermography for the assessment of localised scleroderma in children", *Thermology International,* 10/ 4: 204-209, 2000.

[99] K. J. Howell, A. Lavorato, M. T. Visentin, R. E. Smith, G. Schaefer, C. D. Jones, L. Weibel, C. P. Denton, J. I. Harper and P. Woo, "Validation of a protocol for the assessment of skin temperature and blood flow in childhood localised scleroderma", *Skin Research and Technology, John wileys and Sons*, 15: 346–356, 2009.

[100] K. J. Howell and J. M. Collier, "Thermography of Facial Skin Temperature in Healthy Subjects During Cooling of the Face with Hilotherapy", *EAT2012 Book of Proceedings – Appendix 1 of Thermology international,* 22(3):110-113, 2012.

[101] T. J. Hubbard and C. R. Denegar, "Does cryotherapy improve outcomes with soft tissue injury?", *J Athl Train 2004*, 39:278-279.

[102] I. Hymes, W. Boydell and B. Prescott, "Thermal Radiation: physiological and pathological effects", *Institution of Chemical Engineers, United Kingdom*, 1996.

[103] L. Ikonen, "Distance transforms on gray-level surfaces", *PhD thesis*, Lappeenranta University of Technology, 2006.

[104] Infrared camera series VarioCAM ® hr head 700. Retrieved from `http://www.infratec.de/en/thermography/infrared-camera/variocamr-hr-head-700-series.html`. (Accessed in May 2011).

[105] Thermal imaging based health care provider, "Image of Health". Retrieved from `http://www.fightbc.com/OurServices/Thermography/WomensHealthScreen.aspx`. (Accessed in June 2010).

[106] L. I. Izhar and M. Petrou, "Thermal Imaging in Medicine", *Advances in Imaging and Electron Physics*, 171(2):41–114, 2012.

[107] T. Jakubowska, B. Wiecek, M. Wysocki and C. Drews-Peszynski, "Thermal Signatures for Breast Cancer Screening Comparative Study", *Proceedings of the 25th Annual International Conference of the IEEE EMBS*, 1117-1120, 2003.

[108] T. Jakubowska, B. Wiecek, M. Wysocki, C. Drews-Peszynski, and M. Strzelecki, "Classification of Breast Thermal Images using Artificial Neural Network", *26th International Conference of IEEE Engineering in Medicine and Biology Society, IEMBS'04*, San Francisco, USA, 1-5 Sept, 2:1155-1158, 2004.

[109] A. Jarc, J. Pers, P. Rogelj, M. Perse and S. Kovacic, "Texture features for affine registration of thermal (FLIR) and visible images", *Computer Vision Winter Workshop*, Graz Technical University, St. Lambrecht, Austria, February 6-8, 2007.

[110] L. Jiang, W. Zhan and M. H. Loew, "Modelling Thermography of Tumorous Human Breast: from forward problem to inverse problem solving", *Biomedical Imaging: From Nano to Macro, 2010 IEEE International Symposium*, 205-208, 2010.

[111] B. F. Jones, "A Reappraisal of the Use of Infrared Thermal Image Analysis in Medicine", *IEEE Transactions on Medical Imaging*, 17(6):1019-1027, 1998.

[112] B. F. Jones and P. Plassmann, "Digital Infrared Thermal Imaging of Human Skin:computational approaches to image processing for improved interpretation and analysis", *IEEE Engineering in Medicine and Biology*, 21:41-48, 2002.

[113] A. A. Karamitrou, M. Petrou and G. N. Tsokas, "Registration of geophysical images", *IEEE International Geoscience and Remote Sensing Symposium (IGARSS)*, Vancouver, BC, Canada, July 24-29, 2011, 4184-4187.

[114] D. Kennedy and D. Seely, "Comparative Review of Thermography as a Breast Screening Technique", *Integrative Cancer Therapies*, 8(1):9-16, 2009.

[115] M. L. Kessler, "Image registration and data fusion in radiation therapy", *British Journal of Radiology*, 79:S99-S108, 2006.

[116] P. Keysser, "Observational study with cryotherapy Hilotherm in rheumatoid arthritis", *Orthopedic Specialist*. Retrieved from `http://hiloterapia.es/pdfs/traumatologia.pdf`. (Accessed in October 2013).

[117] Y. S. Kim and Y. E. Cho, "Pre- and Postoperative Thermographic Imagings of Lumbar Disk Herniations", *J Korean Neurosurgical Society*, 22(1):71-82, 1993.

[118] M. M. Khan, M. Ingleby and R. D. Ward, "Automated Facial Expression Classification and Affect Interpretation Using Infrared Measurement of Facial Skin Temperature Variations", *ACM Transactions on Autonomous and Adaptive Systems*, 1(1):91-113, 2006.

[119] M. F. Khan, *Non-rigid Image Registration for Deep Brain Stimulation Surgery*, A PhD Thesis, School of Electrical and Computer Engineering Georgia Institute of Technology, December, 2008.

[120] M. M. Khan, R. D. Ward and M. Ingleby, "Classifying Pretended and Evoked Facial Expressions of Positive and Negative Affective States using Infrared Measurement of Skin Temperature", *ACM Transactions on Applied Perception*, 6(1):1-22, 2009.

[121] J. Kim and J.A. Fessler, "Intensity-based image registration using robust correlation coefficients", *IEEE Transactions on Medical Imaging*, 23(11):1430-1444, 2004.

[122] J. Kittler and P. C. Young, "A New Approach to Feature Selection based on the Karhunen-Loeve Expansion", *Pattern Recognition 5*, 4:335-352, 1973.

[123] H. Knaf, P. Lang and S. Zeiser, "Diagnosis Aiding in Regulation Thermography using Fuzzy Logic", *Fraunhofer ITWM Report No 57(2003)*, 2003.

[124] J. Koay, C. Herry and M. Frize, "Analysis of Breast Thermography with an Artificial Neural Network", *Proceedings of the 26th Annual Int. Conf. of the IEEE EMBS*, 1159-1162, 2004.

[125] S. G. Kong, J. Heo, F. Boughorbel, Y. Zheng, B. R. Abidi, A. Koschan, M. YI and M. A. Abidi, "Multiscale Fusion of Visible and Thermal IR Images for Illumination-Invariant Face Recognition", *International Journal of Computer Vision,* 71(2): 215-233, 2007.

[126] V. A. Kovalev and M. Petrou, "Non-rigid volume registration of medical images", *J Computing and Information Technology, CIT*, 6(2):181-190, 1998.

[127] L. Kudrow, "Thermographic and Doppler Flow Asymmetry in Cluster Headache", *Headache*, 19(4):204-208, 1979.

[128] L. Kudrow, "A Distinctive Facial Thermographic Pattern in Cluster Head-ache the "Chai" Sign", *Headache*, 25:33-36, 1985.

[129] C. D. Kuglin and D. C. Hines, "The phase correlation image alignment method", *Proceeding of IEEE International Conference on Cybernetics and Society*, 163-165, 1975.

[130] A. Lakhssassi, E. Kengne and H. Semmaoui, "Modifed Pennes' Equation Modelling Bioheat Transfer in Living Tissues: analytical and numerical analysis", *Natural Science*, 2(12):1375-1385, 2010.

[131] J. W. Lance, M. Anthony and B. Somerville, "Thermographic, Hormonal and Clinical Studies in Migraine", *Headache*, 10(3):93-104, 1970.

[132] H. Ledoux and C. Gold, "An Efficient Natural Neighbour Interpolation Algorithm for Geoscientific Modelling", *Developments in Spatial Data Handling, Springer Berlin Heidelberg*, 97-108, 2005.

[133] P. A. Legg, P. L. Rosinay, D. Marshallaz and J. E. Morgan. "Incorporating neighbourhood feature derivatives with mutual information to improve accuracy of multi-modal image registration", *Medical Imaging Understanding and Analysis*, 39-43. 2008.

[134] J. P. Lewis, "Fast Normalized Cross-Correlation," *Industrial Light & Magic. An extended version of J. P. Lewis, "Fast template matching," Vis. Inf.*, pp. 120–123, 1995.

[135] E. Levina and P. Bickel, "The Earth Movers Distance is the Mallows Distance: Some Insights from Statistics", *in Proceedings of the IEEE International Conference on Computer Vision (ICCV)*, 251-256, 2001.

[136] T. M. Lillesand and R. W. Kiefer, *Remote Sensing and image interpretation*, John Wiley and Sons, Inc, 4th edition, 2000.

[137] M. Linde, "Migraine: a review and future directions for treatment", *Acta Neurologica Scandinavica*, 114(2):71-83, 2006.

[138] "Literature Review of Breast Cancer Thermography". Retrieved from `http://www.medithermclinic.com/Breast/BREAST%20THERMOGRAPHY%20-%20REVIEWED.pdf`. (Accessed in July 2010).

[139] J. Liu, Y. X. Zhou and Z. S. Deng, "Temperature Sensor Array System for Thermal Diagnostics on Human Disease", *Proceedings of the 23rd Annual Conference IEEE/EMBS*, 4:3188-3191, 2001.

[140] J. Liu and Z. S. Deng, "Numerical Methods for Solving Bioheat Transfer Equations in Complex Situations", *Advances in Numerical Heat Transfer*, 3(3):75-120, 2009.

[141] K. Mabuchi, T. Chinzei, I. Fujimasa, S. Haeno, K. Motomura, Y. Abe and T. Yonezawa, "Evaluating Asymmetrical Thermal Distributions through Image Processing", *IEEE Engineering in Medicine and Biology*, 47-55, 1998.

[142] R. Maini and H. Aggarwal, "Study and Comparison of Various Image Edge Detection Techniques", *International Journal of Image Processing (IJIP)*, 3(1):1-12, 2009.

[143] J. B. A. Maintz and M. A. Viergever, "A survey of medical image registration. Medical Image Analysis", 2(1):1-36, 1998.

[144] D. Mandic, "Spectral Estimation and Adaptive Filtering," *lecture course notes, unpublished,* 2009.

[145] S. Manickam, S.D. Roth and T. Bushman, "Intelligent and optimal normalized correlation for high-speed pattern matching", *In Nepcon West*, 27 February - 2 March2000.

[146] G. Martini, K. J . Murray, K. J. Howell, J. Harper, D. Atherton, P. Woo, F. Zulian and C. M. Black,"Juvenile-onset localized scleroderma activity detection by infrared thermography", *Paediatric Rheumatology/Series Editor: P. Woo, Rheumatology*, 41:1178-1182, 2002.

[147] M. Marzec, R. Koprowski and Z. Wrobel, "Automatic Temperature Measurement on Thermograms for Headache Diagnosis", *Measurements Automation Control Magazine*, 55(11):923-926, 2009.

[148] A. Merla and G. L. Romani, "Functional Infrared Imaging in Medicine: quantitative diagnostic approach", *Proceedings of the 28th IEEE EMBS Ann. Int. Conf.*, 1:224-227, 2006.

[149] M. Mital and E. P. Scott, "Thermal Detection of Embedded Tumors using Infrared Imaging", *J Biomedical Engineering*, 129(1):33-39, 2007.

[150] A. Modabber, M. Rana, A. Ghassemi, M. Gerressen, N. C. Gellrich, F. Hölzle1 and M. Rana, "Three-dimensional evaluation of postoperative swelling in treatment of zygomatic bone fractures using two different cooling therapy methods: a randomized, observer-blind, prospective study", *Trials 2013*, 14:238.

[151] Moro A, Gasparini G, Marianetti TM, Boniello R, Cervelli D, Di Nardo F, Rinaldo F, Alimonti V, "Hilotherm efficacy in controlling postoperative facial edema in patients treated for maxillomandibular malformations", *J Craniofac Surg.*, November 2011, 22(6), 2114-2117.

[152] L. S. Motta, A. Conci1, R. C. F. Lima and E. M. Diniz, "Automatic Segmentation on Thermograms in Order to Aid Diagnosis and 2D Modeling", *Annals 2010 CSBC*, 1610-1619, 2010.

[153] A. Myronenko, *Non-rigid Image Registration: Regularization, Algorithms and Applications,* PhD thesis, Department of Science & Engineering School of Medicine at Oregon Health & Science University, 2010.

[154] National Cancer Institute, U.S. National Institutes of Health, "Breast Cancer". Retrieved from `http://www.cancer.gov/cancertopics/types/breast`. (Accessed in January 2011).

[155] L. Shure, "Computational Geometry in MATLAB R2009a, Part II". Retrieved from `http://blogs.mathworks.com/loren/2009/07/22/computationalgeometryinmatlabr2009apartii/#9`. (Accessed in July 2013).

[156] Natural neighbour. Wikipedia. Retrieved from `http://en.wikipedia.org/wiki/Natural_neighbour`. (Accessed in April 2013).

[157] D. A. Nelson, "Invited Editorial on Pennes 1948 Paper Revisited", *Journal of Applied Physiology*, 85:2-3, 1998.

[158] E. Y. K. Ng, Y. Chen and L. N. Ung, "Computerized Breast Thermography: Study of Image Segmentation and Temperature Cyclic Variations", *J Medical Engineering & Technology*, 25(1):12-16, 2001.

[159] . Y. K Ng and N. M. Sudharsan, "Computer simulation in conjunction with medical thermography as an adjunct tool for early detection of breast cancer", *BMC Cancer*, 4(17), 2004.

[160] E. Y. K. Ng and E. C. Kee, *Fever Mass Screening Tool for Infectious Diseases Outbreak: Integrated Artificial Intelligence with Bio-Statistical Approach in Thermogram Analysis*, Medical Infrared Imaging Book, Edited by N. A. Diakides and J. D. Bronzino, CRC Press (2008), Taylor and Francis Group, Chap 16, 2008.

[161] E. Y. K. Ng, "A Review of Thermography as Promising Non-invasive Detection Modality for Breast Tumor", *International Journal of Thermal Sciences*, 48(5):849-859, 2009.

[162] A. D. Nicholas, M. Diakides, J. C. Lupo, J. L. Paul and R. Balcerak, *Advances in Medical Infrared Imaging*, Medical Infrared Imaging Book, Edited by N. A. Diakides and J. D. Bronzino, CRC Press (2008), Taylor and Francis Group, Chapter 1, 2008.

[163] A. Z. Nowakowski, "Advances of Quantitative IR Thermal Imaging in Medical Diagnostics". Retrieved from `http://qirt.gel.ulaval.ca/archives/qirt2006/papers/101.pdf`. (Accessed in Jun 2010).

[164] O. D. Nurhayati, T. S. Widodo, A. Susanto and M. Tjokronagoro, "First Order Statistical Feature for Breast Cancer Detection using Thermal Images", *in WASET*, 46:382-384, 2010.

[165] J. Orchard, "Efficient Global Weighted Least-Squares Translation Registration in the Frequency Domain", *in Proceedings of ICIAR 2005*, LNCS 3656:116-124, 2005.

[166] M. Palfy and B. J. Papez, "Diagnosis of Carpal Tunnel Syndrome from Thermal Images Using Artificial Neural Networks", *in Twentieth IEEE International Symposium on Computer-Based Medical Systems (CBMS 07)*, 59-64, 2007.

[167] A. S. Paller, "Piecing together the puzzle of cutaneous mosaicism ", *: J Clin. Invest.*, 114:1407–1409, 2004. doi:10.1172/JCI200423580.

[168] W. Pan, K. H. Qin and Y. Chen, "An Adaptive-Multilayer fractional fourier transform approach for image registration", *IEEE Transactions on Pattern Analysis and Machine Intelligence*, 31(3):400-413, 2009.

[169] B. J. Papez, M. Palfy, M. Mertik and Z. Turk, "Infrared Thermography based on Artificial Intelligence as a Screening Method for Carpal Tunnel Syndrome Diagnosis", *The J International Medical Research*, 37:779–790, 2009.

[170] G. Parrinello, S. Paterna, P. Di Pasquale, A. Pinto, A. Cardinale, T. Maniscalchi, C. Cottone, G. Follone, A. Tuttolomondo, P. Bologna, D. Colomba, A. D'Angelo, A. Ortoleva, L. Garofalo, G. Piovana, E. Capo-dieci, A. Bova, A. Giubilato and G. Licata, "Effect of Subcutaneous Suma-Triptan on Head Temperature in Migraines Drugs", *Exp Clin Res*, 24(4):197-205, 1998.

[171] I. Pavlidis, J. Levine and P. Baukol, "Thermal Image Analysis for Anxiety Detection", *in Proceedings of International Conference on Image Processing*, 2:315-318, 2001.

[172] I. Pavlidis and J. Levine, "Thermal Image Analysis for Polygraph Testing", *IEEE Engineering in Medicine and Biology Magazine*, 21(6):56-64, 2002.

[173] I. Pavlidis, "Continuous Physiological Monitoring", *in Proceedings of the 25th Annual International Conference of the IEEE EMBS*, 1084-1087, 2003.

[174] I. Pavlidis, J. Dowdall, N. Sun, C. Puri, J. Fei, and M. Garbey, "Interacting with Human Physiology", *Computer Vision and Image Understanding*, 108:150-170, 2007.

[175] P. Perrone, D. Porazzi, P. L. Carnaghi and G. Landi, "Thermographic Patterns in Migraine", *Acta Thermographica*, 5:129-132, 1980

[176] L. S Peterson, A. M. Nelson, D. W. P. Su, T. Mason, W. M. O'Fallon and S. E. Gabriel, "The epidemiology of morphea (localized scleroderma) in Olmsted County 1960–1993", *J Rheumatol*, 24:73-80, 1997.

[177] M. Petrou, "Image Registration: an overview", *Advances in Imaging and Electron Physics*, 130:243-291, 2004.

[178] M. Petrou and P. Garcia-Sevilla, *Image Processing: dealing with texture*, John Wiley, 2006.

[179] M. Petrou and C. Petrou, *Image Processing: the fundamentals*, 2nd Edition, John Wiley, 2010.

[180] M. Pidwirny, *The Nature of Radiation*, Fundamentals of Physical Geography, 2nd Edition, 2006. Retrieved from `http://www.physicalgeography.net/fundamentals/6f.html`. (Accessed in August 2010).

[181] J. P. W. Pluim, J. B. A. Maintz, M. A. Viergever, "Mutual-Information-Based Registration of Medical Images: A Survey", *IEEE Transactions on Medical Imaging*, 22(8):986-1004, 2003.

[182] M. J. Polizzotto, "Evaluation and Treatment of the Adult Patient with Migraine", *The J Family Practice*, 51(2):161-167, 2002.

[183] P. Poul-Erik, *Somatosensory System and Disorders*, Physiology and Pathophysiology text book, Pharmpedia (The Free Pharmaceutical Encyclopedia), II(3). Retrieved from `http://mednote.dk/index.php/Somatosensory_system_and_disorders`. (Accessed in December 2011).

[184] W. K. Pratt, *Digital Image Processing*, 3rd Edition, A Wiley-Interscience Publication, 5(15):463-469

[185] "Principle of thermal imaging". Retrieved from `http://www.inmes.hr/pdf/thermography.pdf`. (Accessed in August 2010).

[186] R. J. Pryputniewicz, "Lecture 29(2): radiation - heat transfer, properties, shape factor and relations between shape factors", *Based on Textbook by J. P. Holman, 2002, Heat transfer, 9th ed., McGraw-Hill, New York*, Worcester Polytechnic Institute (WPI). Retrieved from `http://users.wpi.edu/chslt/courses/es3003/lect29_2.pdf`. (Accessed in October 2010).

[187] C. Puri, L. Olson, I. Pavlidis, J. Levine and J. Starren, "StressCam: non-contact measurement of users emotional states through thermal imaging", *Conference on Human Factors in Computing Systems, Portland, Oregon, USA, 2-7 April*, 1725-1728, 2005.

[188] H. Qi and J. F. Head, "Asymmetry Analysis using Automatic Segmentation and Classification for Breast Cancer Detection in Thermograms", *in Proceedings of the 23rd Annual EMBS International Conference*, 2866-2869, 2001.

[189] H. Qi, P. T. Kuruganti and Z. Liu, "Early Detection of Breast Cancer using Thermal Texture Maps", *Symposium on Biomedical Imaging: Macro to Nano*, 309-312, 2002.

[190] H. Qi, P. T. Kuruganti and W. E. Snyder, *Detecting Breast Cancer from Thermal Infrared Images by Asymmetry Analysis*, Medical Infrared Imaging Book, Edited by N. A. Diakides and J. D. Bronzino, CRC Press (2008), Taylor and Francis Group, Chapter 11, 2008.

[191] H. Qi and A. D Nicholas, "Infrared Imaging in Medicine", 1998. Retrieved from `http://www.iamtonline.org`. (Accessed in June 2010).

[192] C. Quek, W. Irawan and E. Y. K. Ng, "A novel Brain-inspired Neural Cognitive Approach to SARS Thermal Image Analysis", *Expert Systems with Applications*, 37(4):3040-3054, 2010.

[193] M. Rana, N. C. Gellrich, A. Ghassemi, M. Gerressen, D. Riediger and A. Modabber, "Three-Dimensional Evaluation of Postoperative Swelling After Third Molar Surgery Using 2 Different Cooling Therapy Methods: A Randomized Observer-Blind Prospective Study", *American Association of Oral and Maxillofacial Surgeons J Oral Maxillofac Surg.*, 69:2092-2098, 2011.

[194] B. S. Reddy and B. N. Chatterji, "An FFT-Based technique for translation, rotation and scale-invariant image registration", *IEEE Transactions on Image Processing*, 5(8): 1266-1271, 1996.

[195] A. A. C. Rhodes, K. L. Johnson and J. LeMoigne, "Multiresolution registration of remote sensing imagery by optimization of mutual information using a stochastic gradient", *IEEE Transactions on Image Processing*, 12(12):1495-1511, 2003.

[196] E. F. J. Ring and A. J. Collins, "Quantitative Thermography", *Rheumatology Physical Medicine*, 10(7):337-341, 1970.

[197] E. F. J. Ring, " Cold Stress Test for the Hands", *The Thermal Image in Medicine and Biology*, 237-240, 1995.

[198] E. F. Ring and K. Ammer, "*Thermal Imaging in Diseases of the Skeletal and Neuromuscular Systems*", Medical Infrared Imaging Book, Edited by N. A. Diakides and J. D. Bronzino, CRC Press (2008), Taylor and Francis Group, Chap. 17, 2008.

[199] G. K. Robert, "Migraine and Tension-Type Headache: an assessment of challenges in diagnosis", *Neurology*, 58(9 suppl 6):S15-S20, 2002.

[200] P. Rogelj, *Non-Rigid Registration of Multi-Modality Images*. A PhD thesis, Faculty of Electrical Engineering, University of Ljubljana, 2003.

[201] P. Rogelj, S. Kovacic, and J.C. Gee, "Point similarity measures for non-rigid registration of multi-modal data". *Computer Vision and Image Understanding*, 92:112-140, 2003.

[202] D. Rueckert, L. I. Sonoda, C. Hayes, D. L. G. Hill, M. O. Leach, and D. J. Hawkes. "Deformations: Application to Breast MR Images", *IEEE Transactions on Medical Imaging*, 18(8): 712-721,1999.

[203] J. P. Russ, *The Image Processing Handbook*, 6th Edition, CRC Press, Taylor and Francis Group, 8:488-489, 2011.

[204] G. Schaefer, R. Tait, K. Howell, A. Hopgood, P. Woo and J. Harper, "Automated overlay of infrared and visual medical images", *User Centered Design for Medical Visualization*, 8:174-183, 2008.

[205] G. Schaefer, M. Zavisek and T. Nakashima, "Thermography based Breast Cancer Analysis using Statistical Features and Fuzzy Classification", *J Pattern Recognition*, 42(6):1133-1137, 2009

[206] N. Selvarasu, V. Sangeetha and N. M. Nandhita, "Performance Evaluation of Image Processing Algorithms for Automatic Detection and Quantification of Abnormality in Medical Thermograms", *International Conference on Computational Intelligence and Multimedia Applications*, 3:388-393, 2007.

[207] N. Selvarasu, A. Nachiappan M. D. and N. M. Nandhita, "Feature Extraction Algorithms for Abnormality Quantification from Medical Thermograms", *International Journal of Recent Trends in Engineering*, 1(3):350-352, 2009.

[208] W. K. Seok, M. L. Seung and H. J. Seong, "Validation of Thermography in the Diagnosis of Acute Cervical Sprain", *J of Korean Neurosurgical Society*, 36(4):297–301, 2004.

[209] R. Sherman, R. Barja and G. Bruno, "Thermographic correlates of chronic pain: analysis of 125 patients incorporating evaluations by a blind panel", *Archives of Physical Medical Rehabilitation*, 68(5 pt 1):273-279, 1997.

[210] T. C. Shih, P. Yuan, W. L. Lin and H. S. Kou, "Analytical Analysis of the Pennes Bioheat Transfer Equation with Sinusoidal Heat Flux Condition on Skin Surface", *Medical Engineering & Physics*, 29(9):946-953, 2007.

[211] R. Simpson, G. Machin, H. McEvoy and R. Rusby, "Traceability and calibration in temperature measurement: a clinical necessity", *J Med Eng Technol,* 30: 212-217, 2006.

[212] R. Sibson, *A brief description of natural neighbour interpolation*, In V Barnett, editor, Interpreting Multivariate Data, Wiley, New York, USA, 21–36.

[213] K. B. Siti, *Elastic image registration for landslides monitoring*, A PhD Thesis, University of Surrey, 2006.

[214] K. B. Siti and M. Petrou, "Elastic image registration for landslides monitoring. *International Journal of Signal Processing, Image Processing and Pattern Recognition*, 3(3), 2010.

[215] P. Soille, "Generalized geodesy via geodesic time*", Pattern Recognition Letters*, 15:1235-1240, 1994.

[216] P. Soille, "Morphological Image Analysis:principles and application", *2nd Edition, Secaucus, NJ, Springer-Verlag*, 2(7):234-238, 2003.

[217] A. Sotiras, C. Davatzikos and N. Paragios, "Deformable Image Registration: A Survey", *IEEE Transactions on medical imaging*, 32(7):1153-1189, 2013.

[218] K. Wojaczynska-Stanek and E. Marszal, "Thermographic Examination in Children with Headache", *Thermology International*, 16:53-60, 2006.

[219] J. Steketee, "Spectral Emissivity of the Skin and Pericardium", *Phys. Med. Biol.*, 18(5):686-694, 1973.

[220] T. Strachan and A. P. Read, *Human Molecular Genetics* (2nd ed.). New York: Wiley–Liss. Glossary.

[221] B. Swerdlow and J. N. Dieter, "The Validity of the Vascular 'cold patch' in the Diagnosis of Chronic Headache", *Headache*, 26(1):22-26, 1986.

[222] J. M. Tan, E. Y. K. Ng, R. U. Acharya, L. G. Keith and J. Holmes, "Comparative Study on the Use of Analytical Software to Identify the Different Stages of Breast Cancer using Discrete Temperature Data", *J Med. Syst.*, 33:141-153, 2009.

[223] X. Tang and H. Ding, "Asymmetry Analysis of Breast Thermograms with Morphological Image Segmentation", *in Proceeding of the IEEE Engineering in Medicine and Biology 27th Annual Conference 2005*, 1680-1683.

[224] W. Tarnawski, G. Schaefer,T. Nakashima and L. Miroslaw, *Applications of Fuzzy Rule-based Systems in Medical Image Understanding*, in Rough Fuzzy Image Analysis: foundations and methodologies, S. K. Pal and J. F. Peters (eds), CRC Press, Chap 6, 2010.

[225] S. Theodoridis and K. Koutroumbas, "Pattern Recognition, Fourth Edition", *Academic Press publication*, 2009.

[226] "Understanding Infared Camera Thermal Image", *Quality Electrophysics Resource Center: Scientific Imaging*, Electrophysics Corp. 2011. Retrieved from `http://www.electrophysics.com/e/dl-files/whitepapers_ph/WP-Ph-TIQ-v05.pdf`. (Accessed in October 2013).

[227] S. S. Thunuguntla, *Object tracking using log-polar transformation*, MSc thesis, Louisiana State University, 2005. Retrieved from `http://etd.lsu.edu/docs/available/etd-07072005-113808/`. (Accessed in February 2012).

[228] D. Thomas, D. Cullum and G. Siahamis, "Infrared Thermographic Imaging, Magnetic Resonance Imaging, CT Scan and Myelography in Low Back Pain", *British Society of Rheumatology*, 29(4):268-273, 1990.

[229] D. M. Tsai, "A Fast Thresholding Selection Procedure for Multimodal and Unimodal Histograms", *Pattern Recognition Letters 1995*, 16(6):653-666, 1995.

[230] J. W. Tukey, "An introduction to the calculations of numerical spectrum analysis", *Spectral Analysis of Time Series*, 25–46, 1967.

[231] G. Tzimiroupoulos, V. Argyriou, S. Zafeiriou and T. Stathaki, "Robust FFT-based scale-invariant image registration with image gradients", *IEEE Transactions on Pattern Analysis and Machine Intelligence*, 32(10):1809-1908, 2010.

[232] S. Uematsu, "Symmetry of Skin Temperature Comparing One Side of the Body to the Other", *Thermology*, 1:4-7, 1986.

[233] S. Umbaugh, *Computer Vision and Image Processing*, International Edition, Prentice Hall International Inc. 1998.

[234] P. Underwood, "Analysis of Thermal Images in the Diagnosis of Vascular Disease", *A thesis submitted to the University of Manchester for the Degree of MSc in the Faculty of Medicine Dentistry Nursing & Pharmacy in 2002, Department of Imaging Science and Biomedical Engineering*. Retrieved from www.furbrain.org.uk/thesis_final.pdf. (Accessed in August 2010).

[235] M. J. Varga and R. Hanka, "Automatic Thermal Image Analysis for Medical Diagnosis", *International Conference on Image Processing and its Applications*, 526-529, 1992.

[236] Localized Scleroderma, Virtual Medical Centre. Retrieved from `http://www.myvmc.com/diseases/localized-scleroderma/`. (Accessed in January 2014).

[237] L. Weibel, K. J. Howell, M. T. Visentin, A. Rudiger, C. P. Denton, F. Zulian, P. Woo and J. I. Harper, "Laser doppler flowmetry for assessing localized scleroderma in children", Arthritis and Rheumatism, 56(10):3489-3495, 2007.

[238] L. Weibel and J.I. Harper, "Linear morphoea follows Blaschko's lines", *British Journal of Dermatology*, 159:175-181, 2008.

[239] S. A. Weinstein and G. Weinstein, "A Clinical Comparison of Cervical Thermography with EMG, CT Scanning, Myelography and Surgical Procedures in 500 patients", *in Proceedings of the 1st annual meeting of the Academy of Neuromuscular Thermography*, May 1985, Postgrad Med, Special ed. 44-46, 1986.

[240] B. Wiecek, M. Strzelecki, T. Jakubowska, M. Wysocki, and C. Drews-Peszynski, *Advanced Thermal Image Processing*, Medical Infrared Imaging Book, Edited by N. A. Diakides and J. D. Bronzino, CRC Press (2008), Taylor and Francis Group, Chap 12, 2008.

[241] S. B. Wilson and V. A. Spence, "A Tissue Heat Transfer Model for Relating Dynamic Skin Temperature Changes to Physiological Parameters", *Phys. Medical Biology*, IOP Publishing Ltd., 33(8):895-912, 1988.

[242] J. Woo, B. W. Hong, C. H. Hu, K. K. Shung, C. C. J. Kuo, P. J. Slomka, "Non-Rigid Ultrasound Image Registration Based on Intensity and Local Phase Information*", J Signal Processing System*, 54:33–43, 2009.

[243] J. Wren, D. Loyd and M. Karlsson "Investigation of Medical Thermal Treatment using a Hybrid Bioheat Model", *in Proceedings of the 26th Annual International Conference of the*

IEEE EMBS, 2507-2509, 2004.

[244] Z. Xie, G. Liu, S. Wu, Z. Fang and Y. Gan, "Pennes Equation Based Blood Perfusion Model and its Application in Face Recognition", *in Proceedings of the 2010 IEEE International Conference on Information and Automation*, 2443–2446, 2010.

[245] Z. Yang and J. Pei, "3D Interpolation of Image Elastic Deformation Using Delaunay Triangulation", *Bioinformatics and Biomedical Engineering*, 2009. ICBBE 2009. 3rd International Conference, 1(4):11-13, June 2009.

[246] M. Zavisek, "Breast cancer Diagnostic using Infrared Camera". Retrieved from `http://www.feec.vutbr.cz/EEICT/2003/msbornik/01-Electronics/03-PhD/08-scallop.pdf`. (Accessed in January 2011).

[247] M. Zavisek, "Quantitative Thermography in Breast Cancer Detection - A survey of current research". Retrieved from `http://www.feec.vutbr.cz/EEICT/2004/sbornik/03Doktorske_projekty/01Elektronika/40michal.pdf`. (Accessed in January 2011).

[248] H. Y. Zhang, Y. S. Kim and Y. E. Cho, "Thermatomal Changes in Cervical Disc Herniations", *Yonsei Medical Journal*, 40:401-412, 1999.

[249] J. Y. Zhang, Y. Chen and S. X. Huang, "IR Thermal Image Segmentation Based on Enhanced Genetic Algorithms and Two-Dimensional Classes Square Error", *2009 Second International Conference on Information and Computing Science*, 2:309-312, 2009.

[250] A. Zhang and L. X. Xu, *Numerical Bioheat Transfer in Tumor Detection and Treatment*, Advances in Numerical Heat Transfer, Edited by W.J. Minkowycz, E.M. Sparrow, JP Abraham, Taylor and Francis Group, 3(5):149-196, 2009.

[251] Y. Zhang, L. Ma and R. Zhang, "A Quick Image Registration Algorithm Based on Delaunay Triangulation", *TELKOMNIKA Indonesian Journal of Electrical Engineering*, 11(2):761-773, 2013.

[252] Z. Zhu, P. Tsiamyrtzis and I. Pavlidis, "The Segmentation of the Supraorbital Vessels in Thermal Imagery", *IEEE 5th Int. Conf. on Advanced Video and Signal Based Surveillance*, 237-244, 2008.

[253] B. Zitova and J. Flusser, "Image registration methods: a survey", *Image and Vision Computing*, 21:977-100, 2003.

[254] B. Zitova, J. Flusser and F. Sroubek, "Image Registration: a survey and recent advances", *ICIP Tutorial*, Genoa, Italy, 2005.